The Application of Nuclear Microprobe Analysis in Materials Science

Johan André Mars

The Application of Nuclear Microprobe Analysis

in

Materials Science

by

Johan André Mars (M. Tech)

dissertation submitted in part-fulfilment of the requirements for the degree of

Doctorate of Technology

(D.Tech)

in the Faculty of Science at the

Peninsula Technikon

Internal Supervisor: Dr D Gihwala, Peninsula Technikon, Bellville

External Supervisor: Dr W Przybylowicz, iThemba LABS, Faure

September 2003

DECLARATION

I declare that

The Application of Nuclear Microprobe Analysis in Materials Science

is my own work and that all the sources I have used or quoted have been indicated and acknowledged by means of complete references.

ACKNOWLEDGEMENTS

This thesis was completed with the guidance and generous help of a number of people to whom I express my sincere gratitude: They are:

- Dr D. Gihwala, my internal supervisor, for his supervision and support;
- Dr W. Przybylowicz, my external supervisor, for his support and advice;
- Drs J. V. Pilcher and C. C.Theron for their assistance with the computation;
- Mr. K. Springhorn for his assistance with the electronic diagrams and efficient operation of the Van de Graaff accelerator during experiments;
- Messrs C. Doyle, S. Marsh and N. Stoddardt for efficient operation of the Van de Graaff accelerator during experiments;
- Prof. V. Linkov and Dr B. Bladergroen of the Department of Chemistry, University of the Western Cape for the ceramic-based sorption electrode supplied;
- Dr C. Curran of Infineon Technologies, for assistance in the pulsed laser deposition of the High Temperature Superconducting specimens;
- Messrs T. Beaton, J. Bock and Ms Annelise Baard of Saldanha Steel, for supplying the steel samples and fruitful discussions;
- My children, Caraigne, Brandon and André for their endearing love and moral support;
- To my Creator, to whom I am forever thankful for the health and ability his has given me.

SYNOPSIS

The impetus for the refinement and renewal of daily-used products has spurred international interest in investigating the small inhomogeneities that might exist in these products. This interest has become an important part in the design philosophy, which is based on structural information gained by the analysis of these products.

It is this drive that initiated the study to investigate the simultaneous use of novel nuclear analytical techniques such as micro proton induced X-ray emission (μ-PIXE), micro proton induced gamma-ray emission (μ-PIGE) and micro proton backscattering (μ-RBS) to achieved a broader and yet deeper insight into the fine structure of products. The fundamental underlying physical principles of these techniques are discussed to gain in-depth knowledge on how to them to obtain the desired information. Also determined was the degree of accuracy that could be attained in the application of this knowledge. These principles were evaluated in conjunction with the instrumentation with which the applicability of these techniques could then be further extended. More so is the use of sophisticated software that facilitated the use of both physical and instrumental parameters. After describing the necessary implements to achieve this further know-how, products of industrial origin were investigated to determine inhomogeneities that existed in those products and compared those theoretical values.

The first application was made to ceramic-based sorption electrodes to be used in the purification of wastewater. These sorption electrodes are tubes that consisted primarily of an alumina matrix onto which zirconia and other metals were deposited. The sorption electrodes were coated with rare-earth metals and other metals, which would constitute a conductive layer. A voltage was applied over these sorption electrodes and contaminants would adhere to the conductive surface. After purification the voltage was reversed and the contamination released. The elemental distribution of the metals and the variation in the thickness of the coat-

ing were therefore critical. The base material was analysed to ascertain the chemical composition, which would be used as grounds for further analysis. The mathematical model for the purification, developed in the course of the study, was then used to evaluate the efficiency of the coating on the base material. The chemical analysis of wastewater from the Scientific Services of the Athlone Treatment Works, Athlone, Cape Town was used in the evaluation of the efficiency of the ceramic-based sorption electrode. It was found that, for instance, in the removal of Ca, only 40 mass% of the element is removed.

In the second application, specimens of the high temperature superconductors, YBCO, were prepared by pulsed laser deposition. Together with the instrumental parameters the compositional variation in depth with pulsed laser energy density could be ascertained. Therefore by adjusting the use of the instrumentation, the composition could be quantified as the layer increased in thickness. The simultaneous use of μ-PIXE, μ-PIGE and μ-BS facilitated the objective quantification of high temperature superconductor specimens that were produced by pulsed laser beam. The inhomogeneity of the elemental distribution of the components of the $YBa_2Cu_3O_7$ layer was attributed to the interaction of these elements when the deposition was performed at high laser beam energy

The third instance, in which this demonstration was achieved, was in the quantification of steel, where, with the incorporation of residual elements, the quality of the product could be determined. This quality determination can be based on 1) the effect of elemental distribution of residual elements on the characteristics of the specimen, 2) the diffusion profile of the incorporated carbon in regions of high or low concentration and 3) the significance of chemical composition in cluster formation and the nucleation, even though this nucleation appears to be incomplete. To reach beyond the quantification of the data, this data were also applied to proposed theories, an application to verify its validity.

Whoever acknowledges me before men, I will also acknowledge him before my Father in heaven.

Matthew 10:32

Als je er bij de mensen openlijk voor uitkomt, zal Ik er ook bij mijn hemelse Vader openlijk voor uitkomen.

Mattheüs 10:32

C'est pourquoi, quiconque me confessera devant les hommes, je le confesserai aussi devant mon Père qui est dans les cieux.

Matthieu 10:32

TABLE of CONTENTS

LIST OF FIGURES AND TABLES

FIGURES

TABLES

Chapter 1

Introduction and Scope of Investigation

1.1 Introduction

Continual progress in the development of new materials is impossible without reliable methods to analyse the composition and properties of these materials. Furthermore, the refinement in the selection of materials for particular industrial applications becomes difficult and sometimes impossible without information on the small-sized inhomogeneities of the structure and composition of these materials. The emphasis on small-sized inhomogeneities is due to the present-day scientific shift from large-scale production of commodities to the miniaturisation of systems such as micromachining at the molecular level (Morgan, S., 2001).

These micromachines are of the order of micrometers (10^{-6}meters or μm) and of nanometers (10^{-9}meters or nm) in size, hence the term nanotechnology. In a few decades, they will be used to manufacture consumer goods at the molecular level, piecing together one atom or molecule at a time to make sophisticated materials and applications of various sorts. As cars, aeroplanes and computers have revolutionised the world in the last century, so nanotechnology will have an even more profound effect. So phenomenal is the surge in this direction that the United States government increased their investment in nanotechnology from an amount of $227 million in 2000 to $497 million in 2001 (Morgan, G., 2001). Nanotechnology is therefore the new frontier with a compelling impact. Although much of the basic research will take more than a decade to complete, the process itself will initiate a new industrial revolution. This technology is likely to change the manner in which almost everything is designed and constructed. The vast technical feasibilities include: self-assembling consumer goods, computers that function billions of times faster than those of the present day, novel inventions and smart materials, safe and affordable space travel, medical nanotechnology, which potentially can lead to a virtual end to illnesses. Even though vast amounts of finance have been invested in the science of nanotechnology, mass production is in the early stages of develop-

ment as the manufacture of these micromachines is still too costly (Morgan, S., 2001). There is therefore a growing demand for accurate, sensitive and non-destructive microanalytical techniques and a need to improve existing techniques in order to determine the structure and quantitative composition of specimen materials. For the purpose of this study, the new definition of the term "analytical technique" encompasses both the instrumental analysis and imaging. The techniques should be based on novel methods that arise from the discovery of new physical and chemical effects or improvements that are adaptations of well-established principles. They should also be evaluated against other methods of analysis, since it will emphasise their specific applicability over, or in preference to, other methods and will assist in finding an accurate solution to a specimen matrix by the least costly means.

Ion Beam Analysis (IBA) is a group of generally non-destructive analytical techniques used to obtain quantitative elemental information of specimens. When a specimen is bombarded with a monoenergetic beam of charged particles, moving at high speed, they interact with the electrons and nuclei of the atoms. This can lead to the emission of particles, backscattering of particles or generation of various types of radiation whose energy is characteristic of elements in the specimen matrix. The more common IBA instrumental techniques are Backscattering Spectrometry (BS), Particle Induced X-ray Emission (PIXE), Nuclear Reaction Analysis (NRA), such as Particle Induced Gamma-ray Emission (PIGE), Scanning Transmission Ion Microscopy (STIM), Scanning Electron Imaging (SEI), and Ionoluminescence (IL). This study concentrates on the simultaneous use of the three techniques of PIXE, PIGE and BS. **Figure [1.1]** gives a schematic illustration of these three IBA instrumental techniques and other related techniques. The letter "P" contained in the acronyms given in the figure, normally implies a charged particle, but in this study it will represent the proton. For the techniques of PIXE, PIGE and BS, the distinction between macro- and microanalysis is based on

the beam diameter size used. In macroanalysis, the beam sizes are normally greater than or equal to 2mm × 2mm and the beam is considered as diffused. In contrast, for microanalysis, the beam diameter size varies typically from 10μm × 10μm to less than 1μm × 1μm and the beam is described as being focused. The focusing of the beam down to the micrometer level permits the measurement of trace element inhomogeneities, which makes the IBA techniques microanalytical in nature.

In this study the emphasis is placed on microanalysis of specimens and hence the use of the terms micro-Proton Induced X-ray Emission (μ-PIXE), micro-Proton Induced Gamma-ray Emission (μ-PIGE) and micro-Backscattering Spectrometry (μ-BS). These terms will also collectively be referred to as μ-IBA techniques. Theoretical equations underlying the techniques are discussed in sections [2.2], [2.3] and [2.4]. Detectors associated with these tech-

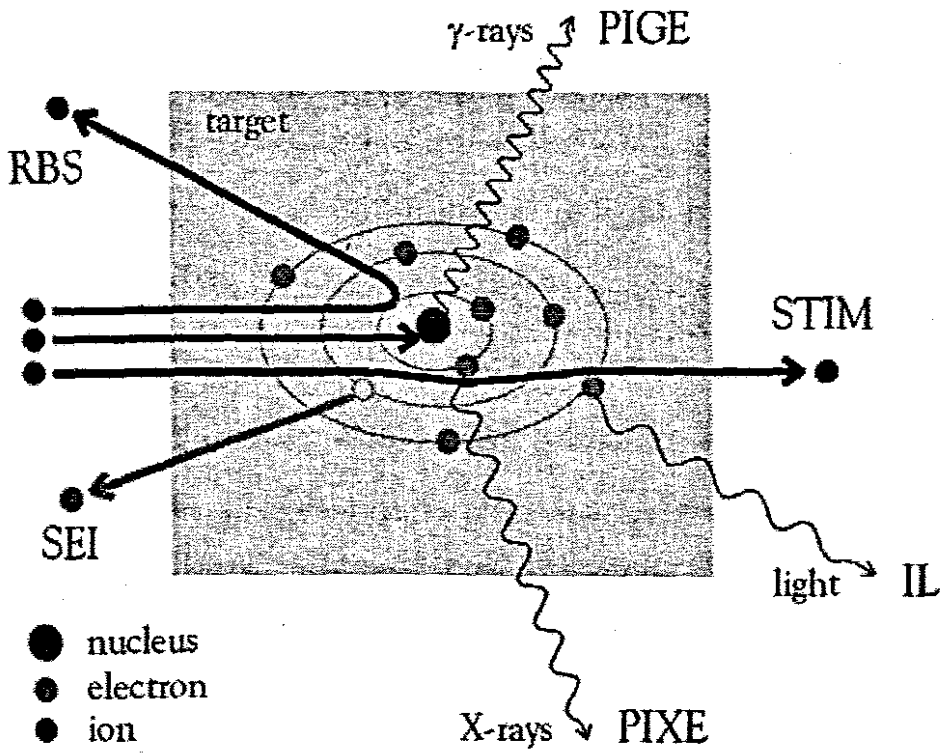

Figure [1.1] ***Schematic illustration of the origins of the Ion Beam Analytical instrumental techniques. PIGE – Proton Induced Gamma-ray Emission, BS – Backscattering Spectrometry, PIXE – Proton Induced X-ray Emission, STIM – Scanning Transmission Ion Microscopy, SEI – Scanning Electron Imaging and IL –Ionoluminescence (Butz, 1997).***

niques are housed in the nuclear microprobe (NMP) chamber. The construction of the chamber is described in section [3.2.2].

1.2 Analysis with μ-PIXE, -PIGE and -BS

In PIXE, the excitation of inner shell electrons in the specimen atoms yields vacancies, which are filled by outer shell electrons. In the process, intensities of the characteristic X-rays emitted are used for quantification of elemental concentrations. It is therefore theoretically possible to apply the ionisation cross sections of the K, L and M X-ray lines when quantifying the concentrations of elements from Na, atomic number, Z=13 to U, Z=92, illustrating the multi-elemental nature of this technique. In PIGE analysis, the excited nuclei of the bombarded specimen elements de-excite by emitting gamma (γ)-rays. The specimen composition is quantified by measuring the intensity of emitted γ-rays of its components. In BS analysis, the incident protons are elastically backscattered by nuclei of the specimen elements. Quantitative elemental concentrations and concentration depth profiles can be obtained. Multi-component and multi-layered specimens can be analysed to a depth of approximately 10 to 20 μm. The theoretical detection limits of the techniques are given in **table [1.1].** The matrices of industrial specimens can therefore be quantified by fixing the instrumental parameters at predetermined values. During irradiation, data associated with these techniques are simultaneously accumulated and applied in the quantification. The beam energy, specimen orientation, detector geometry and other initial parameters are not changed before or during irradiation. Hence, irradiating, for instance, a copper matrix with a 3.0 MeV proton beam and interposing a 125μm thick Be absorber between the specimen and detector, will yield data of all three techniques for Cu analysis. Also, the determination of light elements, such as Na, present in the matrix, which could not be determined with PIXE at these conditions, can be determined with one or both of the other techniques. The quantitative information of Cu and that of Na obtained with

the latter two techniques (PIGE and BS) is therefore complementary to PIXE. Analysis can also be performed at experimental conditions optimised for one technique only. The analysis is repeated by irradiating specimens at often higher beam energies. This is at times necessary to obtain data of better sensitivity and higher resolution from one or two of the techniques.

Table [1.1] ***Theoretical detection limits and critical parameters of the Ion Beam Analysis methods. IL is the Ionoluminescence, PIGE–Proton Induced Gamma-ray Emission, PIXE–Proton Induced X-ray Emission, BS–Backscattering Spectrometry, XRF–X-ray Fluorescence. The techniques used in this study are indicated in bold. Detection limits for macroanalysis are expressed in $\mu g.g^{-1}$, unless otherwise stated and the depth of penetration in micrometers (μm) (Butz, 1997).***

Analytical method	Typical application	Signal detected	Elements detected	Detection limits $\mu g.g^{-1}$	Sampling depth (μm)
IL	Detection and speciation of REE in minerals. Ion beam modification effects on luminescence properties of solids.	Light	Depending on host material	> 0.1	2 – 50
PIGE	**Determination of the elemental content.**	**Gamma-rays**	**B - P**	**100**	**2 – 50**
PIXE	**Determination of the elemental content**	**X-rays**	**Na - U**	**0.3 - 100**	**2 – 30**
BS	**Detection of the main elemental components. Determination of the depth profile of heavier elements in matrices of light elements.**	**Backscattered ions**	**B - U**	**0.1 – 10 at%**	**0.002-0.02**
XRF	Determination of the elemental content.	X-ray Fluorescence	Na - U	1	5

At times, not only the beam energy, but also the detector geometry, the beam particle, specimen orientation and the absorber type and thickness are changed before the irradiation is repeated. In that instance, the lower energy is preferred as resonances of the element may occur at that energy. Also, the different beam particle may induce nuclear reactions and the absorber thickness may attenuate the emitted X-rays. It should be noted that the change in absorber type and thickness only affects the yield of X-rays transmitted through the absorber and may improve the efficiency of the determination for specific ranges of elements. Since all three techniques are simultaneously used to characterise specimen matrices, it is appropriate that

previous investigations using these techniques be discussed, as results obtained in this study will be compared to those of these investigations. In the latter studies, quantitative characterisation of thick specimens was mostly performed with only one or two of the techniques, that is, with PIXE and PIGE, PIXE and BS or with PIGE and BS.

In microanalysis with PIXE and BS, Willemsen and Kuiper (1991) demonstrated that in combination with BS, the X-ray production of N, O and F could be quantified as a function of the incident particle, that is, proton or alpha. Data was accumulated at various primary energies over the range between 0.5 and 2.5 MeV. Using incident particles H^+, H^+_2 and H^+_3 ions, it was shown that X-ray emission is insensitive to the type of H-ion employed, provided the energy per atomic mass unit (amu) is the same. Hence spectra generated with 0.5 MeV H^+ are identical to spectra generate with 1.0 MeV H^+_2 and 1.5 MeV H^+_3. This is indicative of the complete dissociation of the ion into protons as it collides with the specimen surface. Willemsen and Kuiper (1991) also found that the minimum detection limits (MDLs) of PIXE is better than those induced by alpha particles. The differences are however not significant.

Using PIXE and PIGE microanalysis, Valkovic et al. (1995) evaluated standard reference materials (SRMs) that were commonly used in the evaluation of geological and environmental applications. It was established that the required minimum mass as reported in SRM certification was two orders of magnitude more than that used in ion beam analysis because of the small beam size. Therefore, in the application of PIXE, this small mass is further diminished since the major part of the X-ray yield that reaches the detector results from ionisations in the first few microns of the sample surface. This is due to X-ray absorption effects.

Quantification of metal oxides has mostly been performed with the combination of PIXE and

BS. In determining the oxygen stoichiometry in thin metal oxides, Fazinic et al. (1995) performed the determinations of oxygen stoichiometry in thin metals oxides by microanalysis with PIXE and backscattering in combination with Proton Elastic Scattering (PES). The PIXE and PES measurements were performed with a collimated proton beam of energy 2.6 MeV. The current was maintained at a few nanoamperes (nA) to prevent specimen damage. The total integrated charge varied from 0.5 to 1.0 microcoulomb (μC). BS suffers from the drawback that when using $^{4}He^{+}$ ions, a low sensitivity for light elements is exhibited. This is especially the case when the matrix is constituted of high Z elements. The relatively weak oxygen signal is submerged in the high background of the heavy elements of the superconducting YBCO layer. Using the two techniques of PIXE and BS in combination with PES indicated that PES is more sensitive than BS. Due to the relatively poor PES cross section database that exists for various elements, it is preferable to use BS (Fazinic et al., 1995). There are also possible interferences of inelastic scattering and nuclear reactions. The advantage of PIXE over BS is that with PIXE the range of elements that can be analysed is wider and PIXE spectra are relatively easier to interpret. Neither PIXE nor BS nor PES can be used alone for the determination of oxygen, but should be used as complementary techniques. Microanalysis with PIXE and BS has also been applied by Van Kan et al. (1994) to layered specimens such as High Temperature Superconductors (HTS). In this instance, PIXE measurements were performed with a collimated beam of protons of 3.0 MeV. BS analysis was performed with alpha particles at energy 3.05 MeV to measure oxygen resonance, yielded by $^{16}O(\alpha, \alpha)^{16}O$ reaction. In a similar manner, Ishii and Nakamura (1993) used PIXE and BS to quantify HTS specimens prepared by sputter-deposition. The two technique microanalysis was also applied by Ren et al. (1999) to monitor changes in Ca and Fe levels in rat brains during kainite induced epilepsy. Because of the nature of the tissue, measurements were performed at 2 MeV and with a beam spot size of 1mm. They proved that quantitative analytical information on the elemental

distributions could be extracted with PIXE at concentrations down to the $\mu g.g^{-1}$ level. Backscattered data provided information on the matrix composition, thickness and density used in the normalisation of the elemental concentrations.

Gihwala and Peisach (1982) applied two of the techniques in the macroanalysis of minor elements present in a steel matrix. Macro-PIXE determination was performed with a proton beam of energy 2.5 MeV, using currents that varied from 0.5 to 1.0nA. The beam diameter was 3.5 mm (diffused) and the irradiation period lasted for 5 to 10 minutes. The additional analysis with macro-PIGE determination was performed with 5 MeV alpha particles of the same beam diameter. The current was however higher, 100 to 200nA. The irradiation lasted for 15 to 20 minutes. The results of this macroanalysis with two techniques were the improved resolution in peaks and the reduction in the relative intensity of the sum peaks.

There are other investigations in which two or three of the techniques were used at different parameters. The investigations discussed here therefore only serve to illustrate the reason for applying the techniques at different parameters.

1.3 Scope of Investigation

The growing demand for accurate and sensitive microanalytical techniques and the need for novel methods due to the shift of the industry to nanotechnology are discussed. Examples of a combination of two of the three techniques are detailed to indicate how specimens of industrial origin can be quantitatively identified. The extent to which the nuclear microprobe is applied in material science to analysis of industrial specimens is detailed.

Chapter 2 encompasses a discussion on the theoretical fundamentals upon which the tech-

niques are based. In section [2.1], uncertainty in the radiation measurement and minimum detection limits are presented. The theoretical fundamentals of PIXE, PIGE and BS, in sections [2.2], [2.3] and [2.4], are used to elaborate uncertainties and limitations, such as the minimum and maximum energy, the angle of bombardment and minimum detection limits. Previous investigations using the techniques are evaluated and in this manner the experimental conditions for each technique are optimised. The optimisations to reduce the uncertainty of measurement are performed with protons. Improved uncertainty in measurement and MDL in the determination of some elements can however be obtained by using particles other than protons. This is discussed in section [2.5].

Facilities for irradiation and instrumental measurement of the resultant X-rays, γ-rays and backscattered particles are described in Chapter 3. The geometrical arrangements of these instruments are based on the optimisation as detailed in Chapter 2. Special emphasis is placed on the core instrumentation of this study, the Nuclear Microprobe (NMP) section, which encompasses the determination of the beam diameter and a discussion of the scanning procedure. Included is a description of nuclear instrument modules (NIMs) employed in measuring the signals. Examples of NIMs are types of peripherals used such as ADCs (analogue to digital converters), pre-amplifiers and amplifiers for measurement of the resultant radiation.

Chapter 4 describes the simultaneous application of the three techniques in the industrial environment to obtain a detailed quantification of the chemical composition of the matrices and the agreement of this quantification with existing theories or fundamental mathematical models developed in the course of this study, particularly for the zirconia-alumina ceramic-based sorption electrode. In verifying this agreement, the term "adequate description" is applied and indicates that enough existing or derived equations have been included in the model or theory.

This is in contrast to the synonymous term "closure" which normally indicates that there are no further fundamental equations by which the system can be described.

The first application, section [4.2], refers to zirconia-alumina $(Al_2O_3)_nZrO_2$ ceramic-based sorption electrodes coated with metals, particularly P. These sorption electrodes are used in the purification of domestic or industrial wastewater. The essence of this essay is to give detailed information of the distribution of the coatings and the uncertainty with which this information is obtained. This would assist in evaluating the applicability of these electrodes in the purification of wastewater by electrolysis.

The second application, section [4.3], is the analysis of High Temperature Superconductors specimens (HTS). The HTS layer consists of $YBa_2Cu_3O_{7-x}$ (YBCO), deposited on a high purity polycrystalline MgO substrate. YBCO, prepared in tablet form, was used in the pulsed laser deposition of $YBa_2Cu_3O_{7-x}$ layers of various thicknesses. The deposition was performed in an oxygen atmosphere and repeated at various laser energy densities. An investigation of the depth profile and elemental composition and distribution of the constituents of the superconducting layer versus the energy density of the pulsed laser was conducted. Of importance in this investigation is the analysis of the oxygen content in the superconducting YBCO layer at various depths and the interaction, if any, of the YBCO elements with the MgO substrate.

The third application, section [4.4], is to the quantification of steel specimens, obtained from the Saldanha Steel Company in the Western Cape, South Africa. Elements are incorporated into the steel matrix as alloying components, producing products with specific characteristics. In contrast to alloying elements, residual elements are those that are not intentionally incorporated into the steel matrix, but were present in raw materials. Of significance is the accuracy

with which the concentration and homogeneity in distribution of these elements could be determined; distribution correlation between two elements, should such a correlation exist; and, the effect of residual elements present on the distribution of alloying elements. Various solidification models have been proposed to which data obtained in this study can be applied. The Two-level Micro Macro model for dendritic alloy solidification is used to ascertain the applicability of the data. Chapter 4 ends with a discussion of the applicability of other theories or models to the data of each specimen matrix quantified.

Chapter 5 contains the appendices in which additional information pertaining to the sections in each Chapter is given.

All the investigations discussed in this study are acknowledged by detailed references in chapter 6. Information obtained from the Internet is given with respect to the date on which it was accessed, since authors seldom specify the date on which information on the web pages was revised or added. When the authors are not indicated, the web page information is cited as reference.

The simultaneous application of the three techniques PIXE, PIGE and BS was applied to investigate three different types of industrial specimens. Detailed and accurate information on the specimen homogeneity is given. This includes establishing the agreement with existing theories or those derived during the course of the study. Data were obtained by the irradiation, at fixed parameters, of the metal-coated $(Al_2O_3)_nZrO_2$ ceramic-based sorption electrodes; of $YBa_2Cu_3O_{7-x}$ deposited on polycrystalline MgO and of Steel. The simultaneous application of the techniques yielded detailed and accurate information of the elemental distribution.

Chapter 2

Uncertainty in Measurement of

X-rays, γ-rays and Backscattered particles

2.1 Introduction

Many important decisions are based on the results of accurate and precise quantitative chemical analysis. It is therefore essential to know the extent to which these results can be relied upon for the purpose at hand. Since chemical analysis is the guideline to the manufacturing industry, great emphasis is placed on the accuracy of results obtained using a specified analytical method. The uncertainty, u_Z, in instrumental measurement as a percentage of the concentration (c_Z), of any element, Z, in a matrix, m, is the confidence in the validity of the measurement. Hence, establishing the uncertainty requires the analyst to investigate all possible contributing factors. Typical sources are:

- Errors in measurement of parameters such as beam size, beam intensity and the total charge accumulated;
- Instrumental effects translated into inaccuracies of parameters such as beam instability, charge integration and nonlinearity of analogue to digital converters (ADC);
- Sample effects such as speciation; and,
- Computational effects related to the algorithms used for background correction and the accuracy of the databases used for interpolation and extrapolation of theoretical and experimental variables.

Because of the effects of all these parameters, $x_1, x_2, \ldots, x_{k-1}, x_k$, uncertainty in measurement is comprised of individual parameter contributions. In addition, the uncertainty of one parameter may influence the uncertainty of another. An example is the non-linearity of the ADC, which will affect the measurement irrespective of the beam intensity or charge integration. The total uncertainty, termed the combined uncertainty, $u_Z(x_1 \ldots x_k)$, is defined as the estimated standard deviation equal to the positive square root of the total variance obtained by combining the uncertainty of all parameters (Eurachem, 2000, equation 8.2.4, on page 26). Because of the complexity of this equation, Eurachem (2000) suggest two simple rules, namely, rules 1 and 2, for combining standard uncertainties. Rule 1 applies to equations involving only a sum or difference of quantities and Rule 2 applies to equations involving only a product or quotient.

As the theoretical fundamental equations for PIXE, PIGE and RBS only involve products and quotients, Rule 2 is used in this study. The rule is given by equation [2.1.1], where the uncertainties, $\frac{u(x_i)}{x_i}$ are the parameters, expressed as the relative standard deviations.

$$u_Z(x_1 \ldots x_k) = \sqrt{\sum_{i=1}^{k} \frac{u(x_i)}{x_i}} = \sqrt{\frac{u(x_1)^2}{x_1} + \frac{u(x_2)^2}{x_2} + \frac{u(x_3)^2}{x_3} + \ldots\ldots} \qquad \textbf{2.1.1}$$

In ensuing discussions, contributing parameters are not indicated, although their values are incorporated in calculations. Uncertainty in measurement is subject to decisions such as whether 1) the result indicates detection, 2) the analytical procedure rely upon a relatively high probability of detection of a particular element and 3) the procedure is sufficiently precise to give a satisfactory quantification. These concepts, termed respectively the decision limit, the detection limit and the reliability of the limit of determination are extensively detailed by Currie (1968). Although u_Z is important when quantifying c_Z, the general emphasis in IBA, as in any other technique, is on ascertaining the minimum detection limit, MDL (Ishii and Morita (1988), Willemsen and Kuiper (1991) and Jaksic et al. (1995)). MDL is determined to obtain the lower end of the practical operating limit-range of the method, where the method performance may be insufficient for acceptable quantification. MDL is thus not of direct relevance to the uncertainty of the measurement (Euarchem (2000) and Kinney (2002)). However, c_Z near MDL would require careful consideration of u_Z, since at low concentration determination, an increasing variety of effects, such as noise, unstable baseline and the contribution of interferences to the gross signal become important.

In these instances, the criteria recommended by Currie (1968), IUPAC (1978), Eurachem (2000) and Kinney (2002) are applied in quantifying data. In addition, parameters that collectively contribute to uncertainty in measurement may exert the same effect on all measurements performed under exact conditions. Examples of these parameters are detector efficiency, ε, and the fluorescence yield, ω, which pertain to the uncertainty in X-ray measurement.

2.2 Uncertainty in X-ray Measurement

Johansson and Campbell (1988), Tapper et al. (1994) and Johansson et al. (1995) have detailed the theoretical equations underlying X-ray emission. In this study the K, L and M X-ray lines are used for quantification.

The X-ray intensity emitted from any element depends on the concentration of such element in the specimen itself and is therefore proportional to the density of the specimen material. Proton-specimen interaction is gouverned by factors such as the stopping power, which is inversely proportional to the specimen density. Johansson et al. (1995) discussed these aspects in detail and it therefore suffices to state that these factors greatly affect u_Z and MDL, especially at low energies. Furthermore, the target thickness influences the energy loss when protons penetrate the matrix. Three types of thicknesses, namely, thin, intermediate and thick, illustrated in **figure [2.2.1(a), (b) and (c)]** respectively, are considered when formulating the

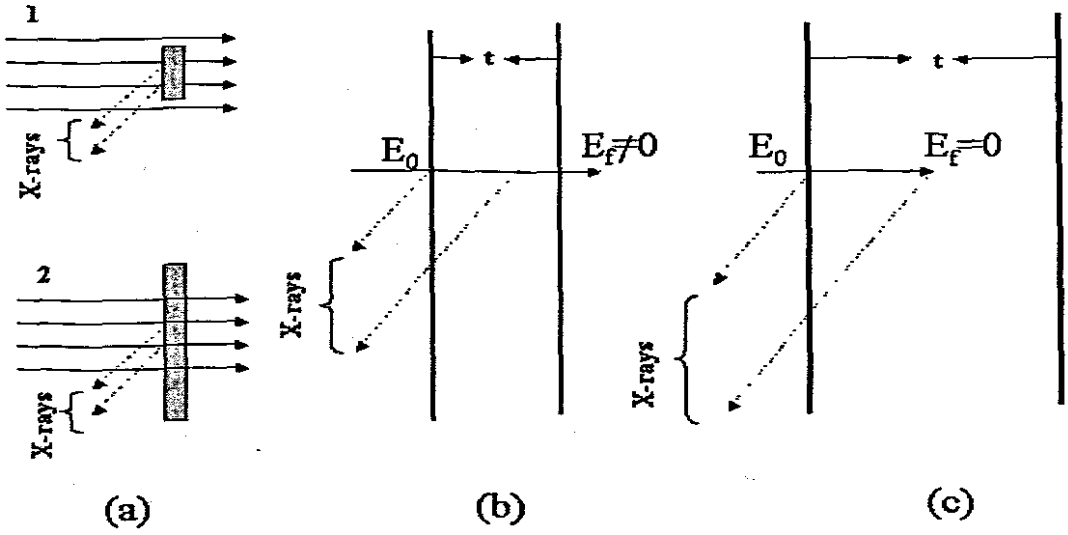

Figure [2.2.1] ***Effect of the specimen thickness on the beam penetration in Proton-Induced X-ray Emission (PIXE). t is the specimen thickness. In (a), the specimen is so thin that the beam energy is considered constant throughout the specimen thickness. In (a1), the specimen is enveloped in the cross sectional areas of the beam, whereas in (a2), the beam only samples a portion of the specimen. In (b), the beam penetrates through the intermediate thick specimen, with the dissipation of energy in the specimen. In (c), the specimen thickness is such that the beam of projectiles is stopped in the target, that is, the final energy, $E_f = 0$.***

X-ray yield, $y_X(Z)$. Johansson et al. (1995) described the derivation of the equation for each type of thickness in detail. All specimens analysed in this study are classified as thick targets. The corresponding X-ray yield is given in equation [2.2.1], where N_{av} is the constant of Avogadro, $\sigma_Z(E)$ the cross-section at energy E, ω_Z the fluorescence yield, b_Z the branching ratio of X-rays, ε_Z the detector efficiency, n_P the number of protons per second, c_Z the element concentration and a_Z the atomic mass. $T_Z(E)$ is the transmission of X-rays from successive depths within the matrix on the way out to the detector, E_0 the initial energy, E_f the final energy and S(E) is the stopping power. All terms except the cross section, stopping power and

$$y_X(Z)=\frac{N_{av}b_Z\varepsilon_Z n_p c_Z}{a_Z}\int_{E_0}^{E_f}\frac{\sigma_Z(E)\omega_Z(E)T_Z(E)}{S(E)}dE \qquad \textbf{2.2.1}$$

the X-ray transmission are not dependent on E during determination. This shows that the yield is mostly dependent on the matrix effect, which imposes the utmost reliance on theoretical and experimental databases for optimisation of MDL and the matrix correction effects.

Databases are necessary for theoretical calculations of the parameters as indicated in equation [2.2.1]. Since the introduction of PIXE in 1970 (Johansson et al., 1995), various databases or models for theoretical determination of ionization cross sections (Chen and Crasemann (1985), Paul and Sacher (1989)) have been established. The more successful of these models is the ECPSSR model of Brandt and Lapicki (1981). In this model, corrections are applied to the energy (E) loss, the electrostatic Coulomb (C) deflection from the atomic nucleus, and perturbation of the (atomic) stationary states (PSS) and inclusion of relativistic (R) effects. Perturbation allows for additional effects of electrons binding (attraction) to the projectiles during collision and ion deflection (deviation from a straight line trajectory) in the target nucleus electric field. For the ionisation cross sections, the theoretical values calculated with the model and compared to the experimental values, the K-shell values vary from 3 to 5% and those of the L-shell, from 5 to 15% (Johansson et al., 1995). During X-ray quantification, an

absorber is generally interposed between the specimen and Si(Li) detector. Backscattered charged particles are in this way prevented from coming into contact with the detector and emitted X-rays, depending on the absorber type and thickness, are attenuated. This, on the other hand, improves the relative efficiency for the determination of specific ranges of elements, particularly those present at the $\mu g.g^{-1}$ level. In this study, the X-ray attenuation through a single element material, such as Be or Al, is determined using formulae of Gullikson (2002). A combined form of these formulae, which was used in this study, is given in equation [2.2.2]. I/I_0 is the intensity ratio, ρ, the material density, d is the thickness of the material, N_{av} is Avogadro's constant, σ_a, the atomic absorption cross section and a_Z the atomic mass. Data for calculating the attenuation were obtained from Henke et al. (1993).

$$I/I_0 = \exp\left(-\rho d \frac{N_{av}\sigma_a}{a_Z}\right) \qquad \textbf{2.2.2}$$

As illustrated in **table [1.1]**, X-ray emission is generally applicable to elements ranging from Na to U, since X-ray lines from elements Li to F are practically all absorbed by the window of the X-ray detector. The interposition of an absorber such as Al would, depending on the thickness, suppress the intensity of K X-ray lines of elements from Al to Ti. In addition, K X-ray lines of Al to Ni fall in the Compton scattering region where secondary electron bremsstrahlung is high. It is therefore expected that MDLs for these elements would be worse.

When considering the range in which K X-ray energy lines may be useful for analysis, Johansson et al. (1995) and Renan (2001) established that, in general terms, the maximum energy of X-rays useful for PIXE analysis is about 35 keV. This energy corresponds to the K_β X-ray line of Cs, for Z=55. Hence, L and M X-ray lines should be used for quantifying elements Ba to U. On the other hand, the choice of K or L lines for analysis should depend ultimately on the choice of ion beam energy as well as on the availability of a particular X-ray detector with a specific efficiency profile.

From equations in Johansson and Campbell (1988) and Johansson et al. (1995), the MDL can be expressed by equation [2.2.3], where B is the background, Q is the charge, usually normalised to 1μC, Ω is the solid angle between detector and the specimen in mSr, and ε_Z^i the detector efficiency. The last term in the denominator is the attenuation of the X-rays through an absorber. The MDL of elements in a matrix is primarily dependent on the peak (area) to back-

$$MDL = \frac{3.29\sqrt{B/Q}}{\Omega y_X(Z)\varepsilon_Z^i e_Z^{-\mu x}} \qquad 2.2.3$$

ground (area) ratio. IUPAC (1978) defines MDL as that area which can reliably be determined as three times the square root of the background under the nett peak. In this study a factor of 3.29 was used instead of 3.00 in determination to increase the confidence level in the validity of the measurement.

Previous studies have been conducted in optimising instrumental parameters, and so reducing uncertainty in X-ray measurement. In assessing angular dependence of the background continuum, Renan (1980) established that the optimal condition is a detector angle of 90°. However, for the quantification of elements such as Fe, a 30% gain could be achieved at an angle of 130° and a bombarding energy of 3.5 MeV. Chu et al. (1981) have found that an angle of 135° is optimum for high sensitivity. At this angle secondary electron bremsstrahlung and atomic bremsstrahlung backgrounds are decreased relative to an angle of 90°, which is frequently used. Ishii and Morita (1988) confirmed this in their investigation into the theoretical estimation of PIXE detection limits.

Satoh et al. (1998) investigated the influence of the Compton background in a PIXE spectrum. A continuous background was found in the X-ray energy region over 23 keV when using an uninhibited signal. Shaping constants of 2μs and 6μs yield a linear relationship between the measured and theoretical counting rates. There were no significant differences in this relation-

ship up to a counting rate of 2000 counts per second (cps) when using these shaping constants. However, such high counting rates will result in pile-ups in the spectrum, which would affect the computational evaluation of the data. There was also no significant difference in the energy resolution as a function of the counting rate. The energy range for PIXE analysis is from 0.5 to 5 MeV and ideal beam energy is at 3 MeV (Ishii and Morita, 1988).

PIXE MDLs for the three specimen matrices were calculated using these parameter optimisations, equations [2.2.1] to [2.2.3] in this study, equations [1] to [7] of Ishii and Morita (1988) and $y_X(Z)$ as calculated with the Gupix program (Maxwell et al., 1988). For the Al_2O_3-ZrO_2 a 125μm Be absorber was used since the matrix contains Al. For both the steel and YBCO specimens a 102μm Al absorber was used. These MDLs are depicted in **figure [2.2.2]**. The comparison of the experimental background, obtained with the GeoPIXE II software (Ryan et al., 1995) with the theoretical background, when using these absorbers, is shown in **appendix [5.2.1]**.

Since the introduction of PIXE in 1970, a plethora of specimen matrices have been quantified. The ensuing discussion on some of these quantifications is by no means regarded as complete. The aim is rather to illustrate uncertainties in measurement, sensitivities and MDLs obtained when using different instrumental parameters. The discussion is restricted to proton induced X-ray emission but may also be applied to sections [2.3] and [2.4]. Emissions induced by particles other than protons are detailed in section [2.5], the overview to this chapter.

Campbell et al. (1988) have determined MDL for X-rays emitted from thick specimens with various matrix elements. A beam diameter varying from 1 to 2mm in diameter and proton energy of 2 MeV was used in that study. The distance between the specimen and the Si(Li) detector was 45mm.

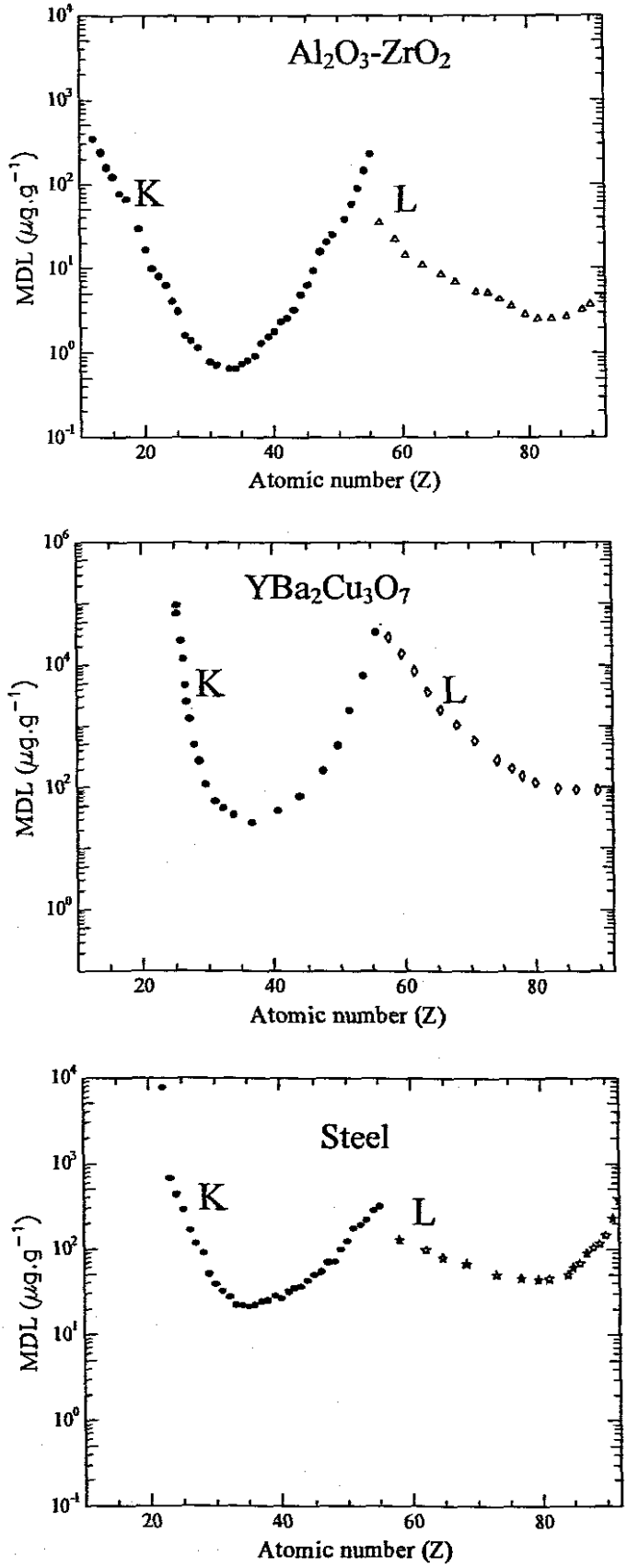

Figure [2.2.2] ***Theoretical PIXE minimum detection limits (MDLs) for elements with 13≤Z≤92 in the three matrices of Al_2O_3-ZrO_2, $YBa_2Cu_3O_7$ and steel. The calculations are based on equations [2.2.1] to [2.2.3] in this study, equations [1] to [7] from Ishii and Morita (1988) and $y_X(Z)$ as calculated with the Gupix program (Maxwell et al., 1988). The absorbers used were a 125μm thick Be for Al_2O_3-ZrO_2, a 153μm thick Al for $YBa_2Cu_3O_7$ and a 102μm thick Al absorber for steel.***

and the resolution of the detector was 170 eV at 5.9 keV. Al absorbers of thicknesses 0.025 and 0.75mm were interposed between the specimen and detector. The ECSPPR cross sections of Brandt and Lapicki (1981) were applied in the data evaluation and equation [2.2.1] was used for quantifying element concentrations. The counting rates were in excess of 5000 counts per second, which is contrary to the results of Satoh et al (1998). The irradiation period for all specimens was less than 6 minutes, which is hardly sufficient time to accumulate adequate statistical data. This rapid data collection adversely affected the MDLs, especially that of trace elements whose X-rays are emitted in the energy regions occupied by the matrix element pile-up peaks. Such pile-up can be reduced by the interposition of thicker absorbers. In this instance there is a concomitant reduction in the X-ray peak intensities of low Z lower matrix elements. MDLs for elements with Z less than and equal to 25, when suppressing X-rays with an Al absorber of 120μm thickness, varied from 100 to 600μg.g^{-1}. Similar results were obtained for matrices of Ti (Z=22), Ge (Z=32) and Mo (Z=42). On the other hand however, the high Z matrix of Sn yielded MDLs that are greater than 1000μg.g^{-1}.

Ryan et al. (1990) used a beam diameter of 20μm and a minimum current of 10 nA during the PIXE microanalysis of the SRMs, glass BCR-1, glass AGV-1 and glass GSP-1. These are primarily geological specimens such as iron-rich chromites and sphalerites. This investigation is discussed since elements in these matrices are present in comparable quantities as in the specimens analysed in this study. The Si(Li) detector used for measuring the X-ray intensities was position at 135° to the incident beam. The specimen detector distance was 25mm and the total charge accumulated was 15μC. An Al absorber of 200μm thickness was used for attenuation of K X-ray lines of elements $Z \geq 26$. The interposition of the absorber caused a hundred-fold increase in the attenuation of these X-ray lines. This permitted the concomitant increase in beam current and therefore improved MDL of the higher Z elements, but worsened

MDL for Z < 26, such as Mn and Cr. For elements with c_Z >100μg.g^{-1}, u_Z was less than 4%. The exception was Ba, Z=56, for which u_Z was ~14%. The MDL of Mn was relatively high, 10μg.g^{-1}, because the thick Al absorber suppressed the intensity of the Mn K_α X-ray line. MDLs for elements Fe to Nb were low, ~2μg.g^{-1}. The exception again was the Ba determination, with MDL given as 75μg.g^{-1}. The ratio of c_Z to the reported value was 1.11±0.05 which indicates the difference in concentration values normally observed in the analysis of SRMs. Similar micro-PIXE studies were also performed by Sie et al. (1991) and Sie et al. (1995).

Savage et al. (1992) investigated the application of PIXE and PIGE to SRM complex matrices of animal bone, coal and coal derived materials. The components of these matrices are also present in the matrix of the ceramic-based sorption electrode. MDL in predominantly Ca, coal and fly ash matrices were determined. Experimental parameters were a beam energy of 2.5 MeV and a beam diameter varying from 5 to 7mm. X-rays were detected with a Si(Li) detector of resolution of 165 eV at 5.9 keV (Mn K_α) and positioned at 135° to the incoming beam. A Mylar absorber of 925μm was interposed between the specimen and detector and the distances varied from 1.4 to 20 cm. The current varied from 40 to 70nA and the irradiation period from 15 to 30 minutes. For animal bone analysis, the relative uncertainty for elements of c_Z greater than 100 μg.g^{-1}, is less than 4%, but for c_Z less than 100μg.g^{-1} it is a maximum of 50%. This applied to both low and high Z elements. These uncertainties were however significantly less than those certified. Although MDL was not certified, the author claims limits of 1μg.g^{-1}. Elements with Z in the range 17<Z<28, lie in the energy region where secondary electron bremsstrahlung is high.

Mutual interference of X-ray lines of adjacent elements may occur. The difference in emission energies between K K_β X-ray line and the Ca K_α X-ray line is 101eV. Similarly, the en-

ergy difference for V and Cr is 16eV. Since most PIXE detectors have resolutions worse than 140 eV, separation of these spectral peaks will not be observed. This mutual interference from elemental pairs would be most severe in instances where the concentration ratio of the one element relative to the other is high. Peisach et al. (1993) investigated the concentration ranges over which each of these two elemental pairs can be quantified separately, especially the minimum concentration of the low concentration element that can still be measured. A 3 MeV beam of diameter 3.5mm was used for specimen irradiation. The X-ray intensity was measured with a $25mm^2$ intrinsic Ge detector of resolution 151 eV at 5.9 keV and 557 eV at 22.16 keV. A 135μm thick methyl metacrylate absorber was placed between the detector and specimen for attenuating the X-ray intensity and preventing backscattered protons from reaching the detector. To cope with varying X-ray fluxes from the target, the detector to target distance was varied from 2 to 22cm. For these element pairs, good accuracy and precision are achieved as long as the concentration ratio is in the order of 200 and greater. This imposes a rather severe limitation on the uncertainty in X-ray measurement when these elements are present in the matrix. Notably, X-rays of K and Ca are located on the tip of the bremsstrahlung region, where tailing effects are more pronounced and the background influences the quantification markedly.

Parameters such as thickness and low energy bremsstrahlung should be monitored to ensure that elemental maps are real images of the inhomogeneities. To demonstrate the significance of these parameters, Jaksic et al. (1995) performed a simulation microprobe scan across a hypothetical Mylar matrix containing $1000\mu g.g^{-1}$ Na and Ca each. Background radiation level was determined experimentally on real Mylar specimens, considered flat and homogenously 2.5, 5.0 and 10 μm thick. The X-ray intensities were measured with a Si(Li) detector positioned at 135° to the incident beam. Resolution was 150 eV at 5.9 keV. The areas scanned

were $1\times1mm^2$ and the charge accumulated was 0.36μC. The current was maintained at 100pA during the irradiation. Specimen to detector distance was 20mm and a 5 μm thick Be absorber was placed between the detector and specimen. MDL was obtained using the IUPAC (1978) criterion. The scanned area was divided in an array of 128×128 pixels and this translates to a pixel size of 7.8×7.8μm and 0.22pC deposited per pixel. The element concentration was selected to be present in a quarter of the specimen and MDL of 5, 15 and 50$\mu g.g^{-1}$ was obtained. It was found that only at the 15$\mu g.g^{-1}$ MDL could inhomogeneities be observed. At this detection level, the concentration of the elements Si, Ti and Co were, respectively, 67, 21 and 12 $\mu g.g^{-1}$. Inhomogeneities were clearly visible at the 50$\mu g.g^{-1}$detection limit.

Murillo et al. (1998) analysed SiO_2-Al_2O_3 matrices with a 2.62 MeV proton beam and a beam diameter of 4mm. The alumina contained in the matrix is also a major component in the matrix of the ceramic-based sorption electrodes. X-ray intensities were measured with a Si(Li) detector, of resolution 220 eV at 6.4 keV which was placed 4.5cm from the specimens. A 28μm thick Al absorber was used to suppress Al and Si X-rays and attenuate those of elements with $Z > 19$. The use of the absorber and the relatively large beam diameter permitted beam currents of up to 4nA to be applied during irradiation. Uncertainty in the X-ray measurement of elements Cl, Ti, Mn, Zn, Rb and Zr present at the $\mu g.g^{-1}$ concentration level, was relatively high, varying from 10 to 50%. At the percentage concentration level the uncertainty was relatively low, less than 4%.

It is emphasised that currents used in these investigations are greater than 1nA. Uncertainty in concentration measurement for $12 \leq Z \leq 92$ is in the range of 2 to10%. Furthermore, the MDLs for these elements were less than 150$\mu g.g^{-1}$ and areas scanned were greater than or equal to 1000×1000 μm.

2.3 Uncertainty in γ-ray Measurement

In section [2.2] it is indicated that elements Li to Mg are not quantifiable with PIXE when placing a 125μm thick Be absorber between the specimen and detector. These elements should therefore be determined by either PIGE or BS. The aim in this section is to ascertain u_Z and MDL with which the determinations can be made by PIGE.

Equations underlying γ-ray emission are discussed by Debertin and Helmer (1988), Gilmore and Hemmingway (1995), Friedlander et al. (1981) and Ehmann and Vance (1991). The energy of γ-rays emitted from nuclei, following proton-induced nuclear reactions, is indicative of the isotope present and the intensity is a measure of the concentration of the isotope. γ-rays, from prompt nuclear reactions occur with typical half lives of about 10^{-14}s. Occasionally by bombardment with protons, nuclear reactions generate excited states, which create delayed radiation after proton irradiation has terminated. Emitted γ-rays are produced by the transitions from excited states in the nuclear levels. The measured γ-ray yield for a particular nuclide, y(Z), is given by equation [2.3.1]. N_{av} is Avogadro's constant, f_Z is the isotopic abundance, $c_Z(x)$ is the nuclide concentration at depth x. M is the nuclide molecular mass, E_i the initial energy and E_0 the energy at the surface. E_1 is the energy at depth x.

$$y(Z) = \frac{N_{av} f_Z c_Z}{M} \int_{E_i=0}^{E_0} \frac{c_Z(x)\,\sigma(E_1)}{S(E_1)} dE \qquad \textbf{2.3.1}$$

The charged particles undergo range effects as they penetrate the specimen. Three known methods for correcting these effects are the method of 1) average thickness 2) average cross section and 3) the method of average stopping power. These methods were evaluated by Gihwala (1982) who found that the method of average cross section was most suitable and the mean energy, ΔE, at which the stopping powers have to be calculated, is given by equation [2.3.2]. All the definitions of symbols are as stated before. Corrections needed for range effects were eliminated by using standard reference materials (Sutton and Clay, 2001) with ma-

trix composition similar as the materials analysed. The uncertainty in measurement is there

$$\langle E \rangle = \frac{\int_0^{E_i} E\,\sigma(E)dE}{\int_0^{E_i} \sigma(E)dE} \qquad 2.3.2$$

by minimised and is mostly dependent on experimental parameters.

Notations representing nuclear reactions differ from one study to another, as detailed by Gihwala (1982), Debertin and Helmer (1988) and Gilmore and Hemmingway (1995). The nuclear reaction occurring between the incident particle, a, and the target nucleus, A, results in a heavy product, B, light products, b, the emission of a gamma-ray, γ, and energy, Q, released or absorbed. The reaction is illustrated by A + a→ B + b+ γ + Q and symbolically by A(a, bγ)B. In this study the incident particles are protons, p, and only the reactions when gamma-rays are emitted are considered. The emitted gamma-ray is generally the result of decay from one level to another. The notation used in this study will be of the form ^{az}A p(l_i, l_f) where az is the isotope number. In the case of Li, a_Z would be 7; l_i is the initial level of the de-excitation and l_f the final level. As examples; 1) the first level de-excitation in the bombardment of the Li nucleus with protons and the gamma-ray emitted at 478 keV, the reaction would be designated by ^{7}Li p(1, 0); 2) for the F nucleus, the first level de-excitation would be designated by ^{19}F p(1, 0) for the gamma-ray at 110 keV and the second level by ^{19}F p(2, 0) for the gamma-ray at 197 keV. Although not indicated in the content, the element symbol will, for clarity, be inserted to separate discussions of individual element quantification. Gihwala (1982) has extensively detailed the quantification of elements Li to Mg, in the energy range from 3.5 to 6.0 MeV. Also provided in that work is statistical information, which was used to extrapolate sensitivities to the corresponding value at 3 MeV. These values are subject to the possibility of γ-ray emissions being induced by 3 MeV proton beam under the typical geometrical conditions of nuclear microprobe analysis.

Following is a discussion about the most likely nuclear reactions considered, detection limits and interfering reactions for every element of interest in this investigation. Although based on the current geometry at the iThemba LABS microprobe where this study was done, not all elements were eventually quantified. This discussion nevertheless serves to highlight the potential of μ-PIGE, especially for industrial material analysis with 3 MeV protons. Energies and extrapolated sensitivities of the gamma rays are based on the work of Gihwala (1982). In that work, beam-induced gamma-rays and radioactive gamma-rays are stated and these background peaks were noted in this investigation.

Li

The most abundant isotope of lithium, ^{7}Li, results from first level de-excitation, for which the reaction is ^{7}Li p(1, 0) emits an intense γ-ray at 478 keV. The required threshold energy according to Gihwala (1982) is 2.37 MeV, which is easily achieved by the 3 MeV proton beam used throughout this study. The experimental geometry in the investigation was a Ge(Li) detector positioned at 45° to the incoming beam. The area detector active was 300mm^2 and MDL at beam energy of 4.5 MeV was 5μg.g^{-1}. It should be noted that the analysis was performed on pure metals. MDL, after extrapolation to 3 MeV, was 15μg.g^{-1}mC^{-1}. Gihwala and Peisach (1982) reported a MDL as 50μg.g^{-1}mC^{-1}. Olivier et al. (1983) used this reaction and found u_Z to be 0.06% for a c_z value of 3.72 mass% and MDL of 50μg.g^{-1}.mC^{-1}. The same reaction was used by Boni et al. (1990) to determine the concentration of lithium in a lithium-nickel oxide matrix. The beam energy was 3.5 MeV and a high purity germanium detector was used for detecting γ-rays. Although information on the detector resolution and uncertainty in measurement was not given, a MDL of approximately 35μg.g^{-1} is claimed. It was also found that the cross section values for ^{7}Li p(1, 0) are higher than the values obtained for the reaction ^{7}Li(p, $n_1\gamma$)^{7}Be. The excitation function for the former reaction is fairly constant in the energy range of 3 to 3.5 MeV. Kim et al. (2000) performed measurements for ^{7}Li p(1, 0) at

energies 2.4 and 3.4 MeV. They found that determination at 3.4 MeV yields better results for multielemental analysis. MDL for Li was approximately 150μg.g^{-1}. Roux et al. (1997) found similar results. However, possible interferences may be caused by the reactions ^{61}Ni n(1, 0) and ^{79}Br n(9, 3), for which a γ-ray is emitted at 477 keV. The threshold energies for these reactions are high and MDLs are greater than 10000μg.g^{-1}mC^{-1}. Li determination is therefore possible at 3.0 MeV, using the ^{7}Li p(1, 0) reaction. The MDL is expected to be 150μg.g^{-1} and u_Z to be 0.6%.

Be

In the quantification of Be by PIGE, Gihwala (1982) found the sensitivity for the γ-rays emitted at 415, 718, and 1022 keV to be in excess of 65000 μg.g^{-1}mC^{-1}. These values are relatively high and it is at this stage not recommended that Be be determined by PIGE at 3 MeV.

B

Gihwala (1982) and Gihwala and Peisach (1982) found that the proton bombardment of a pure boron matrix yielded for ^{11}B p(1, 0) an intense γ-ray at 2125 keV, which was due to Doppler broadening. MDL was 50μg.g^{-1}mC^{-1}. Interferences may be caused by the reaction ^{34}S p(1,0), with the emission of a γ-ray at 2127 keV. The sensitivity for this reaction is however 2000μg.g^{-1}mC^{-1} and the threshold energy is relatively high. In the analysis of a pure B target, Blondiaux et al. (1993) used the (p, p'γ) reaction on ^{10}B, for which a γ-ray is emitted at 718 keV. The irradiation energy was 3.1 MeV and the current maintained between 5 and 10nA for a period of 5 minutes. The γ-ray was measured with a high-purity Ge detector positioned at right angles to the incident beam. This method is rapid, simple and suitable for large numbers of samples. It however suffers from interference of Cu when present in the matrix. The γ-ray for ^{64}Cu n(4,1) is emitted at 715 keV and the sensitivity of 3000μg.g^{-1}mC^{-1}. B can therefore

be determined using this (p, p'γ) reaction should the Cu concentration be less than 3000μg.g^{-1}.

C

Gihwala (1982) reported the sensitivity for C determination as greater than 4.8 mass%.mC^{-1} and it is at this stage not recommended that C be determined by PIGE with 3 MeV protons.

N

For nitrogen determination in steel, Popescu et al. (1994) used the γ-rays emitted at 429 and 710 keV, which resulted from the reactions ^{15}N γ(2, 0) and ^{15}N γ(3, 0), respectively. MDL reported for these low intensity γ-rays are 2000 and 5000μg.g^{-1}mC^{-1} respectively. These values are in agreement with those of Gihwala (1982). Interference is caused by ^{7}Li p(1, 0) at 429 keV energy. It is therefore not recommended that the ^{15}N γ(2, 0) reaction be used to evaluate the nitrogen concentration in the presence of lithium. At E_γ of 710 keV, there is interference from ^{68}Zn γ(4, 1), for which the γ-ray is also emitted at 710 keV. The sensitivity of 50000 mass%.mC^{-1} is relatively high. Quantification of N is therefore possible in matrices of low Zn concentration, which can be preliminary ascertained with PIXE. The reaction ^{15}N γ(2, 0) can be used to quantify N concentration in the absence of Li or low concentration of Zn.

O

The y_γ(Z) and MDLs of the gamma-rays of O, resulting from the specimen bombardment with a 4.5 MeV proton beam, are given by Gihwala (1982). Interference at E_γ = 495 keV could be caused by ^{113}I n(4,0) with E_γ = 497 keV and ^{115}I n(1,0) at 497.3 keV. This interference could be ruled out by the absence of I in the specimen matrices, since iodides and iodates are evaporated at the high temperatures to which the matrices analysed in this study were heated during the manufacturing process. At E_γ = 870 keV interference are caused by ^{67}Zn p(5,0) and ^{69}Ga

p(3,0). The interference caused by Zn being present in the matrix was discussed earlier. For Ga, the sensitivity is high, which indicates that the quantification can be made at low concentrations of the element. At E_γ = 937 keV gamma rays from ^{52}Cr – 934 keV, ^{51}V – 935 keV and ^{69}Ga – 940 keV could interfere. However, at E_γ = 1042 keV or 1984 keV, the only interference could be caused by ^{69}Ga at E_γ = 1040 keV and ^{127}I p(11,0) at E_γ = 1044 keV. For the reaction ^{139}La γ(12,0), a γ-ray is emitted at 1984 keV with $y_\gamma(Z)$ <10 quanta.$sr^{-1}nC^{-1}$ and sensitivity > 23000μg.$g^{-1}mC^{-1}$. These extrapolated sensitivities and yields are only of importance should γ-ray emission be induced by the 3 MeV proton bombardment. In the determination of oxygen in a predominantly Ca matrix, Savage et al. (1992) irradiated a specimen area of 5 × 7mm^2 for a period of 15 to 30 minutes with beam of energy 2.5 MeV. The current was maintained between 40 and 70nA. The resultant γ-rays were measured with Ge detector of 20% efficiency and resolution of 2.5 keV at 1220 keV. The detector was positioned at 90° relative to the incoming beam and the specimen to detector distance was 3 cm. Under these instrumental conditions, c_Z was 35.6 mass% and u_Z was 9.3%. MDL was 1.0 mass%. Investigations made by Roux et al. (1997) to establish the analysis of oxygen by PIGE yielded results that are in close agreement with those of Savage et al. (1992). Therefore, should the nuclear reactions be induced by 3 MeV protons, then u_Z is expected to be less than 10% and MDL is expected to less than or equal to 1 mass%.

F

Fluorine determination has been performed on thick specimens, varying from geological specimens to glass matrices, bone and teeth. Although the latter two matrices are biological in nature, they are considered as thick targets and therefore included in the discussion. Mosbah et al. (1991) analysed F in glass inclusions using a 30×30μm beam-size at 3.4 MeV. Two photons of discrete energies at 110 and 197 keV are emitted following the inelastic diffusion of protons in the reactions ^{19}F p(1, 0) and ^{19}F p(2, 0) respectively. It is asserted that the use of a

3.4 MeV beam corresponds to the best value of the cross section and higher incident energy would produce an increase in the background. The integrated charge was 0.35μC and the high purity Ge detector was positioned at 120° to the incident beam and at a distance of 6.5 cm from the specimen. The resolution was exceptionally good, 1.64 keV at 1.33 MeV. MDL was 30μg.g^{-1} after accumulation of 0.5μC. u_Z relative to c_Z was greater than 10%. Instead of the IUPAC criterion of 3 times, a value of 2 times the $\sqrt{bkg}$ over the nett peak was chosen. Interference from $^{18}O(p, \gamma)^{19}F$ was not observed in the spectrum and this contribution was consequently not considered as effective. Coote (1992) and references therein, also used the ^{19}F p(1, 0) reaction to determine F in teeth and bone matrices. The instrumental parameters were the same as for Mosbah et al. (1991). The excitation functions of the 110 and 197 keV γ-rays were measured in the energy range of 3.5 to 3.8 MeV. The measurement was performed to search for intervals in which the cross section was as high and as constant as possible. MDL was 30 μg.g^{-1}. Savage et al. (1992) investigated the determination in a Ca matrix. Experimental parameters were given in the previous section. The γ-ray energy used for F determination in that work was not explicitly stated. It was rather deduced from the spectrum of the PIGE data, on page 161 of that work, that the ^{19}F p(1, 0) reaction could have been used for quantification. Of importance are the values for MDL of 1μg.g^{-1} and u_Z of 3% that were claimed. The minimum detection limit of 1μg.g^{-1} is relatively low when comparing this value to those values of the previously discussed authors. This may be due to the high current of on average 5.5nA with which the specimen was irradiated for duration of 30 minutes. Although Calastrini et al. (1998) determined F in atmospheric aerosol, the sample was deposited on Mylar foil and considered a thick specimen. The emitted γ-rays were detected with a high purity Ge detector with a resolution of 1.2 keV at 122 keV. The detector was positioned at 120° to the incoming beam. The current was maintained at 3nA during the irradiation period. The beam area was 1×3 mm^2 and the energy was varied from 2.7 to 3.0 MeV. Optimum cross-sections for the 110

keV γ-ray were found at 2.98 MeV and for the 197 keV γ-ray at 3.00 MeV.

Na

For Na quantification by PIGE, Tapper et al. (1990) determined the element in a predominantly Ca (bone) matrix by using a 4 MeV proton beam. The γ radiation was detected with a Ge (Li) detector of resolution of 2.0 keV at E_γ of 1.33 MeV. The detector was positioned at 180° to the incoming beam. The reaction ^{23}Na p(1, 0) with γ-ray emitted at 440 keV, was used in the quantification. MDL was 21μg.g^{-1} and u_Z was 50% relative to c_Z of 1530μg.g^{-1}. Valkovic et al. (1995) investigated the determination of Na and used the same reaction but at 3 MeV. Since this specimen was a NIST-SRM, scans were performed over the area to establish the degree of homogeneity of the specimen. The sizes of these scans varied from 250 to 1000μm^2. The certified average value was 840μg.g^{-1} with a relative uncertainty of 4.7%. However, u_Z varied from 12 to 16%. No minimum detection limit was given. Na can therefore be determined by using the γ-ray emitted at 440 keV. The expected MDL is 21μg.g^{-1} and u_Z would be less than 15%.

Mg

For magnesium quantification, Gihwala (1982) used the γ-rays emitted at 585 and 1369 keV, resulting from the ^{25}Mg p(1, 0) and ^{24}Mg p(1,0) reactions. The sensitivities were 310 and 86μg.g^{-1}mC^{-1} respectively. For the latter reaction, Valkovic et al. (1995) found u_Z to be 15%.

Al

Two prominent γ-rays of aluminium are emitted at 844 keV for the reaction ^{27}Al p(1, 0) with a sensitivity of 1800μg.g^{-1}mC^{-1} and at 1015 keV for the reaction ^{27}Al p(2, 0) with a sensitivity of 600μg.g^{-1}mC^{-1}. For the ^{27}Al p(1, 0) reaction, interference is posed by the gamma ray of

^{56}Fe p(1, 0), which is emitted at 847 keV with an extrapolated sensitivity of 100μg.g^{-1}mC^{-1}. Other reactions, which pose interference, are ^{55}Mn – 847 keV, ^{76}Ge – 847 keV, ^{88}Sr – 843 keV and ^{96}Mo – 843 keV. The minimum extrapolated sensitivities for these reactions are however 0.9 mass%.mC^{-1}. For the ^{27}Al p(2, 0) reaction, the interferences possible are from ^{127}I p(15, 2) with the gamma ray emitted at 1016 keV and extrapolated sensitivity of 1.9 mass%.mC^{-1}. Interferences of iodine are ruled out since the matrices were heated to high temperatures and iodine compounds are evaporated. γ-rays resulting from ^{26}Mg α(2, 0) at 1014 keV and ^{96}Ru n(4, 1) at 1013 keV have high sensitivities, approximately 1.9 mass%.mC^{-1}. Hence, the ^{27}Al p(2, 0) reaction should be used in the quantification of Al.

Murillo et al. (1998) analysed for Al in SiO_2-Al_2O_3 matrices with a 4 MeV proton beam and a beam spot size of 2mm. The ^{27}Al p(2, 0) reaction was used. A HPGe detector, positioned at 90° to the incident beam, was used for detecting the gamma rays. The crystal was 44mm in diameter and 55mm thick. The resolution of the ^{60}Co lines at 1.17 and 1.33 MeV was near to 2 keV. u_Z varied from 3.8% to 8% for c_Z of 8 mass%. No MDL was given.

P

For P quantification, data given by Gihwala (1982) were investigated. It was deduced that the γ-ray emitted at 1266 keV for the reaction ^{31}P p(1, 0) yields the best sensitivity, which was 250μg.g^{-1}mC^{-1}. The only interference posed was that of the reaction ^{65}Cu n(11, 0) for which the γ-ray is emitted at 1264 keV. The sensitivity was 0.5 mass%.mC^{-1}. This gamma ray would then be used for P determination.

Savage et al. (1992) determined P by PIGE in SRM complex matrices of animal bone, coal and coal derived materials. A 20% efficient Ge detector, of resolution of 2.4 keV at 1.27 MeV was used for detecting the γ-rays, emitted at 1266 keV. The detector was positioned at 90° to

the incident beam and 3.0 cm away from the target. u_Z was 3.4% for an average c_Z of 9.88 mass%. The MDL was 600μg.g^{-1}mC^{-1}. Tapper et al. (1990) analysed for P in bone matrices, using a 4 MeV proton beam. The gamma radiation was detected with a Canberra 80 cm^3 detector of 15% efficiency. The resolution was 2 keV at 1.33 MeV. The angle of the detector to the incident beam was 0°. u_Z was relatively high, 51% for an average c_Z of 6.74 mass%. A MDL of 300μg.g^{-1}mC^{-1} was obtained.

Fe

Gamma radiation resulting from the proton bombardment of the Fe nucleus is emitted at various energies. These are 847 keV for the ^{56}Fe p(1, 0) reaction, 1377 keV for ^{56}Fe α(2, 0) and ^{57}Fe n(2, 0) and at 1757 keV for ^{57}Fe α(5, 0). The corresponding extrapolated sensitivities are 1090, 8600 and 5600μg.g^{-1}mC^{-1}. The interference of ^{27}Al p(1, 0) at 845 keV with the 847 keV gamma ray are discussed under Al. From the data given in Gihwala (1982), the interferences at the other gamma ray energies all have sensitivities of 3000μg.g^{-1}mC^{-1} and more. Furthermore, Fe can be determined with PIXE, even when using relatively thick filters such as 102μm aluminium. Hence, for the purpose of this study, the gamma ray emitted at 847 keV will be used for Fe quantification should Al be absent from the matrix, else the gamma ray at 1377 keV will be used.

In the previous discussion, the minimum detection limits cited are relatively low and uncertainties high. The currents and beam diameters used in these determinations are an order of magnitude greater than those intended for this study. For this reason various matrices were irradiated with 3 MeV protons to ascertain whether values, obtained from Gihwala (1982) and extrapolated to this energy, are acceptable. The MDLs are given in **table [2.3.1]**. The chemical composition of the matrices are: Apatite, $Ca_5(PO_4)_3(F,Cl)$, used for Ca, F, and P determination, Kaersutite, $Ca_2Na(Mg,Fe)_4TiSi_6Al_2O_{24}H_2$, in the determination of Na, Mg, Al, Si and

Fe, Spodumene, $LiAlSi_2O_6$ in Li, Al and Si determination, Tugtupite, $Na_4BeAlSi_4O_{12}Cl$,

Table [2.3.1] ***PIGE uncertainties in measurement and minimum detection limits of elements considered as light elements when using a 3 MeV proton beam and a 125μm thick Be absorber for PIXE and of Al, P and Fe. The matrix and element concentrations are indicated. The beam diameter was 3μm × 5μm and the charge accumulated 1μC. The detector to specimen distance was 17 cm.***

Element symbol	γ-ray energy (keV)	Reaction	Matrix	c_Z mass%	u_Z %	MDL ($\mu g.g^{-1}\mu C^{-1}$)
Li	478	^{7}Li p(1, 0)	Spodumene	3.42	2.42	70
B	428	^{10}B α(1, 0)	Boronitride	43.0	4.35	380
	2125	^{10}B α(1, 0)	Boronitride	43.0	1.15	180
F	110	^{19}F p(1, 0)	Apatite	3.63	1.04	50
	197	^{19}F p(2, 0)	Apatite	3.63	0.78	30
	1234	^{19}F p(3, 1)	Apatite	3.63	20.6	880
Na	440	^{23}Na p(1, 0)	Tugtupite	18.6	1.78	250
	440	^{23}Na p(1, 0)	Kaersutite	1.32	3.12	230
	1634	^{23}Na α(1, 0)	Kaersutite	1.32	2.37	250
	1634	^{23}Na α(1, 0)	Tugtupite	18.6	2.38	230
Mg	585	^{25}Mg p(1, 0)	Kaersutite	6.58	17.6	1650
	1369	^{24}Mg p(1, 0)	Kaersutite	6.58	8.59	610
Al	844	^{27}Al p(1, 0)	Kaersutite	6.54	12.2	760
	844	^{27}Al p(1, 0)	Spodumene	14.50	13.3	740
	844	^{27}Al p(1, 0)	Tugtupite	5.77	12.1	780
	1015	^{27}Al p(2, 0)	Kaersutite	6.54	4.45	480
	1015	^{27}Al p(2, 0)	Spodumene	14.50	4.93	420
	1015	^{27}Al p(2, 0)	Tugtupite	5.77	5.11	470
P	1266	^{31}P p(1, 0)	Apatite	18.30	6.45	1260
Fe	847	^{56}Fe p(1, 0)	Kaersutite	9.51	14.5	220
	847	^{56}Fe p(1, 0)	Pentlandite	30.77	5.52	200
	1377	^{56}Fe α(2, 0)	Kaersutite	30.77	16.9	7500
	1377	^{56}Fe α(2, 0)	Pentlandite	9.51	6.59	6090

for Na and Be, boron nitride used for determining B and N and Pentlandite, $(Fe,Ni)_9S_8$, for Fe determination. No γ-rays were observed for C, Be, N and O. With the exception of Mg determination at 1367 keV, the uncertainties in concentrations compare favorably with those values obtained at higher energies, currents, larger beam diameters and smaller detector to specimen distances.

2.4 Uncertainty in Measurement of Backscattered Particles

It is established in section [2.2] that Be, C, N and O could not be determined with PIXE since their X-rays are practically completely absorbed by the window of the X-ray detector. In section [2.3] it was determined that they should not at that stage be determined with PIGE since 1) MDLs at this stage are relatively high or 2) nuclear reactions leading to γ-ray emissions could not be induced. Ion BS is the last of the three techniques used in this study. It is therefore necessary to ascertain u_Z and MDLs with which the determinations can be made. Also, BS data of other elements can be used to establish complementarity with PIXE and PIGE

The underlying fundamental physics principles of BS have been discussed by Chu et al. (1978), Deconninck (1978), Rauhala (1992), and Rauhala (1994). For a smooth surface, bombarded with a beam of protons, the BS yield, $y_{bs}(E)$, (Deconninck, 1978), is given by equation [2.4.1]. n_p is the number of protons, c_Z is the areal concentration in $g.cm^{-2}$, E the energy at depth x, $\sigma(\theta, E)$ the ionisation cross section at back scattering angle θ and energy E, Ω is the detector solid angle, S(E) the stopping power and k_Z is the kinematic factor. (k_Z, instead of K,

$$y_{bs}(E) = \frac{n_p c_Z \sigma(\theta, E) d\Omega}{S(E)\left[\frac{k_Z S(E)}{S(k_Z E)} - \frac{1}{\cos\theta}\right]} \qquad \textbf{2.4.1}$$

represents the kinematic factor to avoid confusion with K in PIXE for K X-ray lines). k_Z is significant as it indicates the ability to perceive mass, a_Z, hence resolving elements and depth at the angle, θ. Since for the proton a_Z and z is 1, k_Z is non-relativistically given by equation [2.4.2] as a monotonically decreasing function of the target mass and the cosine of θ. Values of k_Z for θ and a_Z are found by setting $Mk/M\theta = 0$. For this study, a_Z varies between 6 and 92.

$$k_Z(a_Z, \theta) = \frac{2\cos^2\theta + a_z^{\,2} - 1 - 2\cos\theta\sqrt{a_z^{\,2} + \cos^2\theta - 1}}{(1 + a_z)^2} \qquad \textbf{2.4.2}$$

θ is optimised to yield θ→ 0°, 180° as solution, which have obvious practical implications

when considering the dimensions of the detector. Hence, uncertainty in k_Z is minimised by performing measurements as near to 180° as possible with respect of the incident beam. The mass resolution at the specimen surface is primarily due to the detector resolution. Energy straggling and factors such as contributions by lateral spreading, multiple scattering, beam area on the target and the detector acceptance angle, normally dominate in layers deep in the specimen. With θ constant and the energy separation denoted by ΔE_1, equation [2.4.3] yields the mass resolution for an element M_2. The first term is the total system energy resolution per incident energy. Denoting the kinematic factor of the major matrix element by k_Z^m, the kine-

$$\delta M_2 = \left(\frac{\Delta E_1}{E}\right) \times \left(\frac{dM_2}{dK_{M_2}}\right) \qquad \textbf{2.4.3}$$

matic factor of any other matrix element by k_Z and the silicon surface barrier detector (SSB) resolution by Γ_{SSB}, then the resolution of these two elements are given by equation [2.4.4]. The value of 5 is a useful guideline suggested by Deconnick (1978). The uncertainty parame-

$$E\left|k_Z^m - k_Z\right| \geq 5\Gamma_{SSB} \qquad \textbf{2.4.4}$$

ter introduced by equation [2.4.4] is the ability to resolve, with respect to the detector resolution, two matrix elements. Γ_{SSB} = (28±3) keV and this translates into Z=4 when not considering the useful limit as suggested by Deconninck (1978). The limitation in mass resolution is partly due to the detector system subtending a finite solid angle. Deconninck (1978) indicated that the energy spread introduced by the finite size of the detector is insignificant at large scattering angles. The differential cross section, $d\sigma/d\Omega$, is given by Deconninck (1978), shows the direct dependence of $d\theta/d\Omega$ on Z. Since θ was optimised, $\theta \rightarrow 0°, 180°$, hence $\sin(\theta/2) \rightarrow 1$, the differential cross section, expanded in a power series (L'Ecuyer, 1979), is now given by equation [2.4.5]. It indicates that in thick predominantly light element specimen matrices, heavy

$$\frac{d\sigma}{d\Omega} \propto \left(\frac{Z}{E}\right)^2 \left(1 - \frac{2}{a_z^2}\right) \qquad \textbf{2.4.5}$$

elements, even in low concentrations, will be readily detectable. Light elements however, in

concentrations as high as 30 to 70 atomic% could be left undetected.

The preceding optimisations to minimise uncertainty in ion BS measurement was based on the elastic collision of the energetic proton with the specimen atoms. For non-elastic interaction, that is, where energy is not conserved, ratios of the cross sections to the Rutherford cross sections, σ/σ_R, were obtained from the database Sigmabase (2001). The database is a compilation of contributions of these ratios, at backscattering angles $\leq 170°$, of various authors. However, in this study, the silicon surface barrier detector (SSB) was positioned at 176° to the incident beam. Amirikas et al. (1993) used Breit-Wigner functions to compute the proton resonance at angles of 110°, 150° and 170° in the laboratory frame. The parameters of the resonance formula, used to yield an accuracy of $\leq 2\%$, are only of statistical significance. From this investigation it deduced that the difference between the cross sections at the laboratory angles of 170° and 176° would not be significant. Hence, cross section values at the former angle were used in this study. Proton backscattered resonance spectra for the reactions $^{7}Li(p, p)^{7}Li$ (Knox et al., 1990 and Knox, 1992), $^{9}Be(p, p)^{9}Be$ (Mozer, 1956 and Knox, 1992), $^{10}B(p, p)^{10}B$ (Chiari et al., 2001), $^{12}C(p, p)^{12}C$ (Amirikas et al., 1993, Gurbich, 1997, Gurbich, 1998, Gyarmati et al., 1981, Mazzoni et al. I and Mazzoni et al. II), $^{14}N(p, p)^{14}N$ (Olness et al., 1958, Knox, 1992, Mars et al. I, 2003, and Bashkin et al., 1959), $^{16}O(p, p)^{16}O$ (Amirikas et al., 1993) $^{13}Al(p, p)^{13}Al$ (Chiari et al., 2001), $^{14}Si(p, p)^{14}Si$ (Amirikas et al., 1993) were used.

The MDLs of elements in the three matrices were calculated using the preceding equations, the respective resonance data and Γ_{SSB} of (28.0 ± 3.0) keV. The RUMP software program of Doolittle (1985) was used to simulate the minimum detectable limits. Simulations were done for one element present in the matrix and therefore do not illustrate the effect of one light element on the minimum detection limit of another. In determining the minimum detection limits of these elements in the $(Al_2O_3)_nZrO_2$ matrix, the concentration of Al_2O_3 used was 98

mass% and 2 mass% for ZrO_2, corresponding to the ceramic-based sorption electrode matrix. The porosity of the sorption electrode was not considered. The effect of elements such Cu, Zn, Cr, Mn and P that may be present in each matrix in relatively low concentrations has also not been considered. The energy of backscattered particles from a depth in the specimen depends on the kinematic factor and the energy loss. To be detected the ion must emerge at sufficient energy E_1, for which Chu et al. (1978) established an arbitrary accessible depth criterion of $E_1 \geq 0.25 k_Z E_0$. Variation in atomic bulk density also influences the accessible depth since in certain areas of the specimen, the depth reached would be deeper than in other areas. The MDLs are given in **figure [2.4.1]**.

Ample studies have been done in the use of a proton beam for the determination of oxygen with BS. Of special interest is the geometrical arrangement of the detector to the incoming beam. Most of the BS oxygen determinations were performed on HTS specimens, in which the content of this element is of critical.

In their study of stoichiometric determination of thin metal oxides (ZrO_{2-x}) on Al substrates, Fazinic et al. (1995) increased the proton beam energy to 4.6 MeV to achieve acceptable resolution of the Al and O resonance peaks. In this energy region the oxygen cross section for elastic scattering emits broad resonance behaviour and this was used to resolve the Al and O resonance peaks. Amirikas et al. (1993) established the oxygen resonance peaks at energies 3.47 MeV for protons. However, as stated earlier, the resolution of the proton backscattered resonance peaks for Al and O should still be resolvable, even at 3.0 MeV. In the determination of elemental constituents in high voltage insulator borosilicate glasses under proton bombardment, Borbely et al. (1985) demonstrated that combined PIXE and PIGE measurements are suitable for the accurate determination of oxygen in these specimens.

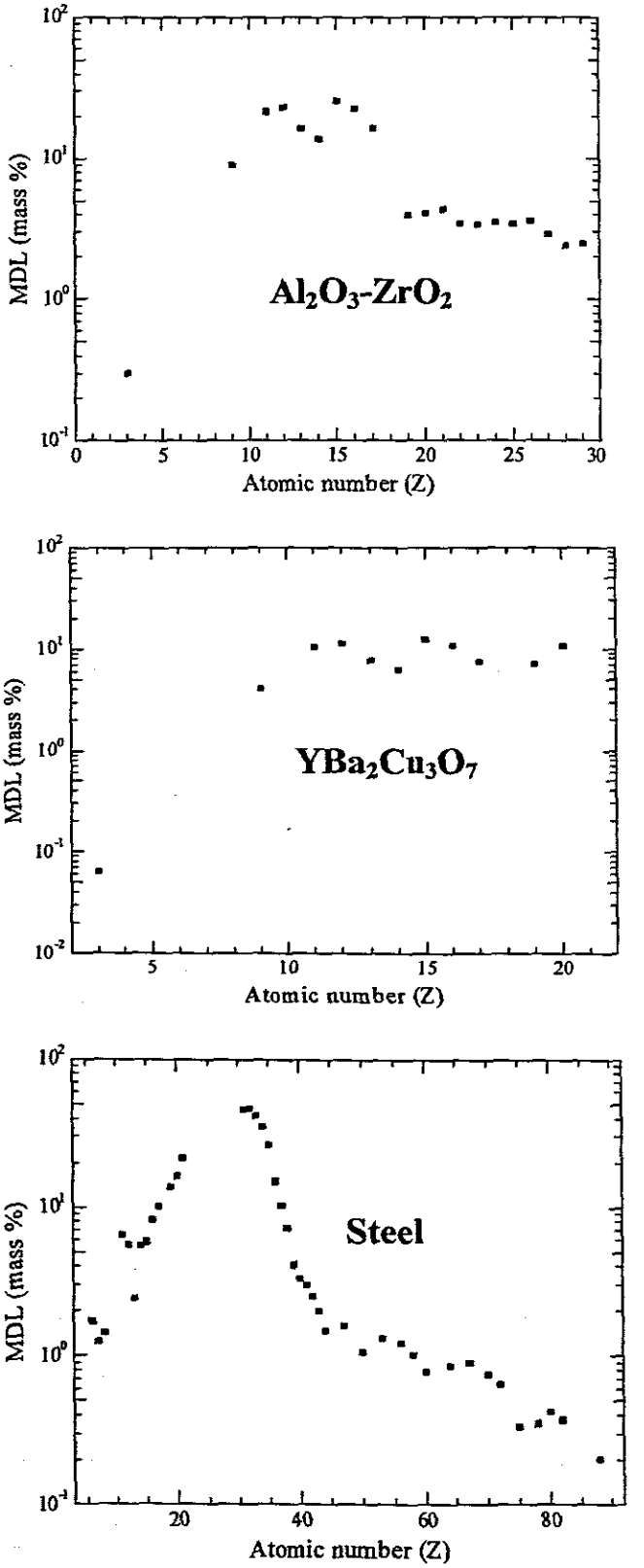

Figure [2.4.1] ***Theoretical proton backscattering minimum detection limits (MDLs) of elements in the matrices of Al_2O_3-ZrO_2, $YBa_2Cu_3O_7$ and Steel. MDLs were determined by simulation at 3.0 MeV and using equation [2.4.4]. Proton resonance data for Al and O, used in the simulation, were obtained from Chiari et al. (2001) and Amirikas et al. (1993) respectively.***

2.5 Overview to Sections [2.2], [2.3] and [2.4]

In the quantification of Li, B and F in section [2.4], it is assumed that PIGE yields minimum detection limits that are lower than those for BS. Although this is evident from the proton resonance data of these elements, as given by the different authors in Sigmabase (2001), it should still be evaluated, as it would influence the complementarity amongst the techniques.

It is stated in Chapter 1 that the purpose of this study is to enable the quantification of elements with MDLs in the $\mu g.g^{-1}$ range. However, from sections [2.2], [2.3] and [2.4], it is apparent that analytical applicability of the three techniques in quantifying the MDLs of elements such as Be, C, N and O, leaves much to be desired. as indicated in section [1], X-ray emission induced by proton bombardment yields slightly better uncertainties and MDLs. The emphasis in this section will therefore be on the effect particles other than protons have on u_Z values and MDLs when inducing the nuclear reactions. Hence, the discussion will focus on the PIGE and BS determinations with these other particles.

Lappalainen et al. (1983) used α-particles to induce γ-ray emission for the verification of minimum detection limits in thick specimens. The beam was passed through a liquid nitrogen cold trap before interacting with the specimen. The γ-rays were detected with a Ge(Li) detector that had a resolution of 1.9 keV at $E\gamma$ = 1.33 MeV and 3.0 keV at $E\gamma$ =2.61 MeV. The detector, of volume 100 cm^3 and efficiency of 21%, was positioned at 55° to the incoming $^4He^+$ beam of 2.4 MeV. The beam diameter size was 4×4 mm^2 and the current varied from 0.5 nA to 10 nA. The exceptionally good detection limits for elements Li, Be, B and F were respectively 0.45, 0.42, 10 and 22$\mu g.g^{-1}$. Moreover, these detection limits were obtained for matrices, of high concentrations of light elements, such as O, Na, Mg, Al and C. The minimum detection limits for N, O and Mg were relatively high. The respective detection limits are 1.1, 2.0 and 1.3 mass%. Only the Na MDL of 260$\mu g.g^{-1}$ was comparable to those discussed in the

previous sections. No uncertainties in measurements were given. γ-rays for C were not emitted, even though 3 mC of charge was accumulated. The MDLs of elements Li, Be, B and F were slightly lower than those induced by proton bombardment. However, the compromise in the minimum detection limits of the other elements is considerably higher. For this reason quantification should preferably be performed with protons. Furthermore, higher currents and bigger beam diameter sizes which, are comparatively greater than those predetermined for this study, were used in the determinations.

Coote (1992), and references therein, have performed investigations into the quantification of F. The experimental parameters have been described earlier in this study. For α-induced γ-ray emissions, they used the nuclear reactions, with the corresponding Q values, $^{19}F(\alpha, \alpha'\gamma)^{19}F$, Q=0 MeV, $^{19}F(\alpha, n\gamma)^{22}Na$ with Q = -1.950 MeV, and $^{19}F(\alpha, p\gamma)^{23}Ne$ with Q = 1.675 MeV. High γ-ray energies were detected with NaI(Tl) and BGO detectors. The minimum detection limits of ~ 10μg.g^{-1} obtained are in agreement with those indicated in the previous discussions. Deuterium-induced γ-ray emission was based on the reactions $^{19}F(d, p)^{20}F$ with Q = 4.379 MeV and $^{19}F(d, \alpha)^{17}O$ with Q = 10.038 MeV. The minimum detection limits for these reactions are comparable with those obtained by bombardment with α-particles.

Volfinger and Robert (1994) used α-beam of 3 MeV to induce γ-ray emission. The beam diameter size was 100×300 μm^2 and the current was 25nA. The specimen was irradiated for duration of 1000 seconds. The respective detection limits for the elements Be, Li, B and F were 20, 25, 900 and 450μg.g^{-1}. Although these values are relatively higher than those stated earlier, it should be noted that the beam diameter is at least an order of magnitude smaller than those of the other investigations. No uncertainty in measurement was provided.

Gihwala and Peisach (1986), in the quantification of oxygen, used deuterium to induce the γ-

ray emission. The prompt γ-ray emitted at 871 keV for the nuclear reaction, $^{16}O(d, p\gamma)^{17}O$ was employed for the quantification. The highly abundant isotope ^{16}O is the target nuclide and the reaction was considered as offering adequate sensitivity for determining low concentrations of oxygen. The deuterium beam energy was 2 MeV and the current varied between 0.5 to 10 nA. The beam was diffused, with a size of 2mm × 2mm and the Ge(Li) detector was shielded with lead. The MDL was 120 $\mu g.g^{-1}mC^{-1}$ and the uncertainty, u_z, was ±3.8%. Giles (1978), in this regard, have also done extensive studies using alpha particles.

Peisach et al. (1989) used a thin intrinsic Ge detector in their survey of low energy photons emitted for 77 elements. The proton beam energy ranged from 3.5 to 6. MeV. The detector resolution was 1.1 keV at 1.33 MeV and hence photons that were potentially useful for analysis could be identified.

Lackay et al. (1990) and Lackay et al. (1991) used low energy photons induced by proton bombardment for the analysis of noble metals. Terwagne et al. (1995) showed that ^3He particles can be utilised for simultaneous quantitative microanalysis of light elements and placed special emphasis on the quantification of C and O. Deuterium-induced nuclear reaction, (d, p) and (d, α) cross sections are relatively higher than the cross sections induced by ^3He. However, reactions induced by ^3He produce two orders of magnitude less neutrons at the same energy.

It evident from this discussion that the choice of the bombarding particle will depend on the element of interest. The use of a thin intrinsic Ge detector is recommend since 1) the resolution of the Ge(Li) is insufficient to cope with the high density of photopeaks that occur in the spectrum and 2) the efficiency of the Si(Li) detector is very low for photons with energies above 30 keV.

Chapter 3

Experimental

3.1 Introduction

The Van de Graaff accelerator facility is capable of generating up to 6 MV. In addition, the multidisciplinary and multi-user design and the nature of data acquisition of the facility comply with demands such as the flexibility to handle a wide variety of experiments.

3.2 Irradiation facilities

3.2.1 Van De Graaff Accelerator

In the Van de Graaff accelerator, the beam of ions is accelerated vertically downwards and the energy stabilization and beam selection are made by a 90^0 analyzing magnet. From the generator the beam passes through the energy control slits and then to the switching magnet, which allows the beam to be directed either to the nuclear microprobe section of to the solid-state section. The ions travel through a horizontal flight path of about 15 meters on the Nuclear Microprobe line. This is illustrated in **figure [3.2.1]**. Although the long flight path of the ions offers possibilities such as ultimate beam spot sizes, it renders the beam more susceptible

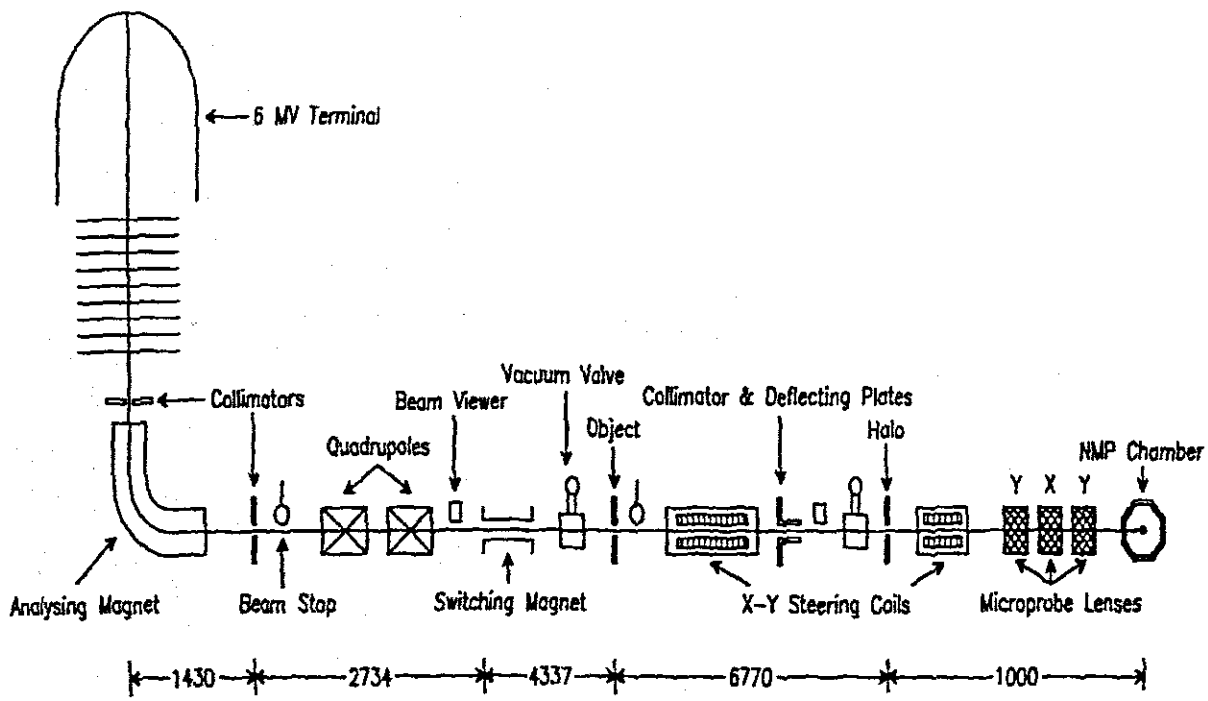

Figure [3.2.1] ***A schematic illustration (drawn not to scale) of the Van de Graaff Accelerator and the nuclear microprobe (NMP) facility at the Materials Research Group, iThemba LABS (Prozesky et al., 1995).***

to instabilities. This invariably leads to vertical movement of the beam (Prozesky et al. (1995)). To reduce the effect of these instabilities on the dead time of X-ray measurements and to reduce the intensity of pileup peaks in the PIXE spectrum, a beam on demand deflection system, discussed in section [3.2.3], was constructed. After the this system, the beam passes through a set of collimators slits to the Oxford standard triple set of lenses. The set of lenses offers small aberration and subsequently small beam sizes.

3.2.2 Nuclear Microprobe

3.2.2.1 Construction

A photograph of the nuclear microprobe system from the collimator slits to the chamber is shown in **figure [3.2.2]**. From the switching magnet the beam passes through object slits to

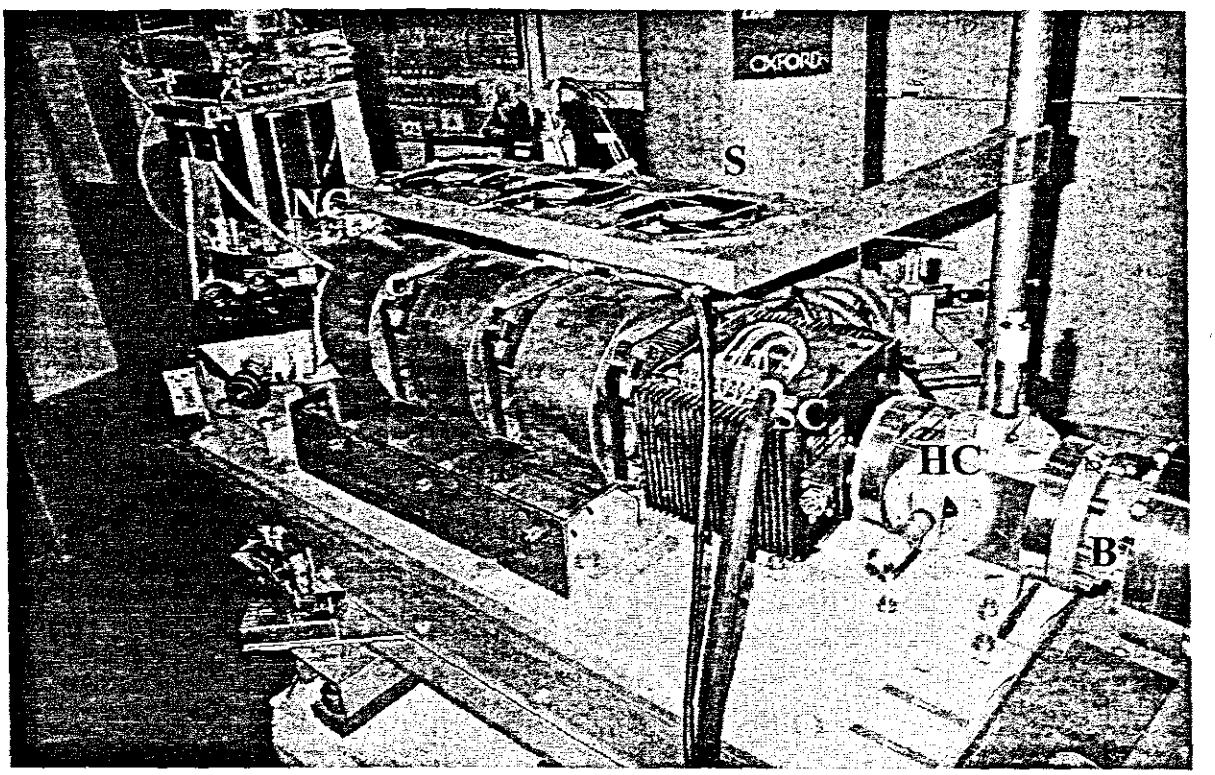

Figure [3.2.2] ***Photograph showing the construction of the nuclear microprobe (NMP) system. B is the beamline, HS the halo slits, SC is the scanning coils used when positioning the beam on the specimen, S is the container for cooling the Si(Li) detector used in the identification of X-rays, C the microprobe lenses, used in the focusing of the beam, M the microscope for viewing the specimens and NC is the nuclear microprobe chamber.***

the steering coils, which are used for corrections of the beam path (mainly corrections for the Earth magnetic field) and operates in the x-y direction. It then passes through the microprobe lenses to the nuclear microprobe chamber. The chamber is the standard chamber, manufactured by Oxford Microbeams (1985), made of stainless steel. Features of the chamber, shown in (**figure [3.2.3]**), include a microscope, a Si(Li) X-ray detector placed about 25 mm away from the specimen at an angle of 135^0 to the incoming ion-beam. An annular silicon surface barrier detector for ion backscattering, is situated at 176^0 to the direction of the incoming ion

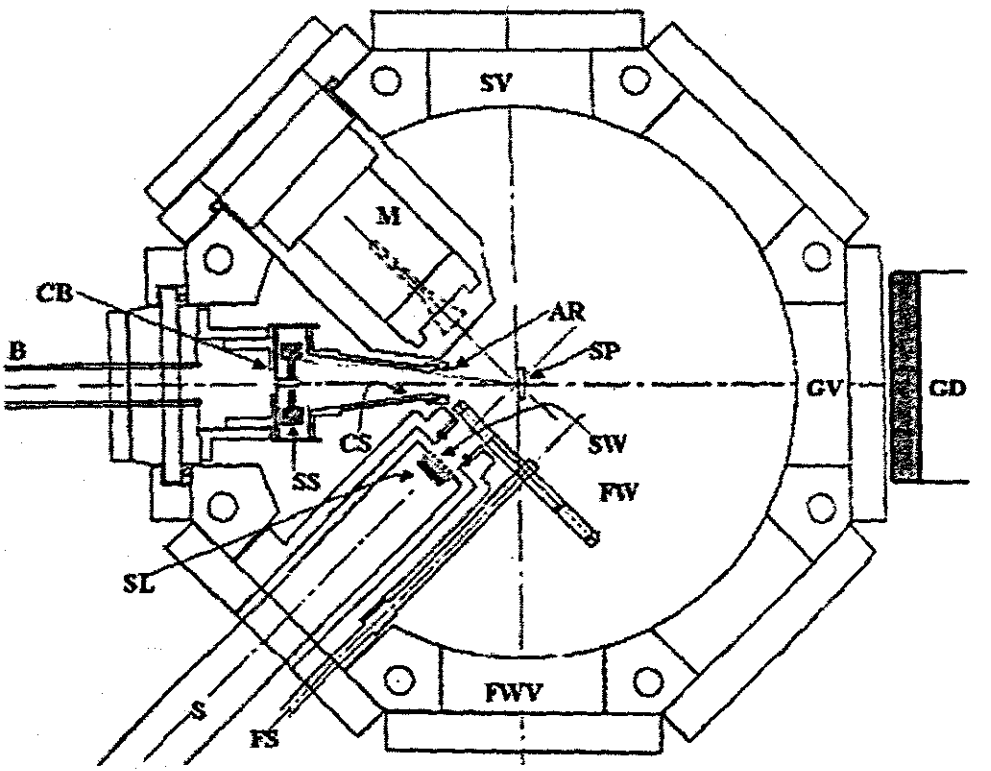

Figure [3.2.3] ***Top cross-sectional view of the NMP chamber. SV is the specimen view port, M the microscope, B the incoming beam, CB the collimator preventing the reflection of beam, AR the suppression ring, SP the specimen, SS the silicon surface barrier detector, CS the collimator prevent the beam from being reflected on the surface barrier detector, S the Si(Li) detector, SL the gold layer, SW is the Si(Li) detector window, FW the filter wheel and FS the shaft for changing filters. FWV is the view port for the filter wheel, GV a view port and GD is the γ-ray detector.***

beam. CB is the collimator of the incoming beam positioned in the inner hole of the annular detector. CS is the collimator preventing backscattered particles from coming into contact with the glue lining of the annular silicon surface barrier detector (SSB). A filter wheel with an array of absorbers, including, Be, Al and Kapton, of various thicknesses, is housed in front

of the Si(Li) detector for selective attenuation of generated X-rays. The gamma-ray detector is positioned at 0° to the incident beam. Two separate light sources are provided, one in front of the specimen, for reflected light, and one behind the target, for transmitted light. The lid of the chamber is custom-made to allow flexibility in specimen loading and movement by means of a stepper motor control. This flexibility permits movement of the specimen ladder 30 mm in the x-direction, 30 mm in the z-direction and 250 mm in the y-direction. This control and large movement enabled the installation of the Astimex standards (Sutton and Clay, 2000).

3.2.2.2 Beam on demand deflection system

This beam on demand system, illustrated in **figure [3.2.4]**, consists of two plates that operate at ground potential, allowing the beam to pass to the target. The plates are 40 cm long and located 2 m from the specimen. They have a 3 mm collimator for protection and this collimator also serves as a beam divergence delimiter. The beam dump is situated 1 m away from the plates and in front of the halo slits. The power supply, based on CMOS switches, was in corporated for this purpose, accepting the high voltage (HV) signals from the normal NIM HV

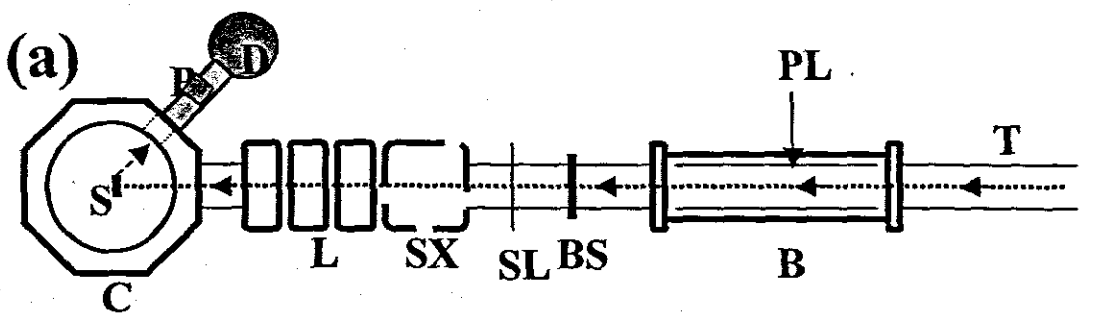

Figure [3.2.4] ***Illustration (not to scale) of the location of the beam on demand deflection system with respect to the nuclear microprobe (NMP) chamber. T is the tube through which the beam is passed, B is the beam-on-demand system, PL indicates one of the plates with which the beam is deflected from the specimen, BS is the beam stop, a valve for opening and closing the passage for the beam, SL are the object slits and S the scanning coils used to position the beam on the specimen. L are the quadruple lenses for focusing the beam, C is the NMP chamber, S the specimen, mounted on a movable ladder, D is the Si(Li) detector and P the detector pre-amplifier. The plates have a length of 40 cm and are situated 2 meters from the specimen.***

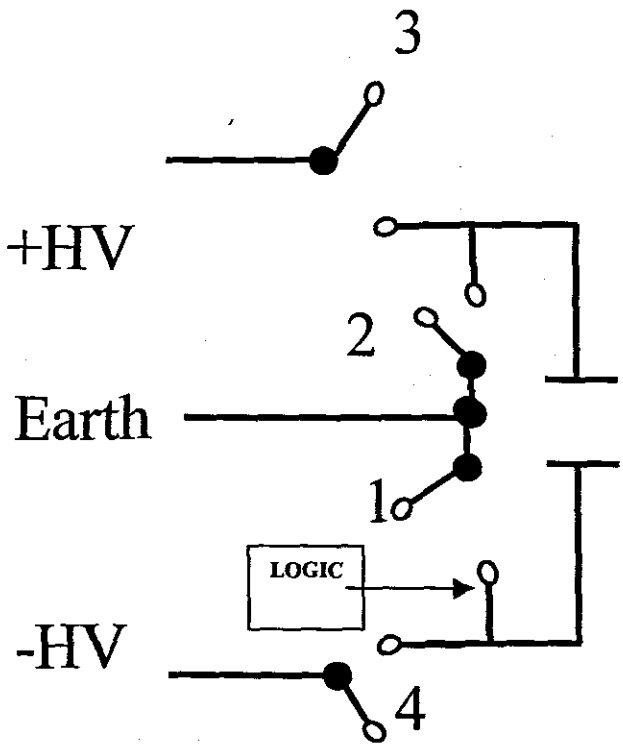

Figure [3.2.5] ***Illustration of the electronics of the beam on demand deflection system used to switch the beam from the specimen. Switches 3 and 4 control the HV supply to the plates, whereas 1 and 2 switch the plates to the ground position.***

power supplies. The design minimises the distance from the deflection plates to the specimen. It also enables different power supplies with the only one set of deflection plates. Novel and unique to this setup is the spectroscopic amplification for performing the energy dispersive processing. This processing provides the signal for triggering the deflection of the plates, as illustrated in **figure [3.2.5]**. It occurs via the fast processing stage, especially for electronic pile-up rejection. This avoids working with two different threshold settings for energy and timing. The compromise is the comparatively slow signal response and the relatively long total loop time of about 900 nanoseconds. This compromise is however advantageous in that sufficient time is allowed to maintain the voltages on the plates for the duration of the engaged signal of the spectroscopic amplifier. The real dead-time of the amplifier can now be applied to determine the time during which the beam is off the target. Fixed deflection times are normally about 60μs. The plates are quickly charged to equal voltage of opposite polarity

after the fast processing of an event in the X-ray detector. The beam is deflected from the target and the slower spectroscopic amplifier is allowed to process the event. The probability of another signal arriving at the detector in this minute time duration depends only on the finite loop time, which in turn depends on time taken to process the event, the time taken to charge the plates and the flight time of ions already past the plates. These signals are illustrated in **figure [3.2.6]**. This excellent performance of the beam-on-demand deflection system has enabled the use of the system in routine PIXE measurements, with counting rates of up to 3500 counts per second. The dead time for such count rates does not exceed a few percent. Other advantage of this system is the elimination of statistical artefacts that may arise due to con-

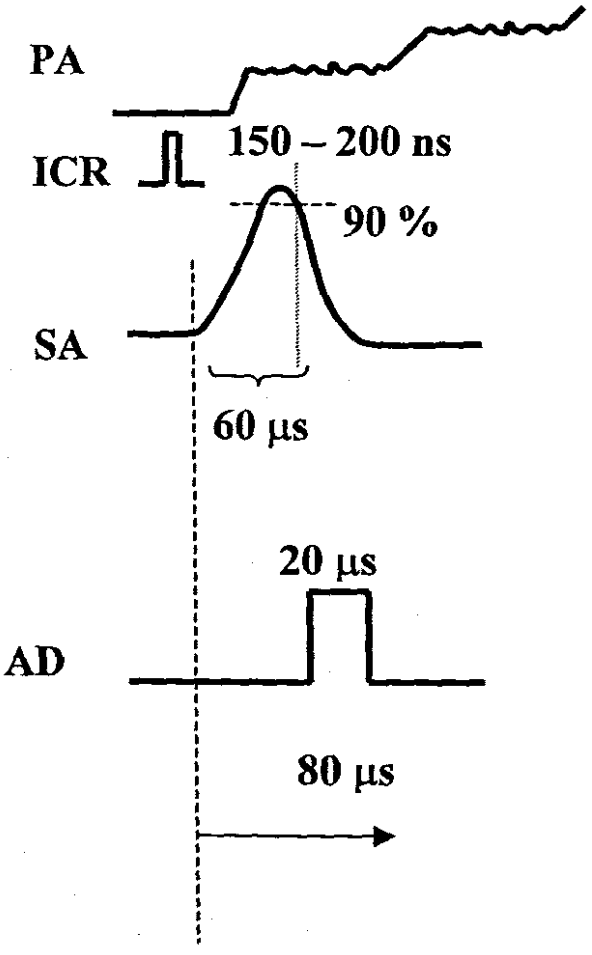

Figure [3.2.6] ***Illustration of the signals emitted during the specimen irradiation. PA represents the signal from the pre-amplifier, ICR the signal from the incoming counting rate unit, SA the signal from the spectroscopic amplifier and AD the analogue to digital converter signal. The signal for the ICR is the faster as it is processed in a time duration of 150 to 200 nanoseconds. The spectroscopic amplifier transmits the signal only after 90 % is processed and the time duration is about 60µs. The AD processing times takes about 20µs. The total time then is about 80µs.***

stant current changes when the specimen is exposed to the beam. However, without this system, the only alternative would be the use of an electronic pile-up rejection system. These systems are available with modern spectroscopic amplifiers and operate on the basis of fast processing of incoming signals. This indicates that when two of more signals are measured during the active stage of the slow energy processing unit then all signals, including the first one, are rejected. Hence, the normal dead time for the usual direct current (DC) operation yielded spectra that contain a relatively high number of pileup peaks. This prompted the design of the beam-on-demand deflection system and the system is thus ideal for PIXE determination of specimens. In contrast, as discussed in sections [2.3] and [2.4], analysis with PIGE and RBS are dependent of the amount of charge deposited and hence high count rates. This translates into large amounts of charge accumulated and would be ideal in the use of these two analytical techniques.

3.2.2.3 Automatic specimen changer

Specimens were mounted on a ladder attached to the shaft of the stepper motor drive of the automatic changer. The ladder is positioned in the center of the chamber and vertically to the incident beam. The stepper motor to which the ladder is attached enables three-dimensional movement. Up to 10 specimens of size 1cm × 1cm can be accommodated on the ladder.

3.2.2.4 Beam diameter

Control of the size of the irradiating beam was done by focusing with the aid of the quadruple lenses. The beam profile is important when desiring detailed images of the specimen from which the small size elemental inhomogeneities can be determined. The CCSCAN software of Churms (1995) enables any signal derived from scanning the beam across a discontinuity to be expressed as a measure thereof. The simplest form of discontinuity is the edge of a specimen with pre-determined spacing such as a Cu-mesh. This is shown in **figure [3.2.7]**. In

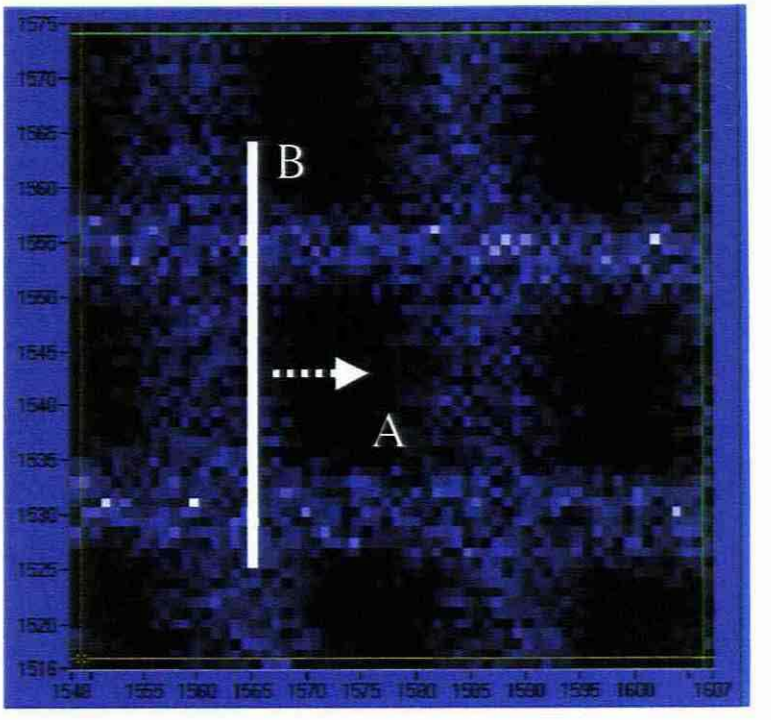

Figure [3.2.7] ***Image of a 25μm Cu grid used in the determination of the beam diameter size. A is the center of the grid and B the edge from which the scan is performed. The arrow indicates the midpoint of the central area of the grid.***

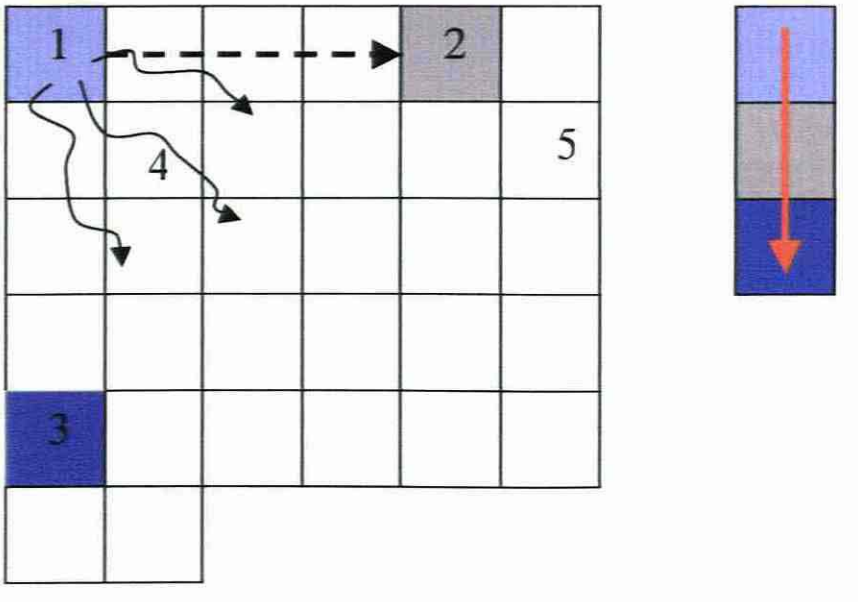

Figure [3.2.8] ***Simplified illustration of the scanning procedure during irradiation. The area dimensions are set to correspond to multiples of a pixel. The size of the beam diameter should correspond to these dimensions, as this would avert overscanning the pixel area and thus yielding invalid results. The pixel in the top and leftmost corner is irradiated for time duration of about 10 ms and the beam position is then displaced to, for instance, the fifth pixel.***

radiation period per pixel is 10ms. This time duration was selected to obtain a reasonable ratio of the time spent on each pixel and the time spent on beam movement from pixel to pixel. Using constant time spent by the beam in every pixel is easier as it avoids problems related to minute amounts of charge. This however, requires many beam passes of the scanned area to average out the artefacts related to instabilities of charge deposition. Hence for a 64 × 64 array of pixels, this translate to approximately 41 seconds per selected area. The minimum analysis time for each scan performed in this study was one hour. The average number of scans performed or beam passes made was therefore 67 for each area.

3.3 Data Acquisition

3.3.1 Introduction

The path of the electronic signal, from the detector to the personal computer, is illustrated in **figure [3.3.1]**. The X-rays, γ-rays and backscattered particles reach the respective detectors and are amplified by the pre-amplifier (also used for charge-to-voltage pulse conversion and pulse shaping) and the spectroscopic amplifier. The ADC converts the analogue signal to digital from where the signal passes to the VME-CAMAC interface and then to the VAX station.

3.3.2 VME data acquisition

The data acquisition application program for the Motorola central processing unit is the real-time pSOS+ kernel (Hogan, 2001). The components used for this application are the pSOS+m real-time kernel with multiprocessing extensions, the probe+ debugger module, the pNA+ module for networking with TCP/IP stream socket services and the pREPC+ module as the ANSI run-time library for C languages applications. A host computer normally communicates through the pNA+ module to the application. The kernel therefore provides multi-tasking and inter-task communication services.

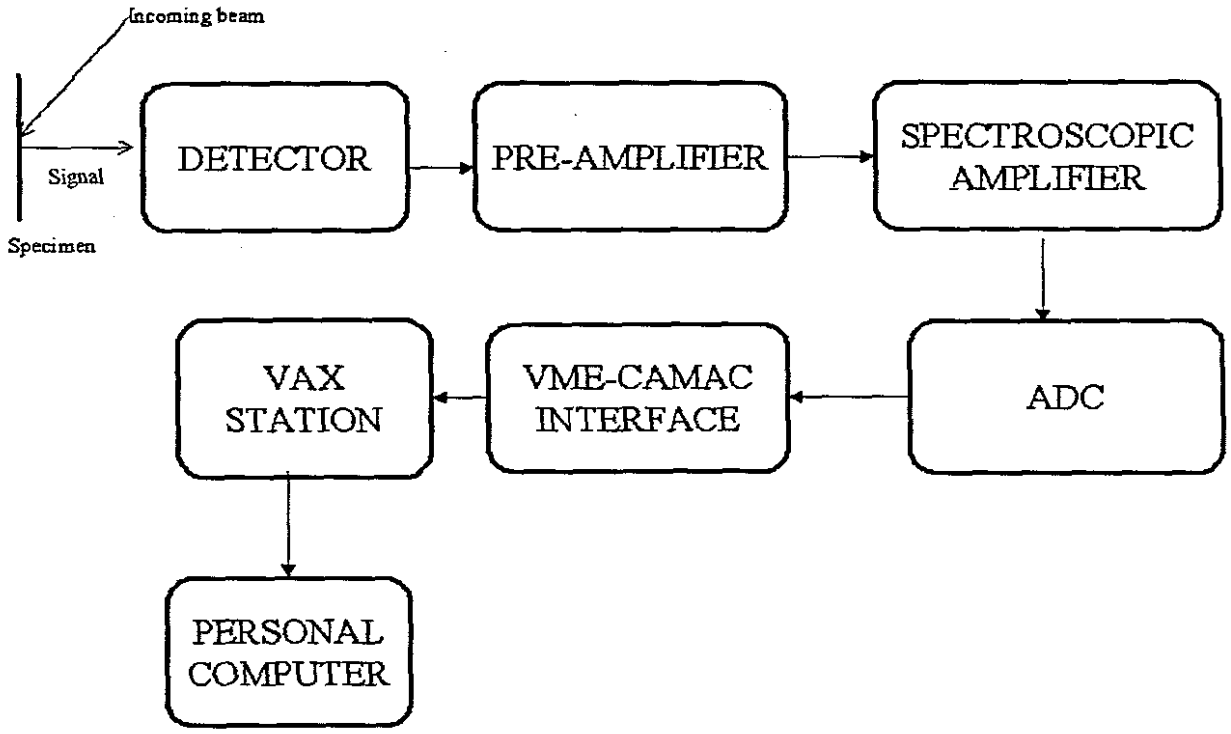

Figure [3.3.1] ***An illustration of path followed by the signal from the detector to the personal computer where the spectrum is evaluated. The signal from the detector is amplified firstly by the pre-amplifier and then by the spectroscopic amplifier. The ADC converts the analogue signal to a digital signal, which is re-layed to the VME-CAMAC interface crate and then to the VAX station and then to the personal computer.***

3.3.3 Detection of X-rays

The Oxford Si(Li) detectors, model 6648, was used for the PIXE determinations in this study. The detector active area is 80 mm^2 and the resolution of (170 ±15) eV at 5.9 keV (Mn K_α). The conventional geometry and a gold contact and Be window are used. This, along with a special shaping amplifier, improved the resolution by at least 10 eV (FWHM) and increased the peak/background by about ten-fold to greater than 10,000:1. The detector, located on a horizontal unitary cryostat, was positioned at 135° to the incoming beam, the optimisation of which is discussed in section [2.2]. A low-noise transistor reset Ortec preamplifier of the pulsed-optical feedback was used for pre-amplification. This pre-amplifier employs a specially fabricated FET (field effect transistor), which is cooled with the detector in the cryostat. A pileup rejector prevented the storage of pulses, which were distorted due to pile up in the main amplifier. A live-time corrector extended the acquisition time to compensate for rejected counts.

3.3.4 Detection of γ-rays

In the discussion of previous investigations, highlighting the potential of μ-PIGE, in section [2.3], the angle of the detector to the incident beam in these investigations was 90°. In the construction of the NMP chamber, a view port for ascertaining the orientation of the specimen was placed at this angle. For this reason a Canberra coaxial germanium-lithium (Ge(Li)) detector, model GC1520, for detecting the γ-rays, was positioned at 0° to the incoming beam. The outer n-type diffused lithium contact of the detector was about 500 μm and the inner contact about 0.3 μm thick. The useful energy range of the detector was from 50 keV to 10 MeV. The active area is 51 cm^2 and the full width at half maximum (fwhm) was 1 keV at 122 keV and 2 keV at 1332 keV. The peak to Compton ratio (P/C) was 40, with the fwtm at 1332 keV was 4.0 keV. The Canberra model 2004 pre-amplifier, which employed a dynamic charge restoration method for discharging the integrator, was used for amplification of the charge being converted into a voltage pulse.

3.3.5 Detection of backscattered particles

The silicon surface barrier (SSB) detector, operating on the principle analogous to that used in gas ionisation chambers, was used for detecting backscattered particles. The resolution was (28±3) keV. For pre-amplification an EG & E Ortec model 142 B, 5.80 V amplifier was used. The signal that was measured and analysed was the current produced by the creation of electron-hole pairs, the current being proportional to the amount of ionizing radiation that reached the detector.

3.3.6 Spectroscopic amplification of X-rays, γ-rays and backscattered particles

The Canberra Spectroscopic amplifier, model 2020, was used for amplification of the signal from the detector pre-amplifier. The model employs unique baseline restorer for optimum performance with high-resolution detector systems. The gated baseline restorer automatically ad-

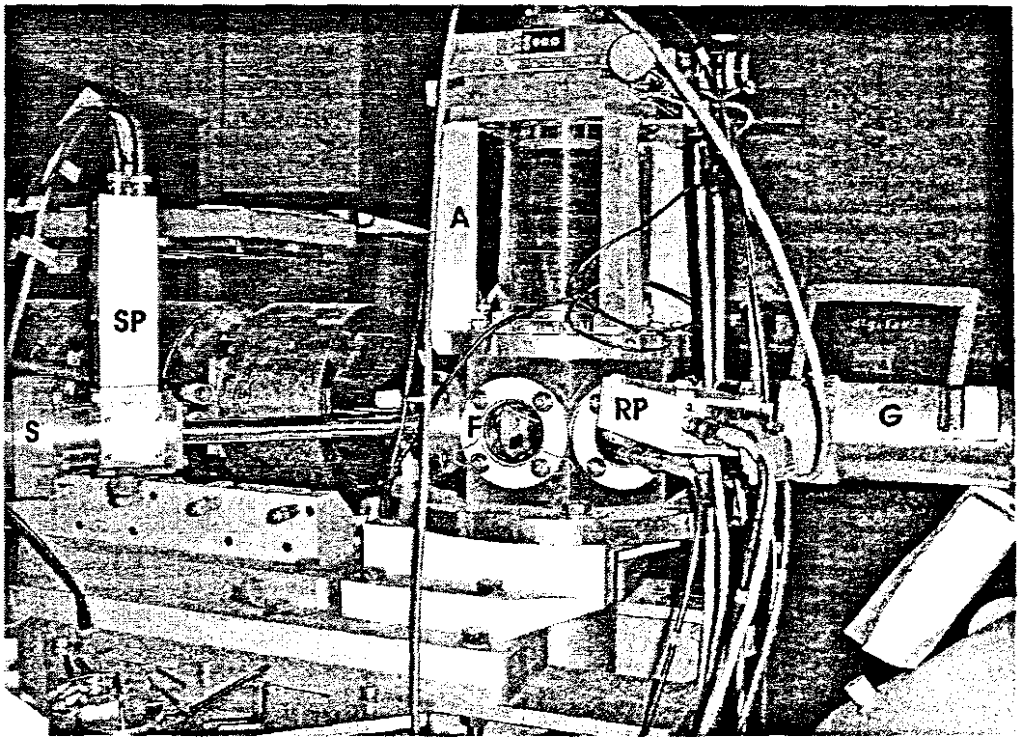

Figure [3.3.2] ***Photograph of the detectors. S is the Si(Li) detector, SP the pre-amplifier of the Si(Li) detector, A is the automatic specimen changer, RP is the pre-amplifier of the silicon surface barrier detector positioned in the chamber, G is the lithium-drifted Ge(Li) detector and F is the view port showing the filter wheel.***

justs the restoration rate and threshold optimizing performance to the incoming count rate and system noise level. Simultaneous unipolar and bipolar outputs are available at both front and rear panel BNC connectors. The unipolar signal can be delayed by 2 μs.

3.3.7 Absorbers

The array of absorbers was mounted on a filter-wheel in front of the Si(Li) detector. The thickness of these absorbers varied from 25 μm to 253 μm. Materials used for the manufacture are Al, Be and Kapton. The Be absorber of 125 μm thickness and Al absorber of thicknesses 100 and 150 μm were used in this study.

3.4 Standardisation

Quantification of SRM is usually performed by wet chemical analysis. The entire specimen is dissolved in normally acidic media and analysed with techniques such as Atomic Absorption

Spectrometry, Atomic Emission Spectrometry and Inductively Coupled Argon Plasma Spectrometry. Subsequent results are representative of the specimen as a whole and no information on the possible small-size inhomogeneity in elemental distribution is reported. In microanalysis the proton microbeam only samples a small portion of the SRM. This area is much smaller than the area normally prescribed by the certifying agency. This indicates that when applying IBA analysis, the level of homogeneity in SRMs introduces limits in their own usefulness.

Valkovic et al. (1995) in the analysis of NIST-SRM-1632a (coal), illustrated this by performing scans of sizes 250 × 250, 500 × 500 and 1000 μm × 1000 μm over the surface of the SRM. u_Z for scan size of 250 × 250 μm, calculated as a percentage, ranged from 4.7 to 13%. As an example, u_Z for potassium analysis was 4.8%, whereas the author's data yielded an uncertainty of only 0.75%. Furthermore, the degree of uncertainty worsened as the scan size decreased. The uncertainty given by the author in this instance is an improvement of an order of magnitude compared to the uncertainty stated by the certifying body. This emphasises the degree of reliability provided in the wet-chemical quantification of SRMs and the importance of the area scanned. Astimex standards, as detailed by Sutton and Clay (2001) were used in the quantification of γ-rays and to establish the geometry of measurement such as the solid angle. A thin layer, approximately 5 Å, of iridium deposited on silicon, was used for calibration of the proton backscattered data.

3.5 Computation

3.5.1 XSYS acquisition

The XSYS software (Xsys, 1985) is a general-purpose data acquisition system that permits complex array data usage, including event by event handling, which is made easy by the high level event handling code EVAL. The software system is linked to the VAX (running VMS as operating system) computer station via the CAMAC and VME interface system. The VME-

based data-acquisition system consists of the CAMAC subsystem, the VME front-end and the host computer. The front-end consists of a Motorola 68040 cpu and a CAMAC branch driver.

3.5.2 Fitting X-ray data

The GeoPIXE II (version 2.5) suite of software programs of Ryan et al. (1995) were used in evaluating X-ray data, since this software package can be used to analyse thin, intermediate and thick specimens and also for elemental mapping. For background correction, the SNIP algorithm of Ryan et al. (1988) and Clayton and Ryan (1990) was used. This programme performs a statistics-sensitive non-linear iterative peak-clipping treatment in the quantitative analysis of PIXE spectra. GeoPIXE II contains the rapid matrix transform method termed dynamic analysis (DA), which facilitates the production of true elemental concentration mapping. Dynamic mapping is based on the DA algorithm with which the concentration gradient of an element in the specimen is quantified. The algorithm formed the basis of most of the analysis in this study. A PIXE spectrum, y_i, is decomposed into the contributions from the component elements and then expressed as a non-linear least-squares fit to the spectrum, using a model function f_i. This model function comprises the line-shape functions for each element and includes the background terms and pile-up at each channel, i. Given that the non-linear parametric fit description of the detector characteristics is determined in a preliminary fit to a prior spectrum, the remaining linear parameters, a_k, is found in the solution of the matrix equation [3.5.1] where α and β are matrices in terms of the partial derivatives $\delta f_i/\delta a_k$ and S the spectrum vector and is given in equation [3.5.1 (a) and (b)], where w_i is the statistical weights as given by Ryan et al. (1988). The element concentration, C_k, is then given

$$\alpha a = \beta S \text{....(a)}\ \varepsilon_{jk} = \sum_i w_i^{-1}\beta_{ji}\beta_{ki} \text{ and } \beta_{ji} = w_i(\partial f_i/\partial a) \text{.....(b)} \qquad \textbf{3.5.1}$$

in equation [3.5.2], where the terms in respective order are the integrated charge, the detector solid angle, the detector efficiency, the X-ray absorber attenuation and the generic X-ray

$$C_k^{-1} = \frac{Q\Omega\Omega_k T_k Y_k}{a_k} \qquad 3.5.2$$

yield,which is assumed to be constant for the element *k* across the image. If Γ, a matrix and the solution to the linear least-square problem in transforming the spectrum vector S in equation [3.5.1] to the concentration, C_k, equation [3.5.2] and Γ is given by equation [3.5.3], then the concentration can be expressed by equation [3.5.4]. This DA algorithm thus enables

$$\Gamma_{ki} = \frac{\sum_j \alpha_{kj}^{-1}\beta_{kj}}{\Omega\varepsilon_k T_k Y_k} \qquad 3.5.3$$

elemental mapping from which analysis of small size inhomogeneities in composition could

$$C = Q^{-1}\Gamma S \qquad 3.5.4$$

be made. With GeoPIXE II, BS and γ-ray emission data can be extracted and processed separately. Markers can be set over the peak areas and background subtraction performed to obtain elemental mapping. This indicates that should any two elements be determinable with the techniques, then element concentrations could be compared to show technique complementarity.

3.5.3 Fitting γ-ray data

γ-ray emission data were extracted using GeoPIXE II. Although the concentration was given in counts, these values could be used with standards to give a complete elemental mapping.

3.5.4 Fitting backscattered data

As is the case of γ-ray emission data, BS data can also be extracted with GeoPIXE II. For quantification, the Rump software program of Doolittle (1985) was used in evaluating backscattering spectra.

Chapter 4

Industrial Applications

4.1 Introduction

The analytical techniques PIXE, PIGE and BS, were applied to specimens of 1) $(Al_2O_3)_nZrO_2$ ceramic-based sorption electrodes obtained from the University of the Western Cape, which was to be used in the purification of wastewater by electrolysis; 2) $YBa_2Cu_3O_{7-x}$ (YBCO), high temperature superconducting samples, deposited by laser on high purity MgO substrates, obtained from the Materials Research Group of iThemba LABS and to 3) steel specimens, into which carbon and nitrogen were incorporated, from Saldanha Steel manufacturers in the Western Cape of south Africa.

The absorber type and thickness varied for each of these studies and is given in the experimental section. To further substantiate the quantitativeness of the PIGE data, the Peak-to-Compton (P/C) ratios were determined for the 1332.5 keV ^{60}Co peak with the Compton range from 1040 keV to 1096 keV. All P/C ratios, obtained experimentally, were within the specified 40:1 to 90:1 range as are given by Gilmore & Hemmingway (1991).

The colour gradient scheme for illustrating elemental distribution is depicted in **figure [4.1.1]**

Figure [4.1.1] ***The relative concentration legend used in mapping in the studies.***

4.2 Zirconia-Alumina ceramic-based sorption electrode

4.2.1 Introduction

During the past decade South Africa experienced an increase of approximately 18% in urbanisation (Stats SA, 2000). This placed an increased emphasis on the more economical treatment of wastewater. To alleviate this situation, Bladergroen (2002) used metal-coated $(Al_2O_3)_nZrO_2$ ceramic tubes for purification of wastewater. The alumina tube was first submerged in ZrO_2 solution at 800°C, forming the base material, $(Al_2O_3)_nZrO_2$, which was then coated by electrodeposition with metals. The principle of purifying the wastewater, using the ceramic-based sorption electrode (CSE), as it is now termed, is illustrated in **figure [4.2.1].**

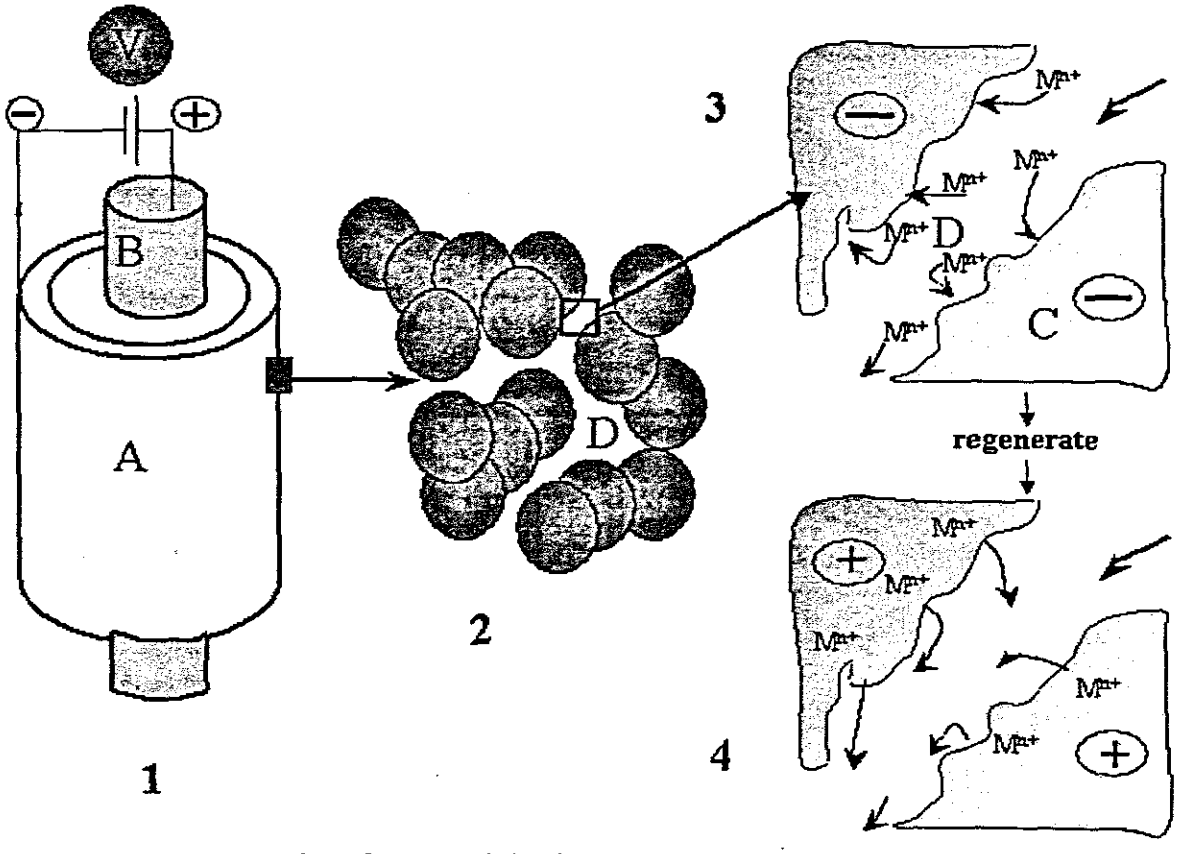

Figure [4.2.1] ***Illustration of the principle of purifying wastewater with the ceramic-based sorption electrode. In 1, A is the ceramic-based sorption electrode, $(Al_2O_3)_nZrO_2$, and B is a counter electrode, serving as the anode. A magnified section of the electrode surface is shown in 2, where D represents uncoated areas or pores on the electrode surface. In 3 the wastewater flows over the electrode and contaminants in the water are adsorbed onto the coating and in this way removed. The regeneration of the electrode, during which the adsorbed contaminants are then released, is illustrated in 4.***

4.2.2 Survey of elements

Although Al_2O_3 is normally well refined during manufacturing, it may contain traces in $\mu g.g^{-1}$ concentration of specific elements predominantly present as oxides. Ga, Y and In occur in Al_2O_3 ores but only at a maximum concentration of, and then rarely, 1%, as indicated by Cotton et al. (1999). Hf is found in most Zr-containing mineral ores, although in fractions of mass percentage of Zr (Cotton et al., 1999). Al, Zr, Y and Hf are therefore expected to be present in the ceramic-based sorption electrode (CSE) matrix as oxides. The design of the CSE is novel and few investigations were done on the matrix. Al_2O_3 and ZrO_2 are however matrices of composition similar to that of the ceramic-based sorption electrode.

Electroless processes have been studied by Baudrand (1995), Chen and Chen (1997), Honwa et al, (1995), Li et al. (1997). Moore et al. (1997), Linkov and Belyakov (1997), Mulder (1996) and Yang and Wen (1998). Oxygen quantification is discussed in sections [2.2] to [2.4], where it is indicated that the element should be determined by BS. The energy of the emitted Al K X-ray lines is 1.487 keV. Possible interference can arise from Rb L X-ray line, emitted at 1.48 keV, and Br L_α line, which is emitted at the same energy.

As shown by Cotton et al. (1999), Br generally occurs as salts, such as NaBr and KBr or oxides, such as BrO_3^-. These compounds would evaporate at high temperatures to which the matrices were heated during manufacturing. $K_{\alpha 1}$ X-ray lines of Y and Zr are emitted at 14.957 and 15.774 keV, respectively. This energy difference can be resolved with the Si(Li) detector. The coating however contains P, for which the K X-rays are emitted at 2.015 keV. Due to the limited resolution of the Si(Li) detector, this X-ray line would partly overlap with Y and Zr L X-ray lines. The intensity of the $K_{\alpha 1}$ lines can be used to quantify Y and Zr. P can be quantified since the ratio of the K to the L X-ray lines remains constant at the same proton energy, as indicated by Johannson et al. (1995).

However, the presence of P should be verified with either PIGE or BS. Furthermore, the X-ray lines for elements with Z ≥19, if present in trace amounts, can be attenuated by positioning a 125 μm thick Be absorber between the specimen and detector.

The Hf K X-ray lines are emitted at 55.76 and 63.21 keV. In this energy range the cross-sections are low and the efficiency of the Si(Li) detector is very poor. As indicated in section [2.2], the L X-ray lines have to be used to quantify the element. The energies at which the L X-ray lines are emitted and the possible interferences posed are given in **table [4.2.1]**.

Table [4.2.1] ***Possible interferences in the PIXE quantification of Hf in $(Al_2O_3)_nZrO_2$ using the L X-ray lines. The resolution of the Si(Li) detector is (170±15) eV.***

Energy (keV) of Hf L X-ray line	Interference		Energy difference (eV)
	Element and X-ray line	Energy (keV) Interfering X-ray line	
7.843			
7.894	Cu K_α	8.047	153
9.021	Cu K_β	8.904	117
9.346			
9.556	Zn K_β	9.571	15
10.51			
10.73			
11.26	Se K_α	11.22	40

As discussed previously, quantification of light elements should be performed by γ-ray emission spectrometry. The technique can also be used to verify the presence of P in the matrix. In this instance, the reaction ^{31}P p(1, 0), for which the γ-ray is emitted at 1266 keV and the reaction ^{31}P α(1, 0), with the γ-ray emitted at 1778 keV, could be used to verify the presence of phosphorus. This will serve as complementary information to the P determination by PIXE. In addition, the Al presence can be confirmed by using the reactions ^{27}Al p(1, 0), for which the γ-ray is emitted at 844 keV and ^{27}Al p(2, 0), with the γ-ray emitted at 1015 keV. This is possible since the expected concentration of Al, c_{Al} > 20 mass%. Because of the PIGE detector

resolution, there is a risk of interference with the 845 keV γ-ray by the γ-ray emitted at 847 keV for the ^{57}Fe p(1, 0) reaction. Based on the work of Gihwala (1982), it is not expected that the 3 MeV protons would induce γ-ray emission for the elements Y, Zr and Hf.

For BS analysis, the proton kinematics factor, k_z, is calculated using equation [2.4.2]. The k_Z values are given in **table [4.4.2]**. For Hf, Y and Zr, the k_z values, at 3 MeV, are 0.978, 0.956 and 0.957 respectively. The values indicate that Y and Zr cannot be resolved with the solid state surface barrier detector, which has a resolution of (28±3) keV. The backscattered data would therefore not provide information complementary to the PIXE quantification of these two elements. Hf could however be quantified, depending on the concentration. k_z values for Al and O indicate an energy difference that can be resolved with the SSB detector. Hence the backscattered data can be used complementarily to the PIXE and PIGE quantification. The energy difference in the k_Z values of P and Al can be resolved by the SSB detector. However, this was not considered because of the useful guide stipulated in equation [2.4.4]. Elements with Z>19, yield k_z values that indicate poor resolution. This is compounded by the expected low concentration of these elements. The quantification by BS of these elements is therefore not feasible. Hence, only complementarity of Al can be expected for PIXE, PIGE and BS.

Table [4.2.2] ***Kinematic factors and energies of the major matrix elements present in the ceramic-based sorption electrode. The absolute values of the energy differences of Al (E_{Al}) with the other elements (E_Z) are indicated. Values for Ir on Si of the Ir on Si backscattering standard are indicated for comparison.***

Element	Kinematic factor	Energy (keV)	$\lvert E_{Al}-E_Z \rvert$ (keV)
Al	0.861	2584	0
O	0.777	2332	252
P	0.878	2634	50
Y	0.956	2867	283
Zr	0.957	2870	286
Hf	0.978	2933	349
Si	0.866	2599	15
Ir	0.979	2938	354

4.2.3 Experimental

4.2.3.1 Specimen preparation

Because of the cylindrical size, 1.5 cm in diameter and 12 cm in length, of the ceramic-based sorption electrodes, it was not possible to mount them in the chamber directly. Small pieces were splintered off such that a minimum arch of curvature was obtained. These splinters were used to quantify the chemical composition of base material and to obtain preliminary identification of the coated specimens. Cross-sections for each tube were made at the top, in the middle and at the bottom of the CSE. Splintered-off sections and cross-sections of the base material and sorption electrode were mounted on Perspex and are shown in **figure [4.2.2]**. Also shown are illustrations of where the cross-sections were made and the width of the cross-section over which the elemental distribution map was performed.

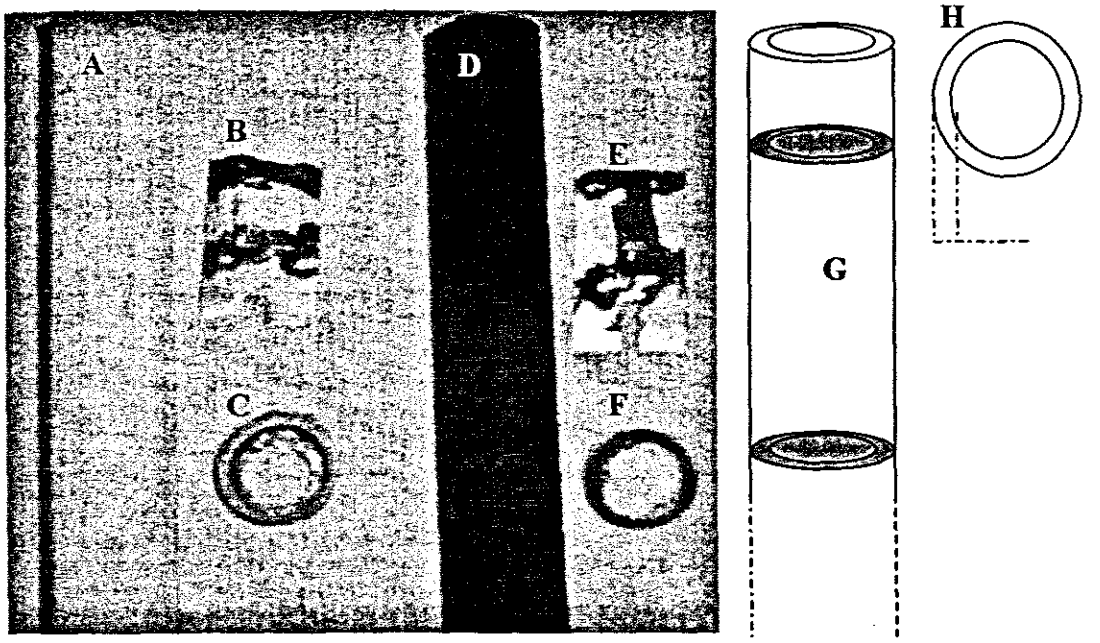

Figure [4.2.2] ***Photograph of the base material, $(Al_2O_3)_n ZrO_2$, and the ceramic-based sorption electrode (CSE) specimen preparation and an illustration of the cross-sections made. Of the base material, A is the cylindrical tube, B the carbon-coated splintered-off section and C the cross-section. D, E and F are respectively the CSE cylindrical tube, the carbon-coated splintered-off section and the cross-section. The cross-section preparation of the top and middle cross-sections are shown in G. The area of the cross-section over which the elemental mapping is performed, is indicated in H.***

4.2.3.2 Instrumental parameters

For X-ray attenuation, a 125μm thick Be absorber was placed between the specimen and Si(Li) detector. The area irradiated was 1500×1500 μm^2, emphasising the cross-section width. The beam current was maintained between 100 and 200 pA. An average charge of 1 μC was accumulated. The beam energy was maintained at 3.0 MeV for the irradiation period. The specifications and geometries of the detectors are those given in section [3].

4.2.4 Results and Discussions

Although three CSEs have been analysed, only the analysis of the base material and three cross-sections of one CSE are detailed. The unevenness of the base material surface area and consequently that of the CSE, is illustrated by the micrograph in **figure [4.2.3]**. The pores were unevenly distributed and varied in size. Therefore, preliminary analysis was performed

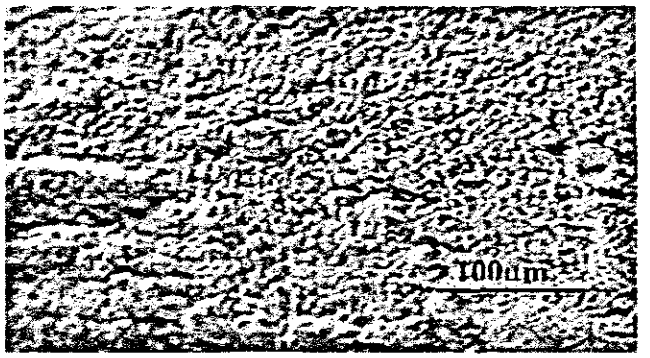

Figure [4.2.3] ***Optical micrograph of a magnified section of the base material, $(Al_2O_3)_nZrO_2$, to illustrate the unevenness of the surface area.***

with a defocused beam of size 2000×2000μm^2. The analysis was repeated over seven areas to obtain average specimen composition (Mars et al. II, 2003). Although stated in section [2.2] that PIXE is a standardless technique, $Al_5Y_3O_{12}$ and ZrO_2 standards (Sutton and Clay, 2001) were used for calibration due to the high degree of Al_2O_3 porosity. The sum spectrum of macro-PIXE data, as an average composition of the scanned areas, is shown in **figure [4.2.4].** The spectrum was fitted with GeoPIXE II. Identification of the peaks is given in **table [4.2.3]**.

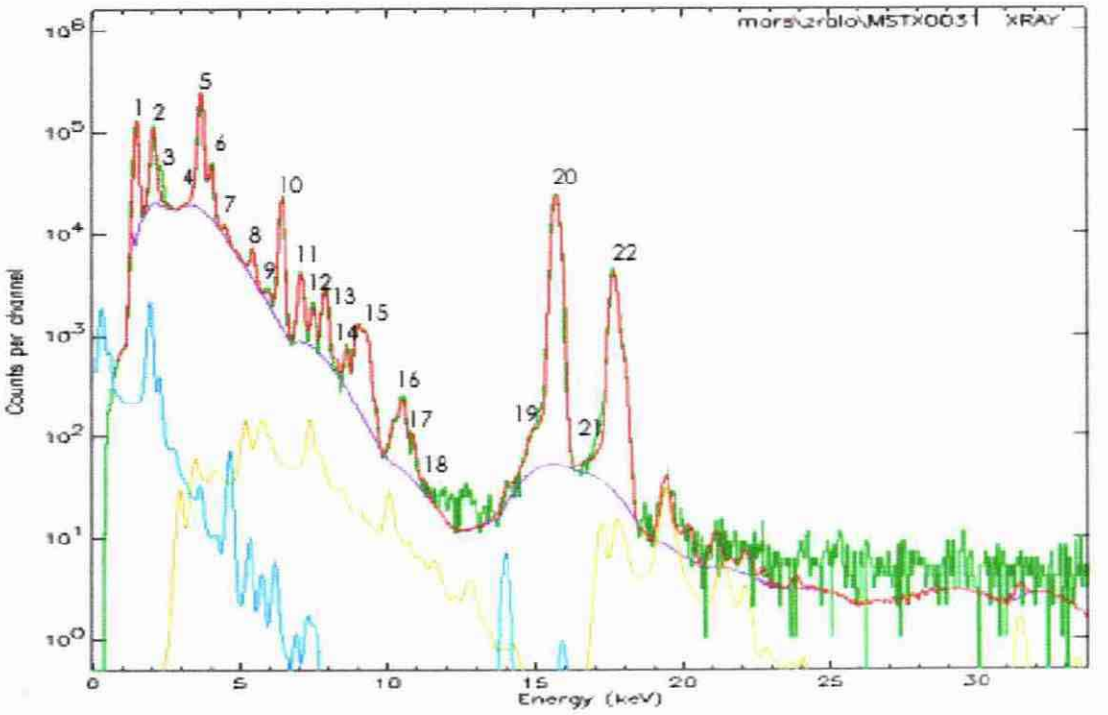

Figure [4.2.4] ***Spectrum of macro-PIXE data, of the base material, $(Al_2O_3)_nZrO_2$, splintered-off section which represents an average composition of the surface areas scanned. The green line represents the data, the red line the GeoPIXE II fit to the data and the purple line the background correction. The blue line represents the Si escape peaks and the yellow line the pile-up from the spectrum.***

Table [4.2.3] ***Identification of peaks in the spectrum of the macro-PIXE data.***

Peak no.	Element and X-ray line	Peak no.	Element and X-ray line
1	K_α of Al	12	L X-ray lines of Hf
2	L lines of Y and Zr	13	
3	K lines of Cl	14	
4	K_α line of K	15	
5	Ca K_α line overlapping the K K_β line	16	
6	K_β line of Ca,	17	
7	Ti K_α line	18	possible L-line of Pb or pile-up
8	Ti K_β, and Cr K_β	19	K_α of Y
9	Cr K_α line	20	K_α of Zr
10	Cr K_β overlapping the Mn K_α line and Cr K-MM transitions	21	K_β of Y
11	Fe K_α	22	K_β of Zr

The macro-PIXE analysis results, as an average chemical composition of the areas scanned, are given in **table [4.2.4]**. The uncertainty in measurement and the minimum detection limits compare well with those given in section [2.2].

Table [4.2.4] ***Macro-PIXE analysis results of the base material, $(Al_2O_3)_nZrO_2$, as an average chemical composition of the areas scanned. Concentrations are given in $\mu g.g^{-1}$ unless values are followed by the percentage sign, which indicates mass%. ND indicates that the element concentration is less than the minimum detection limit.***

Element Symbol	c_Z ($\mu g.g^{-1}$)	u_Z (%)	MDL $\mu g.g^{-1}\mu C^{-1}$
Al	37.8% ± 0.25%	0.7	1700
Cl	590 ± 90	16	50
K	120 ± 27	23	30
Ca	0.12% ± 0.01%	5.4	19
Ti	71 ± 6	8.5	10
V	ND	ND	8.3
Cr	33 ± 6	18	6.2
Fe	278 ± 9	3.2	5.7
Ni	ND	ND	7.7
Cu	8 ± 4	36	7.4
Zn	ND	ND	7.4
Ga	23 ± 4	17	7.3
Y	52 ± 12	23	17
Zr	0.84% ± 0.01%	1.5	23
Hf	173 ± 13	7.5	20

The Al concentration was more than three orders of magnitude greater than that of Fe. Hence, the γ-ray emitted at 844 keV from the reaction ^{27}Al p(1, 0) can be used as PIGE complementary analysis to the Al determination by PIXE. PIXE determination of P shows that it is not present in the matrix. Therefore the BS data for Al can also be used as complementary information. Furthermore, the concentration of Zr exceeds the Y concentration by more than two orders of magnitude. The Zr determination by BS is therefore complementary to the Zr determination by PIXE. The concentration of Hf is relatively low and the element is therefore not quantifiable by BS. The sum spectrum of macro-PIGE data, as an average of the chemical

composition of the surface areas scanned, is given in **figure [4.2.5].**

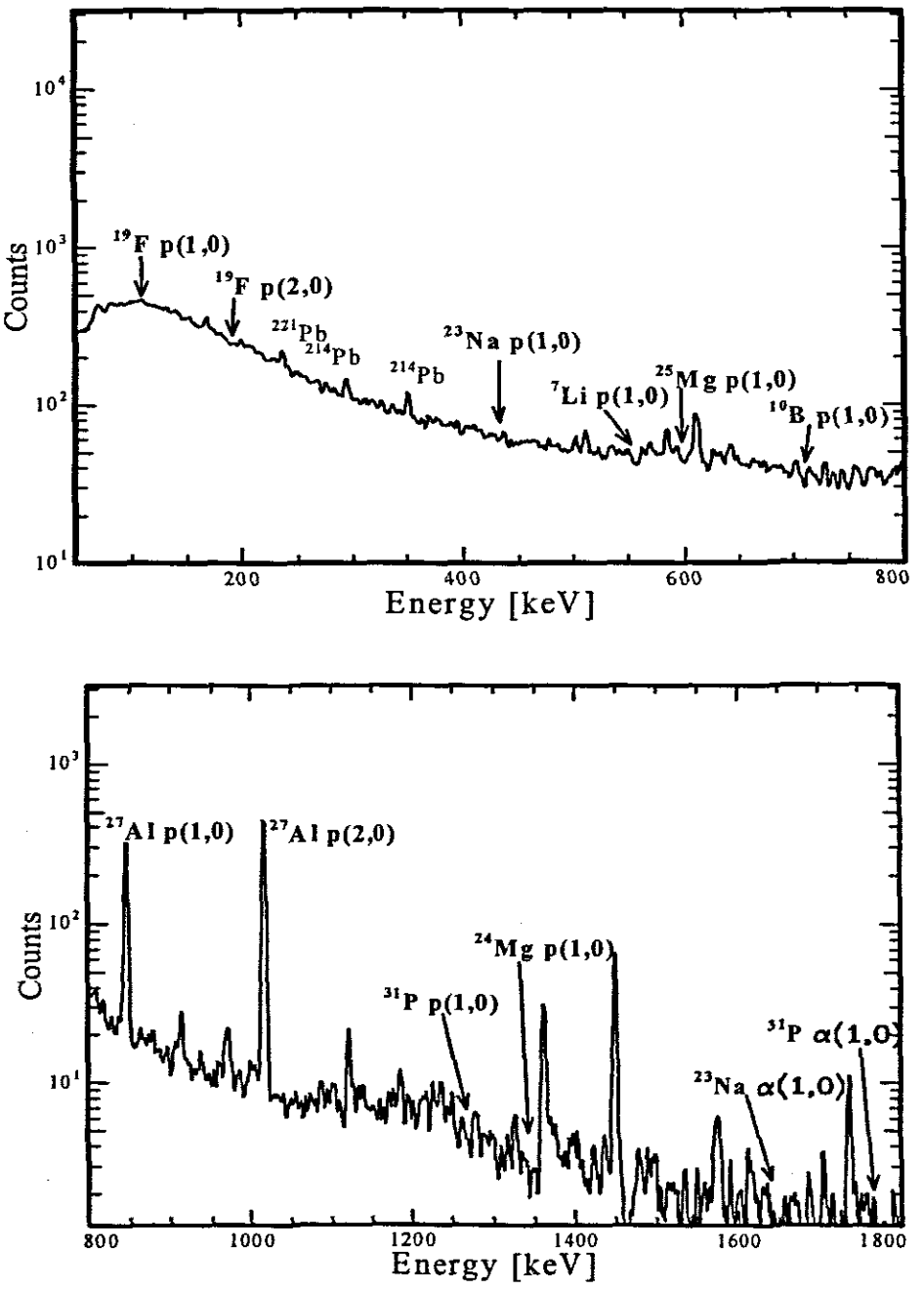

Figure [4.2.5] ***Sum spectra of the macro-PIGE data of the base material $(Al_2O_3)_n ZrO_2$, splintered-off section, which represents the average chemical composition of the surface areas scanned. The spectra show predominantly background radiation. Light elements F, Li, Na, B and Mg, Na and P in the base material are present in concentration less than the respective MDLs. Arrows indicate the positions where the γ-rays are normally emitted for these elements, should the nuclear reaction be induced. γ-rays of Al, used in determining the complementarity of PIGE with PIXE and BS, are indicated.***

Light elements were not present in the matrix of the specimen. For this reason the energies at which the γ-rays are generally emitted are indicated in the spectrum. The spectrum constitutes predominantly natural background radiation and the γ-rays of Al, the intensities of which are used to determine the complementarity with PIXE and BS.

The presence of P cannot 1) be established with PIXE since the L X-ray lines of Y and Zr overlap the P K X-ray line and 2) be verified with BS since Al is the major matrix element and the energy difference for Al and P cannot be resolved with the SSB detector. Hence, for differentiation of P and Al, the reactions ^{31}P p(1,0), with γ-ray emitted at 1266 keV and ^{31}P α(1,0), with γ-ray emitted at 1778 keV are used. As can be seen from this spectrum, P is not present in the matrix. The macro-PIGE analysis results for Al and P are given in **table [4.2.5].** The minimum detection limits of the light elements are those given in **table [2.3.2]**. Al and P minimum detection limits were obtained from the irradiation of apatite, kaersutite and spodumene standards, which were also used to determine MDL of the light elements. The sum spectrum of the macro-BS backscattered data, which is the average chemical composition of the surface areas scanned, is shown in **figure [4.2.6]**. For RUMP evaluation, the proton resonance data for Al and O were obtained respectively from Chiari (2001) and Amirikas (1993).

Table [4.2.5] ***Macro-PIGE analysis results for Al and P as an average of the seven areas scanned of a splintered-off section. The minimum detection limits given in μg.g^{-1}, of the light elements not present in the matrix are given in table [2.4.2], on page 41. Concentrations are given in mass%.***

Element symbol	Eγ (keV)	c_Z mass%	u_Z (%)	MDL μg.g^{-1}μC^{-1}
Al	845	38.1% ± 4.0%	11	760
	1015	37.9% ± 1.6%	4.4	470
P	1266	ND	ND	1200

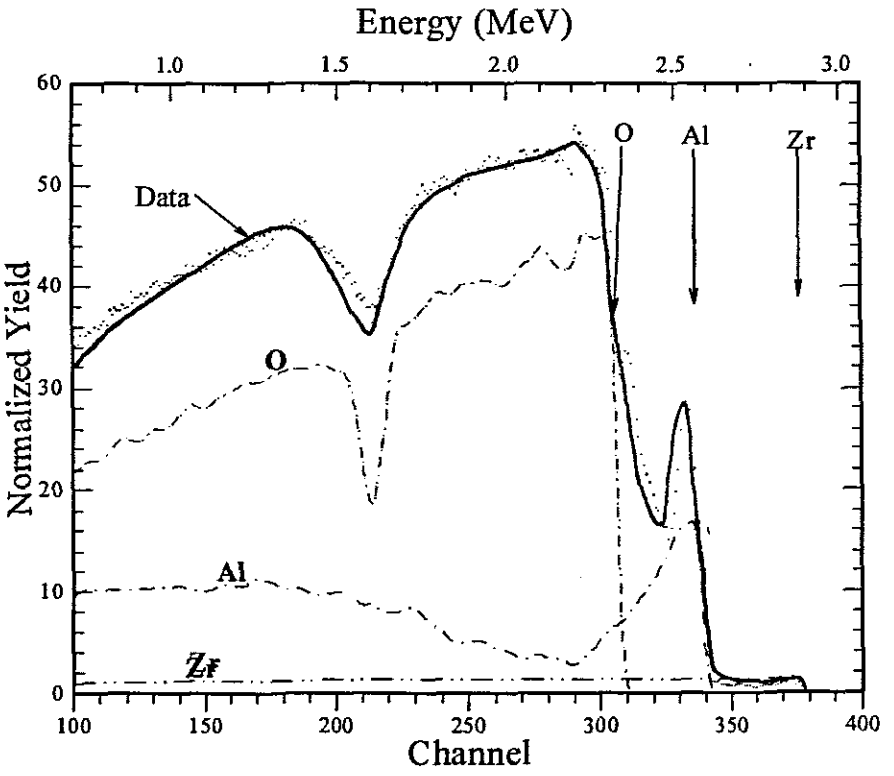

Figure [4.2.6] ***Sum spectrum of the macro-BS backscattered data, which are the average of the chemical composition of the surface areas scanned. The individual elemental contributions of O, Al and Zr to the spectrum, obtained from the simulation, are shown. Proton resonance data for Al and O, used in the simulation, were obtained from Chiari et al. (2001) and Amirikas et al. (1993). Arrows indicate the energies of the respective elements when located at the surface.***

The section of the simulation indicating the contribution of Zr, is the sum of the individual contributions of Y and Zr since, as indicated, these elements cannot be resolved with the SSB detector. This is also applicable for Al, where the contribution to the edge is the sum total for Al, K and Ca, since the energy difference among these elements is smaller than the SSB detector resolution of (28±3) keV. Here again, the Al concentration is at least two orders of magnitude greater than the concentrations of K and Ca. Hence, the Al concentration is regarded as complementary to the PIXE Al and PIGE Al determinations. The macro-BS analysis results are given in **table [4.2.6]**. The uncertainties in measurement and minimum detection limits given in the table differ significantly from those values shown in **figure [2.4.1]**, on **page 41**. The difference is attributable to parameters such as: 1) the uncertainty in measurement of the FWHM, 2) energy calibration with respect to the iridium on silicon standard, 3) the effects of other elements in the matrix and 4) the uncertainty in measurement of the ele-

mental concentrations as obtained by the RUMP fit to the data, are not considered in the simulation. These are incorporated into the uncertainty as indicated by equation [2.1.1].

Table [4.2.6] ***Macro-BS analysis results of the base material, as an average chemical composition of the scanned areas. The absolute error and hence the uncertainty, was calculated using equation [2.1.1] for which additional parameters were the energy calibration, the full width at half maximum and the uncertainty in concentration obtained in the RUMP simulation to the data. Concentrations values are given in mass% and MDLs in mass%.μC^{-1}.***

Element symbol	Backscattered Energy (MeV)	c_Z mass%	u_Z %	MDL mass%.μC^{-1}
O	2.332	33.7 ±1.57	4.7	1.00
Al	2.584	38.1 ± 1.1	2.8	0.38
Zr	2.870	0.91 ± 0.09	10	0.90

Results for Al determined with the techniques are given in **table [4.2.7]**. The good agreement among the values attests to the complementary nature of the techniques with respect to Al.

Table [4.2.7] ***Complementary macro-IBA analysis results of Al. PIGE determination at E_γ of 844 keV is the sum of all elements, such as Fe, exhibiting γ-rays at this energy. The same applies to BS where elements Ca and K have kinematic factors near to that of Al and are all considered as Al. The contribution of uncertainty parameters such as the energy calibration and the resolution of the detectors, calculated using equation [2.1.1], are included in the BS quantification. Concentrations are expressed as mass% and MDLs in $\mu g.g^{-1}\mu C^{-1}$***

Technique	E (keV)	c_Z mass%	u_Z %	MDL $\mu g.g^{-1}\mu C^{-1}$
PIXE	1.48	37.8% ± 0.25	0.7	1700
PIGE	844	38.1% ± 4.0%	11	760
	1015	38.0% ± 1.6%	4.4	470
BS	2584	38.3% ± 1.1%	3.9	15000

The spectra, **figure [4.2.5]**, shown therefore far are representative of the area scanned with the exception of P in the spectra of the PIGE data. All spectra of the areas extracted with the GeoPIXE II software, will be similar to these spectra. For this reason these spectra will not be shown unless elements other than those already quantified are present in these extracted areas.

As previously stated in section [4.2.1], the alumina specimen was either coated, impregnated or both with zirconia and coating with other metals was done in such a way that the resultant system served as a sorption medium to the contaminants in the wastewater. The extent to which the zirconia and the metals were introduced into or onto the Al_2O_3 matrix ultimately defined the applicability of the sorption electrodes. During the coating, possible undesired metals in the ZrO_2 solution might have been introduced into the Al_2O_3 matrix. These metals may also be present in the wastewater. Hence it is important to investigate further the elemental distribution over particular areas. The ceramic-based sorption electrode was cylindrical. The circular cross-section, mounted on Perspex, was consequently overscanned to emphasise the width thereof. This means parts of the scanned areas do not constitute the active matrix of the ceramic-based sorption electrode and quantification would therefore yield incorrect results. The GeoPIXE II software was used to exclude these overscanned areas and the active matrix composition was extracted. Steps taken to exclude the overscanned areas from the active matrix are shown in **figure [4.2.7(1-5)]**.

In this figure, **1** and **2** are the Al elemental distribution maps and **3** and **4**, are those of Zr. After comparison of the figures 1 to 4 and from the fact that the base material consists of relatively pure Al_2O_3, it was deduced that the distribution of Zr does not extend over the entire width of the cross-section. Correction to the top right overscanned area when superimposed first on the Al elemental distribution map, **(2)**, and then on that of Zr, **(4)**, yielded the same Zr elemental distribution pattern. This pattern does not extend over the entire matrix width. Hence, ZrO_2 was deposited onto and incorporated into the Al_2O_3 matrix. For this reason, Al_2O_3 and ZrO_2 were chosen as extreme chemical compositions between which the image matrix composition fluctuates. This served as a basis for assigning the dynamic analysis matrices of pure Al_2O_3 and ZrO_2 when correcting the image for the effect of sample composition on

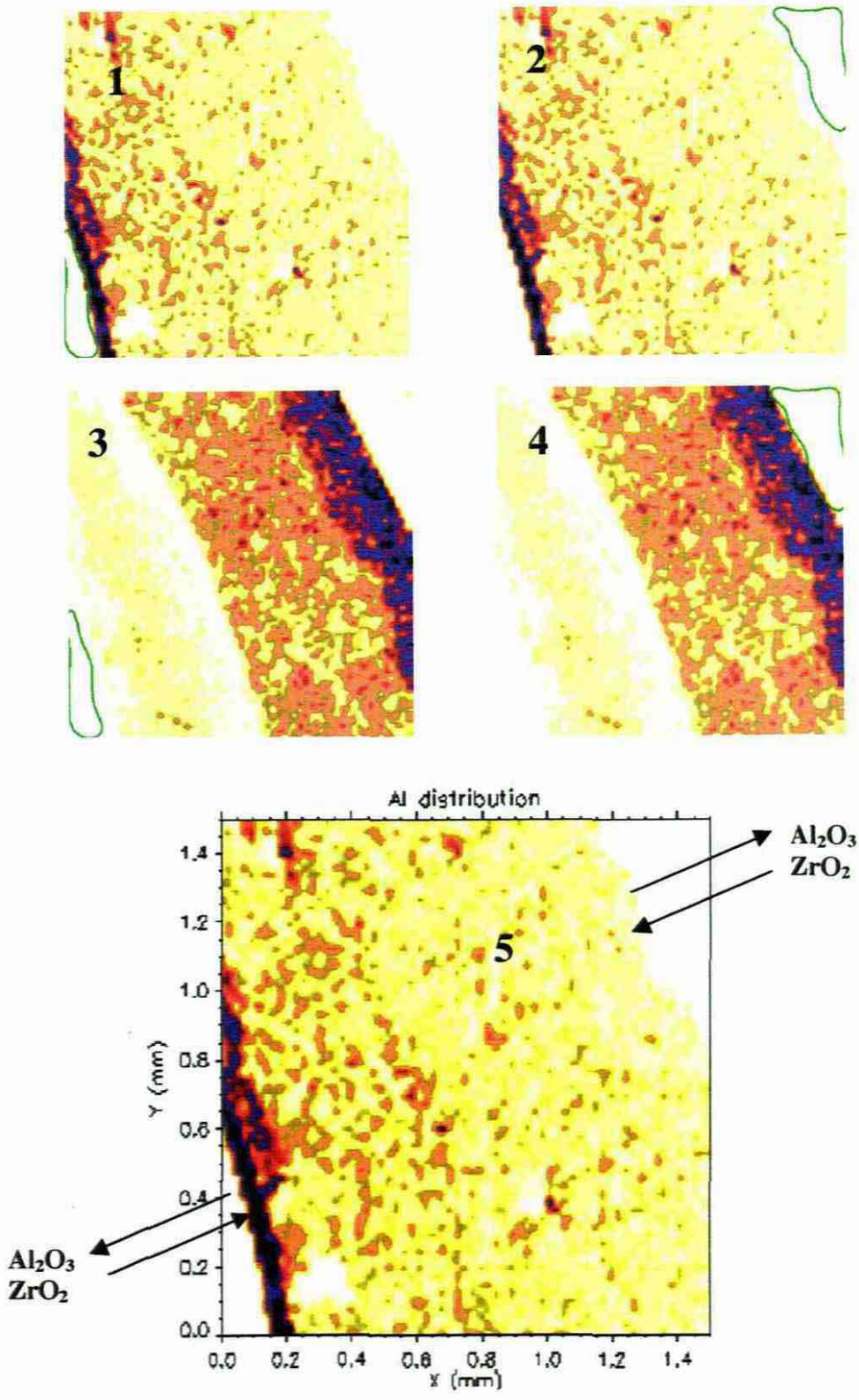

Figure [4.2.7] ***Exclusion of the Perspex areas that were scanned in from the total area scanned to extract the active matrix composition of the ceramic-based sorption electrode. The excluded areas of the top right and bottom left sections are overlaid on both the Al elemental distribution map, 1 and 2, and the Zr elemental distribution map, 3 and 4. The extracted area based on pure Al_2O_3 and ZrO_2 matrices are indicated in 5.***

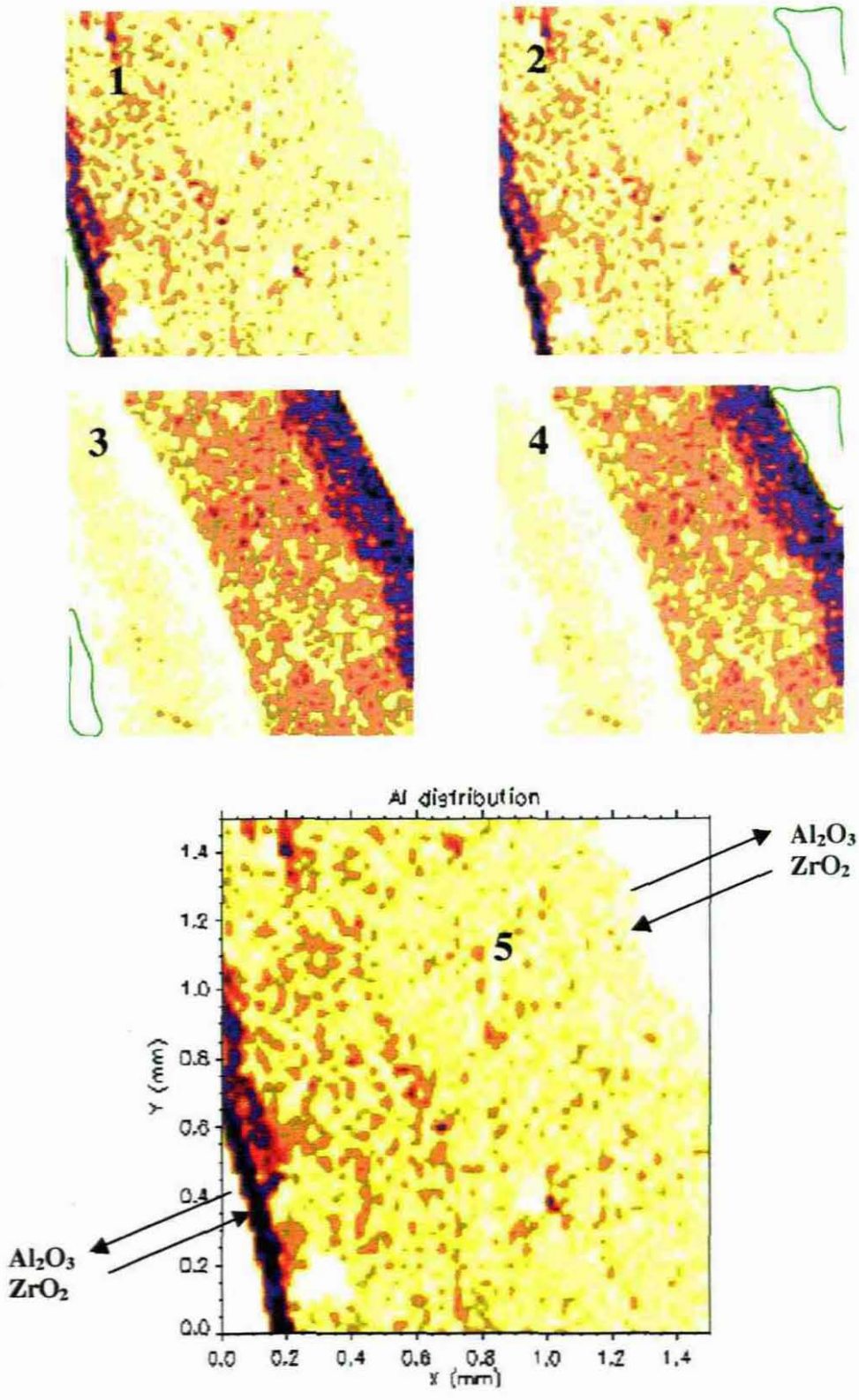

Figure [4.2.7] ***Exclusion of the Perspex areas that were scanned in from the total area scanned to extract the active matrix composition of the ceramic-based sorption electrode. The excluded areas of the top right and bottom left sections are overlaid on both the Al elemental distribution map, 1 and 2, and the Zr elemental distribution map, 3 and 4. The extracted area based on pure Al_2O_3 and ZrO_2 matrices are indicated in 5.***

and differential absorption of X-rays. This correction is shown in **figure [4.2.7(5)]**. The specimens were mounted on Perspex. These areas were considered as a remainder composition after correction of the original image. Therefore they were assigned a chemical composition of $C_5H_8O_2$ as dynamic analysis matrix. These corrections were also applied to the middle- and bottom cross-sections.

A composite of the elemental distribution images of Y to Fe, present in the top cross-section of the ceramic-based sorption electrode, is shown in **figure [4.2.8]**. The concentrations of these elements are comparable to the values given in **table [4.2.1]**. From the figure it is evident that Y, Cu, Ga and Hf have similar concentration distributions. The pattern of these concentration distributions is similar to that of the Zr elemental distribution. These elements were therefore introduced into the Al_2O_3 matrix during the reaction of the alum with the hot Zr solution.

The concentrations of Cl, K, Ti, V and Zn are equal to or below the PIXE minimum detection limits. As shown in sections [2.2] to [2.4], the PIXE MDLs are better that those of PIGE and BS for these elements. For this reason the elements are regarded as virtually absent from the matrix. Also, the concentration values of these elements are at least three orders of magnitude lower than those of Al, Zr, Ca and P. Consequently, these elements are considered as minor matrix components and Al, Zr, Ca and P as the major matrix components in the ceramic-based sorption electrode matrix. The concentration values of the minor elements did not vary significantly, that is, less than an order of magnitude when traversing from the top-, to the middle- and bottom cross-sections of the CSE. The values are therefore not indicated in the PIXE, PIGE and BS macro- or microanalysis. The values are however used when calculating the efficiency, based on the derived mathematical model, of the CSE, in removing contaminants from wastewater.

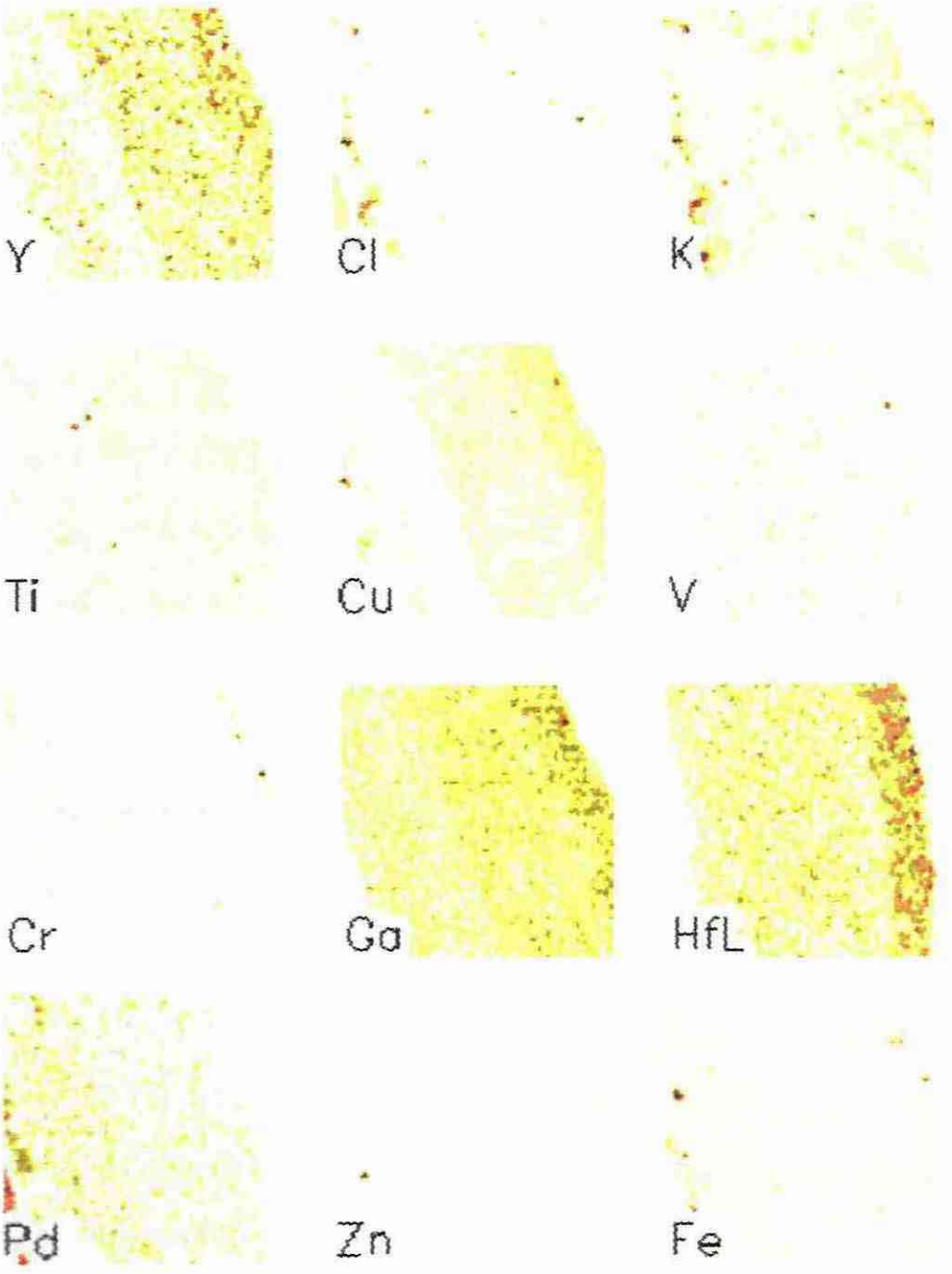

Figure [4.2.8] ***Composite of PIXE elemental distribution images of the minor elements present in the top cross-section of the coated ceramic-based sorption electrode. No relative concentration legends are given as these elements are considered as minor components. K X-ray lines were used in the PIXE quantification, except in the determination of Hf, where L X-ray lines were used. The elements Y, Cu, Ga and Hf have similar concentration distributions. The consequences of this and similar observations based on other elemental distributions are discussed in the text.***

The μ-PIXE quantitative elemental distribution maps of Al and Zr are illustrated in **figure [4.2.9]**. From a comparison of the element distribution images in **figure [4.2.8]** and **figure [4.2.9]**, it can be deduced that Cu, Ga, Y and Hf were introduced from the zirconia solution during the coating process, as these elemental distribution patterns are similar to the Zr elemental distribution.

The distribution of Al is essentially homogenous from the outside to about 75μm from the inside of the CSE. The region, which extends for approximately 75μm from the inside of the ceramic-based sorption electrode, is indicated by the arrow in **figure [4.2.9]**. In this region the Al concentration, determined with PIXE, is approximately 57 mass%. This translates into an inaccurate determination of the alumina matrix, for which the Al concentration is approximately 53 mass%. This is due possibly to some artefact that may be attributed to either an experimental error introduced during coating or to the angle at which the X-rays come into contact with the detector.

It has been shown that Al determination with PIXE is complementary to the Al determination with PIGE and BS. The latter two techniques can at this stage be used to obtain the respective concentration values of Al in this region. The result can then be applied to preliminarily ascertain the origin of the artefact above.

The uncertainty in Al measurement by PIGE, using the nuclear reaction ^{27}Al p(2,0) for which the γ-ray is emitted at 1015 keV, is comparable to the uncertainty in measuring the concentration with the other two techniques. Although the minimum detection limit is lower than for these techniques, as shown in **table [4.2.4]**, Al determination with PIGE will therefore offer a more reliable analysis.

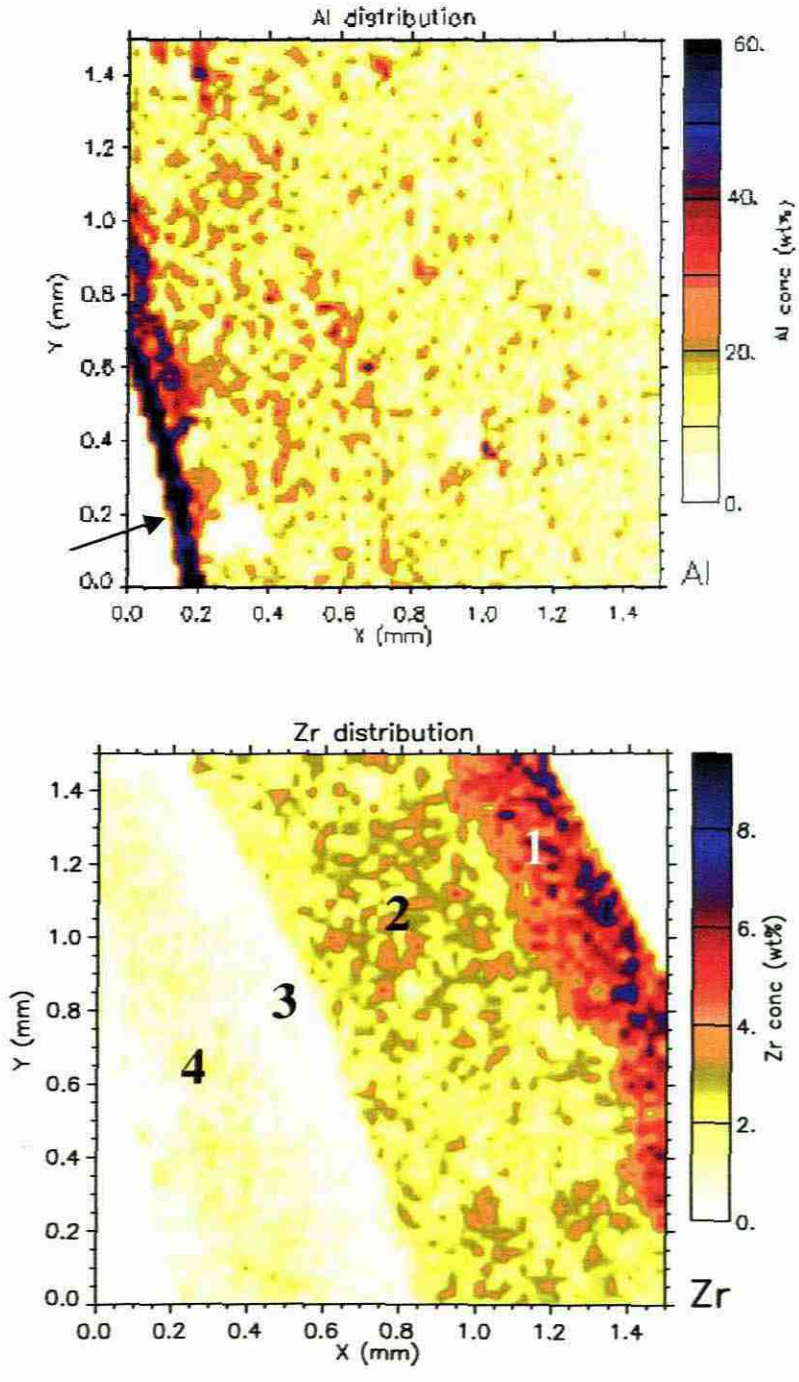

Figure [4.2.9] ***μ-PIXE quantitative elemental distribution maps of Al (top), and Zr (bottom), in the top cross-section of the ceramic-based sorption electrode. The area scanned was 1500 μm × 1500 μm to emphasise the entire width of the tube. The elemental distribution of Al is essentially homogenous, except in the innermost region. However, four distinct regions, indicated numerically, are identifiable in the Zr elemental distribution map.***

The complementary μ-IBA analysis results of the innermost region are given in **table [4.2.8]**. The uncertainties in measurement and the minimum detection limits obtained are in agreement with the analysis shown in **table [4.2.5]**, considering that a smaller charge was accumulated than for the larger areas. The statistical evaluation of the PIXE concentration and uncertainty translates to an improbable matrix composition. However, in a similar way to the base material results, evaluation of the PIGE and BS data yielded an inaccurate Al_2O_3 matrix. It is assumed from these results that the artefact is attributable to the experimental error introduced during the coating process.

Table [4.2.8] ***Complementary μ-IBA analysis results of Al for the innermost region identified in the Al elemental distribution map. The region is indicated by the arrow in figure [4.2.9], top, in the top cross-section of the ceramic-based sorption electrode. The charge accumulated was 0.118 μC.***

Technique	Energy (keV)	c_Z (mass%)	u_Z (%)	MDL ($\mu g.g^{-1}.\mu C^{-1}$)
PIXE	1.48	57.6 ± 1.97	3.42	850
PIGE	845	53.4 ± 6.71	12.57	750
	1015	53.0 ± 2.54	4.82	420
BS	2015	53.3 ± 3.13	5.85	2350

Four distinct concentration regions, which can numerically be denoted 1 to 4 from the outside of the top cross-section, are identifiable in the Zr elemental distribution. Fick's second law of diffusion, as discussed by Atkins (1999), has been included in the mathematical model. Therefore, the variation in the concentration profiles among these regions will ultimately influence the adsorption to the electrode of contaminants in the wastewater.

As the ionic contaminant traverses the width of the ceramic-based sorption electrode, it comes in contact with the first (25±3) μm thick and extremely porous ZrO_2 coating. Afterwards, there is a negative concentration profile among the three outer regions and then the sudden positive concentration profile between the two innermost regions. Furthermore, in region three, the Zr, Ca and P concentrations are relatively low with the correspondingly high Al concentration. The microanalysis of the elements for the regions is given in **table [4.2.9]**. The

reason for the relatively high BS MDL for the sum peaks elements of Al and P and of Zr and Y is the incorporation of the uncertainties in energy calibration and full width at half maximum, as obtained with the RUMP software, into the combined uncertainty. The PIXE Y concentration is relatively low, in the $\mu g.g^{-1}$ range and about two orders of magnitude lower than the Zr concentration. It should therefore not significantly affect the uncertainty in BS measurement of Zr and the corresponding minimum detection limit.

The uncertainty in measurement of Zr would therefore be influenced by the low concentration of the element. The analysis, however, compared favourably with the investigations discussed in sections [2.2] to [2.4], considering the total integrated charge accumulated for the extracted area was at least an order of magnitude smaller than those indicated in these sections.

Table [4.2.9] ***μ-IBA analysis results of the major elements, Al, Zr, Ca and P, in the four regions identified in the Zr elemental distribution map of the top cross-section of the ceramic-based sorption electrode. The total charge accumulated was 1μC. The corresponding charge and size of the individual regions analysed are indicated.***

Technique, Symbol and E_γ (keV)	REGION 1			REGION 2			REGION 3			REGION 4		
	c_Z mass%	u_Z %	MDL $\mu g.g^{-1}$	c_Z mass%	u_Z %	MDL $\mu g.g^{-1}$	c_Z mass%	u_Z %	MDL $\mu g.g^{-1}$	c_Z mass%	u_Z %	MDL $\mu g.g^{-1}$
PIXE Al	35.1	1.00	750	42.7	1.7	520	50.1	2.20	680	37.8	0.7	1700
BS (Al+P)	36.6	12.5	1350	44.3	13.1	1310	51.5	11.0	1200	39.1	14.3	1400
PIGE Al-845	35.7	10.8	1450	43.4	9.3	1380	51.6	8.9	1300	38.7	11.3	1490
PIGE Al-1015	35.4	6.9	850	42.5	5.8	800	50.3	5.4	350	38.1	4.9	510
PIXE P	1.33	2.2	25	1.20	10.3	60	0.05	7.3	70	0.89	16	59
PIGE P-1266	1.39	10.8	1300	1.22	12.0	1350	0.02	23.2	1410	0.92	10.2	1260
PIXE Ca	0.10	6.00	6	0.10	5.40	5	0.02	7.5	6	0.12	5.4	19
PIXE Zr	2.16	2.5	17	1.19	1.50	10	0.02	3.10	10	0.84	1.5	23
BS (Zr+Y)	2.22	38.5	12500	1.63	48.1	12900	ND	ND	12100	ND	ND	12400
Charge (μC)	0.199			0.649			0.179			0.318		
Area	250 μm × 740 μm			550 μm × 1100 μm			100 μm × 1110 μm			400 μm × 740 μm		

The μ-PIXE quantified elemental maps of Ca and P are shown in **figure [4.2.10]**. Compared to the Zr quantified true elemental distribution, shown in **figure [4.2.9]**, it is apparent that these elements exhibit similar distribution patterns as Zr. Therefore Ca and P were introduced into the matrix during the coating process. Pd was introduced through the zirconia solution into the ceramic-based sorption electrode matrix during the coating process. It is expected that the element will exhibit an elemental distribution similar to that of the Zr. The Pd elemental distribution pattern was however opposite and the concentration was equal to or slightly more than the minimum detection limit. This elemental distribution is consequently ascribed to statistical fluctuation and is therefore considered a minor component in the matrix

From **figure [4.2.10]** it is clear that Ca and P exhibit similar elemental distribution trends. Therefore, only the Ca elemental distribution was used for comparison with the elemental distribution of Zr. As with the Zr elemental distribution, region demarcations were also made in the elemental distribution of Ca and P; two demarcations in the instance of Ca and three in the case of P. In the outermost regions of the Zr distribution, the extent to which Ca and P are distributed, showed the same distance range to which these elements were incorporated into the CSE matrix.

The P distribution in the second innermost region, where the P concentration is low, corresponds to the low Zr content region in this element's distribution. Furthermore, the Ca concentration in the outermost region begins from a shorter linear distance range than that of P. This indicates that over this linear distance, the matrix is composed of CaO, Al_2O_3 and ZrO_2.

Therefore, during the incorporation of Zr and P into the matrix, the experimental error introduced, affected the diffusion of Ca and P into the Al_2O_3 matrix, even though the temperature during incorporation was maintained at 800°C.

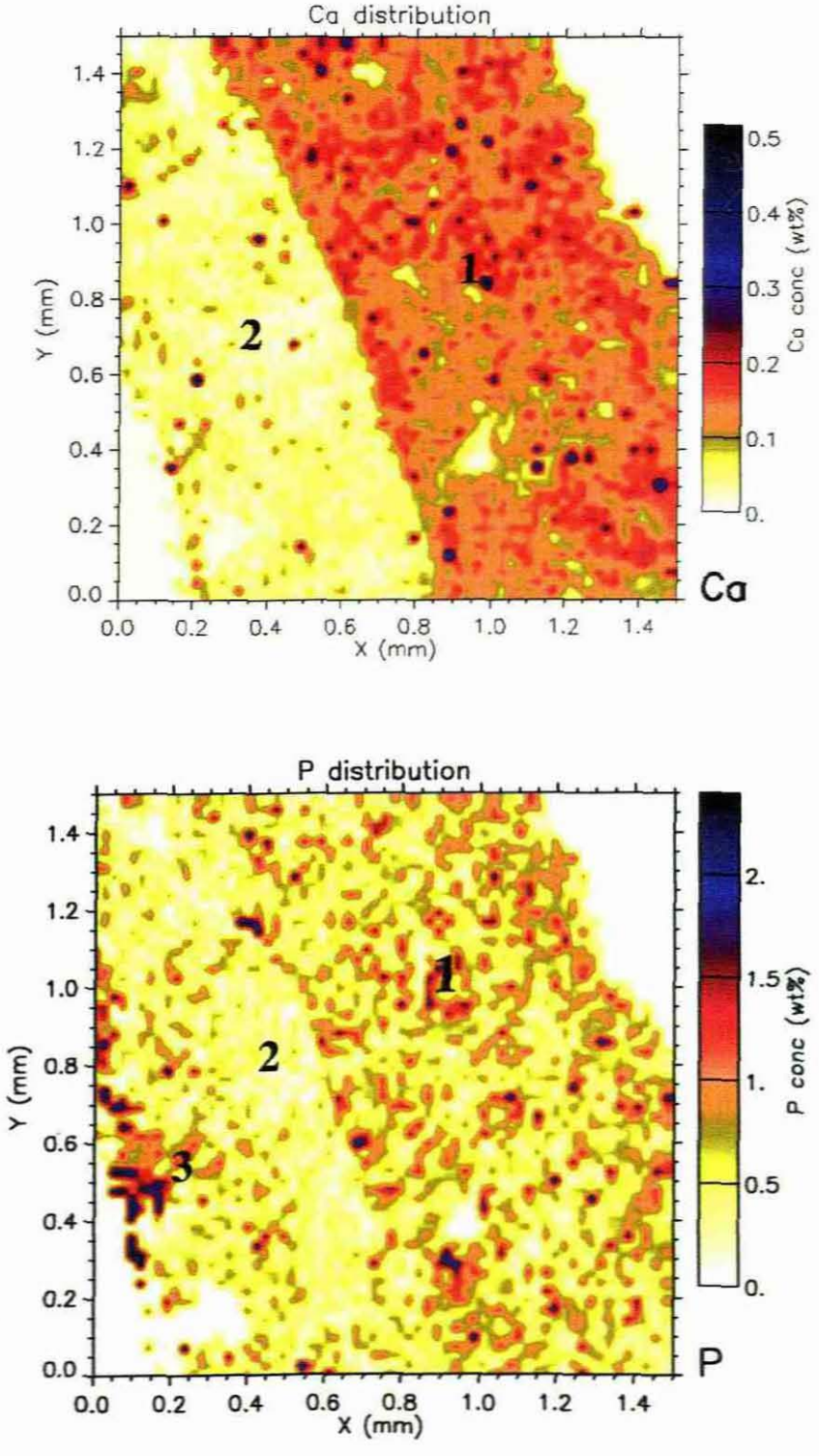

Figure [4.2.10] ***μ-PIXE quantified elemental distribution maps of elements Ca and P in the top cross-section of the ceramic-based sorption electrode matrix. These elements exhibit distributions similar to that of Zr (figure [4.2.9]). However, whereas four distinct regions are observed in the Zr distribution, only two regions for Ca and three regions for P are visible in the respective elemental distribution maps.***

Because of the varying concentration, even within the demarcated regions, a μ-PIXE linear traverse analysis was performed and is shown in **figure [4.2.11]**. The analysis extended over the entire width of 1500μm. This width is now regarded as the length of the top cross-section of the ceramic-based sorption electrode. It contrasts with the infinitesimally small cubic element assumed in the proposed mathematical model, discussed in section [4.2.4]. The assumption was however made to facilitate the derivation of the mathematical model by using a discrete width interval. In addition, a linear traverse analysis has been performed to determine elemental concentrations at periodic intervals, which corresponded to the size of the beam diameter. The relative uncertainty of measurement was low and the error per periodic interval is therefore not easily discernible in the figure.

In the μ-PIXE linear traverse analysis, the composition in the linear distance range of 1375 to 1400μm indicated only Zr as element present. For the distance of 1375μm to the inside of the ceramic-based sorption electrode, the Al concentration is approximately equal to the average value of 37.8 mass%. It is also from this distance that the Ca and P concentrations increase. These elements are therefore incorporated into and not onto the Al_2O_3 matrix. For the linear distance range 800 to 1200μm, the P concentration is relatively constant, whereas for Ca, five concentration profiles are observed. However, the concentration profiles are not prevalent over the entire demarcated region. Hence, linear traverse analyses performed in different locations within the demarcated area would yield different concentration profiles for Ca. For Zr, only one concentration profile was present in this linear distance range of 1100 to 1400μm, whereas the concentration was relatively constant in the distance range of 800 to 1100μm. As indicated on the elemental distribution map, the concentration of Zr was significantly low in the distance range of 450 to 525μm, with the corresponding decrease in P and Ca concentrations and increase in Al concentration.

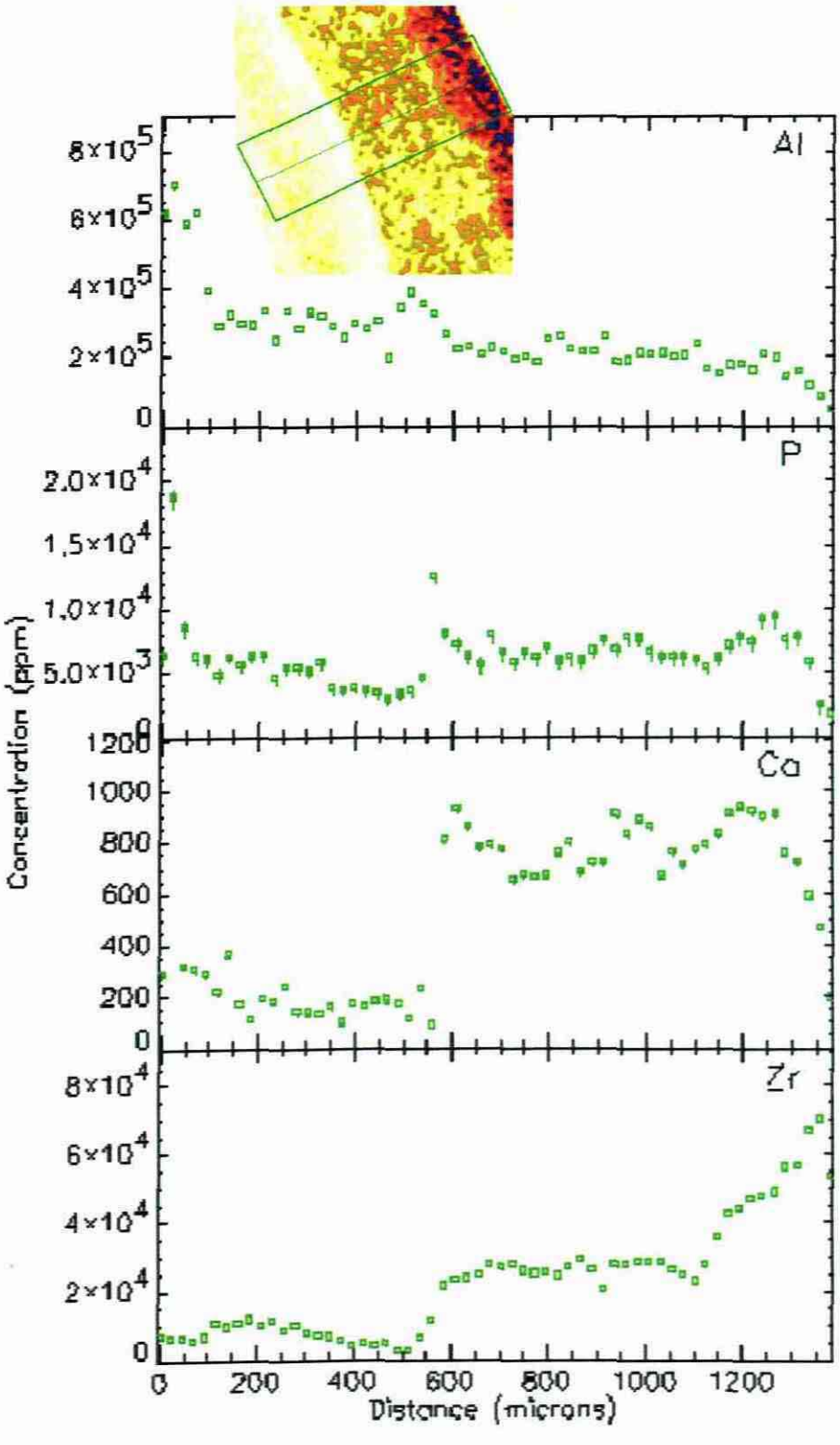

Figure [4.2.11] ***μ-PIXE linear traverse analysis across the width of the top cross-section of the ceramic-based sorption electrode, showing the variation in concentrations with linear distance of the elements Al, Zr, Ca and P. The size of the area analysed, based on the Zr elemental distribution map (inset), is 500μm × 1300μm and the corresponding integrated charge was 0.855 μC.***

From the preceding discussions, it is suggested that the coating process of the base material had been interrupted, which retarded the incorporation of the Zr solution content into the base material matrix.

This accuracy is detailed by correlating the elemental distributions of Ca and Zr. The pixel in the map of the elemental distribution represents a data point in the multi-element space (Ryan et al. (1995)). The concentration correlation between two elements therefore shows a two-element projection from this space. This revealed small-size inhomogeneities, which may be discrete phases. For this reason emphasis was placed on the beam diameter and the area to be scanned, as indicated in section [3.2]. The relationship between Ca and Zr distributions could at first approximation be described as positive linear correlation. However, closer inspection revealed that in the four regions considered, this relationship did not always apply. The two-element correlation between Ca and Zr in the four demarcated regions are shown in **figure [4.2.12]**. The correlation distributions in these four regions are overlaid in green colour on the Zr elemental distribution map to emphasise the pertaining area. Therefore, as the cationic contaminant in the wastewater was transported under the potential difference and the mass flow through the ceramic-based sorption electrode, it came into contact for the first (25±3) μm with the porous ZrO_2 matrix. As indicated before, there was no Ca-Zr correlation for **region 1** in **figure [4.2.12]**, since elements other than Zr are present in this region in quantities below the minimum detection limits. In the correlation graph, **regions 2 to 4** represent a decreasing concentration difference to the ionic contaminant. Hence, adsorptions in these regions would depend on the concentration of the contaminant in the wastewater. It is expected that removal of the ionic contaminants will not be effective in this region and desorption may instead occur. In the innermost region, the Ca-Zr correlation was negative and an increasing P concentration difference was experienced. The path of an anionic contaminant through the ceramic-based sorption electrode can be described in a similar manner with the exception that opposite

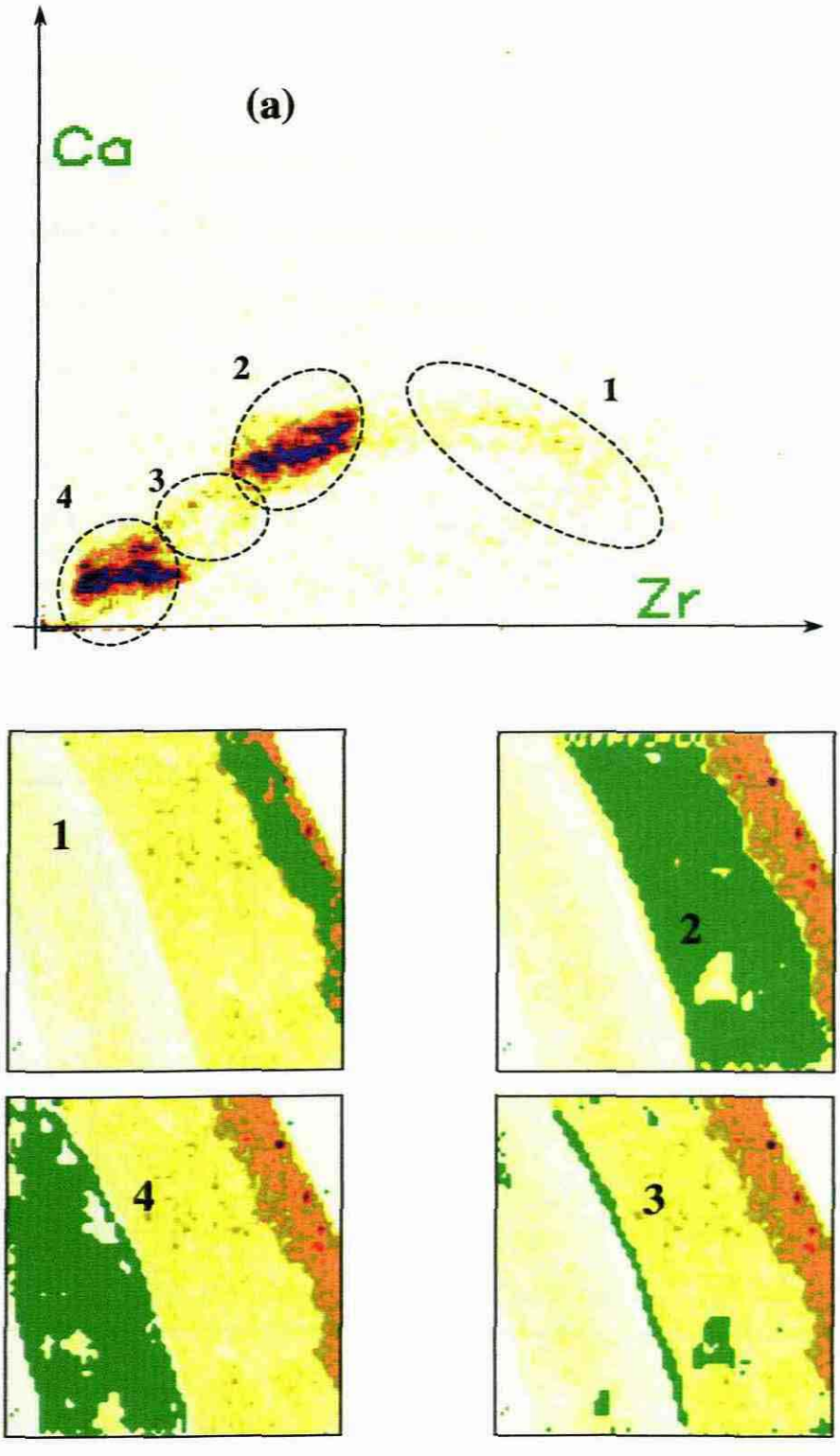

Figure [4.2.12] ***μ-PIXE elemental distribution correlation between Ca and Zr in the four regions identifiable in the Zr elemental distribution map in the top cross-section of the ceramic-based sorption electrode. The direction of the axes indicates increasing element concentrations. The respective correlations of the two-element projections in the four regions (numbered 1 to 4) are overlaid in green colour on the Zr elemental distribution map.***

concentration profiles would be experienced.

For the middle cross-section of the ceramic-based sorption electrode, the μ-PIXE quantified elemental distribution maps of Al, Ca, P and Zr are shown in **figure [4.2.13]**. Only three concentration regions can be identified in the Zr elemental distribution map. The μ-IBA analysis results of Al, Zr, Ca and P in the regions are given in **table [4.2.10]**.

Table [4.2.10] ***μ-IBA analysis results of Al, Zr, Ca and P in the three regions identified in the Zr elemental distribution map in the middle cross-section of the ceramic-based sorption electrode. The total charge accumulated was 1μC. The corresponding charge and size of the individual regions analysed are indicated.***

Technique and Element	REGION 1			REGION 2			REGION 3		
	c_Z mass%	u_Z %	MDL $\mu g.g^{-1}$	c_Z mass%	u_Z %	MDL $\mu g.g^{-1}$	c_Z mass%	u_Z %	MDL $\mu g.g^{-1}$
PIXE Al	22.3	4.3	360	25.7	4.3	380	27.4	4.5	390
BS (Al+P)	23.9	10.2	1450	26.8	9.5	1450	28.5	8.8	1450
PIGE Al-845	22.9	10.1	1380	26.3	8.7	1450	27.9	9.2	1390
PIGE Al-1015	22.2	6.4	870	26.1	6.8	800	27.5	6.9	850
PIXE P	0.81	9.8	40	0.77	8.9	40	0.68	8.0	40
PIGE P-1266	0.82	3.8	80	0.82	5.1	90	0.02	23.2	1410
PIXE Ca	0.24	3.9	6	0.22	4.6	3	0.23	4.8	3
PIXE Zr	1.47	1.3	16	0.88	1.5	6	0.81	1.9	7
BS (Zr+Y)	1.50	36.3	11200	ND	ND	11200	ND	ND	11200
Charge (μC)	0.142			0.417			0.181		
Area	250 μm × 740 μm			550 μm × 1100 μm			100 μm × 1110 μm		

As in the case of the Zr distribution map in the top cross-section of the CSE, the outer region has a high Zr concentration, which decreases as the cross-section width of the SE towards the innermost region is traversed. Ca distribution is homogenous and there is no apparent correlation with the Zr distribution, as is the case in the top cross-section. P distribution is diffused, yielding high uncertainties in the elemental quantification. In the Al elemental distribution map, the same artefact as found in the top cross-section of the ceramic-based sorption elect-

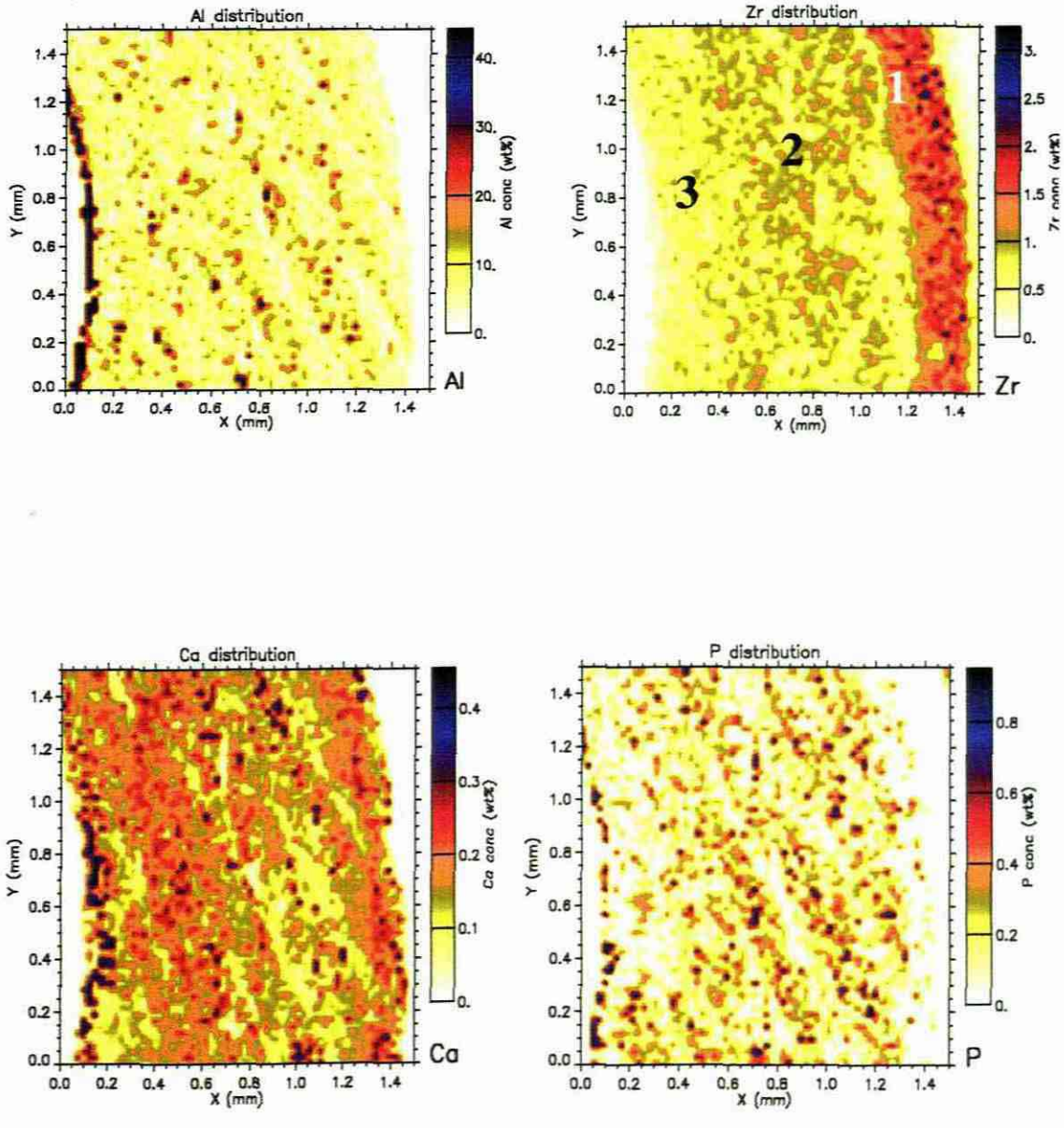

Figure [4.2.13] ***μ-PIXE quantified elemental distribution maps of the elements Al, Zr, Ca and P in the middle cross-section of the ceramic-based sorption electrode. Three distinct regions, indicated numerically by 1, 2 and 3, are identifiable in the Zr distribution map. No regions are identifiable in the Ca and P elemental distribution maps. These elemental distributions are described as diffused.***

rode is visible. The width of this region was smaller than the width in the top cross-section of the ceramic-based sorption electrode. The μ-IBA analysis results of the artefact visible in the Al distribution are given in **table [4.2.11]**. Also visible in the elemental distributions in **figure [4.2.13]**, is the Zr concentration distribution extending further than the other 3 element concentration distributions. This indicates that the Al_2O_3 tube is coated with a layer of ZrO_2.

Table [4.2.11] ***Complementary μ-IBA analysis results of Al for the innermost region seen in the quantified elemental distribution of Al in the middle cross-section of the ceramic-based sorption electrode. The total charge accumulated was 0.099 μC.***

Technique	E (keV)	c_Z (mass%)	u_Z (%)	MDL ($\mu g.g^{-1}.\mu C^{-1}$)
PIXE	**1.48**	48.7 ± 1.67	3.4	850
PIGE	**845**	50.0 ± 6.35	12.8	760
	1015	48.4 ± 2.15	2.8	420
BS	**2015**	49.5 ± 3.71	7.5	11500

The total elemental matrix composition in the middle cross-section was relatively higher than in the top cross-section, signifying that a smaller degree of porosity exists than in the top cross-section of the CSE. This means that a smaller mass of elements has been coated onto and incorporated into in the top cross-section of the alum matrix than the middle cross-section. The uncertainty in P determination is indicative of the diffused elemental distribution.

The μ-PIXE linear traverse analysis of the middle cross-section is shown in **figure [4.2.14]**. Al is omitted, as Al_2O_3 is considered to constitute the remainder of the matrix composition. The Ca and P linear traverse analyses indicate that these elements are present in quantities below the MDL in the first linear distance range of approximately 25μm.

Hence a coating of this thickness range, consisting of extremely porous ZrO_2, has been deposited on the surface of the base material. The Ca concentration remains constant in the linear distance range of 220 to 1200μm. The distribution of P in this distance range is however diffused and no regions could be identified in the elemental distribution map.

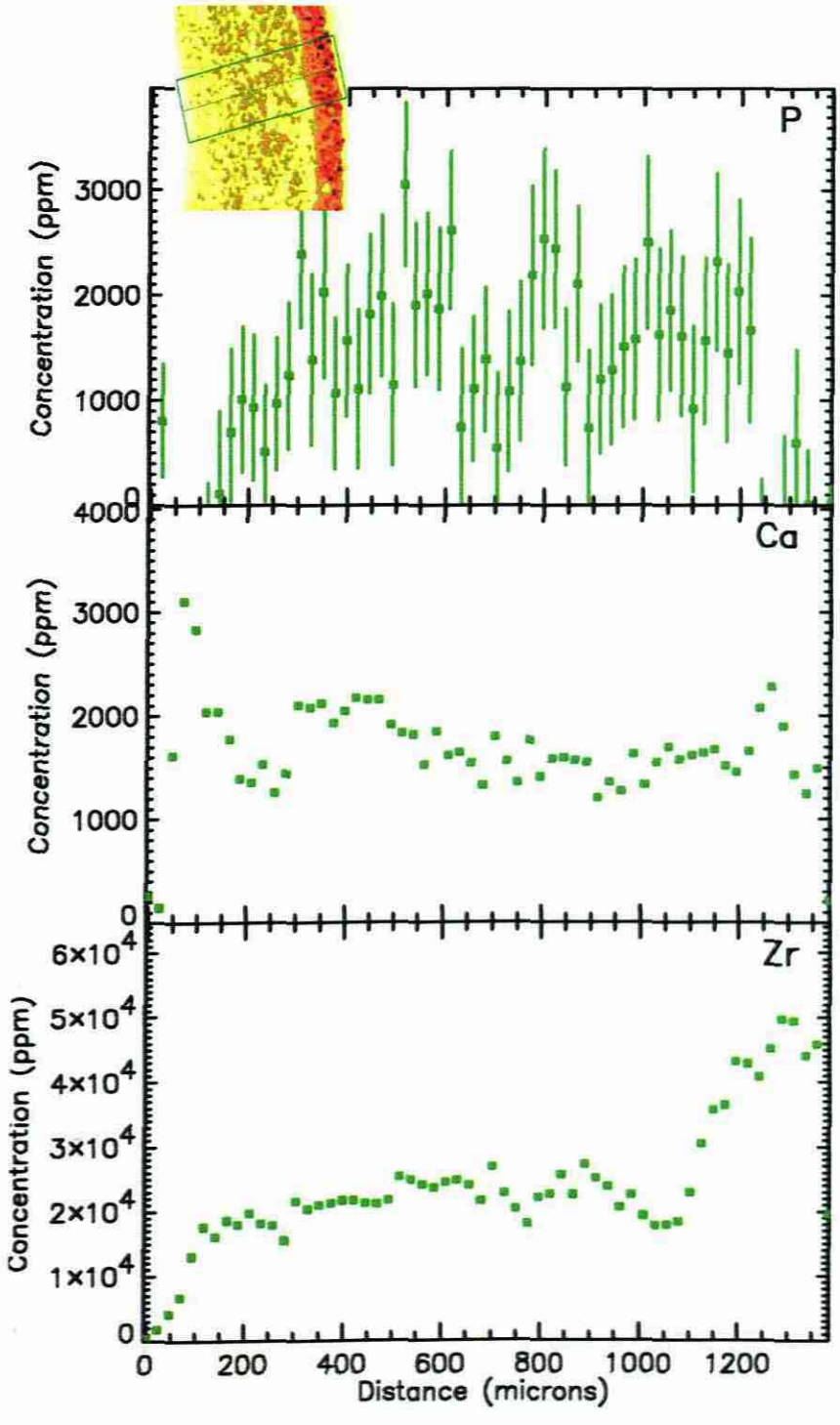

Figure [4.2.14] ***μ-PIXE linear traverse analysis across the width of the middle cross-section of the ceramic-based sorption electrode (CSE), showing the variation in concentrations of P, Ca and Zr with linear distance. The linear traverse analysis of Al is omitted as Al_2O_3 is assumed to constitute the remainder of the CSE matrix. The size of the area analysed, which is based on the Zr elemental distribution, (inset), was 500μm×1300μm and the total accumulated charge was 0.860 μC.***

This can be deduced from the microanalysis given in **table [4.2.7]**. The Zr distribution trend in the distance range from 1100 to 1400 μm resembled the distribution of the element in the top cross-section. The distance range of 0 to200 μm was composed of almost pure Al_2O_3, indicated by the significantly low concentrations of P and Zr. This confirmed the assertion that the coating procedure could have been disrupted.

Although the Ca concentration remained fairly constant for most of the distance range in the μ-PIXE linear traverse analysis of the middle cross-section, the Ca and Zr two-element correlation was extracted to ascertain any inhomogeneities that might exist. The concentration correlation between the elements Ca and Zr is shown in **figure [4.2.15]**.

The two-element correlation in the three regions discerned in the Zr elemental distribution was readily observable. The concentration profile that would be experienced by the ionic contaminants was considerably discontinuous when compared to the Ca and Zr two-element correlation in the top cross-section. Therefore, even though the Ca distribution was apparently homogenous with respect to colour concentration profile, there still existed areas with element concentrations that varied significantly, giving rise to the discontinuity in the two-element projection.

The discontinuous region correlations were also diffused. This indicates that even if more than one path through the ceramic-based sorption electrode cross-section is followed by the ionic species, the resultant removal of contamination from the wastewater would be different. A number of calculations of the removal of these contaminants would therefore have to be performed for each path followed through the cross-section to obtain reliable results to which the mathematical model can be applied.

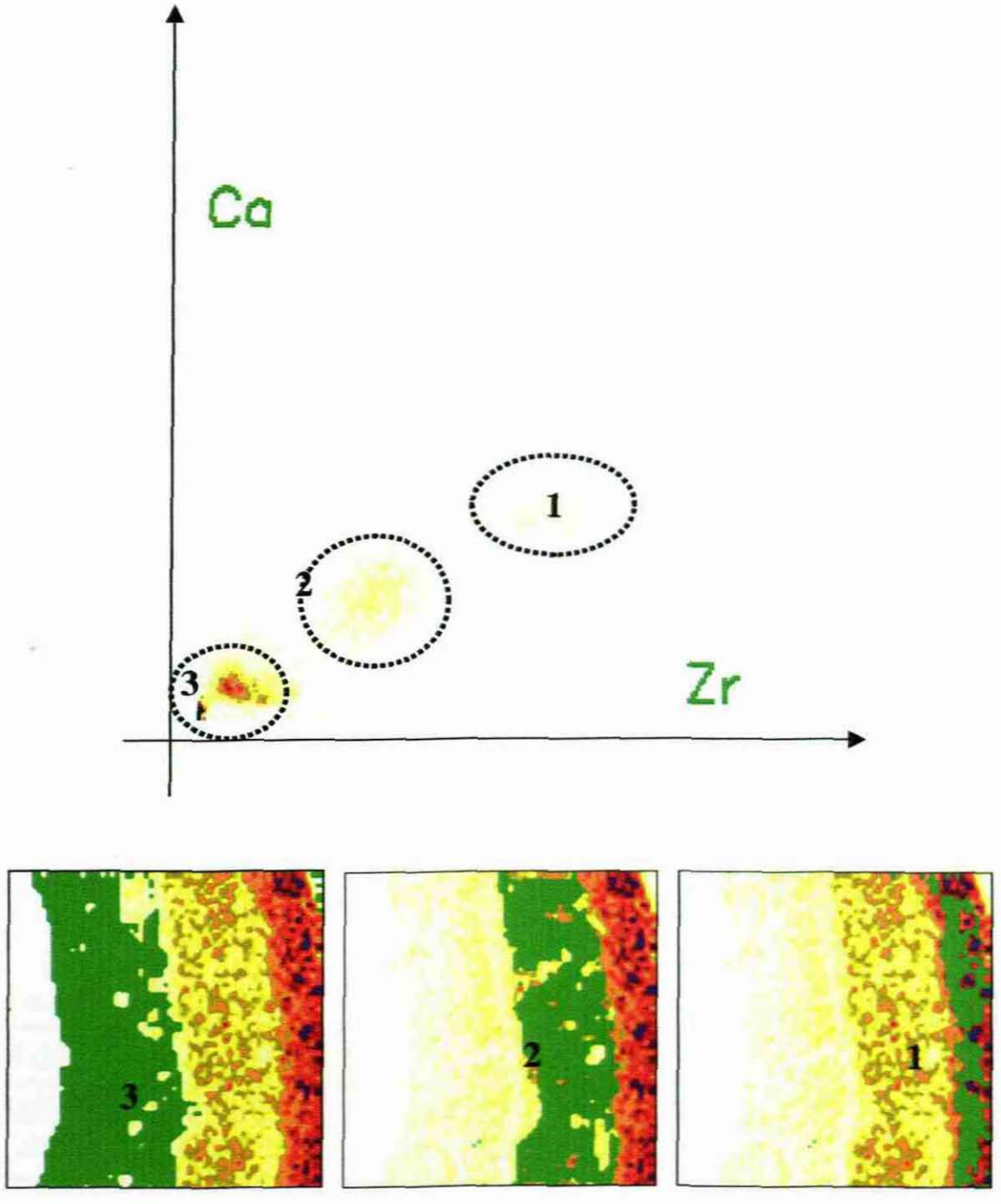

Figure [4.2.15] ***μ-PIXE elemental distribution correlation between Ca and Zr in the three regions identifiable in the Zr elemental distribution map of the middle cross-section of the ceramic-based sorption electrode. The direction of the axes indicates increasing concentrations of the two elements. The respective correlations of the two-element projections in the regions (numbered 1 to 3) are overlaid in green colour on the Zr elemental distribution map.***

The μ-IBA analysis results of the major elements, Al, Zr, Ca and P in the bottom cross-section of the ceramic-based sorption electrode are indicated in **table [4.2.12]**. The quantified elemental distribution maps of the major elements Al, Zr, Ca and P in the bottom cross-section are shown in **figure [4.2.16]**. As in the top cross-section of the ceramic-based sorption electrode,

Table [4.2.12] ***μ-IBA analysis results of Al, Zr, Ca and P in the four regions identifiable in the Zr quantified elemental distribution map of the bottom cross-section of the ceramic-based sorption electrode. The total charge accumulated was 1μC. The corresponding charge and size of the individual regions analysed are indicated.***

Technique and Element	REGION 1			REGION 2			REGION 3			REGION 4		
	c_z mass%	u_z %	MDL $\mu g.g^{-1}$	c_z mass%	u_z %	MDL $\mu g.g^{-1}$	c_z mass%	u_z %	MDL $\mu g.g^{-1}$	c_z mass%	u_z %	MDL $\mu g.g^{-1}$
PIXE Al	35.1	1.00	750	42.7	1.7	520	50.1	2.20	680	37.8	0.7	1700
BS (Al+P)	36.6	12.5	1350	44.3	13.1	1310	51.5	11.0	1200	39.1	14.3	1400
PIGE Al-845	35.7	10.8	1450	43.4	9.3	1380	51.6	8.9	1300	38.7	11.3	1490
PIGE Al-1015	35.4	6.9	850	42.5	5.8	800	50.3	5.4	350	38.1	4.9	510
PIXE P	1.33	2.2	25	1.20	10.3	60	0.05	7.3	70	0.89	16	59
PIGE P-1266	1.39	10.8	1300	1.22	12.0	1350	0.02	23.2	1410	0.92	10.2	1260
PIXE Ca	0.10	6.00	6	0.10	5.40	5	0.02	7.5	6	0.12	5.4	19
PIXE Zr	2.16	2.5	17	1.19	1.50	10	0.02	3.10	10	0.84	1.5	23
BS (Zr+Y)	2.22	38.5	12500	1.63	48.1	12900	ND	ND	12100	ND	ND	12400
Charge (μC)	0.199			0.649			0.179			0.318		
Area	250μm × 740μm			550μm × 1100μm			100μm × 1110μm			400μm × 740μm		

four regions could be discerned in the Zr elemental distribution map, but only two regions in the Ca distribution map. The P distribution was diffused and hence regions could not be demarcated in this elemental distribution map. The mass transfer of the contaminated water was from region 1 to region 4. The concentration profile was considered as positive when the concentration in region 1 was less than in region 2. When starting from the innermost region, no. 4 and of thickness 650 μm, there was essentially a constant Ca concentration profile. The

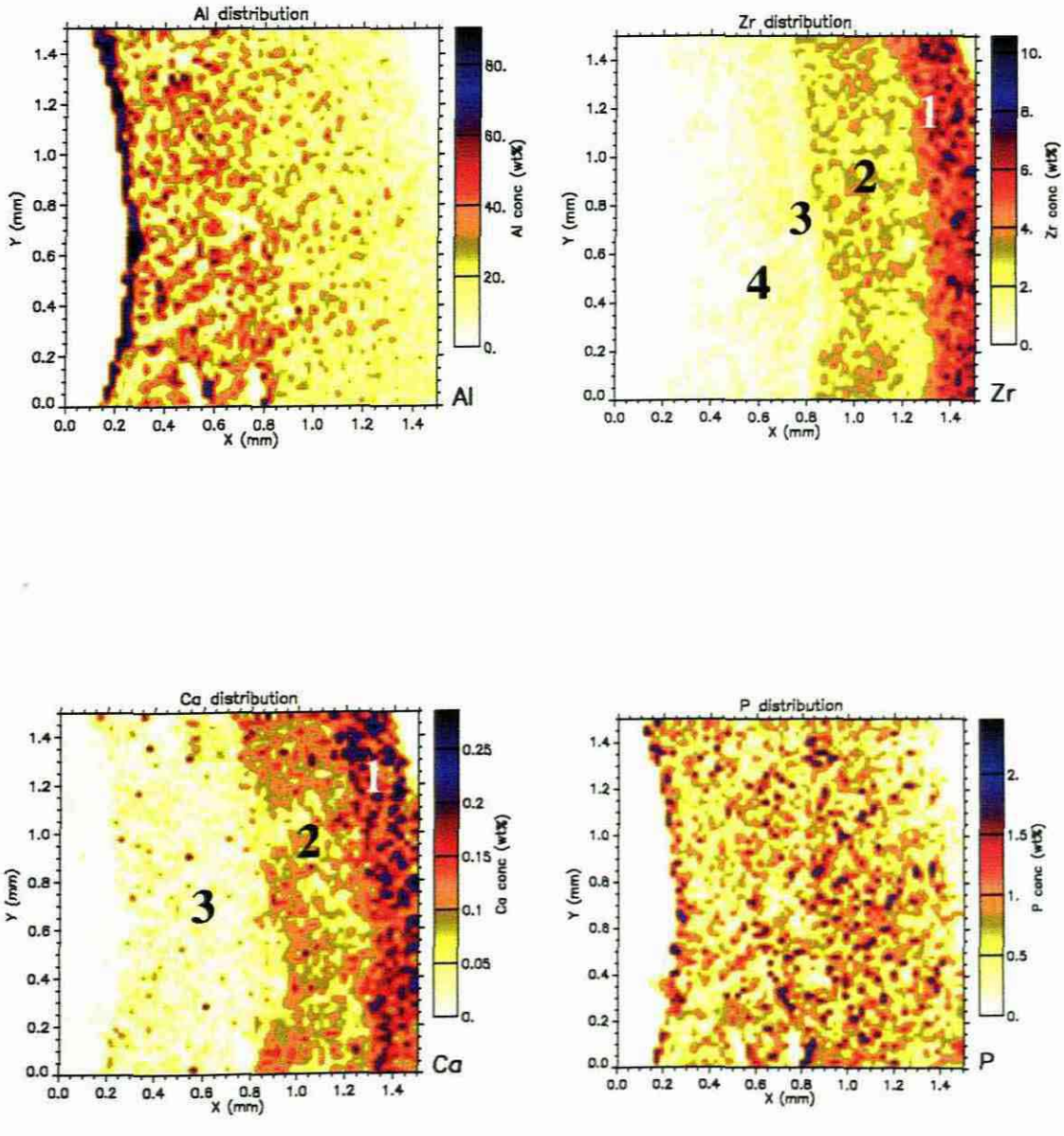

Figure [4.2.16] ***μ-PIXE quantified elemental distribution maps of elements Al, Zr, Ca and P in the bottom cross-section of the ceramic-based sorption electrode. As in the top cross-section, four regions are identifiable in the Zr elemental distribution map. However, in contrast to the top cross-section, where only two regions are identifiable in the Ca elemental distribution map, three regions are identifiable in the bottom cross-section. No regions can be discerned in the P elemental distribution map.***

negative profile was due to the statistical fluctuations caused by the high values at about 100 and 200μm. In the 30μm thick region 3, the correlation was negative. This region was relatively thin and statistics available were low since only a charge of 0.05 μC was accumulated.

Region 2 has a thickness of 600μm for which the charge accumulated was 0.847 μC. Here the correlation was negative. It should be noted that in this region the concentrations of all the major elements, except Al, were relatively high. The next outer region, region 1, had a thickness of 250μm and here the correlation was positive. The outer layer is not demarcated as a region in the Ca elemental distribution map, since the Ca concentration in this region was below the MDL. This layer was (60±3) μm thick and consisted of highly porous ZrO_2. The elemental distributions of minor elements yielded results similar to those in the top- and middle cross-sections of the ceramic-based sorption electrode. The μ-PIXE linear traverse analysis across the bottom cross-section of the ceramic-based sorption electrode is shown in **figure [4.2.17]**. Here again the concentration profile of Al is omitted as Al_2O_3 was considered to constitute the remainder of the matrix composition. Only the P concentration profile increased with the linear distance traversed. Both Ca and Zr had a decreasing concentration profile. The Ca-Zr two-element correlation showed a similar pattern as that in the top cross-section of the ceramic-based sorption electrode and is for this reason not shown.

A detailed elemental quantification of the three cross-sections of the ceramic-based sorption electrode is provided. From this quantification it is evident that the cross-sectional elemental compositions of the top- and bottom cross-sections are similar. These elemental compositions differed markedly from that of the middle cross-section. Since the sorption electrode would be orientated perpendicularly to the direction of the wastewater flow, it is assumed that the radial elemental distribution varies linearly with the radial distance between the top (or bottom) cross-section and the middle cross-section.

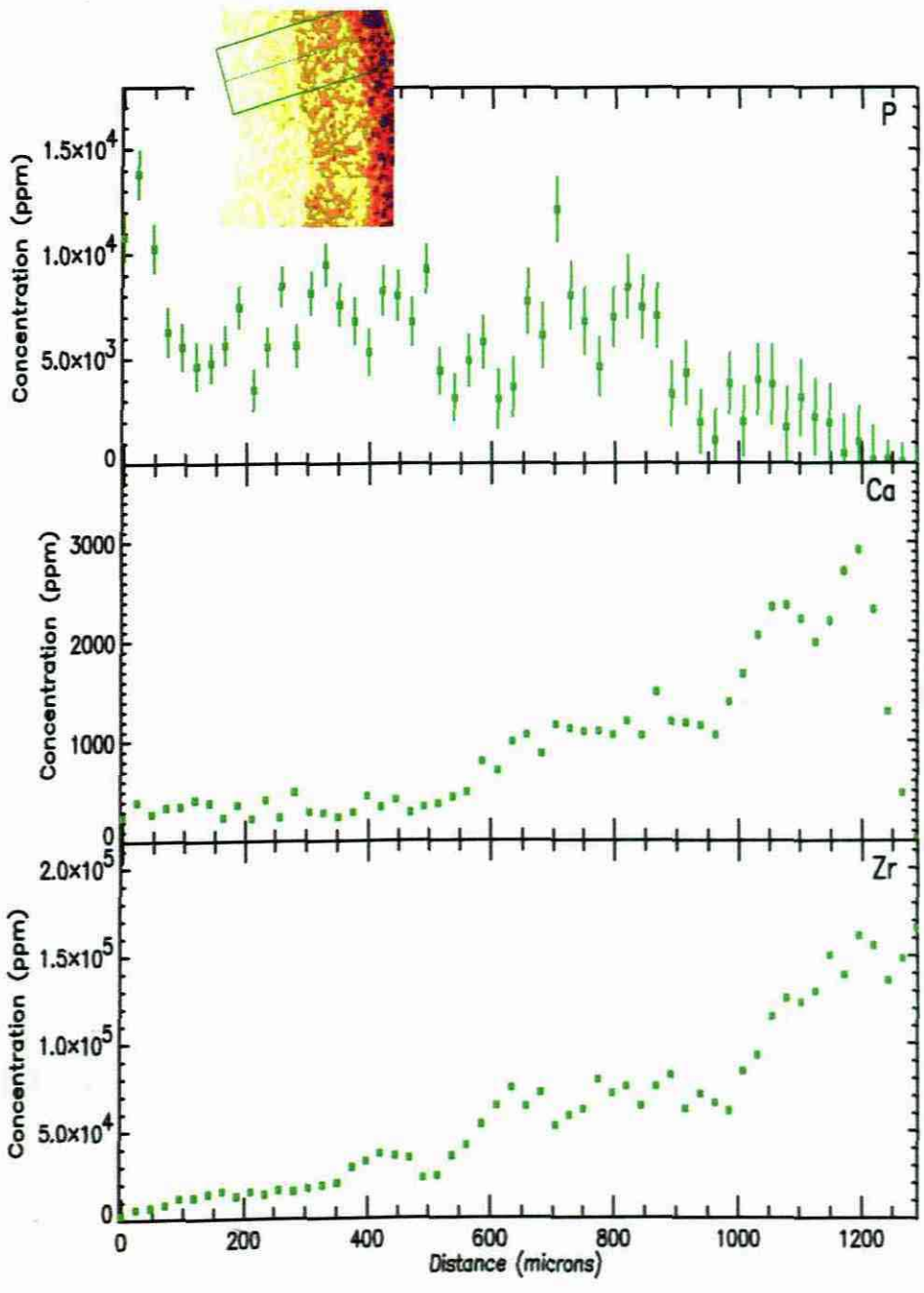

Figure [4.2.17] ***μ-PIXE linear traverse analysis across the width of the bottom cross-section of the ceramic-based sorption electrode (CSE), showing the variation in concentrations with linear distance of the elements P, Ca and Zr, which were selected as major components. The linear traverse analysis for Al is omitted as Al_2O_3 is assumed to constitute the remainder of the CSE matrix. The size of the area analysed (inset), was 500μm × 1300μm and the corresponding total integrated charge was 0.858 μC.***

As there are four discernible regions in the top (or bottom) cross-section and only three regions in the middle cross-section, the elemental composition per unit linear distance traversed in regions 2 and 3 in the top (or bottom) cross-section can be averaged to yield a composition that would ultimately result in the elemental composition per unit linear distance traversed in region 2 of the middle cross-section. Hence, in this manner the radial elemental composition of the ceramic-based sorption electrode can be obtained. The concept is illustrated in **figure [4.2.18(A)]**.

The principle use of these electrodes is for the purification of contaminated water. An infinitesimally small cubic element, dx.dy.dz, shown in **figure [4.2.18(B)]**, can now be assumed. The surface area, dx.dz, represents the previously quantified cross-sections. The side area is represented by dx.dy and the face area by dy.dz. Although the quantified area is finite, the cubic element is assumed to be infinitesimally small for derivation of the mathematical model.

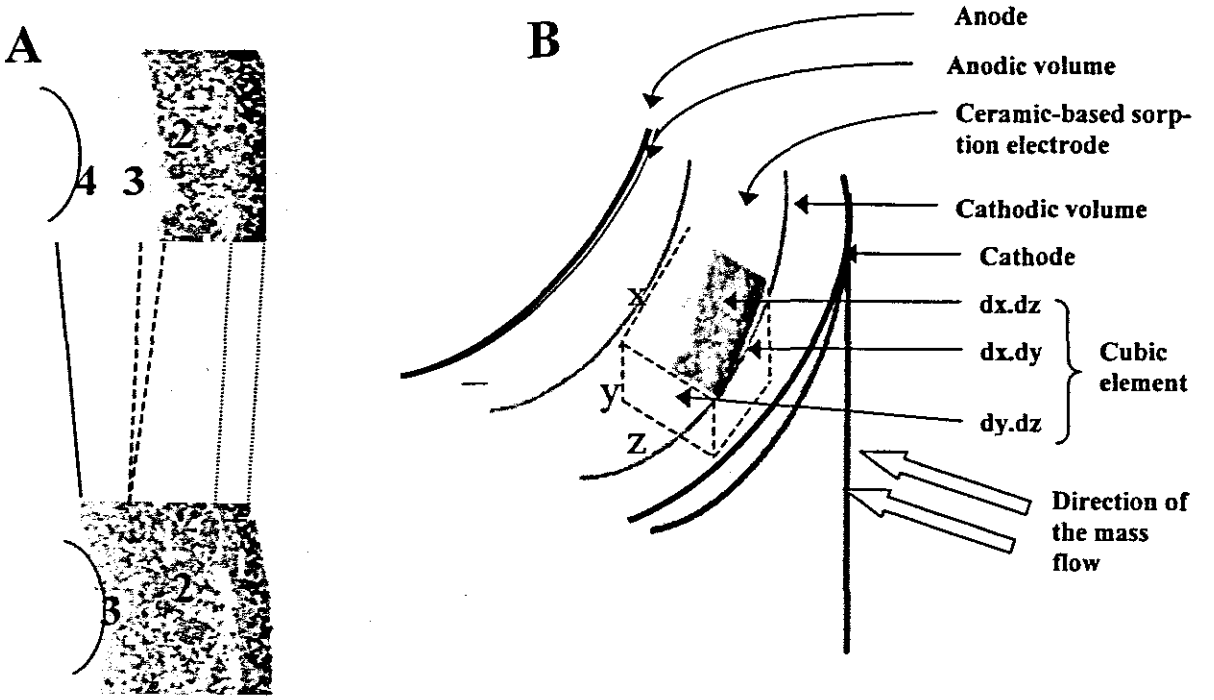

Figure [4.2.18] ***Illustrations of (A) the concept used in establishing the radial elemental composition of the ceramic-based sorption electrode (CSE) and (B) the infinitesimally small cubic element, dx.dy.dz, assumed in the derivation of the mathematical model for evaluating the efficiency of the CSE.***

The electrolytic system consisted of the anode, the quantified cross-section and the cathode. A horizontal cross-section through the system to illustrate dz of the cubic element is shown in **figure [4.2.19]**.

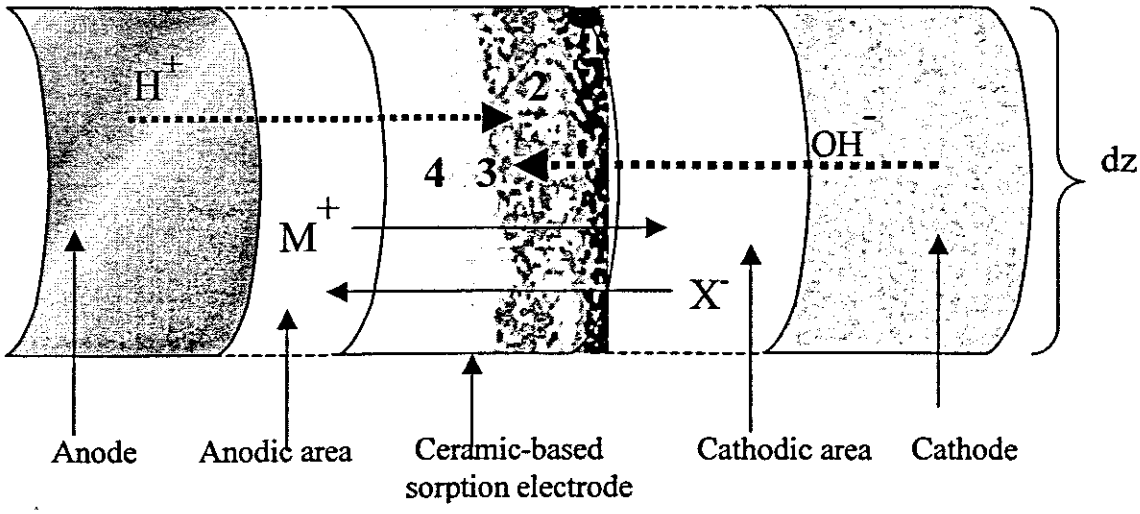

Figure [4.2.19] ***Top cross-sectional view through the electrolytic system to illustrate dz of the infinitesimally small cubic element, dx.dy.dz, assumed in the derivation of the mathematical model for evaluating the efficiency of the ceramic-based sorption electrode.***

The mass flow is therefore in the direction perpendicular to dx.dy. In aqueous solution, interactions of the solute and the solvent molecules result in transport processes, which are predominantly limited by the equivalent of frictional forces. Hence, when an ionic species of charge, ±, used as superscript, and molecular mass, az, used as subscript, is acted upon by a potential difference, dE/dx, it moves with a drift velocity, v. The drift velocity is proportional to the force provided by the field. However, when the ionic species moves through the ceramic-based sorption electrode, it comes into contact with concentration profiles, c. v is defined in terms of dE/dx, c, the mobility, μ, of the species, and the diffusion coefficient, D, by equation [4.2.1] (Atkins, 1999). The mobility is related to the diffusion coefficient by equation [4.2.2], where k is the Boltzmann constant, ±ez is the charge of the ionic species and T is the temperature (in Kelvin). The fraction of charge, q, carried by the ionic species, is the pro-

$$\left|v_{az}^{\pm}\right| = \mu_{az}^{\pm} dE/dx + \frac{D_{az}^{\pm}}{c_{az}^{\pm}} dc_{az}^{\pm}/dx \qquad \textbf{4.2.1}$$

$$D_{az}^{\pm} = \frac{kT\mu_{az}^{\pm}}{\pm ez} \qquad 4.2.2$$

duct of the velocity and concentration and is given by equation [4.2.3]. The total current is the sum of the current fractions, $i_{az}^{\pm}$, of all species, which is product of the sum of charge frac-

$$q_{az}^{\pm} = \left|v_{az}^{\pm}\right| c_{az}^{\pm} \qquad 4.2.3$$

tions, the area through which each charge is transferred and the faraday constant, F. No initial values are given on the summation since these can be initialised with any ionic species present in the water. n is the total number of ionic species which, for water analysis is usually 21. It

$$I = \sum^{n} i_{az}^{\pm} = F\left(\sum^{n} dy.dz\right)\left(\sum^{n} q_{az}^{\pm}\right) \qquad 4.2.4$$

should be noted that the surface area through which all charges are transferred is the surface area, equation [4.2.5], of the ceramic-based sorption electrode.

$$\sum^{n} dy.dz = \int^{n} dy.dz = A \text{ the total surface area.} \qquad 4.2.5$$

These equations give an adequate description of the wastewater flow through the ceramic-based sorption electrode of the mass of contaminated water. Hence, the rate of mass accumulation within each of regions is equal to the rate at which the mass is transported to the region less the rate at which mass is transported out of the region. In describing the momentum flow, it should be noted that as the contaminated water passes through each of the regions, it would decrease in density as the elements are removed. Considering now an infinitesimal cubic element, dx.dy.dz, then the mass flux, φ, through the face area, dx.dy where v is the velocity, is given in equation [4.2.6]. The mass transport rate out of the region in the direction z + dz,

$$\varphi = \left(\rho_{v_x}\right)_z (dx.dy) \qquad 4.2.6$$

and still through the face dx.dy can be determined in a similar manner. This derivation is independent of factors such as suspended matter that would clog pores in the sorption electrodes, the ion exchange that normally occurs at the region face area, desorbing species pre-

sent in the mass flow, activity of ions near the region face area, fluctuations in the velocity of the mass, pH dependence of the sorption electrodes and change in the direction of flow, even though such changes might or might not be significant.

Various models for surface complexations were proposed. These models have been reviewed by Davis and Kent (2002) who found that the Triple-layer model has the widest application.

Equations [4.2.1] to [4.2.6] in this study, the equations in Davis and Kent (2002) and the equations and electrode specifications of Bladergroen (2001) can now be used to simulate the removal of ionic contaminants from the wastewater. The parameters used in simulating the removal of Ca from the wastewater are given in **table [4.2.13]**.

Table [4.2.13] ***Parameters used the evaluation of the efficiency, based on the derived mathematical model, of the ceramic-based sorption electrode in the removal of ionic species (here Ca) from wastewater at 25 ℃. Those indicated by [a] were obtained from Bladergroen (2001), those by [b] from Moollan (2002), given in appendix [5.4.2.1], and those by [c] from Atkins (1999). The constants are given in appendix [5.1.1].***

Parameter	Value	Unit	Parameter	Value	Unit
Flow rate[b]	1.023	m^3s^{-1}	Mobility of Ca[c]	6.17×10^{-8}	$m^2s^{-1}V^{-1}$
Catholyte volume[a]	9.012×10^{-9}	m^3	Voltage[a]	10	V
Anolyte volume[a]	5.832×10^{-9}	m^3	Current[a]	2×10^{-1}	A
Area of cathode[a]	4.7×10^{-4}	m^2	Temperature	298.15	K
Area of anode[a]	1.8×10^{-4}	m^2	Faraday constant	9.6485×10^4	$Cmol^{-1}$
Ca concentration[b]	104	$\mu g.g^{-1}$	Gas constant	8.3144	$Jmol^{-1}.K^{-1}$

In **figure [4.2.20]**, the corresponding concentration of Ca being removed from the wastewater is plotted against the linear traverse analysis from the innermost section of the ceramic-based sorption electrode as shown in **figure [4.2.19]**.

The analysis of the sorption electrodes by using μ-PIXE, μ-PIGE and μ-BS, have exposed the small inhomogeneities that might exist in the composition of the specimen. μ-PIXE was used to show the elemental distribution of the constituents of the electrode. This was taken a step further by using μ-PIGE to verify the presence of light elements in the specimen matrix. μ-BS

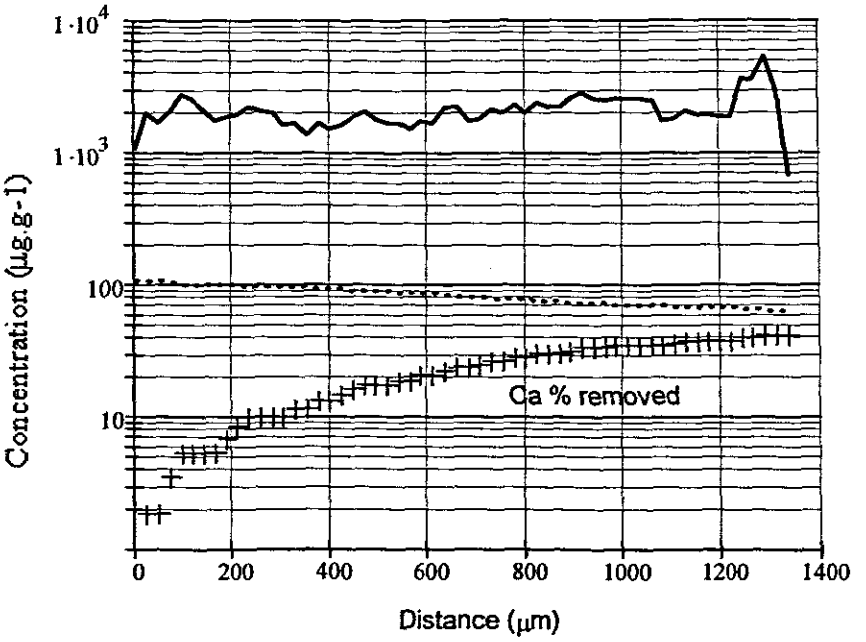

Figure [4.2.20] ***Plots obtained from the simulation of the efficiency, based on the derived mathematical model, of the ceramic-based sorption electrode, in the removal of Ca from wastewater. A typical analysis of wastewater was obtained from Moollan (2002). The continuous line indicates the Ca concentration in the ceramic-based sorption electrode, the dotted line the as analysed Ca concentration in the wastewater and the + sign indicates the percentage of Ca removed from the wastewater.***

was used to determine the presence of elements such as C, N and Be in the matrix. The use of μ-PIXE exposed the inhomogeneity of the elemental distribution of composition and how this inhomogeneity affected the distribution of other elements in the matrix (Mars et al., 2000). It was found that elements such as Ca, usually present in contaminated water, was introduced during the impregnation procedure. Only 40 mass% of Ca is removed by the ceramic-based sorption electrode.

4.3 High Temperature Superconductors (HTS)

4.3.1 Introduction

When current flows in an ordinary conductor, for example copper wire, some energy is lost (Giancoli, 1997). In contrast, superconductors have the ability to conduct electricity without the loss of energy (Eisberg and Resnick, 1985). The temperature at which superconductivity occurs is referred to as the critical temperature, T_c. Superconductors could therefore eliminate the problem of resistance in everything from common household currents to huge electrical plants to the high-energy particle accelerators. They could also be used to create powerful electromagnets. Those superconductors that have T_c greater that 77K, the boiling point of nitrogen, are referred to as high temperature superconductors (HTS). This high T_c is an advantage since the cost of liquid helium, which has to be used for evaluating superconductors of T_c less than 77K, is prohibitive.

Generally, HTSs are ceramic compounds that consist of the rare-earth elements such as yttrium and lanthanum. The most investigated HTS is $YBa_2Cu_3O_{7-x}$ (YBCO), which is the oxygen deficient form of $YBa_2Cu_3O_7$. The oxygen deficiency, x, occurs in the lattice structure of the compound. YBCO has a transition temperature of about 92K. The structure of $YBa_2Cu_3O_7$ (Eisberg and Resnick, 1985) is depicted in **figure [4.3.1 (a)]**).

The layer of YBCO is usually deposited on high purity polycrystalline substrates such as MgO and $SrTiO_3$. The oxygen deficiency causes a huge difference in the T_c of YBCO (Eisberg and Resnick, 1985). This variation of T_c with oxygen deficiency is shown in **figure [4.3.1 (b)]**. From this figure it is evident that the optimum critical temperature is obtained at a deficiency of 0.1. This corresponds to a concentration of 16.8 mass% oxygen. The preparation of HTS is therefore critical for obtaining the ideal deficiency, and hence the optimum T_c. This was the impetus for varying the energy density of the laser during the pulsed laser deposition

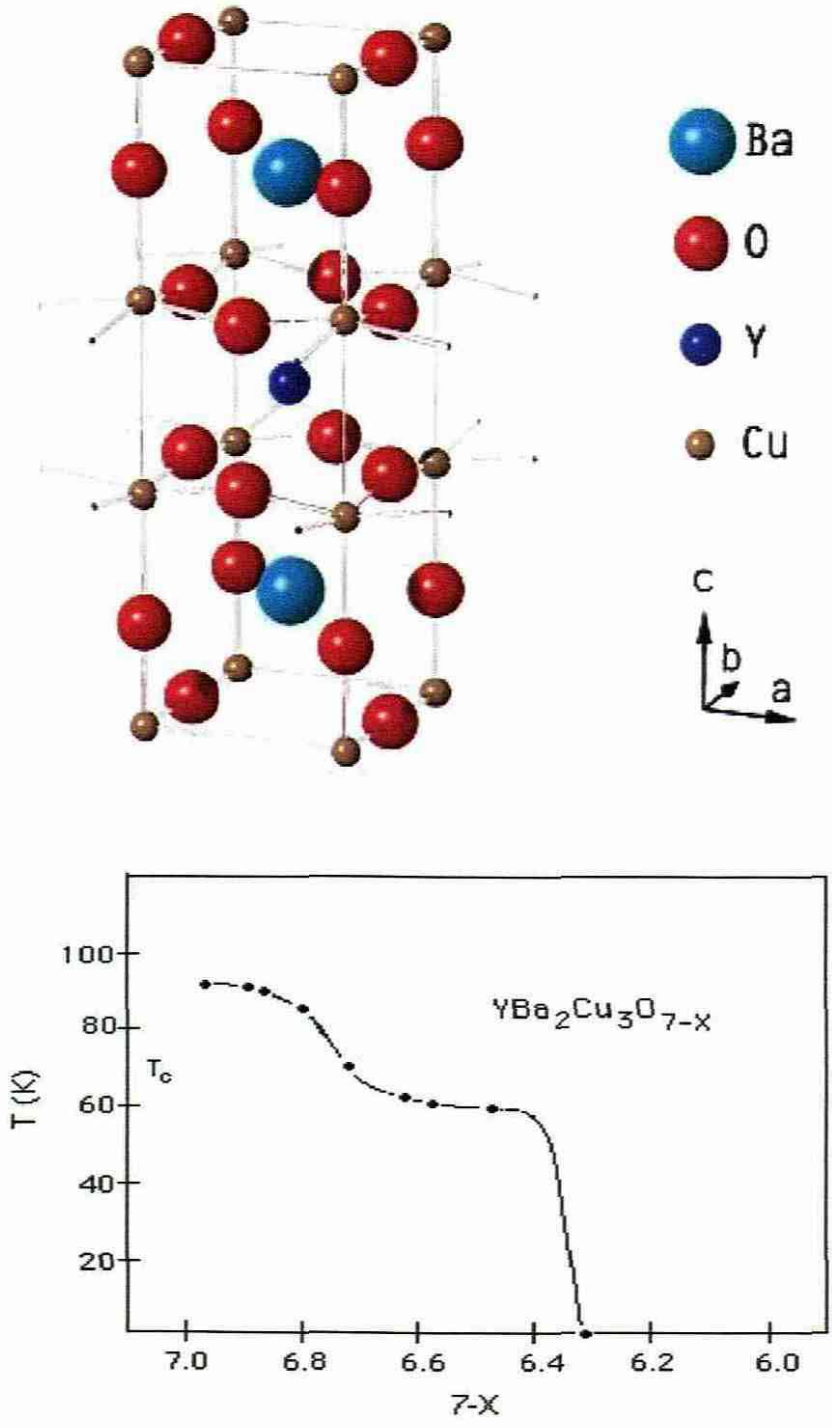

Figure [4.3.1] ***Illustration of (a) the structure of $YBa_2Cu_3O_7$, rendered with the POV-Ray software (Obukhov et al., 2002). It is orthorhombic, with llattice constants of a = 3.8231 Å, b = 3.8864 Å, c = 11.6807 Å. The corresponding colours of the balls, representing the atoms, are indicated. The superconductor has a transition temperature of 92K, which is above the boiling point of liquid nitrogen. In (b) the variation of oxygen content, with the superconducting temperature, T_c, (Eisberg and Resnick, 1985), is shown. The maximum superconductivity is achieved when the oxygen content is 16.8 mass %.***

of the YBCO layer. It would then be of interest to 1) investigate the variation in elemental composition as the layer increased in thickness and 2) ascertain the uniformity and homogeneity with which the specimen was formed, that is, if any interaction between the elements of the substrate and the superconducting YBCO layer occurred.

4.3.2 Survey of elements

The YBCO tablet was prepared from high purity BaO, Y_2O_3 and CuO. Hence, any other elements would be present in concentrations at the $\mu g.g^{-1}$ level only. The determination of elements Y and O have been described in the previous section. Of essence in this section is the quantification of Cu and Ba by PIXE, PIGE and BS.

For PIXE, the Cu K_α X-rays and K_β X-rays are emitted at 8.047 keV and 8.904 keV, respectively. Interferences with the Cu K_α X-rays are expected from the Ni K_β X-rays, emitted at 8.264 keV, and the L_α X-rays of Ta, emitted at 8.145 keV. Interferences with the Cu K_β X-rays are expected from the Zn K_α X-rays, emitted at 8.638 keV, and the L_α X-rays of Os, emitted at 8.145 keV. The energy differences of Cu K_α X-rays with L_α X-rays of Ta and the Cu K_β X-rays with the L_α X-rays of Os lie outside the detector resolution. However, the expected concentrations of these elements are in the $\mu g.g^{-1}$ level. The relative intensities of these X-rays would therefore be low, that is, at least three orders of magnitude lower than the intensity of the Cu K_α X-rays lines. The energy differences of Cu K_α X-rays with the Ni K_β X-rays and the Cu K_β X-rays with the Zn K_α X-rays lie within the resolution of the Si(Li) detector. The concentrations of Ni and Zn are also expected to be in the $\mu g.g^{-1}$ level. In this instance, the mutual interference of the element pairs, based on the work of Peisach (1993), would be insignificant. Most copper ore contains Fe (Atkins, 1999) and the element is therefore expected to be present in the YBCO matrix, though also at the $\mu g.g^{-1}$ level. The quantification of

Ba was done by using the intensities of the L_α X-ray lines, emitted at 4.467 keV and the L_β lines, emitted at 4.828 keV. No other elements, when bombarded with particles emit X-rays at these respective energies, and interferences were therefore not expected.

Because of the ultra high purity of the oxides used in preparing the YBCO layer, light elements were not expected to be present in the matrix. Consequently, the PIGE MDLs in **table [2.3.2]** were assumed applicable to this matrix. Based on the work of Gihwala (1982) and MacFarlane and Moller (1997), the γ-rays of Cu, which could possibly be induced by 3 MeV protons, would be emitted at 115 keV, 194 keV and 670 keV. The respective reactions are ^{65}Cu p(5, 2), ^{63}Cu n(1, 0) and ^{63}Cu p(1, 0). Interferences at the three γ-ray energies are only posed by elements with $Z \geq 71$. The regressed sensitivities for these elements are all in excess of 2 mass%. Since the base components were of high purity, these interferences were ruled out. MDLs of Cu for the three reactions have not been included in **table [2.3.2]**, since Cu was not considered a light element. The PIGE MDLs for Cu, as regressed from the data of Gihwala (1982), is of the order 1 mass% and greater. However, as YBCO contains Cu concentrations of 13 mass% and more, the MDLs were evaluated using pure copper as a standard. These MDLs are given in **table [4.3.1]**. Because of the high u_Z values and MDLs obtained for

Table [4.3.1] ***Uncertainty in measurement and minimum detection limits for Cu, which are determinable with PIGE when using a 3 MeV proton beam. The matrix and element concentrations hereof are indicated. The beam diameter size was 3μm × 5μm and the total integrated charge 1μC. The detector to specimen distance was 17 cm.***

Element symbol	γ-ray energy (keV)	Reaction	Matrix	c_Z mass%	u_Z %	MDL (mass%.μC^{-1})
Cu	115	^{65}Cu p(5, 2)	Pure Cu	100.0	18.4	19.3
	194	^{63}Cu n(1, 0)	Pure Cu	100.0	21.7	30.5
	670	^{63}Cu p(1, 0)	Pure Cu	100.0	3.45	1.88

the ^{65}Cu p(5, 2) and ^{63}Cu n(1, 0) reactions, the corresponding γ-rays were not used for quantification. Only the first level de-excitation, ^{63}Cu p(1, 0), was used to establish complementarity with the PIXE and BS determinations of Cu.

As indicated, the concentration of O in the specimen gouverns the T_c of the YBCO layer and hence quantification of this element is of cardinal importance. For BS quantification of oxygen, the reaction $^{16}O(p,p)^{16}O$ exhibits a resonance at 3.50 MeV (Amirikas et al., 1993). The energy used in this study is 3 MeV. In this respect it could be argued that better resolution would be obtained when performing this determination at this energy. However, the concentration of O in the specimen is relatively high and such quantification would not yield a significantly higher accuracy. The proton k_Z values of the substrate elements, those of the YBCO layer and of the Ir on Si standard are given in **table [4.3.1]**. Energy differences for O, Mg and Cu lie within the resolution of the SSB detector. Poor resolution is however indicated for Y and Ba of the YBCO layer. However, the essence here is the determination of O in the superconducting layer with the afore-knowledge that O is also present in the polycrystalline MgO substrate, of which the composition is known.

Table [4.3.2] ***Kinematic factor values and energies of the major matrix elements present in the $YBa_2Cu_3O_{7-x}$ (YBCO) layer and of the polycrystalline MgO substrate, on which the YBCO layer was deposited. The absolute values of the energy differences of O (E_O) with the other elements (E_Z) are shown. Values for Ir and Si of the Ir on Si backscattering standard are indicated for comparison.***

Element	Kinematic factor	Energy (keV)	$\lvert E_O-E_Z \rvert$ (keV)
O	0.777	2332	0
Mg	0.847	2542	210
Cu	0.939	2816	484
Y	0.956	2867	535
Ba	0.971	2913	581
Si	0.866	2599	267
Ir	0.979	2938	606

4.3.3 Experimental

4.3.3.1 Specimen preparation

Stoichiometric amounts of the oxides of Ba, Cu and Y were weighed to prepare the YBCO tablet. The oxide powders were then thoroughly mixed, using acetone as medium. The mixture was heated to 70°C to evaporate the acetone. Afterwards the temperature was gradually increased to 1200°C in oxygen ambient. The powder mixture was cooled and pressed into a

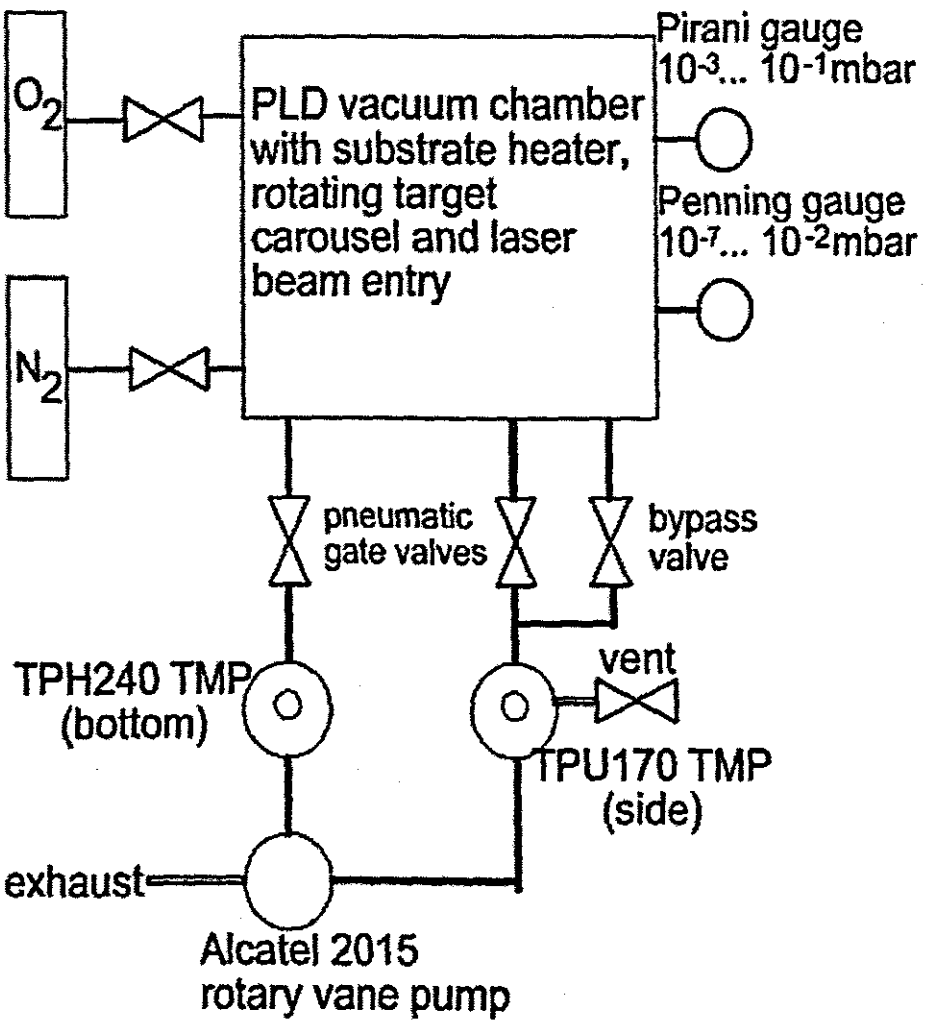

Figure [4.3.2] ***Illustration of the pulsed deposition instrumentation used to perform the deposition of $YBa_2Cu_3O_{7-x}$ on polycrystalline MgO substrate.***

ıblet form. The tablet was then heated in oxygen ambient to 1600°C for about 70 hours and ıen cooled to room temperature. An illustration of the pulsed deposition instrumentation is ıown in **figure [4.3.2]**. However, prior to the deposition process the correct position of the

focused laser beam spot on the target with regard to the substrate was verified. If in this instance chamber movement was necessary, it was slightly rotated to maintain the laser entry lens in a fixed position. This assured proper lens irradiation by the laser beam. For removal of undesired remnants on the target surface resulting from cross-contamination by other targets, the target was pre-ablated with the shutter in front of the substrate closed. It was then opened with the shutter away from the laser beam and the target ablated for the desired time. The temperature and the oxygen pressure were verified regularly. No target rotation was made.

YBCO specimens were annealed at 490 °C (achieved by the temperature controller) and oxygen ambient of 900 mbar was maintained for duration of 30 minutes. For a high O_2 ambient, the bypass valve had to be closed and the needle valve to be opened accordingly. The chamber pressure did not exceed 900 mbar during this operation. After the annealing, the specimens were cooled to 200 °C and the chamber then evacuated (Mars et al. III, 2003).

4.3.3.2 Instrumental Parameters

The instrumentation parameters, including the geometries of the detectors, as detailed in section [3] of this study, were applied in the quantification of the HTS. The diameter of the proton beam was 3μm × 5μm. The current was maintained between 100 and 200pA and a charge of 1μC was accumulated. As indicated previously the base components were of high purity. Light elements were therefore not expected in the matrix. Consequently, a 153μm thick Al filter was used for the attenuation of the Cu, Y and Ba X-rays.

4.3.4 Results and discussions

The spectrum of the macro-PIXE data of the YBCO layer deposited on polycrystalline MgO is shown in **figure [4.3.3]**. The X-ray peaks are identified in **table [4.3.3]**. In the spectrum,

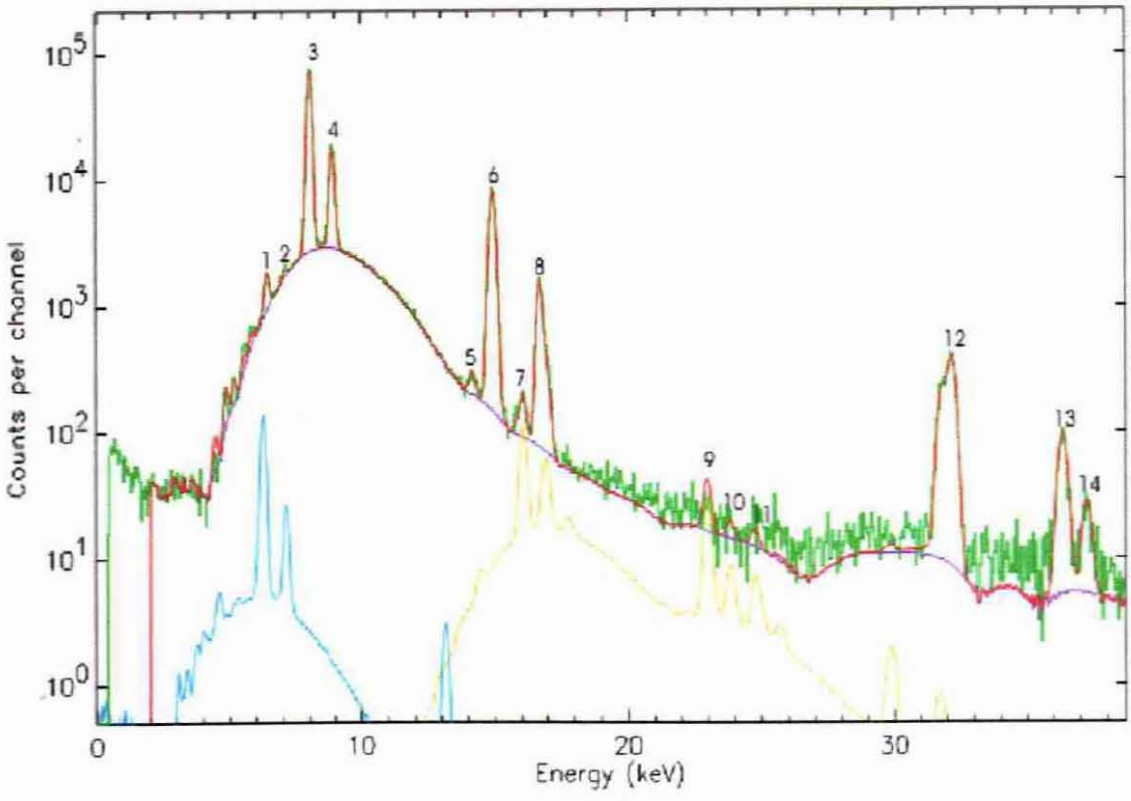

Figure [4.3.3] ***Spectrum of macro-PIXE data of the YBCO layer deposited on polycrystalline MgO. The green line represents the data, the orange line the GeoPIXE II fit to the data and the purple line the background correction. The blue line represents the Si escape peaks and the yellow line the pile-up from the spectrum.***

Table [4.3.3] ***Identification of peaks in the spectrum of the macro-PIXE data.***

Peak no.	Element and X-ray line	Peak no.	Element and X-ray line
1	K_α lines of Fe	8	K_β lines of Y
2	K_β lines of Fe	9	Pile-up peak
3	K_α lines of Cu	10	Pile-up peak
4	K_β lines of Cu	11	Pile-up peak
5	K_α lines of Sr	12	$K_{\alpha1}$ and $K_{\alpha2}$ lines of Ba
6	K_α lines of Y	13	$K_{\beta1}$ lines of Ba
7	K_β lines of Sr	14	$K_{\beta2}$ lines of Ba

peaks 1 and 2 indicate the K_α and K_β X-ray lines of Fe. The element was expected to be present in the YBCO matrix, as indicated previously. The presence of peaks 5 and 7, indicating the K_α and K_β X-ray lines of Sr, are however surprising. The element could only have originated from either Y_2O_3 or BaO or both (Atkins, 1999). The use of a 153μm thick Al absorber suppressed the L X-ray lines of Ba. In this instance it can be argued that a less thicker absorber, that is, 102μm Al could have been used. Both the L- and K X-ray lines of Ba could then have been used in the quantification of the element. However, the $K_{\alpha 1}$ and the $K_{\alpha 2}$ X-ray lines emitted at 32.19 keV and the $K_{\beta 1}$ and $K_{\beta 2}$ emitted at respectively 36.38 and 37.26 keV are well resolved. The use of the 153μm thick Al absorber yielded peaks of higher intensity and hence better MDLs. The macro-PIXE analysis is given in **table [4.3.4]**. The MDL and u_Z values of Fe, Cu and Y compare favourably with those values given in **table [4.2.4]** of the previous section.

Table [4.3.4] ***Macro-PIXE analysis results of the $YBa_2Cu_3O_{7-x}$ (YBCO) layer deposited on polycrystalline MgO as substrate.***

Element Symbol	c_Z	u_Z (%)	MDL $\mu g.g^{-1}\mu C^{-1}$
Fe	120 $\mu g.g^{-1}\mu C^{-1}$	3.3	5.7
Cu	29.5 mass%	1.3	7.9
Sr	0.08 mass%	1.7	30
Y	15.4 mass%	5.4	19
Ba	37.2 mass%	8.5	120

The spectrum of macro-PIGE data of the YBCO layer deposited on polycrystalline MgO is shown in **figure [4.3.4]**. The corresponding identification of the peaks is given in **table [4.3.5]**. Peaks 7 and 15 are the γ-rays emitted at respectively 585 and 1367 keV and are the results of the reactions ^{25}Mg p(1, 0) and ^{24}Mg p(1, 0) which are due to the Mg present in the substrate. The γ-ray emitted at 670 keV for the reaction ^{63}Cu p(1, 0) was used in the quantification of Cu and hence to establish complementarity with the PIXE and BS determinations of Cu. The γ-ray emitted at 153 keV for the reaction ^{63}Cu n(3, 1) is also indicated. Most of the

other peaks present in the spectrum of the macro-PIGE data are due to natural background ra-

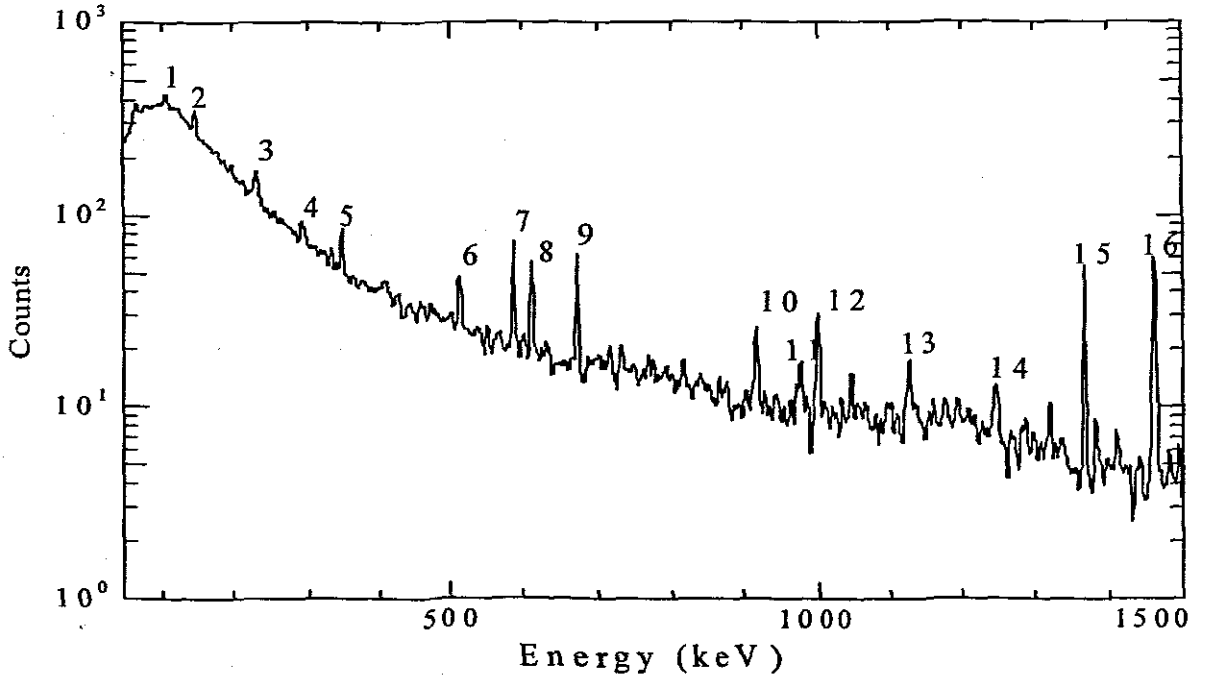

Figure [4.3.4] ***Spectrum of the macro-PIGE data of YBCO layer deposited on polycrystalline MgO. The energy range is from 50 to 1500 keV. The proton beam energy was 3 MeV. The current was maintained between 100 and 200 pA until a fluence of 1 μC was accumulated.***

diation. From the macro-PIXE analysis the concentration of Fe was below the PIGE MDL, given in **table [2.3.1]**. The 847 keV γ-ray peak for the reaction ^{56}Fe p(1, 0) is therefore not visible in **figure [4.3.4]**. γ-rays of Sr were also not observed in the spectrum of the macro-

Table [4.3.5] ***Identification of peaks in the spectrum of the macro-PIGE data.***

Peak no.	γ-ray Energy (keV)	Assignment	Peak no.	γ-ray Energy (keV)	Assignment
1	88	^{208}Bi; ^{212}Pb	9	670	^{63}Cu p(1, 0)
2	153	^{63}Cu n(3, 1)	10	911	^{228}Ac;
3	239	^{212}Pb; ^{214}Pb	11	969	^{228}Ac
4	296	^{210}Ti; ^{214}Pb	12	992	^{63}Cu γ(1, 0)
5	352	^{214}Pb	13	1120	^{214}Bi
6	511	β^+; ^{208}Tl	14	1238	^{214}Bi
7	585	^{25}Mg p(1, 0)	15	1367	^{24}Mg p(1, 0)
8	609	^{214}Bi	16	1461	^{40}K

PIGE data and were therefore not induced by the 3 MeV proton beam. The macro-PIGE analysis results are given in **table [4.3.6]**. Results for Cu from the ^{63}Cu p(1, 0) are in good agree-

Table [4.3.6] ***Macro-PIGE analysis results of $YBa_2Cu_3O_{7-x}$ (YBCO) layer deposited on polycrystalline MgO as substrate.***

Element symbol	γ-ray energy (keV)	Reaction	c_Z mass%	u_Z %	MDL
Cu	670	^{63}Cu p(1, 0)	29.8	3.56	1.88 mass%.μC^{-1}

ment with those given in **table [4.3.1]**. The spectrum of the macro-BS data is shown in **figure [4.3.5]**. As was indicated in by k_Z values in **table [4.3.2]**, Mg and O are well resolved. From the front edges of Mg and Ba it is however evident that interaction between the YBCO ele-

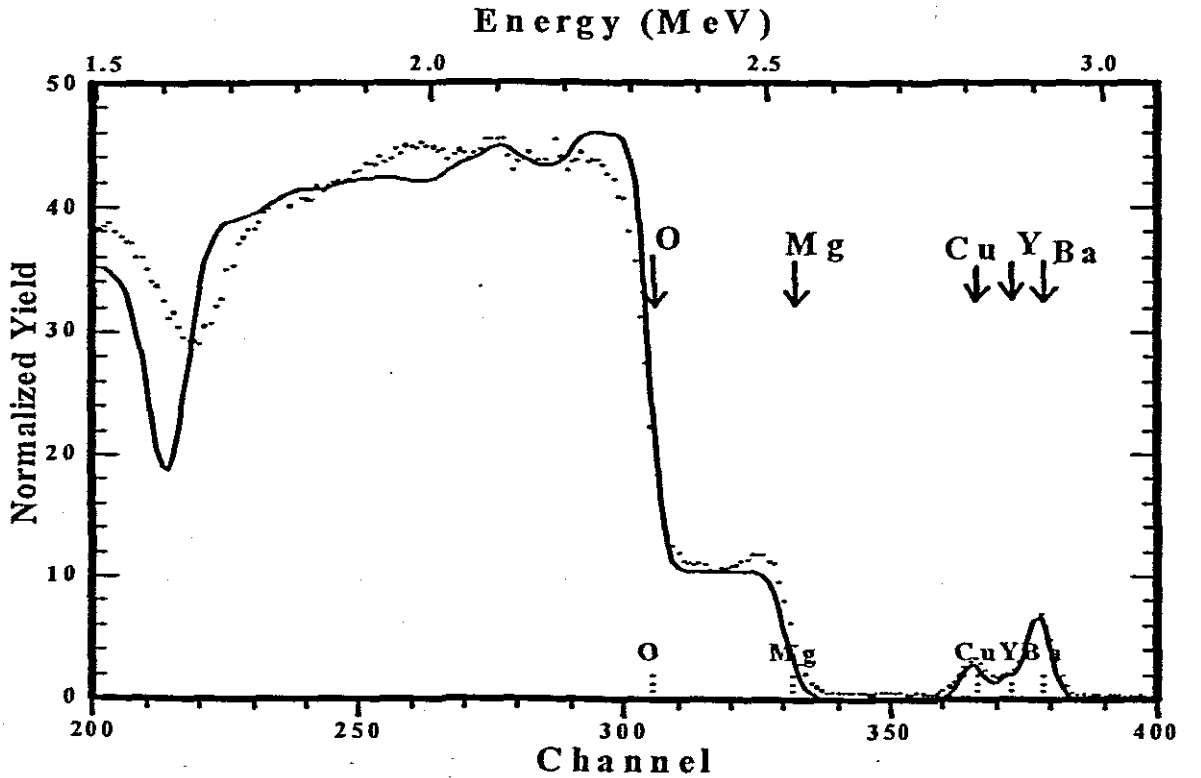

Figure [4.3.5] ***Spectrum of the macro-BS data of $YBa_2Cu_3O_{7-x}$ (YBCO) layer deposited on polycrystalline MgO. The dotted line is the plot of the actual data and the continuous line the RUMP simulation to the data. Arrows indicate respectively the energy of O, Mg, Cu, Y and Ba when located at the surface. Oxygen resonance data used in simulating the data was obtained from Amirikas et al. (1993). The front edge of elements Mg and Ba indicates an uneven thickness distribution of the YBCO layer and possible interaction between the elements of the superconducting layer and the MgO substrate.***

ments and the substrate occurred.

The macro-BS analysis of the YBCO layer is given in **table [4.3.7]**. Based on equations [2.4.1] to [2.4.4], these values could not be compared with those shown in **figure [2.4.1]**.

Table [4.3.7] ***Macro-BS analysis results of macro-BS data of the YBCO layer deposited on polycrystalline MgO. Concentrations and MDLs are given in mass%. The k_Z values and energies of the elements when located at the surface are also given.***

Element	Kinematic factor	Energy (keV)	c_Z mass%	u_Z %	MDL mass%. μC^{-1}
O	0.777	2332	18.51	3.55	0.61
Cu	0.939	2816	29.62	4.56	1.45
Y	0.956	2867	14.96	4.25	0.89
Ba	0.971	2913	36.91	4.59	1.24

The complementary analysis of copper with PIXE, PIGE and BS is given in **table [4.3.8]**.

Table [4.3.8] ***Complementary micro-μIBA analysis results of Cu in the $YBa_2Cu_3O_{7-x}$ (YBCO) layer deposited on polycrystalline MgO as substrate. Concentrations are given in mass%.***

Technique	Energy (keV)	c_Z (mass%)	u_Z (%)	MDL
PIXE	8.047	29.74	3.42	7.9 $\mu g.g^{-1}\mu C^{-1}$
PIGE	670	29.8	3.56	1.88 mass%.μC^{-1}
BS	2816	29.62	4.56	1.45 mass%.μC^{-1}

The μ-PIXE quantified elemental distribution maps of major elements, Cu, Y, and Ba, are shown in **figure [4.3.6]**. The inhomogeneity of these elemental distributions is clearly visible. From these images it was determined that in the areas of low concentrations of Cu, Y and Ba, the resultant oxygen concentrations were high, deviating from the oxygen stoichiometry ratio of 1:2:3:6.9 to the other elements. The low concentration areas in the Ba elemental distribution corresponded to high concentration of both O and Y, but not so of Cu.

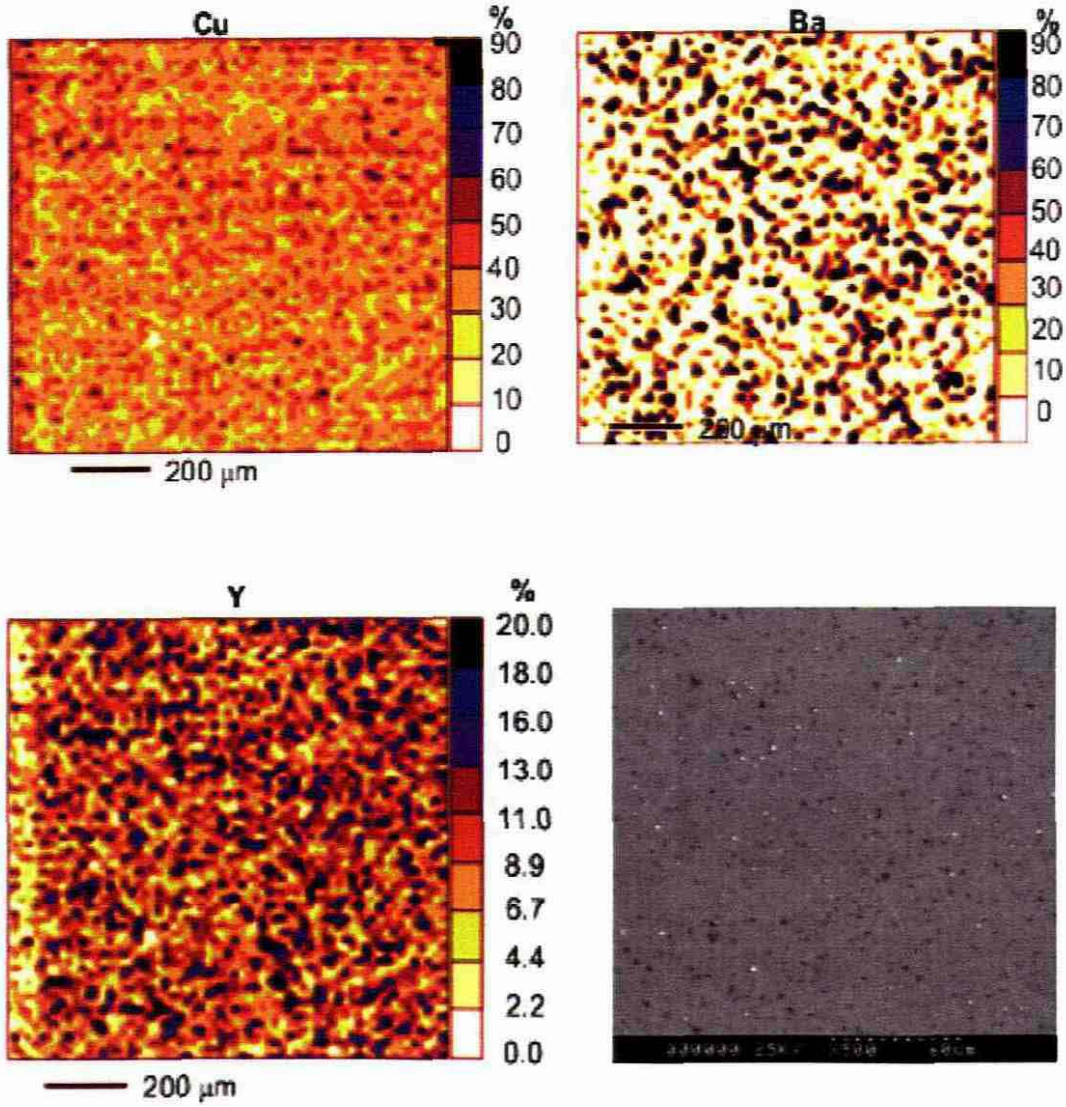

Figure [4.3.6] ***μ-PIXE quantified elemental distribution maps of major elements, Cu, Y, and Ba the YBCO layer deposited on polycrystalline MgO. An area 1200 × 1200 μm scanned was with a proton beam of energy 3 MeV. A fluence of 1 μC was accumulated and the current was maintained between 100 and 200 pA during the irradiation period. An Al absorber of thickness 153 μm was used to filter undesired X-rays. The inhomogeneity of these elemental distributions is clearly visible. From these images could also be determined that in the areas of low concentration, the sum total of Cu, Y and Ba, the resultant oxygen concentration would be high. The low concentration areas in the Ba distribution correspond to areas of high concentration of both O and Y. To emphasis these element distributions, a scanning electron micrograph (bottom left) was included. The energy of the electron beam for obtaining this micrograph was 25 keV with a 500× magnification of the image. In this micrograph the white spots correspond to areas of high O concentration and the dark spots to areas of high Y concentration.***

To emphasise these elemental distributions, a scanning electron micrograph was included. The energy of the electron beam for obtaining this micrograph was 25 keV with a 500× magnification of the image. In this micrograph the white spots correspond to areas of high O concentration with the corresponding increase in Cu concentration. The dark spots correspond to areas of high Y concentration. To determine the compositional variation in element concentration, at the various laser beam energies, with depth achieved, the beam energy was started from 3.038 MeV. This compositional variation with depth is given in **table [4.3.1]**.

Table [4.3.9] ***The variation of elemental concentration normalised to that of Y, with depth (Å) at the various laser beam energies, in J.cm^{-2}, during the pulsed laser deposition of the $YBa_2Cu_3O_{7-x}$ (YBCO) layer on polycrystalline MgO as substrate.***

		MAR 98 C				APR 98 B				MAR 98 A				APR 98 D			
		1.48 J.cm^{-2}				1.30 J.cm^{-2}				1.66 J.cm^{-2}				1.84 J.cm^{-2}			
		1800Å				2500Å				4200Å				7100Å			
Depth (Å)	MeV	Y	Ba	Cu	O	Y	Ba	Cu	O	Y	Ba	Cu	O	Y	Ba	Cu	O
Surface	3.038	1	1.68	2.58	6.90	1	1.80	2.57	6.75	1	1.84	2.91	6.92	1	1.81	1.92	6.50
520	3.058	1	1.69	2.55	6.90	1	1.73	2.57	6.60	1	1.68	2.86	6.65	1	1.75	2.01	6.34
1200	3.078	1	1.74	2.54	7.20	1	1.61	2.70	6.56	1	1.60	2.79	6.51	1	1.68	1.98	6.16
1700	3.096	1	1.68	2.58	6.33	1	1.50	2.72	6.44	1	1.60	2.82	6.70	1	1.65	2.43	6.14
2200	3.114					1	1.48	2.90	6.40	1	1.80	3.00	6.68	1	1.65	3.00	5.85
2700	3.132									1	1.70	3.00	6.40	1	1.69	3.00	5.60
3800	3.168									1	1.60	2.80	6.30	1	1.71	2.80	5.60
4300	3.184													1	1.30	2.30	5.40
4800	3.202													1	1.30	2.30	5.41
5400	3.220													1	1.65	4.28	4.28
6500	3.254													1	1.50	3.33	3.33

From **figure [4.3.5]** and the results in **table [4.3.9]** it is deduced that:

- The oxygen concentration is non-stoichiometric during the initial stages, for a thickness of approximately 500Å, of the pulsed laser deposition;

- This oxygen stoichiometric tends to the ideal value of 6.9 as the thickness of the YBCO layer increased;
- For thin layers, less than 3000Å, the compositional variation of the elements with thickness is minimal;
- In the instance of thick layers, that is 7200Å and thicker, the degree of non-stoichiometry is maximum;
- The high degree of non-stoichiometry for the 7100Å thick YBCO layer at depths of 4300 and 4800Å is attributed to instrumental error;
- Interaction between the YBCO layer elements and the polycrystalline substrate occurred;
- The interaction was most prominent when the high energy density of 1.84 $J.cm^{-2}$ was applied and less severe in the case of the relatively low energy density of 1.30 $J.cm^{-2}$;
- The ideal laser energy density is 1.66 $J.cm^{-2}$ and the thickness of the YBCO layer should preferably be less than 5000Å.

The simultaneous use of μ-PIXE, μ-PIGE and μ-BS facilitated the objective quantification of HTS specimens that were produced by pulsed laser beam (Mars et al., 2000). The inhomogeneity of the elemental distribution of the components of the $YBa_2Cu_3O_{7-x}$ layer was attributed to the interaction of these elements when the deposition was performed at high laser beam energy densities. Ideally, depositions should be performed at maximum density of 1.66 $J.cm^{-2}$.

4.4 Steel

4.4.1 Introduction

One of the greatest challenges in the production of steel is the incorporation into the primarily iron matrix of alloying elements that would alter the properties of the steel. Each of these elements exhibits a specific property. As examples, C and N are included as hardening agents, Mn contributes to the strength, hot-shortness and hardness, Cr exerts a toughening effect and Mo promotes hardenability. The presence of O may induce brittleness in the steel. For this reason Si, although it also contributes to the strength and hardness, is incorporated with Al as deoxidisers due to the great affinity of these two elements for oxygen (Stenden et al., 1997).

In contrast to alloying elements, residual elements are those that were not intentionally added to the steel matrix, but were present in the raw materials. Most steel manufacturers carefully minimise the amount of residual elements because of possible undesired properties. Alloying elements are incorporated first by heating to and holding at a certain temperature (annealing) and then cooling (solidifying) at a suitable rate. The aim of these processes is to improve the crystalline structure and obtain an elemental distribution as homogenous and globular as possible.

On cooling, non-uniform elemental distribution (chemical segregation) may occur. It causes two or more elements to exhibit the same uniform or non-uniform distribution (aggregation). This usually results in cluster formation. It may also give rise to regions, which are actually microphases of Fe and the alloying and residual elements. The term microphase is used since the area is normally less than 2000μm^2 and are relatively smaller than those of the macrophases such as austenite, cementite, ledeburite or martensite.

The manufacturing processes at Saldanha Steel are illustrated in figure [4.4.1]. Stenden et al.

(1997) discussed these individual processes in detail. Cooling (solidification) occurs in the Thin Slab Caster process. According to Stenden et al. (1997), segregation can result from three aspects. The first aspect is defined as average segregation, which is the average shifting of the chemical composition in the central zone of the slab when compared to the composition in the rest of the slab. It depends on the normal laws of alloy solidification (Bhadeshia, 2001). The second aspect is defined as periodical segregation.

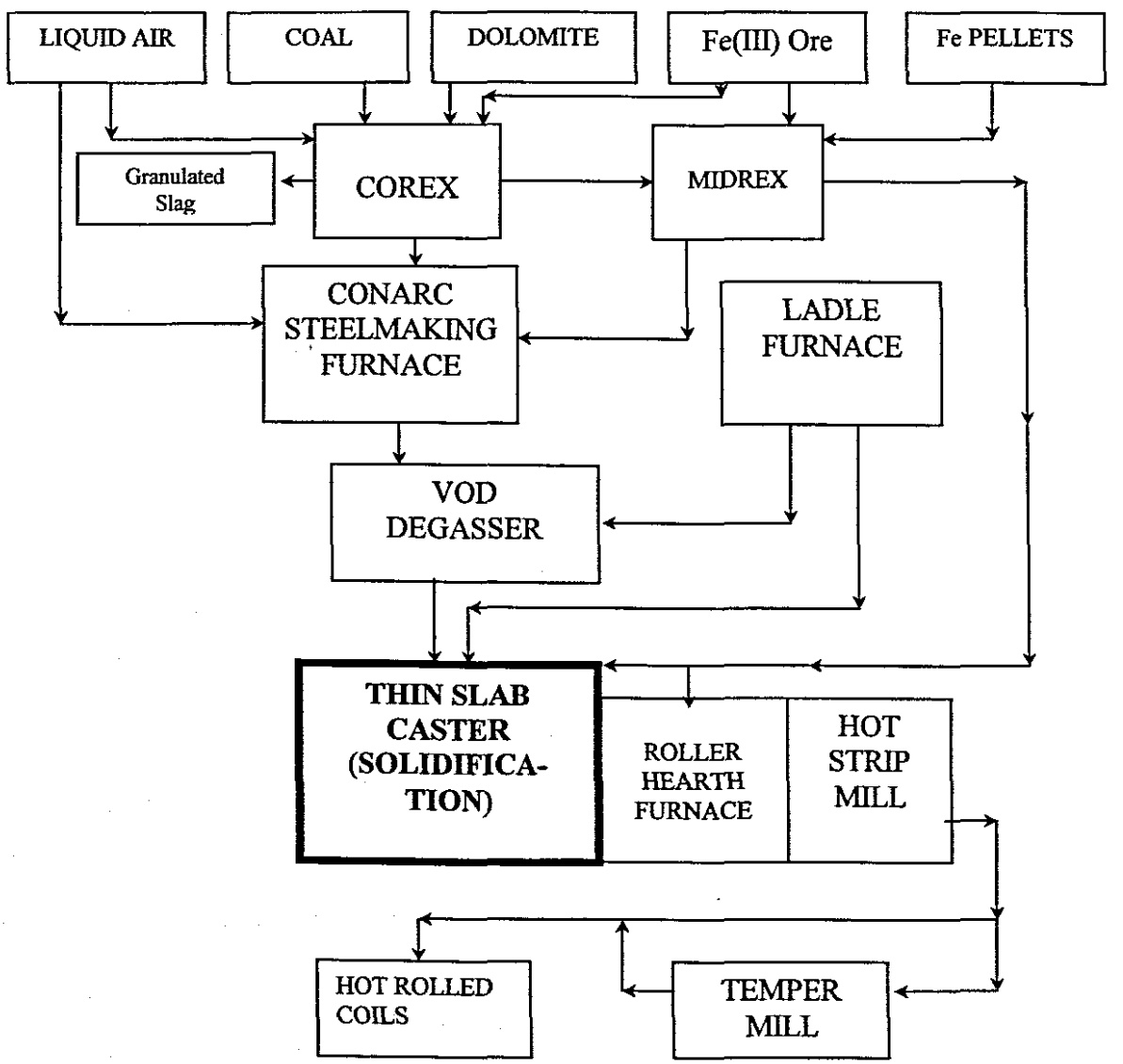

Figure [4.4.1] ***A schematic diagram of the manufacturing processes at Saldanha Steel, Saldanha Bay, based on the work of Stenden et al. (1997), showing the raw material and individual processes. Cooling (solidification) occurs in the Thin Slab Caster process. The aim is to obtain a homogenous and globular elemental distribution of C and N in the steel matrix***

It depends on the formation of solidification bridges during the final stages of the cooling process. These bridges have a significantly different composition when compared to that of the generating liquid. The third form is microsegregation and depends on the dimensions of the dendrites during dendritic formation (Bhadeshia, 2001). Microsegregation can result in regions of high alloying element concentrations, which are usually confined to the last interdendritic liquid areas.

Carbon and nitrogen have been incorporated as alloying elements into the steel matrix. **Figure [4.4.2]** illustrates the equilibrium phase diagram of C in a solid solution of Fe with respect to the concentration and temperature. The phase diagram, to a maximum temperature of 1600°C, is shown since the overall concentration of C for the area scanned is approximately 3.0 atomic%. In the figure, the region to the left of the 2.0% carbon concentration shows Fe combined with small percentages of C, resulting in steel alloys. Here three significant regions are demarcated relative to the carbon concentration in the alloy. These regions are the eutectoid at E, the hypoeutectoid at A, for which the carbon concentration ranges from 0.2 to 0.83%, and the hypereutectoid at B, where the carbon concentration ranges from 0.83 to 2.0 %.

On the right of the 2% carbon concentration, higher concentrations in combination with various macrophases of iron are illustrated. These are ferrite, austenite and delta iron and are referred to as cast iron macrophases. The Fe-Fe_3-C form in which the C at% is 6.67 is also shown. These regions indicated in the phase diagram are used in the evaluation of the data when establishing the phases present in the matrix. In this instance, the uncertainty in measurement is important, as it would assist in ascribing the necessary phases to the element composition. However, as indicated earlier, these high carbon concentration areas are found in the interdendritic liquid regions.

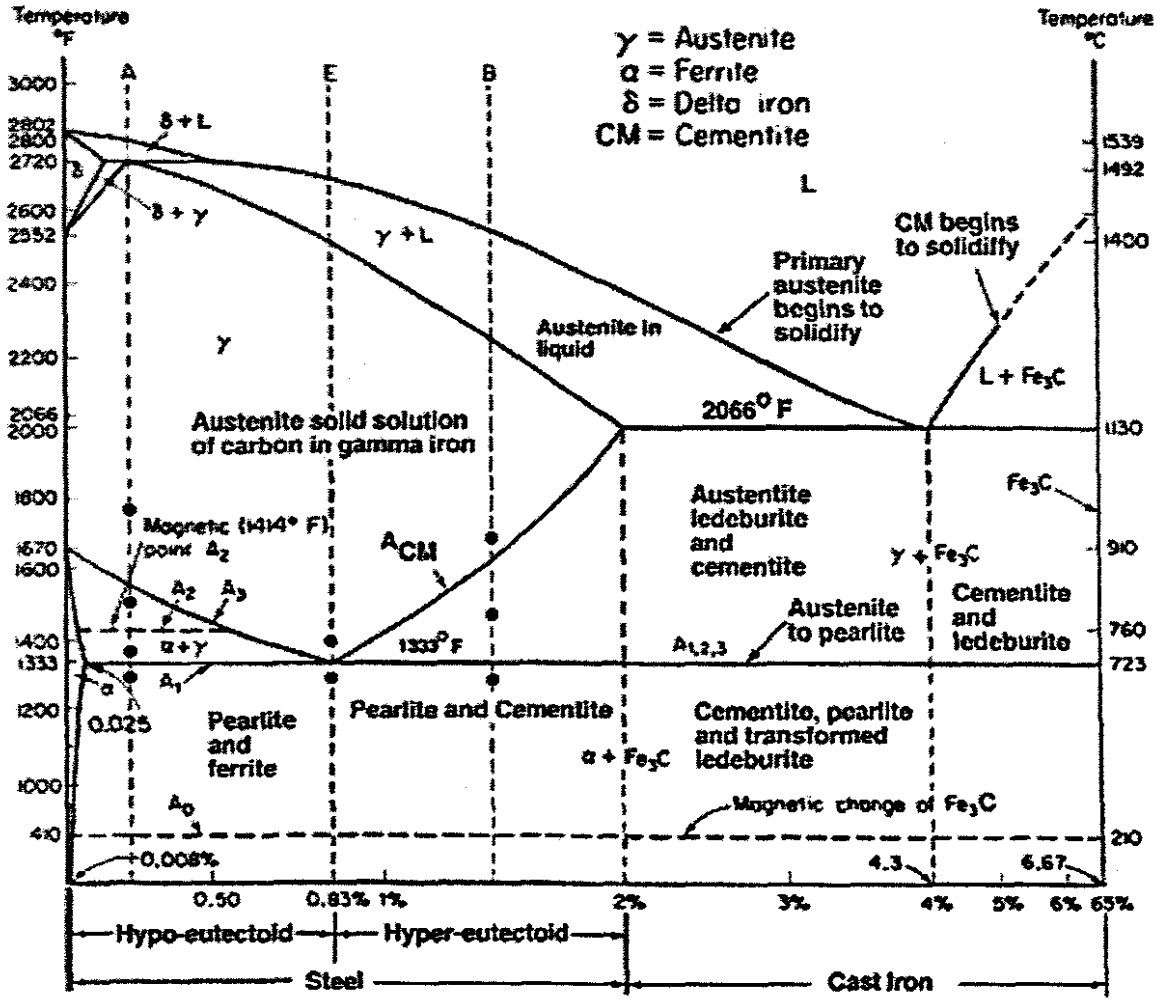

Figure [4.4.2] ***Equilibrium phase diagram of combinations of C in a solid solution of Fe, obtained from Cornell and Bhadeshia (2001), and illustrated in terms of the concentration and temperature. To the left of the 2% carbon concentration, is Fe combined with small amounts of C, resulting in steel alloys. Three significant regions, relative to the low carbon concentration in the steel matrix, are demarcated. These regions are the eutectoid at E, the hypoeutectoid at A and hypereutectoid at B. To the right of the 2% concentration line, are shown combinations of high carbon concentrations combined with the macrophases of cast iron.***

The equilibrium phase diagram of carbon in high atomic% concentration (40 at%) and temperature, obtained from Cornell and Bhadeshia (2001), is depicted in **figure [4.4.3]**. It is an extension of **figure [4.4.2]** and indicates the phases present in these high carbon concentration regions. It is emphasised that these phase diagrams are applicable to a carbon-iron matrix only. These PDs therefore do not reflect any effects that may result due the presence of nitrogen and other elements present in the matrix.

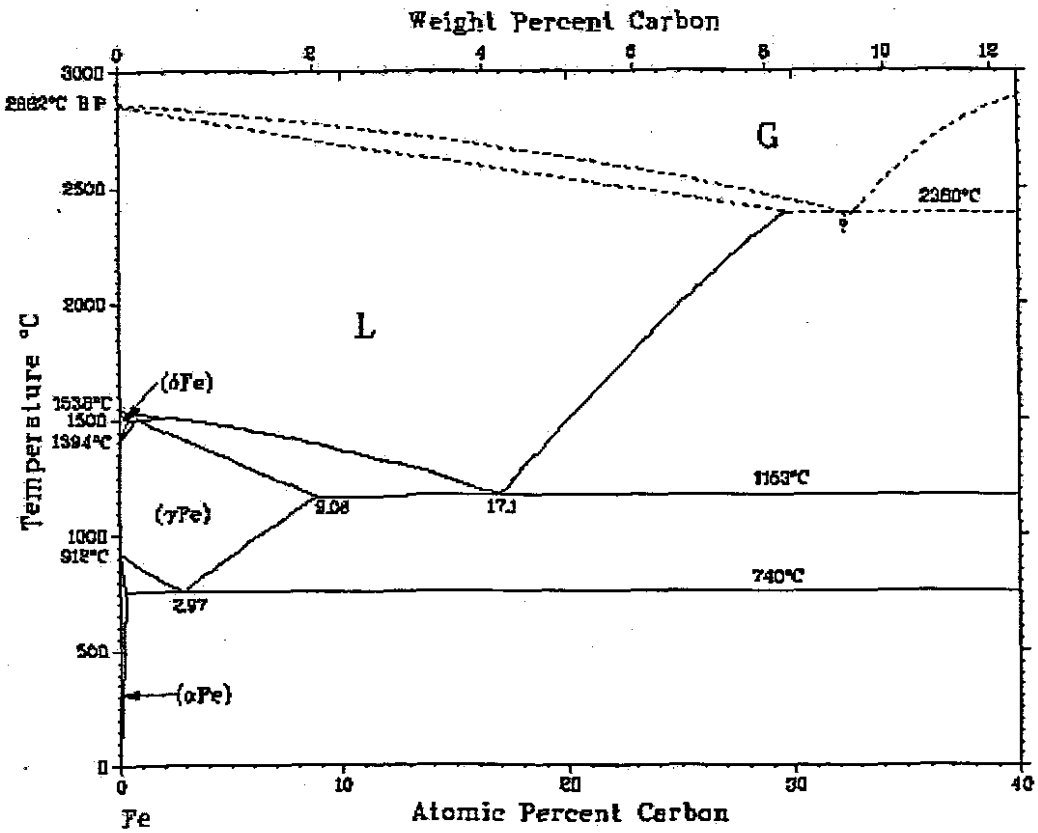

Figure [4.4.3] ***Equilibrium phase diagram of temperature and high carbon concentration (40 atomic %) in a solid solution of Fe, obtained from Banks et al. (2001). The diagram is an extension of the figure [4.4.2] and is included to indicate Fe-C phases present in the high concentrated interdendritic liquid regions.***

The equilibrium phase diagram of combinations of N in solid solution of Fe, as given by Banks et al. (2001), is depicted in **figure [4.4.4]**. The maximum temperature of the Fe-N phase diagram is 1000°C and in the Fe-C phase diagram it is 1600°C. The liquidus line of the fcc phase of Fe-N and the solidus line of the ε phase of Fe-N have a gradients of 0.25mass% per 100°C. It is therefore assumed that in the temperature range 1000 to 1600°C, the gradients would attain a constant change of 0.01 mass% per 100°C. As with the Fe-C equilibrium phase diagram, the effects, should there be any, of carbon or other matrix elements in the Fe-N phase structure, are not illustrated. Although Banks et al. (2001) regard the phase diagrams not applicable for critical evaluation of similar data, Sundman (1998) indicated that these PDs are of high significance. These diagrams are used to establish critical parameters, such as the liquidus temperature, partition coefficient and the fraction of solid in the liquid, f_s in the eva-

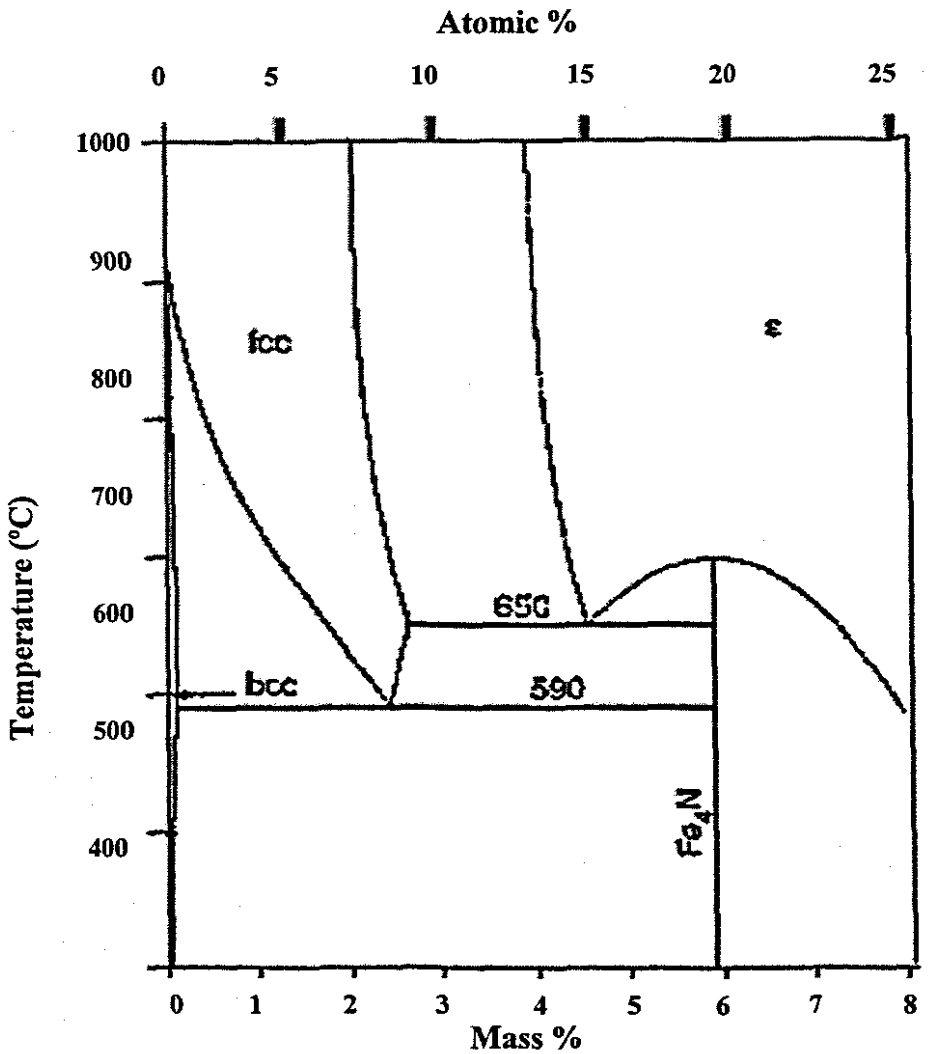

Figure [4.4.4] ***Equilibrium phase diagram of combinations of N in a solid solution of Fe in terms of the concentration and temperature (Banks et al., 2001). The different phases of Fe-N are indicated.***

luation of accuracy in the measurements.

4.4.2 Experimental

4.4.2.1 Specimen preparation

Specimens of 1cm^2 area and thickness less than 2mm were prepared from the samples, obtained as *lollies* from the Thin Slab Caster process. A typical sample and specimen of the *lolly* and the steel standard are shown in **figure [4.4.5]**. Before analysis, specimens were treated with analytical reagent grade (AR) organic solvents to remove any contaminants that adhered to the surface. They were then submerged in a volume of 10% aqueous HCl acid solution to

remove surface contamination, such as Fe(II) and Fe(III) oxides, and then washed in deionised water to remove residual acid and finally dried with acetone.

4.4.2.2 Instrumental Parameters

The characterisation of the steel specimens was performed with a 3 MeV protons beam. The current was maintained at 100 to 200pA during the irradiation period until a charge of 1 μC

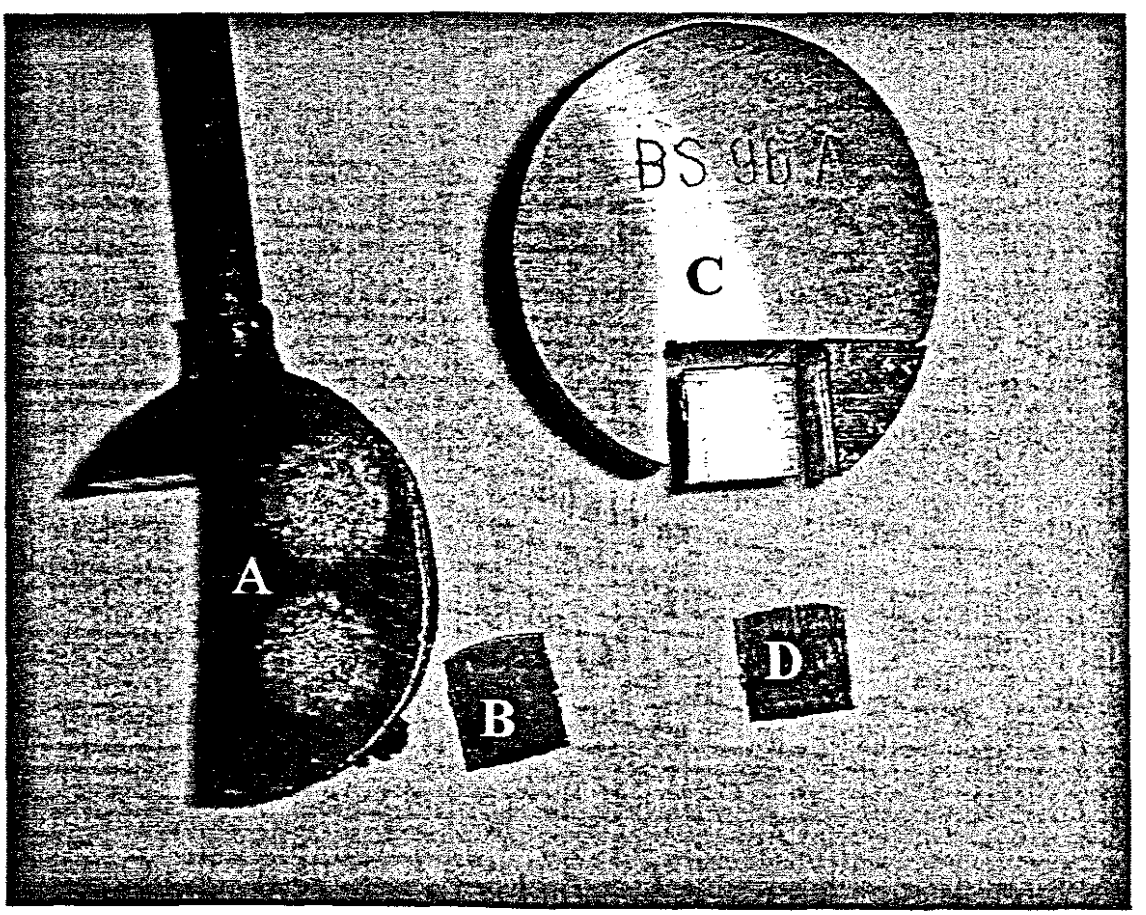

Figure [4.4.5] ***Picture of the "lolly" steel specimen (A) and the standard steel specimen (C) used in the analysis of steel. The 1cm x 1cm in area and about 1.5 mm thick samples (B) and (D) were prepared from the "lolly" and standard and were used in the analysis.***

was accumulated. A 100μm thick Al absorber was placed between the Si(Li) detector and the specimen. The absorber thickness was changed to 250μm to investigate the presence of Ag and Pb in the specimen matrix.

4.4.3 Results and discussions

The light elements (Li to Mg), discussed in section [2.3], were not found in the matrix of the steel specimens from Saldanha. Spectra of the μ-PIGE data would therefore only show natural background radiation and the γ-rays emitted at 847 and 1376 keV for the respective reactions ^{56}Fe p(1, 0) and ^{56} Fe p(2, 0) at 843 keV. The spectrum of the μ-PIGE data for the scanned area, shown in **figure [4.4.6]**, is therefore representative of all spectra of extracted μ-PIGE data. Hence, these other spectra will not be shown. The exception is made in the instances where γ-rays of elements other than those already indicated, are present in the PIGE data and in concentrations greater than the MDLs given in **table [2.3.2]**.

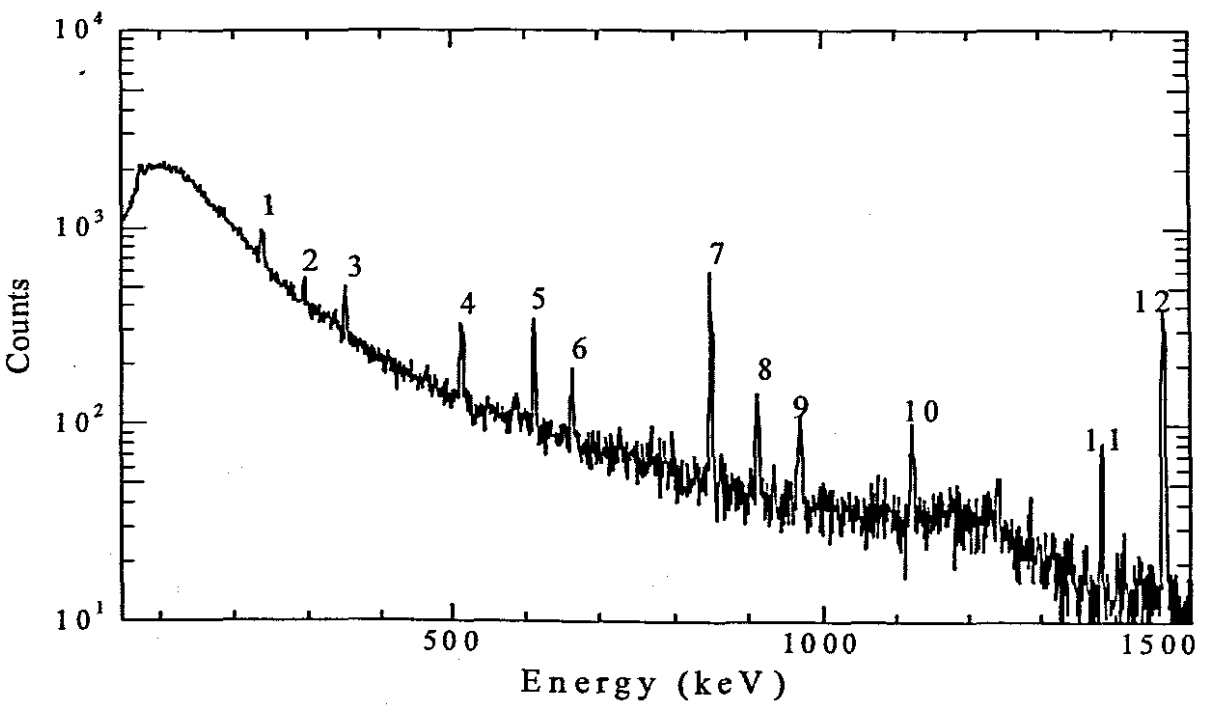

Figure [4.4.6] ***Spectrum of the μ-PIGE data in the energy range 50 to 1500 keV of the scanned area of the steel specimen. The spectrum constitutes mostly natural background radiation and the γ-rays emitted at 847 and 1377 keV for the reactions ^{56}Fe p(1, 0) and ^{56}Fe p(2,0).***

The γ-ray emitted at 847 keV, indicated by peak 7 in **figure [4.4.6]**, is indicative of both the ^{27}Al p(1, 0) and ^{56}Fe p(1, 0) nuclear reactions. The γ-ray at 1015keV for ^{26}Al p(2, 0) is however not present in the figure and hence the concentration of Al is less than the MDL. The identification of the peaks in the PIGE spectrum of the scanned area is given in **table [4.4.1]**.

Table [4.4.1] ***Identification of peaks in the spectrum of the μ-PIGE data of the scanned area of the steel specimen.***

Peak no.	γ-ray Energy (keV)	Assignment	Peak no.	γ-ray Energy (keV)	Assignment
1	239	^{212}Pb; ^{214}Pb	7	847	^{56}Fe p(1, 0)
2	296	^{210}Ti; ^{214}Pb	8	911	^{228}Ac;
3	352	^{214}Pb	9	969	^{228}Ac
4	511	β^+; ^{208}Tl	10	1120	^{214}Bi
5	609	^{214}Bi	11	1377	^{56}Fe p(2, 0)
6	669	^{214}Bi	12	1462	^{40}K

The μ-PIGE analysis results are shown in **table [4.4.2]**. The MDLs obtained are in close agreement with those given in **table [2.3.1]** of section [2.3].

Table [4.4.2] ***μ-PIGE analysis results of Fe in the scanned area for the ^{56}Fe p(1, 0) and 56Fe p(2, 0) reactions.***

Assignment	Energy (keV)	c_Z (mass%)	u_Z (%)	MDL ($\mu g.g^{-1}\mu C^{-1}$)
^{56}Fe p(1, 0)	847	97.8 ± 3.0	3.1	200
^{56}Fe p(2, 0)	1377	97.5 ± 6.25	6.8	7200

Spectra of the μ-BS data had similar structure, except when the C and N concentration varied or when the elemental diffusion profiles changed. Therefore only the spectrum of the scanned area is shown. As with the μ-PIGE, the same exception was applied when showing the μ-BS spectra. In this instance the MDL are given in **figure [2.4.1]**. The spectrum of the μ-BS data, as the normalised yield vs. channel/energy, of the scanned area and the RUMP simulation to the data are shown in **figure [4.4.7]**. The dotted line represents the backscattered data and the continuous line the RUMP simulation (Doolittle, 1985) to the data. Arrows indicate the energy of the respective elements when located at the surface. The concentration of C was 8.9 at% and indicates that the area scanned had a L-Fe_3-C phase structure. The marked deviation of the data to the simulation in the energy range of 1.50 to 2.00 MeV, is due to the carbon diffusion not being linear, as is assumed in the simulation. The two peaks at 2.22 and 2.32 MeV

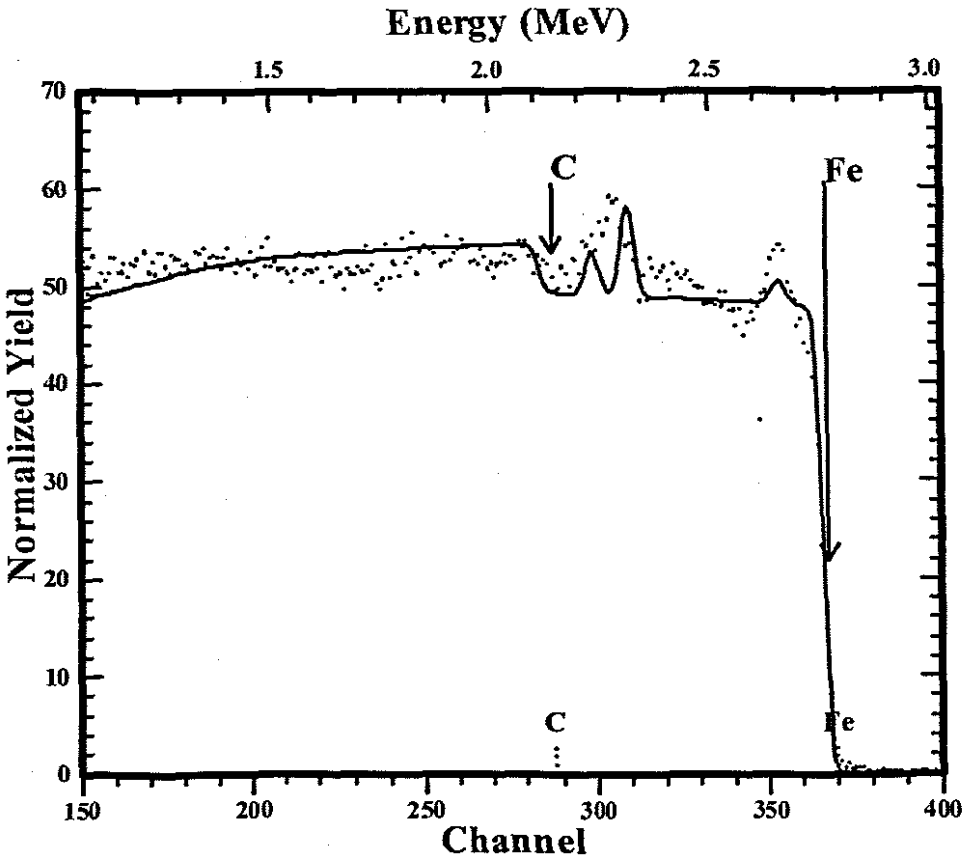

Figure [4.4.7] ***Spectrum of the μ-BS data of the scanned area of the steel specimen. The dotted line represents the data and the continuous line the RUMP simulation to the data. Arrows indicate the energies of the respective elements when located at the surface. Proton resonance data for carbon and nitrogen, used in the simulation, were obtained from Amirikas et al. (1993) and Olness et al. (1959).***

represent N and O, respectively. The elements Zn, Mn and Cr are present in the $\mu g.g^{-1}$ concentration range, as was determined with PIXE. These elements have kinematic factors, calculated using equation [2.4.1], similar to the kinematic factor of Fe. They could therefore not be resolved with the SSB detector and would not be discernable in the spectrum. The μ-BS analysis results are given in **table [4.4.3]**, where the Fe mass% is the sum total of the Fe, Zn,

Table [4.4.3] ***μ-BS analysis results of the scanned area of the steel specimen.***

Element	Energy (MeV)	c_Z (mass%)	u_Z (%)	MDL (mass%.μC^{-1})
Fe	2.77	97.8	3.2	1.6
C	2.16	2.99	8.4	1.6
N	2.26	1.2	15	1.2

Mn and Cr concentrations. Simulations to obtain the minimum detection limits are only applicable to a Fe-C matrix.

X-ray emission data were treated similarly as those obtained by PIGE and BS measurements. Here the exception is the Mn and Cr concentrations, since these elemental distributions varied from region to region within the scanned area. The spectrum of the μ-PIXE data, as evaluated with the GeoPIXE II software, is shown in **figure [4.4.8]**. The identification of the peaks is given in **table [4.4.4]**. Peaks of the Fe K_α and K_β X-ray lines, at respectively 6.403 and 7.057 keV, are prominent in the spectra. Zr was introduced during sampling of the *lolly* with a Zr container and was not considered part of matrix. The K_α and K_β X-ray lines of Cr, at respectively 5.414 and 5.946 keV, are weak due to the low Cr concentration and are partly overlapped by the relatively intense escape peaks of the Fe K_α and K_β X-ray lines. These escape peaks are located at respectively 4.703 and 5.457 keV and are adequately resolved with respect to the K_β escape peak and the Cr K_α X-ray lines by the Si(Li) detector. For Mn, although the K_β lines overlap with the Fe K_α lines, the Mn K_α lines could be used to quantify the element. In resolving Ni, the Ni K_α lines are overlapped by the Fe K_β lines and the Ni K_β lines by the Cu K_α lines. As seen in the spectrum, the K_α lines of Cu are very weak, which indicates the low Ni concentration. This weak Cu K_α line signifies that the concentration of Cu itself was low. This is acceptable since, as stated previously, these two elements are undesirable in the steel matrix. The relatively high intensity of the Cu K_β lines is due to its overlap with the Zn K_α lines, indicating that Zn concentration was higher than the Cu and Ni concentrations. The peaks at 10.54 and 11.73 keV are indicative of As K_α and K_β X-ray lines. The Pb L_α X-ray line, which is emitted at 10.53 keV, coincides with the As K_α line. Since the Pb $L_{\alpha 1}$ X-ray line at 10.55 keV and $L_{\alpha 2}$ line at 10.44 keV cannot be resolved with the Si(Li) detector,

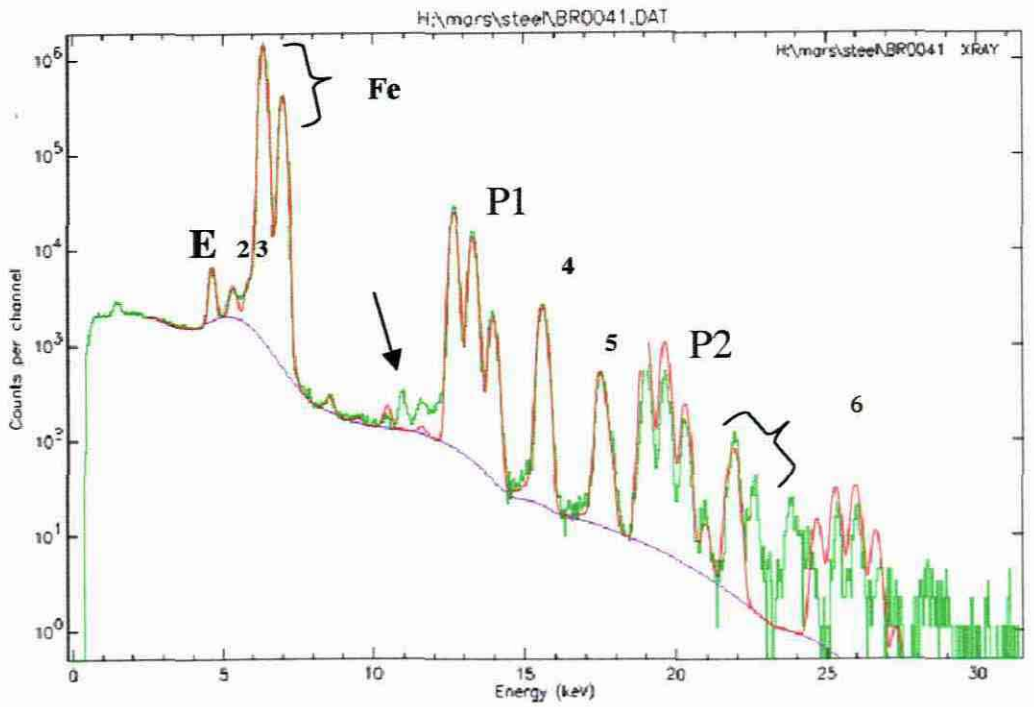

Figure [4.4.8] ***Spectrum of the μ-PIXE data, evaluated with the GeoPIXE II software. A 100μm thick Al absorber was used for attenuating the X-rays. The data are represented in green, the fit to the data in orange and the background in purple. E is the intense escape Fe K_α and K_β X-ray peaks and PU or P is the pile-up peaks. X-ray lines of Cr and Mn are overlapped by the intense K_α and K_β escape peaks. The arrow indicates the artefact of Ag and Pb being present in the matrix.***

Table [4.4.4] ***Identification of peaks as indicated in the spectrum of the μ-PIXE data, shown in figure [4.4.8].***

Peak no.	Element and X-ray line
E	K_α escape peak of Fe
2	K_α X-ray line of Cr overlapped By the Fe K_β escape peak
3	K_α X-ray line of Mn
P1	First set of pile-up peaks
4	$K_{\alpha 1}$ X-ray line of Zr
5	$K_{\beta 1}$ X-ray line of Zr
P2	Second set of pile-up peaks
6	Possible $K_{\alpha 1}$ line of the elements Ag or Pb

the sum Pd ($L_{\alpha 1}$ and $L_{\alpha 2}$) could be used to verify the presence of Pb. Similarly, the Pb L_{β} X-ray line at 12.61 keV can not be used since it overlaps with the intense Fe pile-up peak at ~12.7 keV.

The weak intensity peak at 9.89 keV corresponds to the K_{α} X-ray lines of Ge, but there is no Ge K_{β} lines at 10.981 keV, hence Ge is absent from the matrix and these peaks are attributed as pile-up. This was confirmed by changing the Al absorber thickness to 250 μm. The artefact of Pb and Ag, with K_{α} and K_{β} X-ray lines emitted at respectively at 22.162 and 24.942 keV, being present in the matrix, was resolved in the same manner and these peaks were ascribed as pile-up. Discussions with the manufactures who had performed X-ray Fluorescent analysis revealed that As rather than Pb is present in the matrix. The artefact arose from the compromise between PIXE and PIGE and BS analysis. A high current is required for the PIGE and BS measurements. Bombardment with 3 MeV protons does not guarantee a high cross section for the production of the ^{208}Pb n(1, 0) and ^{208}Pb n(2, 0) nuclear reactions. γ-rays for the latter reaction are also subjected to interference from those resulting from the ^{65}Cu p(4, 2) and ^{70}Zn n(1, 0) nuclear reactions, should these be present and induced by proton bombardment. Furthermore, since the concentration of Pb is in the $\mu g.g^{-1}$ range, it could not be determined with BS.

As is gaseous (Cotton et al., 1999) at the extremely high temperatures to which the steel was heated. The element would therefore be occluded in the steel structure and would exhibit an inhomogeneous elemental distribution.

The μ-PIXE analysis results, obtained with the GeoPIXE II software, are shown in **table [4.4.5]**. The matrix of the steel was therefore composed of the elements Fe, Zn, As, Cr, Mn, N and C.

Table [4.4.5] ***μ-PIXE analysis results of the scanned area of the steel specimen.***

Element	c_Z value	Unit	u_Z (%)	MDL ($\mu g.g^{-1}.\mu C^{-1}$)
Cr	840 ± 120	$\mu g.g^{-1}$	14	70
Mn	0.19 ± 0.1	mass%	5.3	70
Fe	97.3 ± 1.99	mass%	3.1	20
Zn	100 ± 30	$\mu g.g^{-1}$	30	20
As	40 ± 20	$\mu g.g^{-1}$	50	20

The complementary μ-IBA analysis results of Fe in the scanned area of the steel specimen are given in **table [4.4.6]**.

Table [4.4.6] ***μ-IBA analysis results of Fe in the scanned area of the steel specimen. The BS results is the sum total of the Fe, Mn, Cr and Zn concentrations, since these elements have kinematic factors similar to that of Fe. For the PIGE analysis, the results may include the concentration of Al, even though the element is present concentration less than the MDL.***

Technique	Energy (keV)	c_Z (mass%)	u_Z (%)	MDL ($\mu g.g^{-1}.\mu C^{-1}$)
BS	2780	97.8 ± 3.0	3.2	16000
PIGE	854	97.8 ± 3.0	3.1	100
PIXE	6.4	97.3 ± 1.99	3.1	20

The μ-PIXE quantitative elemental distribution maps of Cr, Mn, As, Fe and Zn and the μ-BS elemental distribution maps of Fe, C and N, obtained form the event-by-event analysis, are shown in **figure [4.4.9]**. The Cr, Mn and As elemental distributions are homogenous and predominantly biglobular. Because of the homogeneity of these elemental distributions, it is deduced that these distributions were not affected by other matrix elements or any internal or external variables such as the solidification temperature.

The As elemental distribution was unexpected homogeneous. This homogeneity could be attributed to statistical fluctuations, as the As concentration was only twice the value of the minimum detection limit and that the uncertainty in measurement was relatively high.

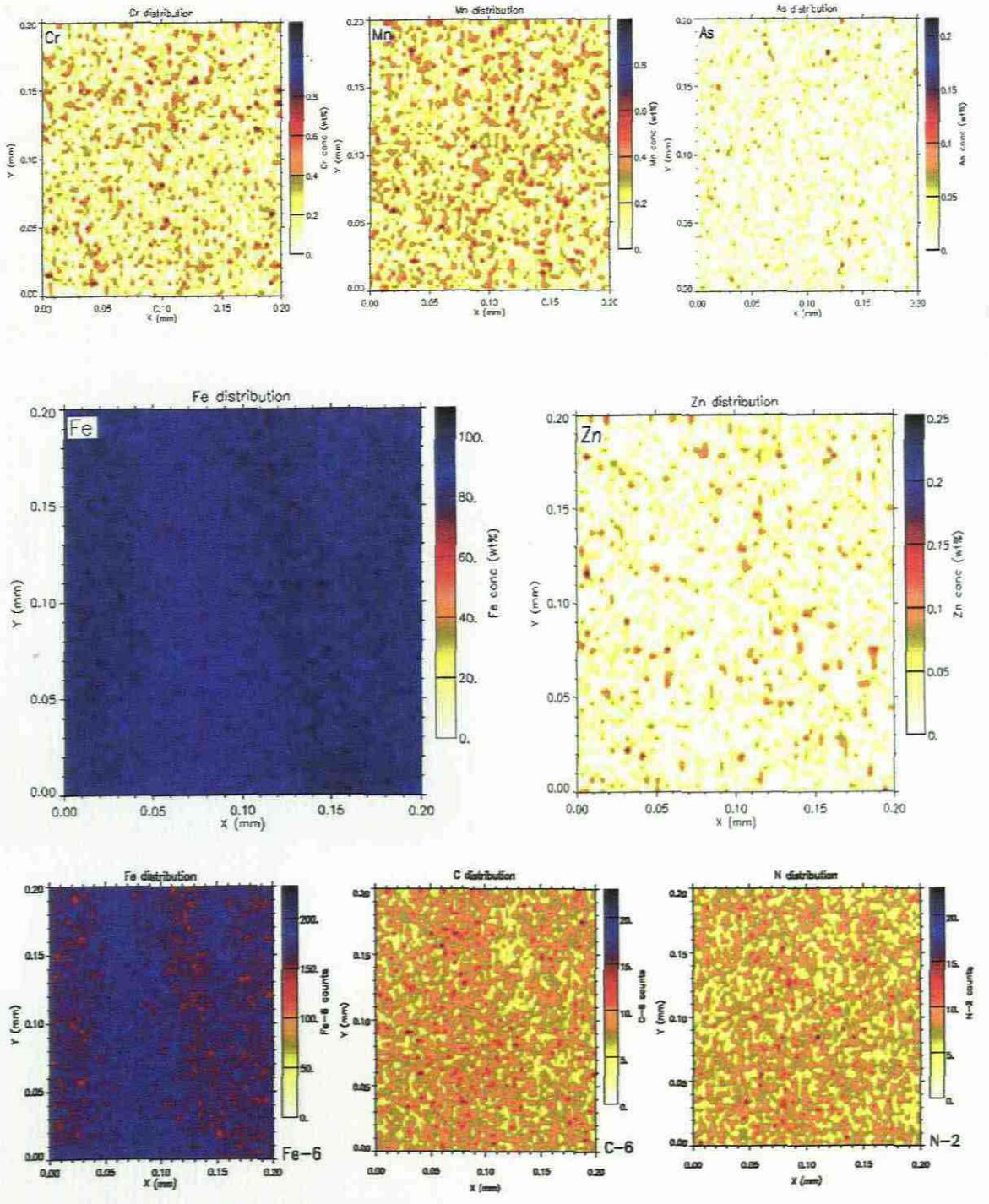

Figure [4.4.9] ***The μ-PIXE quantitative elemental distribution maps of Cr, Mn, As, Fe and Zn and the μ-BS elemental distribution maps of Fe, C and N, extracted form the event-by-event analysis data. The 6 in the μ-BS elemental distribution maps indicates that 6 points, 2 subtending the peak and 2 on both sides of the peak, were considered in establishing the background by linear interpolation. The 2 indicates that only the peak was considered, hence the nomenclature elemental distribution map rather than quantified elemental distribution map. Cr, Mn and As are homogenously distributed. The marked inhomogeneity in the μ-PIXE Fe elemental distribution is ascribed to the presence of C and N in the matrix. The Fe μ-BS elemental distribution map is shown for comparison.***

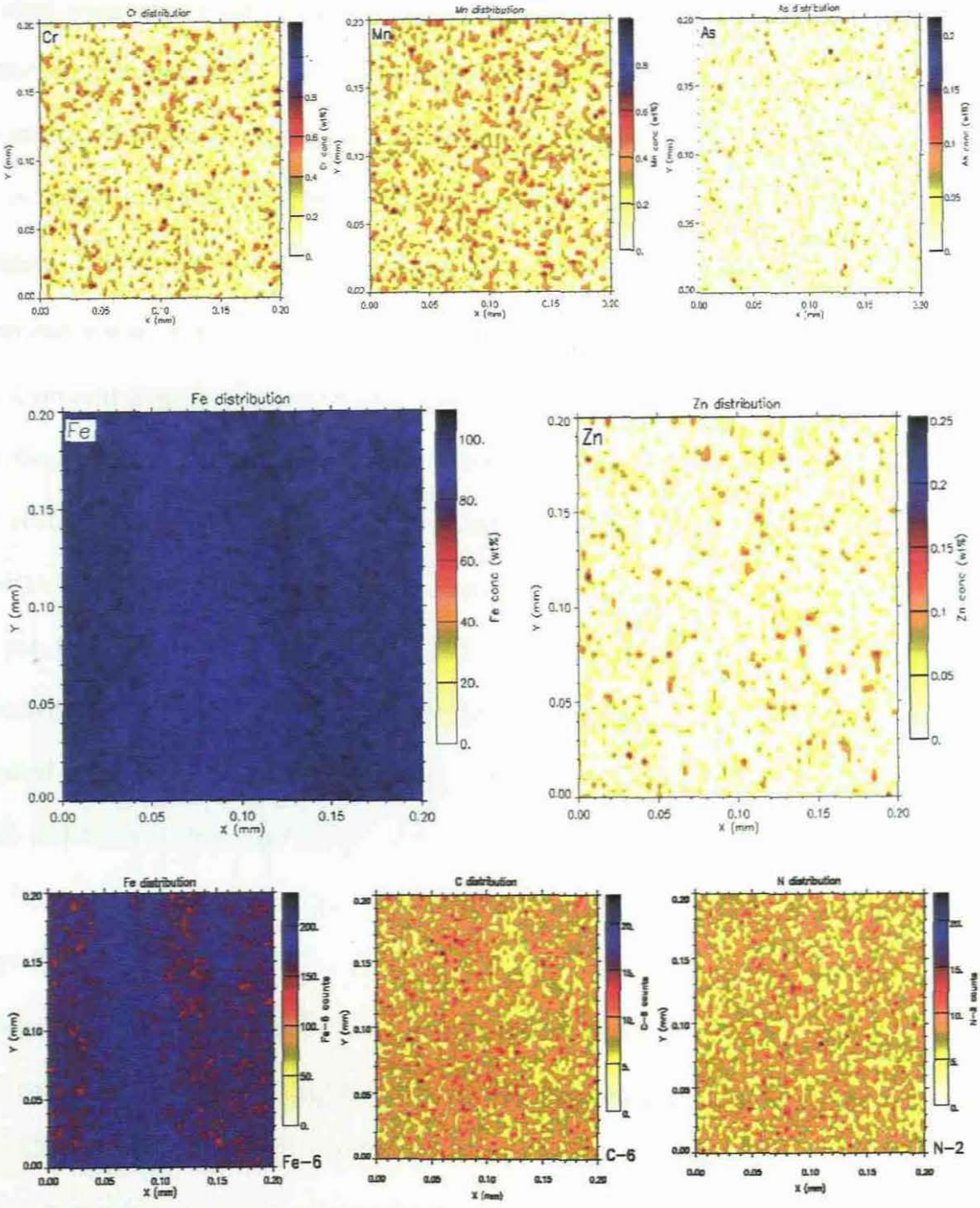

Figure [4.4.9] ***The μ-PIXE quantitative elemental distribution maps of Cr, Mn, As, Fe and Zn and the μ-BS elemental distribution maps of Fe, C and N, extracted form the event-by-event analysis data. The 6 in the μ-BS elemental distribution maps indicates that 6 points, 2 subtending the peak and 2 on both sides of the peak, were considered in establishing the background by linear interpolation. The 2 indicates that only the peak was considered, hence the nomenclature elemental distribution map rather than quantified elemental distribution map. Cr, Mn and As are homogenously distributed. The marked inhomogeneity in the μ-PIXE Fe elemental distribution is ascribed to the presence of C and N in the matrix. The Fe μ-BS elemental distribution map is shown for comparison.***

Marked concentration profiles are however present in the Fe elemental distribution and to a lesser extent in that of Zn. The profiles in the Fe elemental distribution map are by definition ascribed to the carbon and nitrogen alloying elements present in the matrix. The inhomogeneity in the Zn elemental distribution indicated that either the elemental distribution of another element or an internal or external variable had a direct effect on the distribution. The μ-PIXE quantitative true element concentration correlations of Cr, Mn, Fe and Zn and the μ-BS element concentration correlations of Fe, C and N are depicted in **figure [4.4.10]**. Form the figure, the Zn and Fe elemental concentration correlation indicates a positive linear correlation in the concentrations of Zn and Fe. These elements therefore agglomerated positively with respect to each other or this agglomeration was caused by a third external or internal variable. As per definition, the Fe concentration correlates negatively with that of C. It was therefore expected that the Zn concentration would correlate negatively with that of C. however, the physical properties of Cr, Mn, Fe and Zn are similar. Furthermore, the elemental distributions of Cr and Mn were homogenous and were also at least two orders of magnitude greater than the Zn concentration. These elemental distributions could therefore not have induced inhomogeneity in the carbon elemental distribution. Hence, they cannot be used to identify any inhomogeneities. The Fe concentration was more than an order of magnitude greater than that of C and the uncertainty in Fe measurement by PIXE was equivalent to the carbon concentration. The Fe distribution could therefore also not be used to demarcate inhomogeneities in the carbon distribution. It is deduced that the Zn concentration, even when present in concentrations equivalent to that of Mn and Cr, could have same effect on the C distribution. The low concentration of Zn, considered as a residual element, was therefore advantageous in isolating possible carbon distribution inhomogeneity and information such as clustering or single formed nuclei can be identified.

The observable inhomogeneity in the μ-PIXE Fe elemental distribution map corresponds to

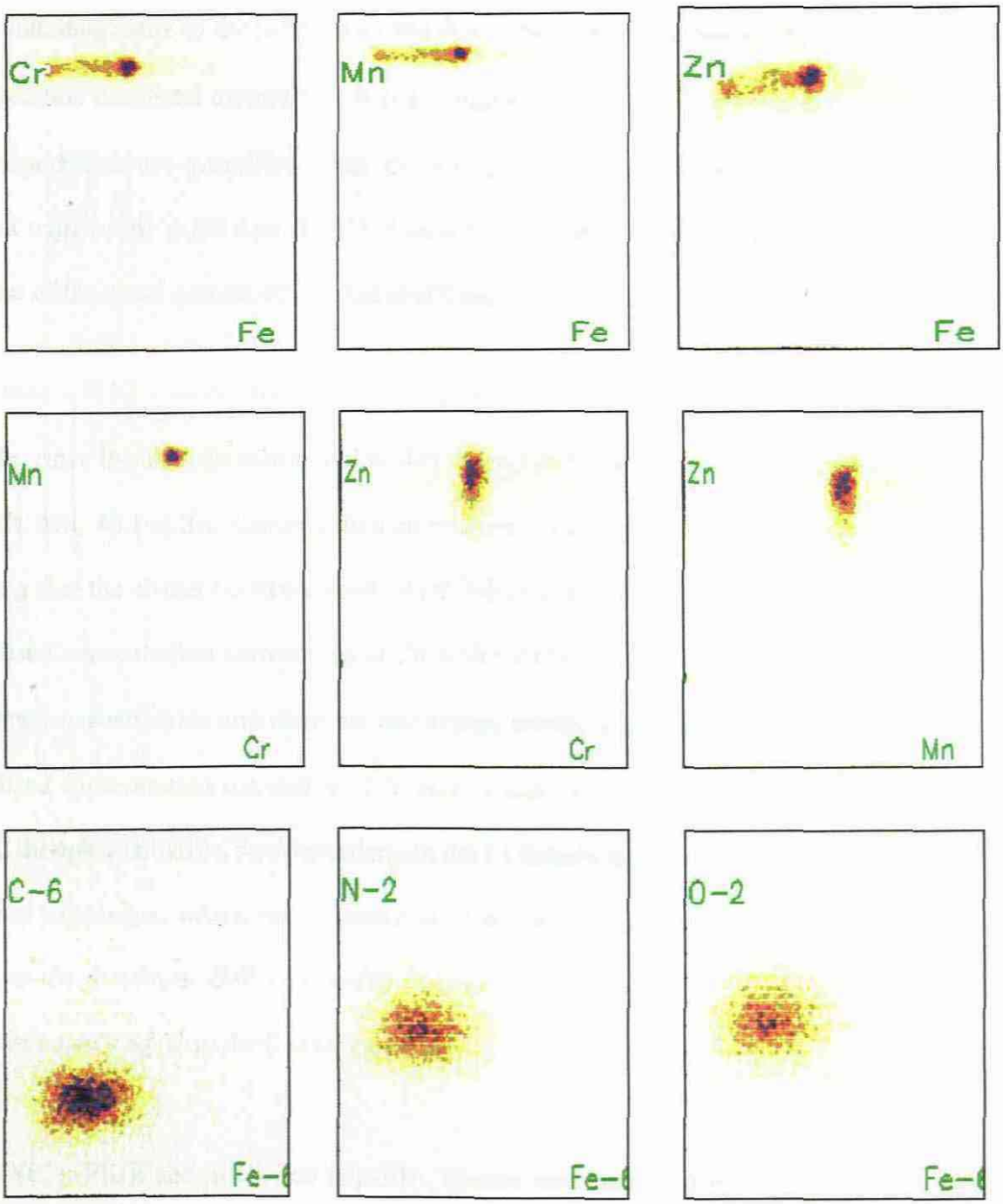

Figure [4.4.10] ***μ-PIXE quantitative true concentration correlations of Cr, Mn, Zn and Fe with another (first 6 images) and μ-BS quantitative true elemental distribution of C and Fe and the elemental concentration correlations of Fe with N and O (last 3 images). For the Fe μ-PIXE correlations, the concentration of Fe is in logarithmic scale since the element concentration is at least two orders of magnitude greater than the concentration of the other elements. The 6 in the μ-BS correlations indicate that background subtraction was performed to give quantitative results. The 2 indicates that both the peak and the background were considered.***

the inhomogeneity in the μ-BS elemental distribution, which correlates negatively with the μ-BS carbon elemental distribution. It is emphasised that the μ-BS elemental distribution of Fe is regarded as not quantified, since the background subtraction was performed over the Fe front edge of the μ-BS data. The N elemental distribution image could not be quantified because of the small amount of O in the specimen, which influenced the demarcation.

In these μ-PIXE concentration correlations, the Fe concentration was expressed in logarithmic scale, since the element concentration was at least two orders of magnitude greater than those of Cr, Mn, As and Zn. Concentration correlations of Cr and Mn with Fe were constant, indicating that the element concentrations were independent of the Fe elemental distribution. The diffused concentration correlations of Zn with Cr and Mn could be attributed to low Zn elemental concentrations and therefore encompass mostly statistical fluctuations. For μ-BS, the diffused concentration correlation of N with Fe indicates that the nitrogen elemental distribution, though qualitative, was dependent on the Fe distribution. However, the C and Fe concentration correlation, which was expected to be linear and negative, was diffused. This may be due to the non-linear diffusion profile of C and the uncertainty in Fe measurement that was approximately equal to the C concentration.

μ-PIXE, μ-PIGE and μ-BS, that is μ-IBA, spectra were extracted from the low Fe concentration region in the elemental distribution of Fe, as indicated in **figure [4.4.11(a)]**. The demarcation was overlaid on the Zn elemental distribution, over the same micro-region, as indicated in **figure [4.4.11(b)]**. The extracted micro-region represents only part of the scanned area. Therefore the charge accumulated was less than the charge for the scanned area. This lesser charge consequently influences the uncertainty in measurement and minimum detection limits of the element quantification. The spectrum of the μ-PIXE data, fitted with the GeoPIXE II software, is shown in **figure [4.4.11(c)]**. In the figure the arrows indicate the peaks of the K

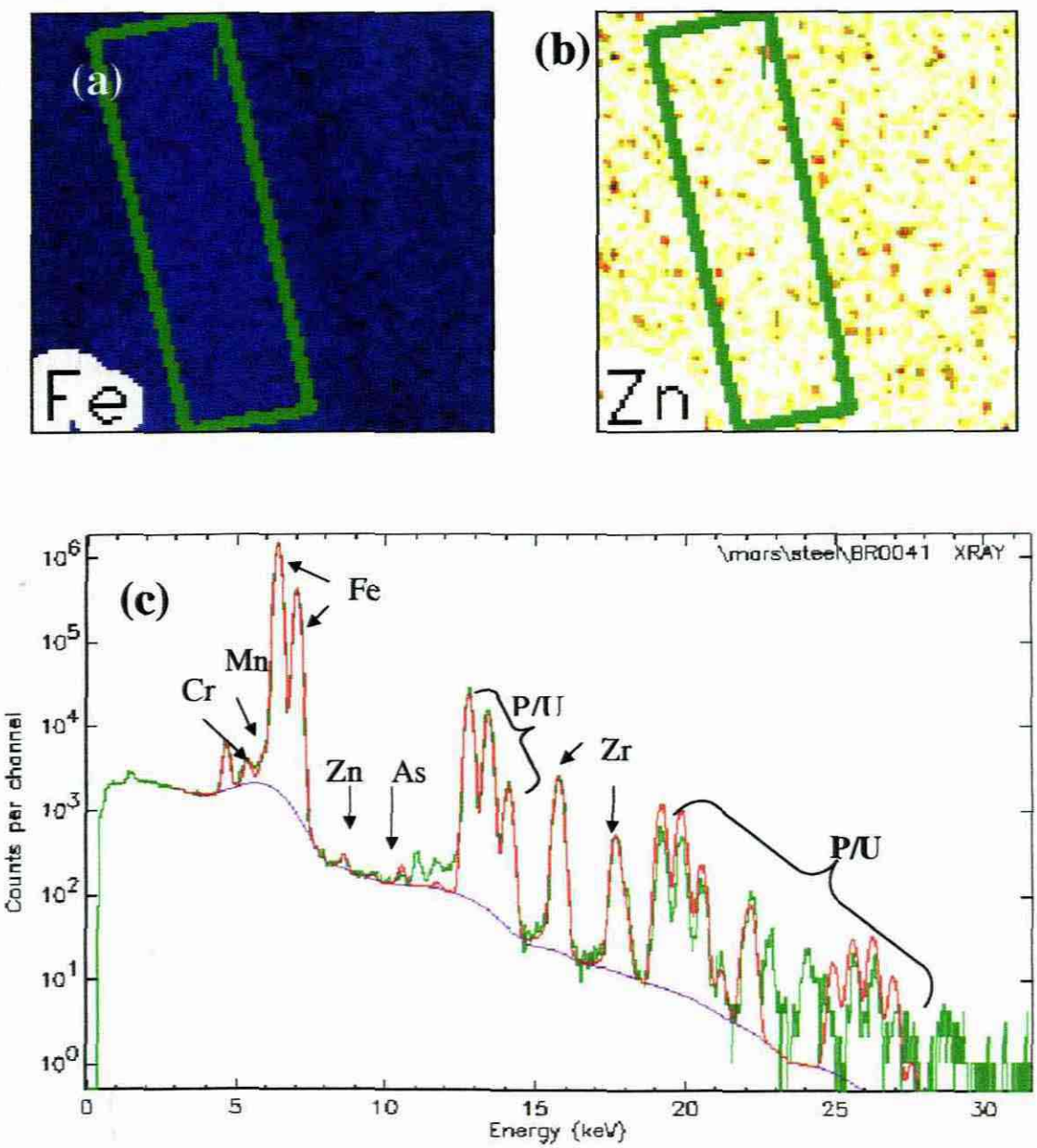

Figure [4.4.11] ***Demarcation of (a) the low Fe concentration region. The area dimensions are 50μm × 185μm. The total integrated charge was 0.236μC. In (b) the demarcation is superimposed on the Zn concentration distribution. The spectrum of the μ-PIXE data, fitted with the GeoPIXE II software, is shown in (c). The data are represented by the green line, the GeoPIXE II fit to the data by the continuous red line and the purple line represents the background. Arrows indicate the peaks of the K X-ray lines of the respective elements.***

X-ray lines of the matrix elements. The high number of pile-up peaks in the spectrum was due to the high beam current suitable for both PIGE and BS but not so much for PIXE, which results from the methodological compromise between PIXE and BS and PIGE. The data are plotted in logarithmic scale and the pile-up area is therefore approximately a tenth of the peak area.

The spectrum of the extracted μ-BS data is shown in **figure [4.4.12]**. The dotted line represents the data and the continuous line the RUMP simulation to the data. Data in the energy range 1.50 to 2.00 MeV did not deviate significantly from the RUMP simulation to the data, since the carbon diffusion profile was assumed to be linear. This was in contrast to the μ-BS data of the scanned area, depicted in **figure [4.4.7]**, which showed that the carbon diffusion profile was non-linear.

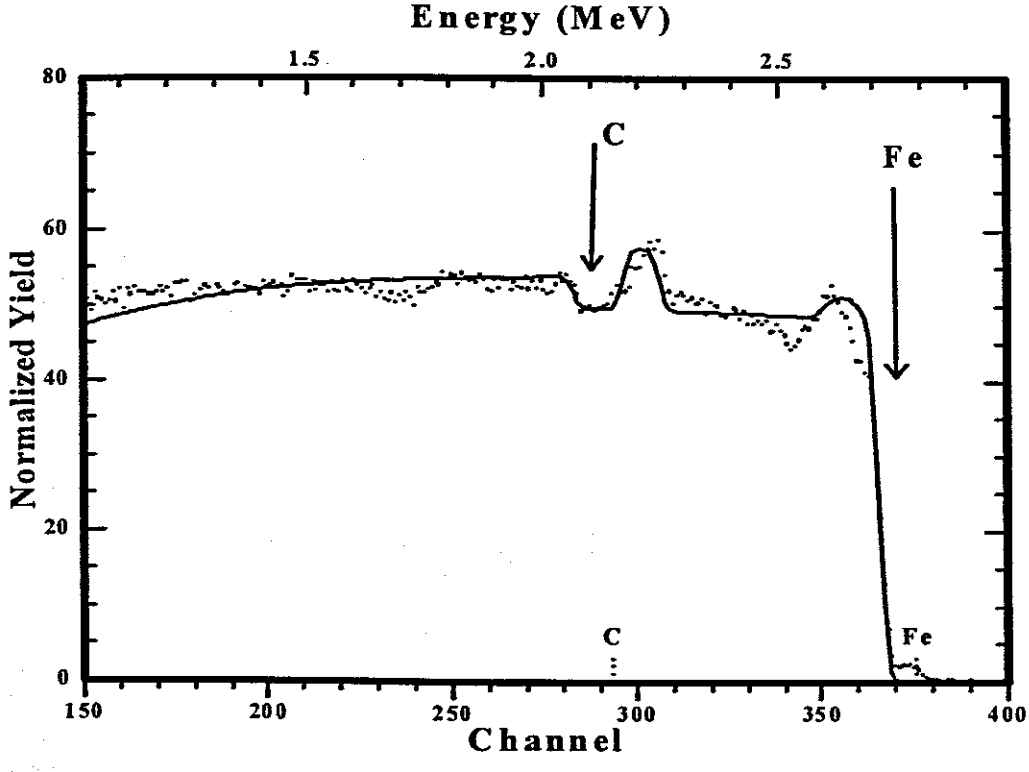

Figure [4.4.12] ***Spectrum of the extracted μ-BS data. The dotted line represents the data and the continuous line the RUMP simulation of the data. In the energy range 1.50 to 2.00 MeV, the carbon diffusion profile did not deviate significantly from the simulation in which it was assumed to be linear. Arrows indicate the energies of the respective elements when located at the surface.***

No light elements were found in the extracted area. Therefore the spectrum shown in **figure [4.4.6]**, also represents the spectrum of the extracted μ-PIGE data, though poorer statistics were found. The μ-IBA analysis results of the extracted region are given in **table [4.4.7]**. The relative increase in uncertainty and minimum detection limits are due to the poorer statistics of the smaller area. The close agreement in the Fe analysis results attests the complementarity of IBA techniques.

Table [4.4.7] ***μ-IBA analysis results of low Fe concentration region extracted from the area scanned. The concentration is given in μg.g^{-1} and in mass%, where the percentage sign follows the element symbol. The technique used for the analysis was PIXE unless otherwise indicated.***

Element and Technique	Energy (keV)	c_Z value	Unit μg.g^{-1} or mass%	u_Z %	MDL μg.g^{-1}.μC^{-1}
Cr	5.41	890 ± 190	μg.g^{-1}	21	110
Mn	5.89	0.19 ± 0.04	mass%	21	60
Fe	6.40	95.7 ± 0.9	mass%	1.0	50
Fe-PIGE	847	96.3 ± 3.6	mass%	3.7	200
Fe-BS	2780	95.9 ± 3.8	mass%	4.0	1.6 mass%
Zn	8.64	110 ± 10	μg.g^{-1}	9.1	20
As	10.54	80 ± 20	μg.g^{-1}	25	10
C-BS	2260	3.7 ± 0.3	mass%	8.1	1.6 mass%

So far only analyses of the scanned area and the demarcated region have been performed. Since the diffusion profile of C was predominantly non-linear over the entire scanned area and, in contrast, linear in the extracted area, it was essential to obtain a clearer view, especially with regard to the C concentration. This was achieved by performing a linear traverse analysis, shown in **figure [4.4.13]**, across the scanned area. The linear traverse analysis does not serve to emphasise the Fe inhomogenous elemental distribution per se, but that of the other matrix elements. The μ-PIXE linear traverse analysis for Cr, Mn, Zn, As and Fe for comparison was shown in **figure [4.4.13(c)]**. The μ-BS linear traverse analysis for Fe and C was depicted in **figure [4.4.13(d)]**. No linear traverse analysis was done for μ-PIGE, since

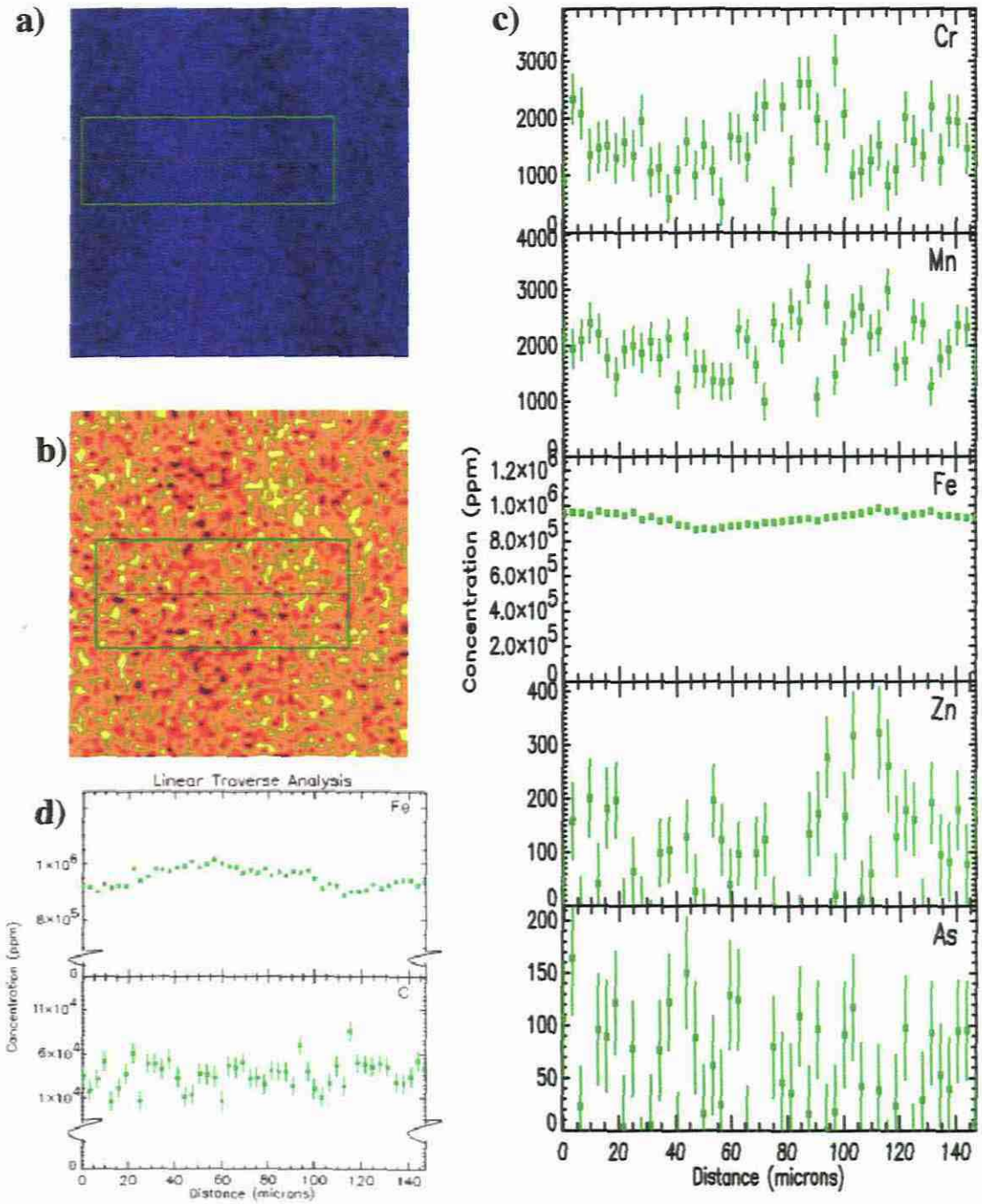

Figure [4.4.13] ***μ-PIXE and μ-BS linear traverse analyses across the Fe and C concentration distributions respectively. The image of the Fe element distribution (a) indicates the area of the linear traverse analysis. The C elemental distribution image and the area over which the linear traverse analysis is performed is shown in (b). In (c) is shown the μ-PIXE linear traverse analysis across the Fe quantitative true elemental distribution map. The μ-BS linear traverse analysis across the C elemental distribution is shown in (b). The linear distance is approximately 150μm. All values are expressed in μg.g^{-1}.***

light elements were not detected in the scanned area and only Fe could be quantified with PIGE. The GeoPIXE II software is specific to analysis by PIXE data. A routine for obtaining a PIXE linear traverse analysis is included in the software. It is therefore not necessary to set demarcations over X-ray peaks in spectrum of the PIXE data. However, for BS- and PIGE linear traverse analyses, demarcations had to be set over the energy range in the spectrum of the data that included the element peak. The demarcations or cuts setup were then used to generate a dynamic analysis map, which was applied in extracting information from the event-by-event analysis data. It was hence unavoidable that the linear traverse analysis for PIXE and BS or PIGE would not start at the same initial point.

The diffused distributions of Cr and Mn showed no correlation with the distributions of other elements over the entire linear distance. This also agrees with the homogenous elemental distribution of these elements. In the linear distance range from 40 to approximately 100μm, there is a corresponding decrease in Fe concentration, as the high C concentration region, the nucleus, was traversed. The pronounced positive concentration correlation between Fe and Zn is evident in this linear distance range.

The linear traverse analysis of As shows that the element distribution was independent of the distributions of all other elements. In the μ-BS linear traverse analysis of Fe and C, the traverse of the C nucleus starts at 70μm and extended to 130 μm, giving the nucleus a linear distance range of 60μm, as determined in the μ-PIXE linear traverse analysis. A correlation is visible even though the linear traverse analysis is not well defined.

The preceding analyses were possible since the variation in Fe concentration enabled concentration profiles to be visible in the elemental distribution map. It was crucial to investigate other regions in the scanned area where there are no concentration profiles visible in the Fe

elemental distribution map. The aim was to expose different elemental distributions that may indicate phenomena closely associated with inclusion of elements in the steel matrix. Examples of these are cluster formation or other aggregation and incomplete carbon nucleation.

Cluster formation, consisting of three agglomerates, is illustrated in **figure [4.4.14]**, in which the Fe elemental distribution, the demarcation of the center and the periphery of the agglomerate are shown. As can be seen from the Fe elemental distribution, there are no visible concentration profiles that would otherwise indicate inhomogeneities.

Adjustment of the maximum concentration value to which the Zn elemental distribution was displayed, enables the demarcation of the cluster formation. The presence of Zn, as a residual element, was therefore beneficial. Since the Zn concentration was comparatively low, it indicates that in the cluster formation there are small changes in concentration between the cluster and the solid solution. The agglomerate was quantified by the elemental composition analysis of the center and the periphery regions.

Although the GeoPIXE II software version was well advanced, the demarcations, illustrated in **figure [4.4.14]**, could only be superimposed on other elemental distributions and not one demarcation on the other. It was therefore vital to state that since the demarcation was solely dependent on the Zn elemental concentration distribution, concentration differences not visible are included in the demarcation.

It was expected that this feature would not significantly influence the respective elemental compositions of the regions. This is significant in that it is desired that results should not differ by more than the uncertainty in measurement of the Zn concentration.

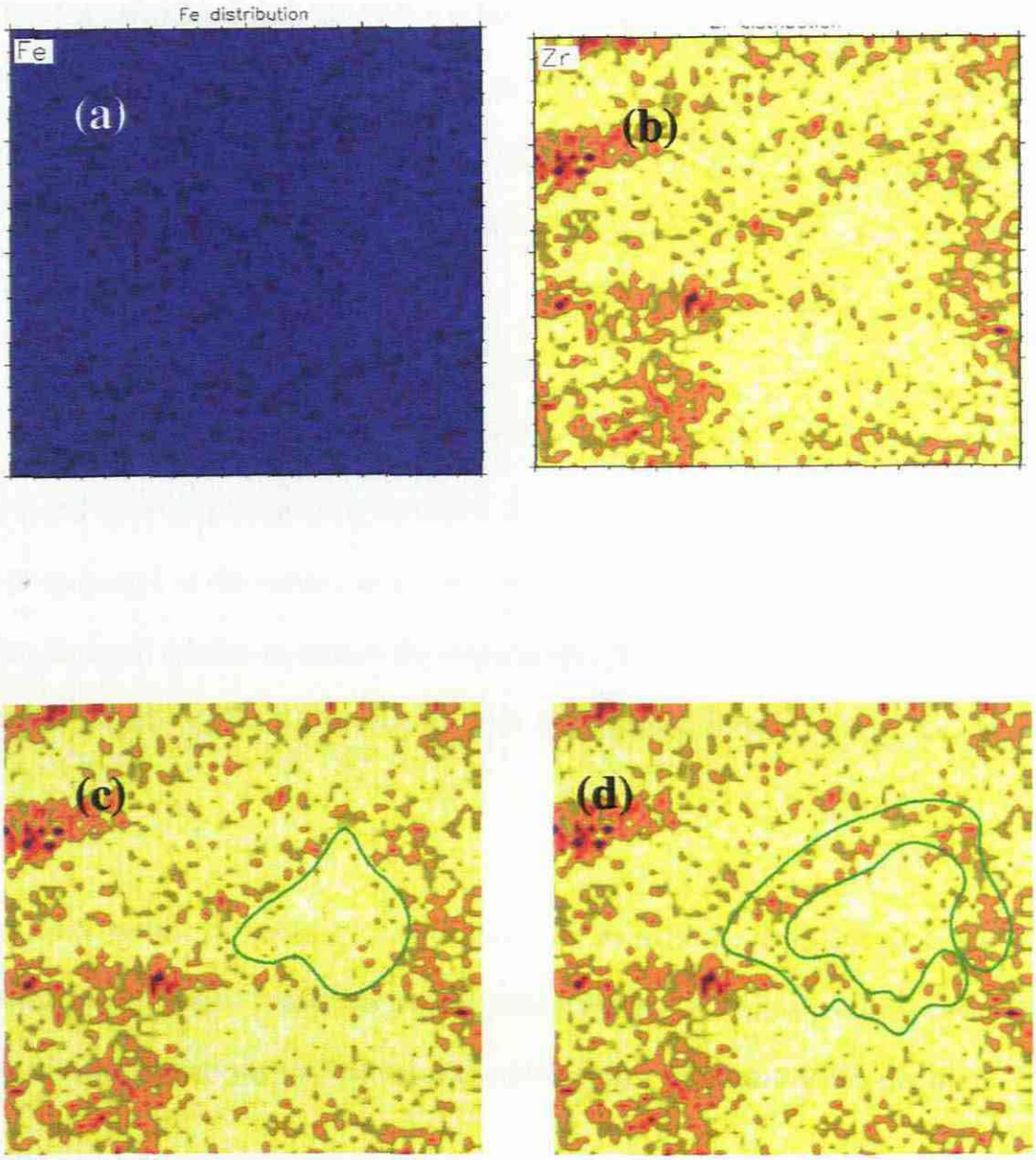

Figure [4.4.14] ***Illustration of cluster formation during the solidification of carbon. In (a) is shown the Fe elemental distribution to indicate that no concentration profiles are visible, even though cluster formation occurred. The cluster agglomerates are shown in (b), the demarcation of the agglomerate center, with a resultant charge of 0.378 μC, in (c) and the periphery of the agglomerate, with a resultant charge was 0.453μC, in (d).***

The spectra of the extracted μ-PIXE, μ-PIGE and μ-BS data are shown in **figure [4.4.15]**. The PIXE data are displayed in the energy range of 4 to 25 keV, in which the K X-ray lines of the matrix elements are emitted. The high number of pile-up peaks in the PIXE spectra was due to the compromise in the PIXE analysis with the PIGE and BS analysis when a relatively high current are normally required for PIGE and BS. The more intense Zn X-ray line peak of 8.64 keV in the periphery of the agglomerate than the peak in the center of the agglomerate can be discerned.

The γ-rays emitted at 847 and 1377 keV for the reactions ^{57}Fe p(1, 0) and ^{56}Fe p(2, 0) were the only useful γ-rays for quantifying the matrix element Fe as there were no light elements present in the matrix of the scanned area. The former reaction however has a better minimum detection limit and smaller uncertainty in measurement. This reaction was consequently used for quantification of Fe. For this reason, the data are displayed in the energy range 800 to 900 keV.

In the μ-BS spectra, the energy of B when located at the surface is indicated. This was done to show the energy range to which the carbon concentration distribution profile was demarcated and to discern whether the element's concentration profile was linear or non-linear.

These respective μ-IBA spectra do appear to be based on the same data. This means there is hardly any visible difference in the μ-PIGE spectra and similarly, in the μ-BS spectra. However, the data for each respective spectrum differed by a maximum of only 3%. This is indicative of the small concentration difference between the elements in the center and those in the periphery of the agglomerate. It is for this reason that the maximum scale to which the Zn elemental distribution was displayed was increased.

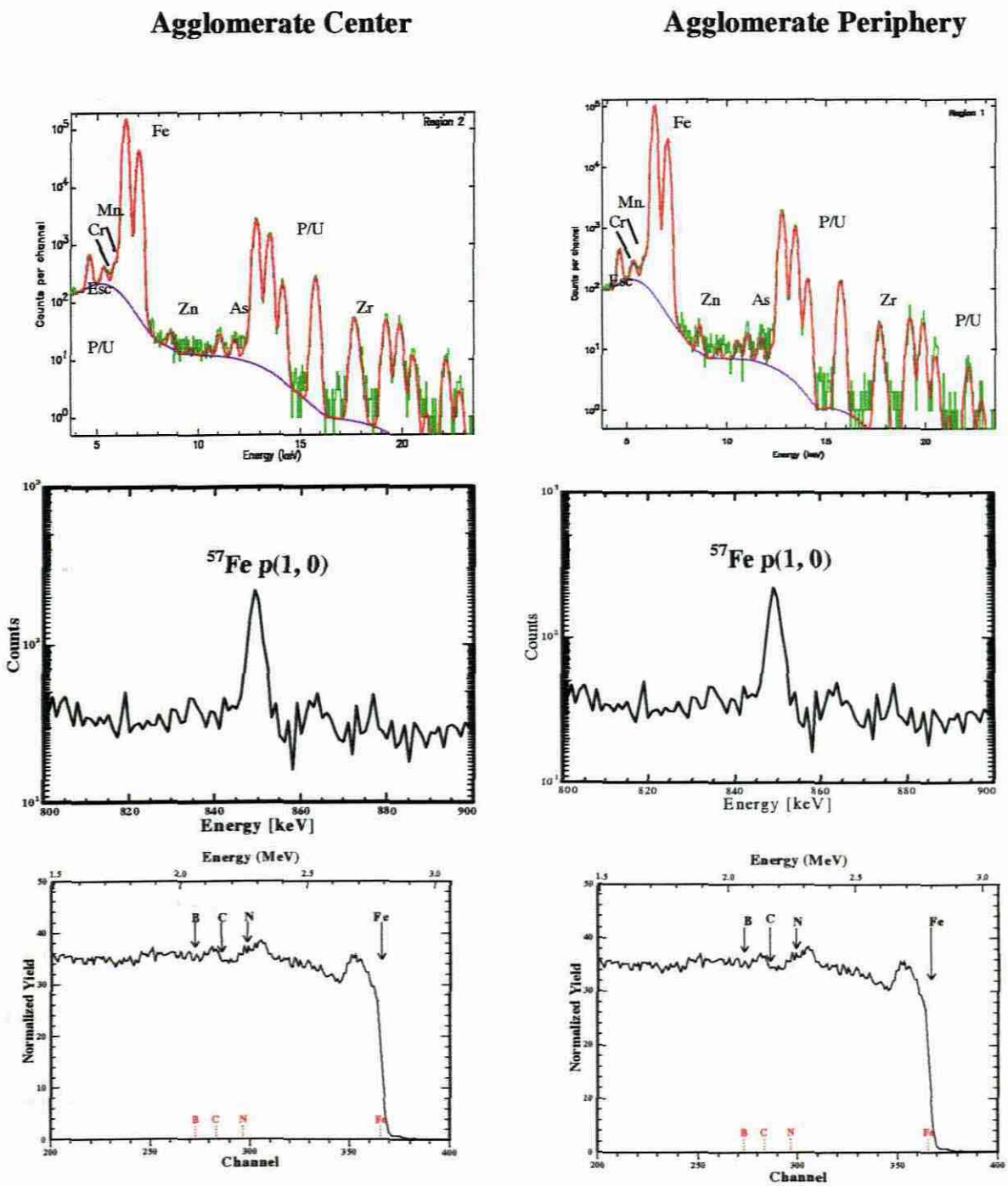

Figure [4.4.15] ***Spectra of the extracted μ-PIGE and μ-BS data of the center, on the left, and the periphery, on the right, of the agglomerate. In the μ-PIXE spectra the green line represents the data, the red line the GeoPIXE II fit to the data and the purple line represents the background. The X-ray line peaks of the elements, escape and pile-up peaks are indicated. The μ-PIGE data was displayed in the energy range 800 to 900 keV since the γ-ray for ^{57}Fe p(1, 0) was emitted at (845±2)keV. Boron was included in the μ-BS spectra to indicate the demarcation set in determining the carbon diffusion profile. Arrows indicate the energies of the respective elements when located at the surface.***

The μ-IBA analysis results of the agglomerate are given in **table [4.4.8]**. The results indicate that a relatively small difference in carbon concentration lead to cluster formation. The Zn concentration in the peripheral region was greater than in the center. The difference in Fe concentration was relatively low and hence the reason for not observing any concentration profiles in the Fe elemental distribution map. For both regions there were small differences in 1) concentrations of Cr and Mn and 2) the absolute error in the Zn quantification. This signifies that in the demarcation of the agglomerate center and periphery, the inclusion of regions where Zn elemental concentration profiles were not visible, do not significantly affect the results. No significance could be ascribed to the difference in As concentration, since these values were slightly more than the MDL and less than the element uncertainty in measurement.

Table [4.4.8] ***μ-IBA analysis results of the agglomerate resulting form cluster formation during solidification of carbon in a solid solution of Fe. Values are given $\mu g.g^{-1}$ unless indicated by % after the element symbol for mass%.***

Element symbol	Agglomerate center			Agglomerate periphery		
	c_Z	u_Z	MDL	c_Z	u_Z	MDL
Cr	920 ± 400	44	110	900 ± 430	48	120
Mn	1430 ± 440	31	60	1420 ± 420	30	70
Fe%	98.4 ± 1.61	1.6	50	97.1 ± 1.01	1.1	60
Fe%-PIGE	98.9 ± 3.6	3.7	200	98.6 ± 1.05	1.1	200
Fe%-BS	98.7 ± 3.8	3.9	1.6	98.6 ± 1.05	1.1	1.6
Zn	110 ± 60	55	20	190 ± 50	26	30
As	60 ± 20	33	30	40 ± 20	50	30
C%-BS	2.87 ± 0.2	7.0	1.6	1.57 ± 0.2	13	1.6

Another phenomenon, closely associated with the incorporation of carbon into the steel matrix, is incomplete nucleation. An example of this is shown in **figure [4.4.16(a)]**. The nucleation is termed incomplete when compared with the theoretically determined forms of complete nucleation, which are reproduced **figures [4.4.16(b)** and **(c)]**. These examples were obtained from, respectively, Bhadeshia (2001) and Shyy and Udaykumar (2002).

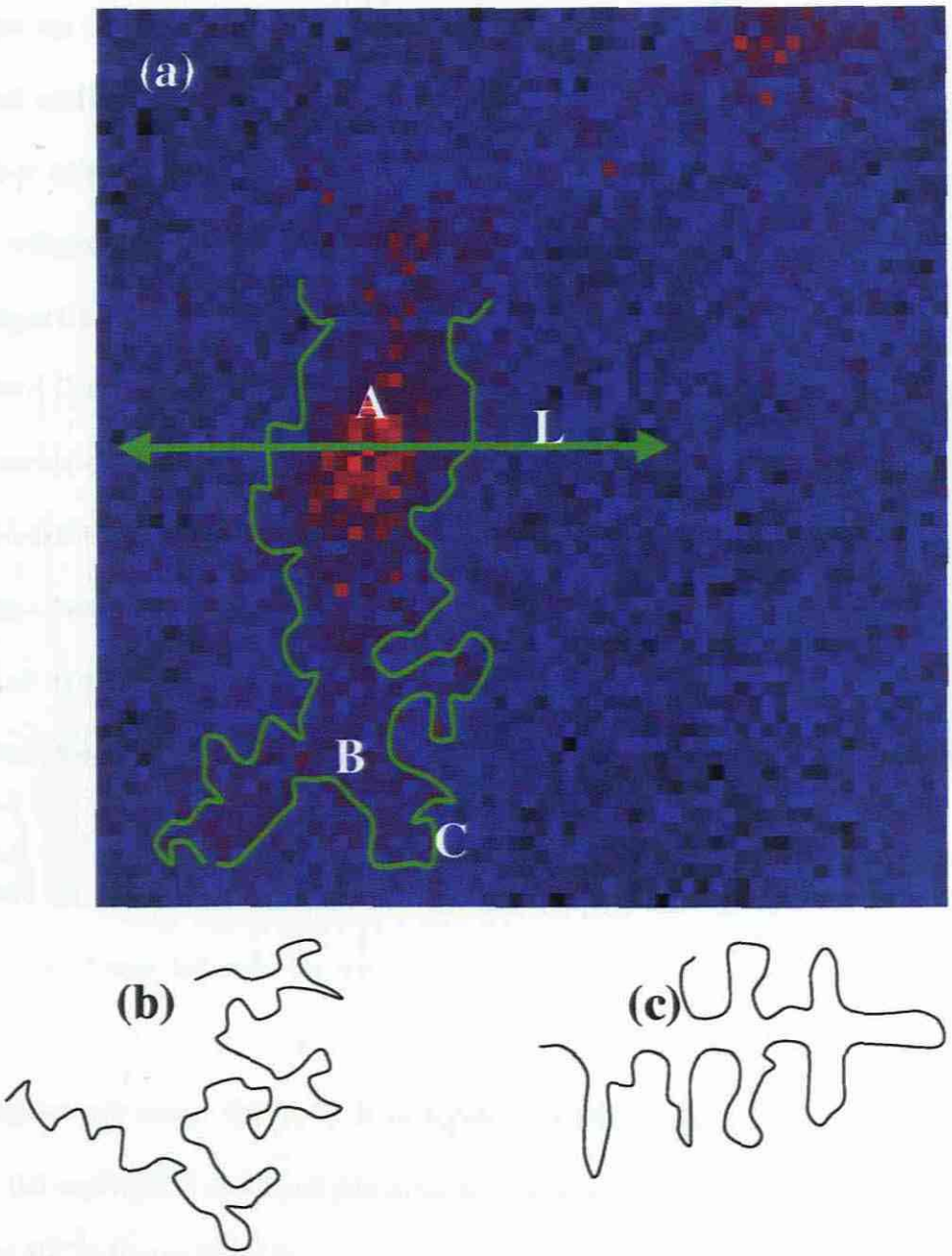

Figure [4.4.16] ***Illustration of incomplete nucleation of carbon from the μ-PIXE elemental distribution map of Fe (Mars et al. IV, 2003). In (a) is shown the solidification of the carbon in steel. The area scanned was 200μm ×200μm. A indicates the center of the nucleus, AB the primary dendrite and BC the secondary dendrite. L indicates the position of the linear traverse analysis performed across the nucleus to illustrate the carbon concentration profile. The theoretically determined forms of complete nucleation, in respectively (b), from Bhadeshia (2001) and in (c) from Shyy & Udaykumar (2000), are shown for comparison.***

In this figure, A is the center of the nucleus, the region of high carbon concentration. From the nucleus the carbon diffused outward into the regions of high Fe concentration. The imposed thermal profile in the interface between this high carbon concentration region and the region of lower concentration was lower than the local region temperature. This condition is normally referred to as constitutional supercooling. A disturbance of the planar interface, towards **B in figure [4.4.16],** occurred. This caused a protrusion of the solid C into the Fe liquid. The perturbed C solid found itself in a metastable state; metastable since this region was below the temperature of the nucleus. Further solidification of the solid carbon ensued and the solute was released into the Fe liquid ahead of this perturbation, (from **B to C** in **figure [4.4.16]**), causing a runaway. Unstable growth of the perturbation resulted, since this small perturbation ended up in more supercooled liquid. The resultant morphological instabilities, indicated by **C** in **figure [4.4.16]**) are referred to as dendrites.

Dendritic formation was common in alloying, especially with carbon, since the carbon solute normally partitions between the solid and the liquid phases. Segregation does not normally occur ahead of the dendrite tip since the main partitioning is that of solute trapped between the dendrite side-arms, shown by **B** in **figure [4.4.16]**. Increasing the solidification rate can reduce the segregation scale and subsequently the size of the dendrite arm decreases, as indicated by **BC** in **figure [4.4.16]**.

The carbon concentration profile is illustrated by the linear traverse analysis, performed across the nucleus, in **figure [4.4.17]**. The high carbon concentration could be deduced from the decreasing Fe concentration in the linear distance range from 20 to approximately 100μm. There was also the corresponding increase in Cr concentration. The uncertainty in the Cr concentration measurement in this region was relatively high.

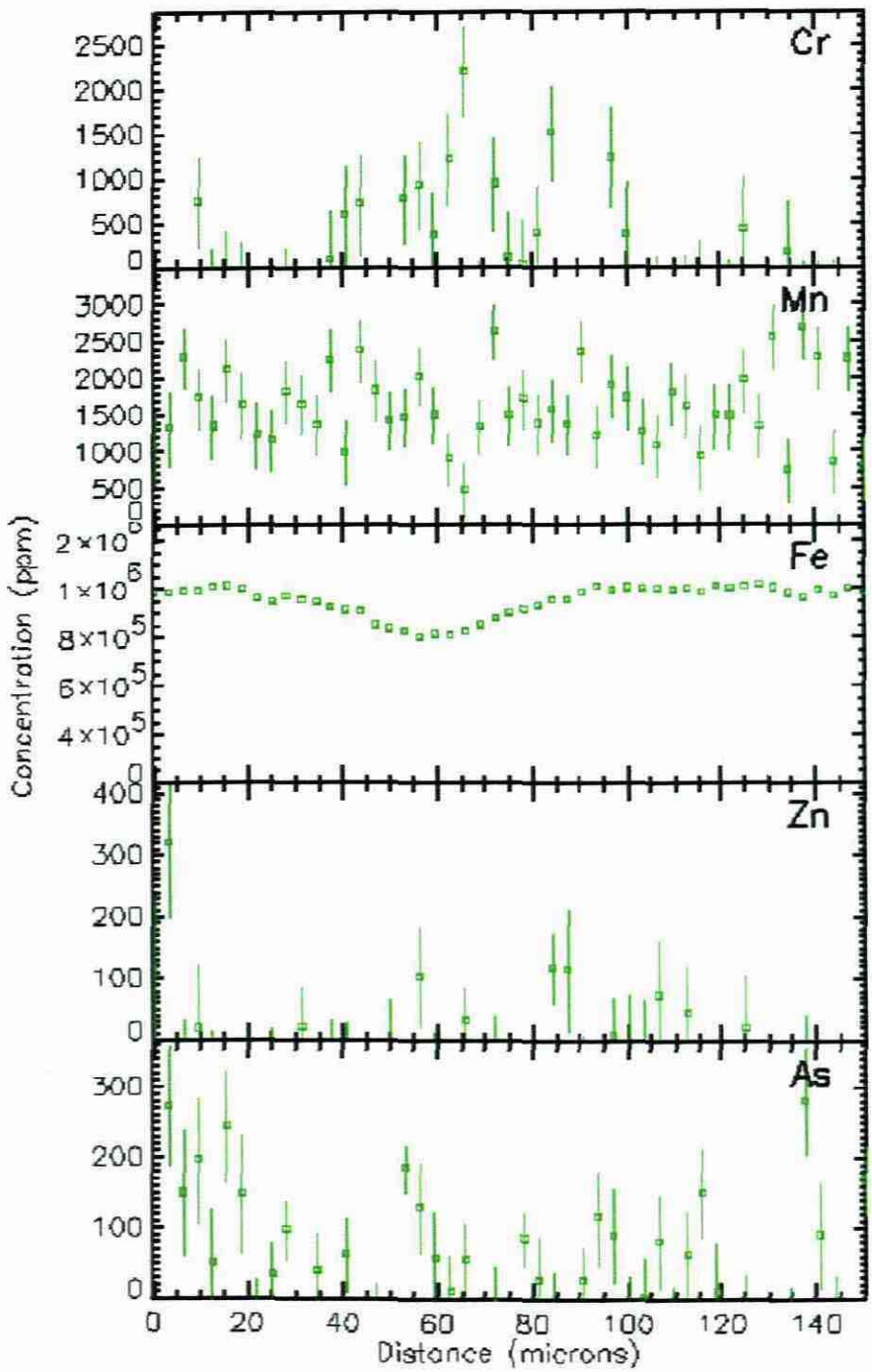

Figure [4.4.17] ***Linear traverse analysis across the nucleus (A), as indicated by the solid line in figure [4.4.16]. The high carbon concentration is deduced from the decrease in Fe concentration. Further discussions are in the text.***

For this reason it can only be tentatively stated that Cr exhibited a positive correlation with carbon in regions where the carbon concentration was greater than 10 mass%. The distribution of Mn and As are diffused and no trend in the correlation could be discerned. The carbon concentration, in the linear distance range of 20 to 100μm, ranges from 10 to 25 mass%. Hence, in this region the phase structure changes are from Fe_4C through Fe_3C and Fe_2C to FeC_2 in the center of the nucleus. Based on **figure [4.4.2]**, these phases are described as cementite and ledeburite cast iron (Bhadeshia, 2001).

μ-PIXE, μ-PIGE and μ-BS have been applied in the investigation and quantification of the elemental distribution in steel. It is of interest to model this type of micro-segregation in particular with respect to 1) the overall pattern of segregation knowing that C diffusion was linear in high concentrations and non-linear in low concentrations and, 2) the resultant microstructure with reference to **figure [4.4.13]**.

Since microstructural features are of considerable importance to the materials scientist, a second level of inhomogeneity was necessary. As an example, during steel processing, the solutal inhomogeneity arose from the rejection of solute from the solid into the liquid (Bhadeshia, 2000). The solute therefore microsegregated in the final product and this segregation should ideally culminate in a globular distribution. Shyy and Udaykumar (2002) provided a guideline for the diffusion length scales with which the microsegregation generally occurs. It was therefore of interest to establish the scales and the dendritic arm spacing, which resulted in grain size distribution. The aim was to simulate the elemental concentrations obtained from x-ray, γ-ray and backscattered data onto existing theories of microstructural segregation. In this manner the extent of agreement between the data and theory would be ascertained.

Various theories to explain microsegregation have been proposed. Of these, Beckerman and

Viskanta (1993) detailed the volume averaging or filtering theories (VA); Shyy and Udaykumar (2000) proposed the multi-scale modeling for solidification (MSM); the theory of Stenden et al. (1997) is discussed in section [4.4.1]; and, Thevosz et al. (1989) proposed the two-level micro-macro modeling strategies (TMM).

Concepts such as the solid-, interdendritic- and extradendritic phases and the corresponding volumes, areas and concentrations of these phases are used in the model. These concepts are however defined in the VA theory and are, for clarity, illustrated in **figures [4.4.18]** and **[4.4.19]**, which were obtained from Shyy and Udaykumar (2002). The TMM model has been chosen for data simulation, since the physics at the macro-level as well as the grain growth phenomena, encompassed in the theory, are computed separately. The mesoscale physics are then periodically transferred to and incorporated into the macroscale.

The primary and secondary dendritic lengths are the basis for determining the diffusion length of each of the phases. The profile of the secondary dendrite arm, as obtained in this study, is shown in **figure [4.4.16]**.

Computation of macro-level physics and grain growth offers bi-directional information exchange as the evolution of the subgrid model is time-stepped in small increments. The dynamics of the meso-scale, pointed out by Shyy and Udaykumar (2002), was periodically transferred to the macro-scale. The evolving microstructure also utilises information from the micro-scale.

Before discussing the physics equations underlying the TMM model, it was necessary to define internal- and external variables. The internal variable changes as the system changes, whereas the external variable remains the same, whether the system was static or dynamic.

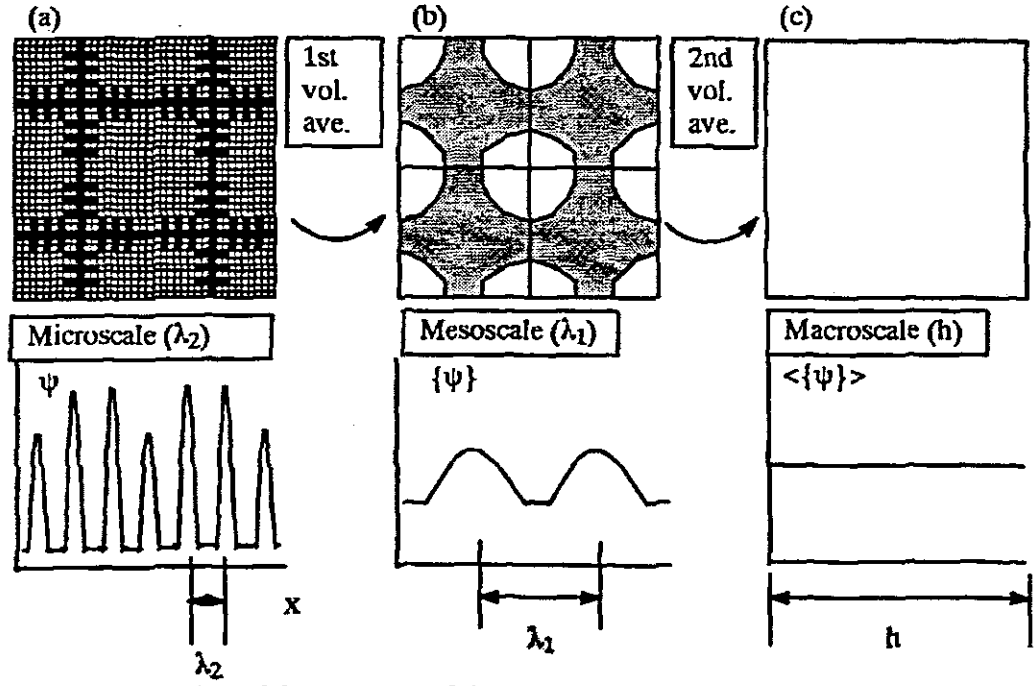

Figure [4.4.18] ***Illustration of the concepts of the averaging process on the macro-, meso- and microscale, involved in the dual-scale averaging to obtain macroscopic volume-average equations, the secondary arm spacing, λ_2, the primary arm spacing, λ_1 and the computational grid spacing with ψ the averaging (Shyy and Udaykumar, 2002).***

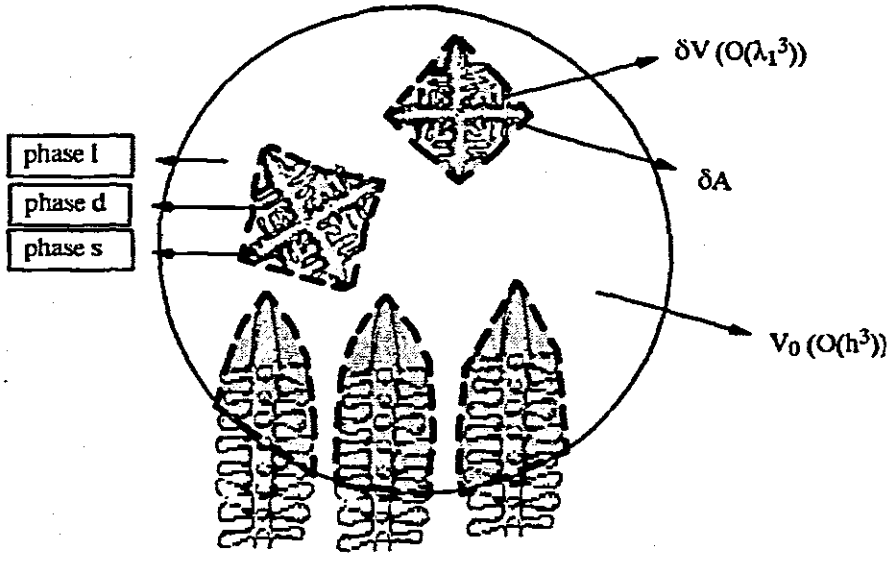

Figure [4.4.19] ***Illustration to emphasise the definitions of the averaging volumes for the first and second averaging processes. The respective phases are indicated and the envelopes are shown shaded (Shyy and Udaykumar, 2002).***

The average concentration in the solid phase, c_{av}, was regarded as an internal variable since it changes as the system changes. The physics at the macro-level encompasses parameters such as enthalpy, h, specific heat, c^p, temperature, T, fraction of solute, f_s, latent heat, L, D_s, the diffusion coefficient and the partition coefficient, k. Should the thermophysical properties remain constant and the solid and liquid densities equal, then the enthalpy, as discussed by Atkins (1999), is given in equation [4.4.1]. For a pore-free material, c_{av} was defined in terms of

$$h = c^p T + l(1 - f_s) \qquad \textbf{4.4.1}$$

solid concentration, c_s, and the liquid concentration, c_l, by equation [4.4.2]. Furthermore,

$$c_{av} = (1 - f_s) + f_s c_s \qquad \textbf{4.4.2}$$

should the liquidus be constant then the melting temperature, T_m, and the partition coefficient are expressed by equations [4.4.3] and [4.4.4]. To adequately describe the system, it was nec-

$$T = T_m + mc_l \qquad \textbf{4.4.3}$$

$$k = c_s / c_l \qquad \textbf{4.4.4}$$

essary to define c_s in terms of c_l. Both these parameters at the micro-level depend on the solidification at the dendrite level. To express this relationship, Thevosz et al. (2000) defined a dimensionless parameter, η, which was normalised with respect to half of the secondary arm spacing. They also assumed that the diffusion proceeds by Fick's second law, which is detailed by Atkins (1999). This relationship is given by equation [4.4.5]. However, for c_s, Mo

$$\frac{dc_s}{dt} = \left(\frac{kc_l - c_s}{f_s} \right) \frac{df_s}{dt} + \frac{1}{f_s} \frac{D_s}{\lambda_2^2} \frac{\partial c_s}{\partial \eta} \qquad \textbf{4.4.5}$$

(1994), using an adjustable parameter, ξ, introduced an evolution relationship, equation [4.4.6], which was based on the investigations of Ganesan and Poirier (1990) and Ni and Beckermann (1990). ξ is merely an empirical constant. It was introduced since the equation

$$\frac{dc_s}{dt} = \left(\frac{kc_l - c_s}{f_s} \right) \left(\frac{df_s}{dt} + \frac{D_s}{\lambda_2^2} \frac{\xi}{1 - (1 - k) f_s} \right) \qquad \textbf{4.4.6}$$

contains internal variables. The purpose of ξ was to provide an exact simulation to the exp-

erimental data. In view of this internal variable approach, Thevosz et al. (2000) and references therein, proposed the power-law approximation approach to the evolution of c_s, given in equation [4.4.7]. γ has the same definition as ξ and was the result of assuming that the total solute redistribution in the liquid and solid-liquid interface is in equilibrium. The solute flux at the

$$\frac{dc_s}{dt} = \left(\frac{kc_l - c_s}{f_s}\right)\left(\frac{df_s}{dt} + \frac{D_s}{\lambda_2^2}\frac{\gamma+1}{f_s}\right) \qquad \textbf{4.4.7}$$

solid-liquid interface, j_{sl}, can be introduced by applying the previous equations, which yields equation [4.4.8]. This in turn yields equation [4.4.9] with respect to the internal variable ap-

$$\frac{dc}{dt} = \frac{d((1-f_s)c_l}{dt} + kc_l\frac{df_s}{dt} + j_{sl} \qquad \textbf{4.4.8}$$

proach and equation [4.2.10] with respect to the power-law approximation approach. These equations can therefore be used to adequately describe the system.

$$j_{sl} = \frac{D_s}{\lambda_2^2}\xi\frac{kc_l - c_s}{1-(1-k)f_s} \qquad \textbf{4.4.9}$$

$$j_{sl} = \frac{D_s}{\lambda_2^2}(1+\gamma)\frac{kc_l - c_s}{f_s} \qquad \textbf{4.4.10}$$

μ-PIXE, μ-PIGE and μ-BS could be used for emphasizing the small inhomogeneities in the structure of the steel. The event-by-event analysis facilitated the extraction of both μ-PIGE and μ-BS data, which could afterwards be quantified. In this quantification it was found that the elemental distribution of elements Mn and Cr is homogenous and primarily biglobular. Because of this homogeneity and the relatively high concentration of these alloying elements it is inferred that the distribution is not affected by the presence of other elements or by any external variable such as the solidification temperature. The concentration of Zn is comparatively low, but this residual element aggregates with Fe, exhibiting a positive correlation. Elemental distribution of C showed a negative correlation with the distribution of Fe and Zn. The negative correlation of the Fe- with C distribution was expected since C was added as a

hardening alloying element. However the presence of Zn made the identification of subtle inhomogeneities of the C distribution, such as cluster formation, possible. Although Fe correlates positively with Zn the Fe distribution could not be used to identify these inhomogeneities as the concentration of Fe was at least an order of magnitude greater that the concentration of C. The distribution of C was however biglobular or colloidal as is usually intended when alloying C with Fe. The presence of As in the steel matrix could have occurred during the processing of raw materials. The quantity found is relatively low, and in many instances lower than the MDL. However, the distribution of As did not have any visible effect on the distribution of the other elements.

The μ-PIGE data extracted from the total scanned area showed the absence of light elements in the matrix of the steel, and consequently also in the extracted regions.

μ-BS could be used to quantify the elemental distribution of C in the steel specimen. The BS data showed that the diffusion of C over the entire scanned area was undoubtedly non-linear, but in regions of high C concentration the diffusion was essential linear. From this it was inferred that the diffusion profile of C in low concentration regions of the element is non-linear. Cluster formation of C only occurred in regions where the C concentration is relatively low and the phase of the agglomerates that constitute the cluster was L-Fe_3-C. Incomplete nucleation is present in the matrix and the concentration of Cr in the nucleus was relatively high compared to the concentration in the surrounding regions. The ratio of the primary to secondary arms of the micro-segregation agrees with the value determined theoretically by various authors.

4.5 Overview

The advanced instrumentation, discussed in section [3] and the theoretical fundamentals, explained in section [2], on which this instrumentation is based, are mere implements available to the researcher, with which the ultimate aim would be to not only contribute to present-day science, but to establish further in-roads. The onus therefore rests with the researcher to demonstrate unique applications of these theories and instrumentation to the industrial sector of the economy.

This demonstration was achieved firstly to the identification of sorption electrodes, destined to be used in the purification of contaminated water. This purification is essential in the world where frontiers of industrial development are extended often further than it could be sustained by present circumstances. The sorption electrode matrix consists primarily of alumina into which was incorporated zirconia and the electrode was coated with metals and rare-earth metals. Use of the implements facilitated the complete quantification of the sorption electrodes from the purely elemental composition to the determination of inhomogeneities that varied in dimension of micrometers. In addition, this micro-variation was the applied to establish degree to which the applicability of the sorption electrodes would purify the contaminated water. The model applied for the evaluation of the ceramic-based sorption electrode compares well with those of Bladergroen (2002).

In the second instance, new information was made available on the preparation of high temperature superconductors, where the compositional variation in depth with pulsed laser energy density could be ascertained. Hence by adjusting the use of the instrumentation, the composition could be quantified as the layer increased in thickness.

The third instance, in which this demonstration was achieved is in the quantification of steel, where, with the incorporation of residual elements the quality of the product could at will be pre-determined. This pre-determination was based in the results such as the effect of elemental distribution of residual elements on the characteristics of the specimen; the diffusion profile of the incorporated carbon in region of high or low concentration; the significance of chemical composition in cluster formation and the nucleation, even though this nucleation appears to be incomplete. To reach beyond the quantification of the available data, this data were also applied to proposed theories, an application, which proved that there, exists an agreement between the two.

In these three instances the unique application of the micro-analytical techniques was demonstrated.

Chapter 5

APPENDICES

Appendix [5.1]

Appendix [5.1] ***Values of universal constants used in this study. The symbol of the constant, the uncertainty, u_Z, in determination, expressed as ppm ($\mu g.g^{-1}$), and where necessary, the equation are given. Other constants have been included for completion (Nist, 2001).***

Quantity	Symbol, equation	Value	Uncert. (ppm)
speed of light in vacuum[4]	c	2.997 924 58×10^{10} cm s^{-1}	0
Planck constant	h	6.626 075 5(40)×10^{-27} erg s	0.60
Planck constant, reduced	$\hbar = h/2\pi$	1.054 572 66(63)×10^{-27} erg s	0.60
		= 6.582 122 0(20)×10^{-22} MeV s	0.30
electron charge magnitude	e	4.803 206 8(15)×10^{-10} esu	0.30
		= 1.602 177 33(49)×10^{-19} coulomb	0.30
conversion constant	$\hbar c$	197.327 053(59) MeV fm	0.30
conversion constant	$(\hbar c)^2$	0.389 379 66(23) GeV^2 mbarn	0.59
electron mass	m_e	0.510 999 06(15) MeV/c^2 = 9.109 389 7(54)×10^{-28} g	0.30, 0.59
proton mass	m_p	938.272 31(28) MeV/c^2 = 1.672 623 1(10)×10^{-24} g	0.30, 0.59
neutron mass	m_n	939.565 63(28) MeV/c^2 = 1.674 928 6(10)×10^{-24} g	0.30, 0.59
		= 1.008 664 904(14) amu	0.014
deuteron mass	m_d	1875.613 39(57) MeV/c^2	0.30
atomic mass unit (amu)	(mass C^{12} atom)/12 = (1 g)/N_A	931.494 32(28) MeV/c^2 = 1.660 540 2(10)×10^{-24} g	0.30, 0.59
electron charge to mass ratio	e/m_e	5.272 808 6(16)×10^{17} esu g^{-1}	0.30
		= 1.758 819 62(53)×10^8 coulomb g^{-1}	0.30
quantum of magnetic flux	h/e	4.135 669 2(12)×10^{-15} joule s coulomb^{-1}	0.30
Josephson frequency-voltage ratio	2e/h	4.835 976 7(14)×10^{14} cycles s^{-1} v^{-1}	0.30
Faraday constant	F	9.648 530 9(29)×10^4 coulomb mol^{-1}	0.30
fine-structure constant	$\alpha = e^2/\hbar c$	1/137.035 989 5(61)	0.045
classical electron radius	$r_e = e^2/m_e c^2$	2.817 940 92(38) fm	0.13
electron Compton wavelength	$\lambda_e = \hbar/m_e c = r_e \alpha^{-1}$	3.861 593 23(35)×10^{-11} cm	0.089
proton Compton wavelength	$\lambda_p = \hbar/m_p c$	2.103 089 37(19)×10^{-14} cm	0.089
neutron Compton wavelength	$\lambda_n = \hbar/m_n c$	2.100 194 45(19)×10^{-14} cm	0.089
Bohr radius ($m_{nucleus} = \infty$)	$a_\infty = \hbar^2/m_e e^2 = r_e \alpha^{-2}$	0.529 177 249(24)×10^{-8} cm	0.045
Rydberg energy	$hcR_\infty = m_e e^4/2\hbar^2 = m_e c^2\alpha^2/2$	13.605 698 1(40) eV	0.30
Thomson cross section	$\sigma_T = 8\pi r_e^2/3$	0.665 246 16(18) barn	0.27
Bohr magneton	$\mu_B = e\hbar/2m_e c$	5.788 382 63(52)×10^{-15} MeV gauss^{-1}	0.089
nuclear magneton	$\mu_N = e\hbar/2m_p c$	3.152 451 66(28)×10^{-18} MeV gauss^{-1}	0.089
electron cyclotron frequency/field	$\omega^e_{cycl}/B = e/m_e c$	1.758 819 62(53)×10^7 radian s^{-1} gauss^{-1}	0.30
proton cyclotron frequency/field	$\omega^p_{cycl}/B = e/m_p c$	9.578 830 9(29)×10^3 radian s^{-1} gauss^{-1}	0.30
gravitational constant	G_N	6.672 59(85)×10^{-8} cm^{3}g^{-1} s^{-2}	128
grav. acceleration, sea level, 45° lat.	g	980.665 cm s^{-2}	0
Fermi coupling constant	$G_F/(\hbar c)^3$	1.166 39(2)×10^{-5} GeV^{-2}	20
Avogadro number	N_A	6.022 136 7(36)×10^{23} mol^{-1}	0.59
molar gas constant, ideal gas at STP	R	8.314 510(70)×10^7 erg mol^{-1} K^{-1}	8.4
Boltzmann constant	k	1.380 658(12)×10^{-16} erg K^{-1}	8.5
		= 8.617 385(73)×10^{-5} eV K^{-1}	8.4
molar volume, ideal gas at STP	$N_A k(273.15\ K)/(\text{atmosphere})$	22 414.10(19) cm^3 mol^{-1}	8.4
Stefan-Boltzmann constant	$\sigma = \pi^2 k^4/60\hbar^3 c^2$	5.670 51(19)×10^{-5} erg s^{-1} cm^{-2} K^{-4}	34
first radiation constant	$2\pi hc^2$	3.741 774 9(22)×10^{-5} erg cm^2 s^{-1}	0.60
second radiation constant	hc/k	1.438 769(12) cm K	8.4

Appendix [5.2.2]

Figure [5.2.2(a)] ***Background correction using a 125μm thick Be absorber. The continuous line is the average of 10 spectral backgrounds digitized from the GeoPIXE II spectra and the discontinuous line is the theoretical background calculated from equations in Ishii and Morita (1988).***

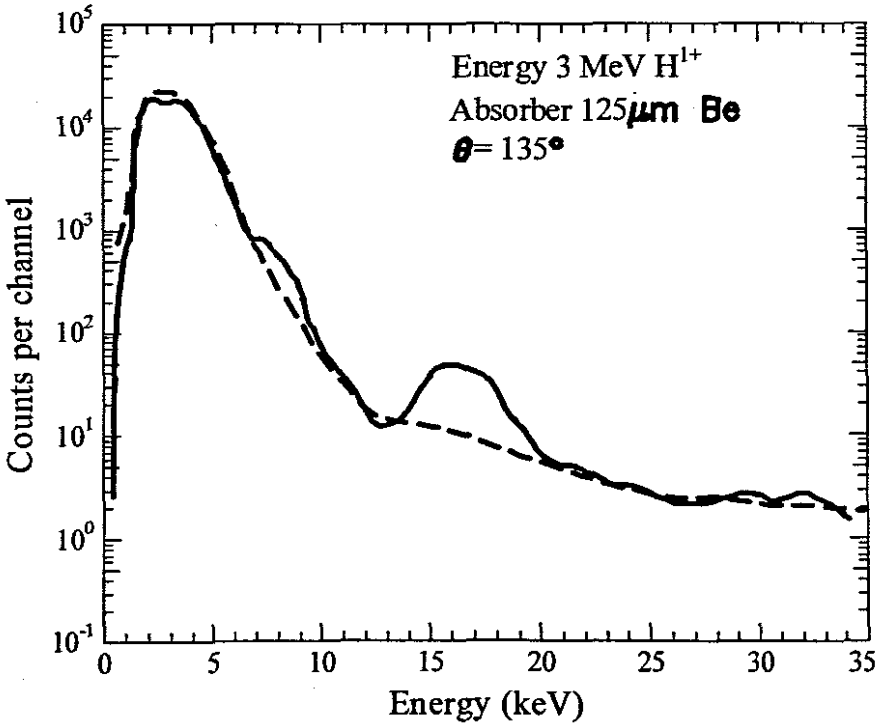

Figure [5.2.2.(b)] ***Background correction using a 102μm thick Al absorber. The continuous line is the average of 10 spectral backgrounds digitized from the GeoPIXE II spectra and the discontinuous line is the theoretical background calculated from equations in Ishii and Morita (1988).***

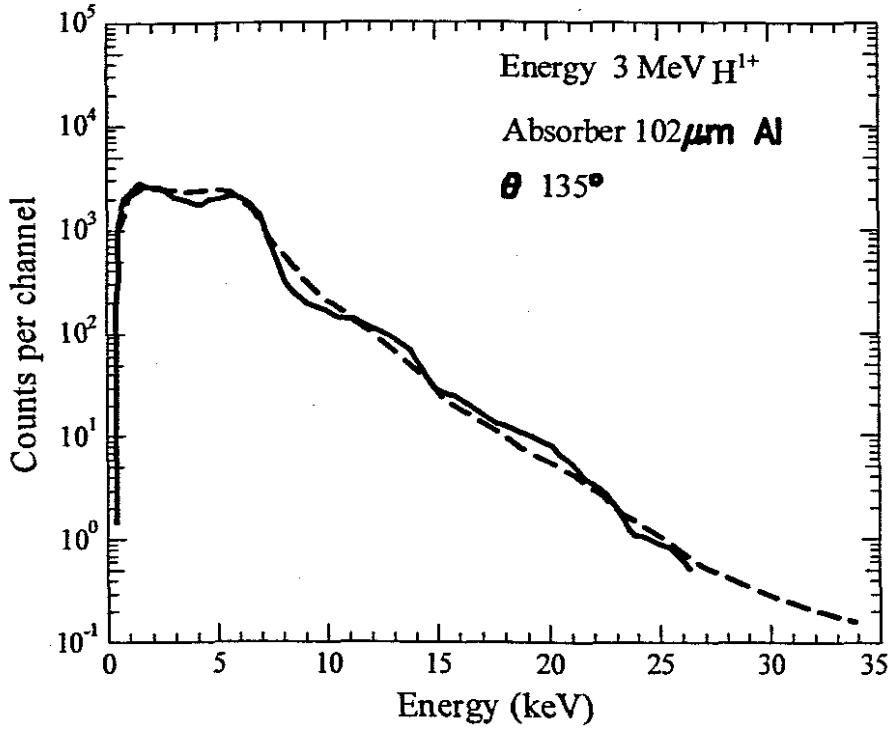

Appendix [5.2.3]

Appendix [5.2.3] ***The channels of possible nuclear reactions when the nuclei of elements lithium to magnesium, regarded in this study as light elements, are bombarded with 3 MeV protons. The calculations are based on the work of Moller et al. (1995). Both the corresponding Q-values and threshold energies, in MeV, are given.***

Lithium

Reaction Products	*Q*-Value (MeV)	Threshold (MeV)
2α	17.34696	0.00000
$^{8}Be + \gamma$	17.25512	0.00000
$^{7}Li + p$	0.00000	0.00000
$^{7}Be + n$	-1.64418	1.88036
$p + t + \alpha$	-2.46705	2.82143

Beryllium

Reaction Products	*Q*-Value (MeV)	Threshold (MeV)
$^{10}B + \gamma$	6.58585	0.00000
$^{6}Li + \alpha$	2.12535	0.00000
$d + 2\alpha$	0.65102	0.00000
$^{8}Be + d$	0.55918	0.00000
$^{9}Be + p$	0.00000	0.00000
$n + p + 2\alpha$	-1.57357	1.74955
$^{8}Be + n + p$	-1.66541	1.85166
$^{9}B + n$	-1.85049	2.05743
$^{5}He + p + \alpha$	-2.46358	2.73908

Boron

Reaction Products	*Q*-Value (MeV)	Threshold (MeV)
$^{12}C + \gamma$	15.95708	0.00000
3α	8.68229	0.00000
$^{8}Be + \alpha$	8.59045	0.00000
$^{11}B + p$	0.00000	0.00000

Appendix [5.2.3] (continued) ***The products of possible nuclear reactions when the nuclei of elements lithium to magnesium, regarded in this study as light elements, are bombarded with 3 MeV protons. The calculations are based on the work of Moller et al. (1995). The corresponding Q-values and threshold energies, both in MeV, are given.***

Carbon

Reaction Products	*Q*-Value (MeV)	Threshold (MeV)
$^{13}N + \gamma$	1.94353	0.00000
$^{12}C + p$	0.00000	0.00000

Nitrogen

Reaction Products	*Q*-Value (MeV)	Threshold (MeV)
$^{15}O + \gamma$	7.29706	0.00000
$^{14}N + p$	0.00000	0.00000

Oxygen

Reaction Products	*Q*-Value (MeV)	Threshold (MeV)
$^{17}F + \gamma$	0.60027	0.00000
$^{16}O + p$	0.00000	0.00000

Fluorine

Reaction Products	*Q*-Value (MeV)	Threshold (MeV)
$^{20}Ne + \gamma$	12.84360	0.00000
$^{16}O + \alpha$	8.11372	0.00000
$^{12}C + 2\alpha$	0.95175	0.00000
$^{19}F + p$	0.00000	0.00000

Appendix [5.2.3] (continued) ***The products of possible nuclear reactions when the nuclei of elements lithium to magnesium, regarded in this study as light elements, are bombarded with 3 MeV protons. The calculations are based on the work of Moller et al. (1995). The corresponding Q-values and threshold energies, both in MeV, are given.***

Sodium

Reaction Products	*Q*-Value (MeV)	Threshold (MeV)
$^{24}Mg + \gamma$	11.69296	0.00000
$^{20}Ne + \alpha$	2.37652	0.00000
$^{23}Na + p$	0.00000	0.00000
$^{16}O + 2\alpha$	-2.35336	2.45653

Magnesium

Reaction Products	*Q*-Value (MeV)	Threshold (MeV)
$^{25}Al + \gamma$	2.27135	0.00000
$^{24}Mg + \alpha$	0.00000	0.00000

Aluminium

Reaction Products	*Q*-Value (MeV)	Threshold (MeV)
$^{28}Si + \gamma$	11.58503	0.00000
$^{24}Mg + \alpha$	1.60062	0.00000
$^{27}Al + p$	0.00000	0.00000

Phosphorus

Reaction Products	*Q*-Value (MeV)	Threshold (MeV)
$^{32}S + \gamma$	8.86403	0.00000
$^{28}Si + \alpha$	1.91587	0.00000
$^{31}P + p$	0.00000	0.00000

Appendix [5.2.3] (continued) ***The products of possible nuclear reactions when the nuclei of elements lithium to magnesium, regarded in this study as light elements, are bombarded with 3 MeV protons. The calculations are based on the work of Moller et al. (1995). The corresponding Q-values and threshold energies, both in MeV, are given.***

Potassium

Reaction Products	*Q*-Value (MeV)	Threshold (MeV)
$^{41}Ca + \gamma$	8.89152	0.00000
$^{37}Ar + \alpha$	2.27709	0.00000
$^{40}Ca + n$	0.52874	0.00000
$^{40}K + p$	0.00000	0.00000

Calcium

Reaction Products	*Q*-Value (MeV)	Threshold (MeV)
$^{41}Sc + \gamma$	1.08508	0.00000
$^{40}Ca + p$	0.00000	0.00000

Chromium

Reaction Products	*Q*-Value (MeV)	Threshold (MeV)
$^{24}Mg + \gamma$	11.69296	0.00000
$^{20}Ne + \alpha$	2.37652	0.00000
$^{23}Na + p$	0.00000	0.00000
$^{16}O + 2\alpha$	-2.35336	2.45653

Manganese

Reaction Products	*Q*-Value (MeV)	Threshold (MeV)
$^{56}Fe + \gamma$	10.18367	0.00000
$^{52}Cr + \alpha$	2.57049	0.00000
$^{55}Mn + p$	0.00000	0.00000
$^{55}Fe + n$	-1.01374	1.03234

Appendix [5.2.3] (continued) ***The products of possible nuclear reactions when the nuclei of elements lithium to magnesium, regarded in this study as light elements, are bombarded with 3 MeV protons. The calculations are based on the work of Moller et al. (1995). The corresponding Q-values and threshold energies, both in MeV, are given.***

Iron

Reaction Products	*Q*-Value (MeV)	Threshold (MeV)
$^{57}Co + \gamma$	6.02768	0.00000
$^{56}Fe + p$	0.00000	0.00000
$^{53}Mn + \alpha$	-1.05333	1.07231

Copper

Reaction Products	*Q*-Value (MeV)	Threshold (MeV)
$^{65}Zn + \gamma$	7.77601	0.00000
$^{61}Ni + \alpha$	3.66006	0.00000
$^{64}Cu + p$	0.00000	0.00000
$^{64}Zn + n$	-0.20362	0.20683
$^{57}Fe + 2\alpha$	-2.80596	2.85020

Zinc

Reaction Products	*Q*-Value (MeV)	Threshold (MeV)
$^{66}Ga + \gamma$	5.10254	0.00000
$^{62}Cu + \alpha$	1.75082	0.00000
$^{65}Zn + p$	0.00000	0.00000

Yttrium

Reaction Products	*Q*-Value (MeV)	Threshold (MeV)
$^{90}Zr + \gamma$	8.35487	0.00000
$^{86}Sr + \alpha$	1.68353	0.00000
$^{89}Y + p$	0.00000	0.00000

Appendix [5.2.3] (continued) ***The products of possible nuclear reactions when the nuclei of elements lithium to magnesium, regarded in this study as light elements, are bombarded with 3 MeV protons. The calculations are based on the work of Moller et al. (1995). The corresponding Q-values and threshold energies, both in MeV, are given.***

Zirconium

Reaction Products	*Q*-Value (MeV)	Threshold (MeV)
$^{92}Nb + \gamma$	5.84684	0.00000
$^{88}Y + \alpha$	1.27000	0.00000
$^{91}Zr + p$	0.00000	0.00000
$^{91}Nb + n$	-2.03576	2.05833

Barium

Reaction Products	*Q*-Value (MeV)	Threshold (MeV)
$^{138}La + \gamma$	6.09166	0.00000
$^{134}Cs + \alpha$	4.03318	0.00000
$^{130}I + 2\alpha$	1.64496	0.00000
$^{137}Ba + p$	0.00000	0.00000
$^{126}Sb + 3\alpha$	-1.31478	1.32446
$^{137}La + n$	-1.38248	1.39265
$^{133}Xe + p + \alpha$	-2.50341	2.52184
$^{133}Cs + n + \alpha$	-2.85841	2.87946

Appendix [5.2.4] ***Proton backscattered spectrum of the Ir on Si standard used in the calibration of backscattering data. The inset shows the Ir peak.***

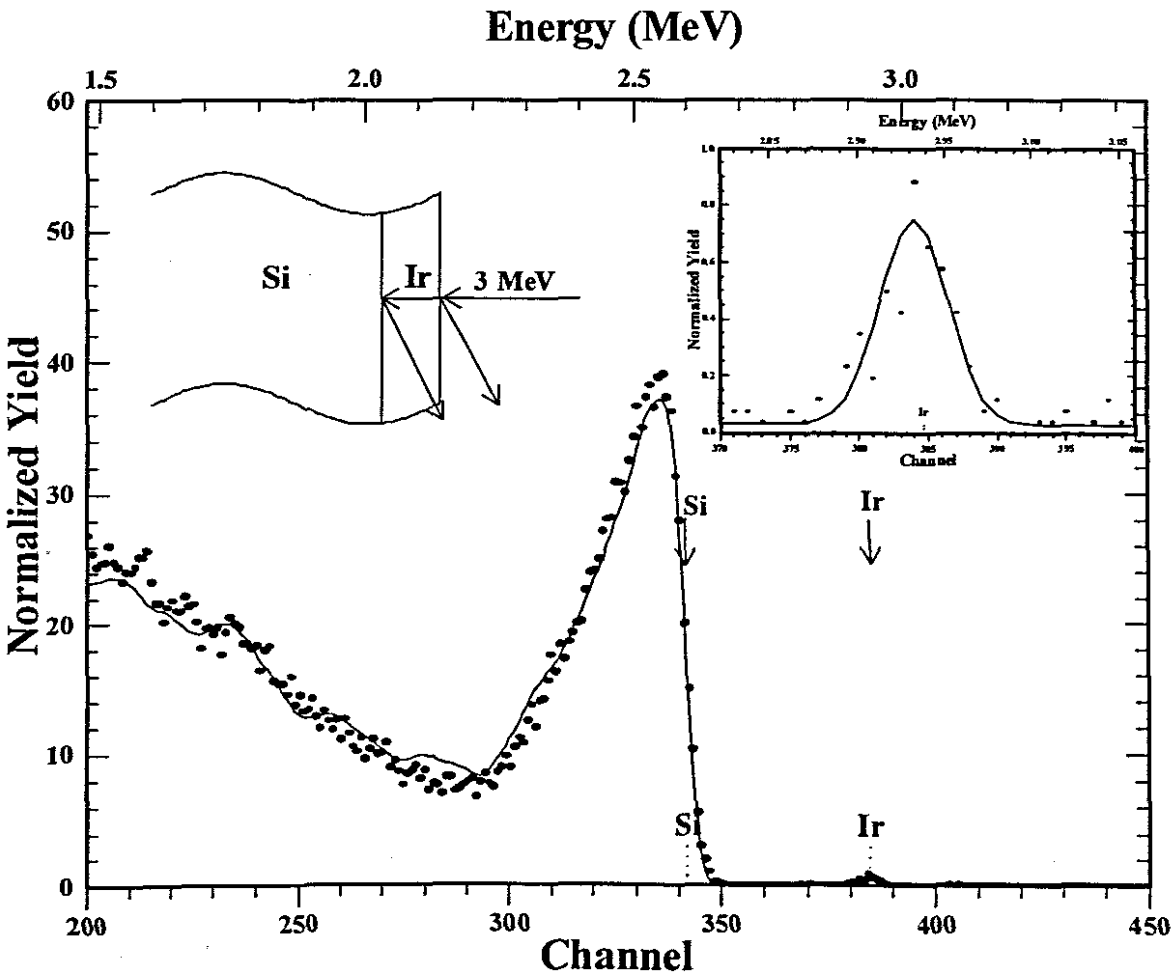

Chapter 6

Bibliography

AMIRIKAS, R., JAMIESON, D.N. & DOOLEY, S.P. (1993) Measurement of (p,p) elastic cross sections for C, O, and Si in the energy range 1.0-3.5 MeV. Nuclear Instruments and Methods Research in Physics Research B., vol. 77, pp 110-116.

ATKINS, P. (1999) The Elements of Physical Chemistry. 3rd Edition, Oxford University Press, London.

BANKS, T., BEAM, C. & BERTA, Y. (2001) The Phase Diagram Web. [Internet] Available from :<http://cyberbuzz.gatech.edu/asm_tms/phase-diagrams/pd> [Accessed July 30th, 2001].

BASHKIN, S., CARLSON, R.R & DOUGLAS, R.A. (1957) Cross section for elastic scattering of protons by N^{14}. Physical Review., vol. 114, pp. 114-115.

BAUDRAND, D. (1995) Electroless processes. Plating and Surface Finishing, vol. 50, pp. 57-59.

BECKERMANN, C. & VISKANTA, R. (1993) Mathematical modeling of transport phenomena during alloy solidification. Applied Mechanics Review., vol. 46, pp.1-27.

BEDNORZ, J.G. & MULLER, K.A. (1986) Possible High T_c Superconductivity in the Ba-La-Cu-O system. Zeitschrift fur Phyzik B., vol. 64, pp. 189-193.

BHADESHIA, K.D.H. (2001) Dendritic solidification. [Internet] Available from :<http://www.msm.cam.ac.uk/phase-trans/dendrites.html> [Accessed July 30th, 2001].

BLADERGROEN, B.J. (2001) Electrochemically Activated Ceramic-based Sorption Electrodes. Ph.D. Thesis, University of the Western Cape, Bellville.

BLONDIAUX, G., DUCOURET, G., DEBRUN, J.L., GOUJARD, S. & VAN DEN BULCKE, L. (1993) Development of a nuclear analytical technique for the analysis of ternary compounds (boron plus carbon plus silicon) and application to the optimization of a chemical vapour deposition process. Nuclear Instruments and Methods Research in Physics Research B., vol. 79, pp. 521-523.

BONI, C., CARIDI, A., CEREDA, E., PARMIGIANI, F., BRAGA-MARCAZZAN, G.M. & SCAGLIOTTI, M. (1990) Determination of the Li/Ni ratio in Li_xNi_{1-x0} thin films by PIXE/ PIGE analysis. Nuclear Instruments and Methods in Physics Research B., vol. 50(1-4), pp. 243-246.

BORBELY, K., JOZA, M., KISS, A.Z., KOLTAY, E., NYAKO, B., SOMORJAI, E. & SZABO, G.Y. (1985) Determination of elemental constituents in high voltage insulator borosilicate glasses under proton bombardment. Journal of Radioanalytical and Nuclear Chemistry Articles., vol. 92(2), pp. 391-398.

BRANDT, W. & LAPICKI, G. (1981) Energy-loss effect in inner-shell Coulomb ionisation by heavy charge particles. Physical Review A., vol. 23, pp. 1717-1729.

BUTZ, T. (1997) Nukleare Festkorperphyzik. [Internet] Available from:< http://www.uni-leipzig.de/~nfp/met_fr.htm> [Accessed July 30th, 2001].

CALASTRINI, F., DEL CARMINE, P., LUCARELLI, F., MANDO, P.A. & PRATI, P. (1998) External-beam PIGE for fluorine determination in atmospheric aerosol. Nuclear Instruments and Methods in Physics Research B., vols. 136-138, pp. 975-980.

CAMPBELL, J.L., PERUJO, A. & TEESDALE, W.J. (1988) Minimum Detection Analysis of Thick Samples. Nuclear Instruments and Methods Research in Physics Research B., vol. 30, pp. 317-323.

CHEN, K. & CHEN, Y. (1997) A new electroless nickel plating process. Plating and Surface Finishing, vol. 84, pp. 80-82.

CHEN, M.H. & CRASEMANN, B. (1985) Relativistic Cross Sections for Atomic K- and L-shell Ionization by Protons, calculated from a Dirac-Hartree-Slater model. Atomic Data and Nuclear Data Tables., VOL. 33, PP. 217-234.

CHIARI, M., GIUNTINI, L., MANDO, P.A. & TACCETTI, N. (2001) Proton elastic scattering cross section on aluminium from 0.8 to 3 MeV. Nuclear Instruments and Methods in Physics Research B., vol. 174, pp. 259-261

CHIARI, M., GIUNTINI, L., MANDO, P.A. & TACCETTI, N. (2001) Proton elastic scattering cross section on boron from 0.8 to 3 MeV. Nuclear Instruments and Methods in Physics Research B., vol. 184, pp. 309-311

CHU, T.C., ISHII, K., YAMADERA, A., SEBATA, M. & MORITA, S. (1981) Angular dependence of the detection limit of PIXE. Nuclear Instruments and Methods in Physics Research B.,

vol. 190, pp. 395-399.

CHU, W-K., MAYER, J.W. & NICOLET. M-A. (1978) Backscattering Spectrometry. Academic Press, New York.

CHURMS, C. (1995) Facilitating the Identification of Solid state Phases and Concentrations in Micro-volumes. Ph.D. Thesis, University of Stellenbosch.

CLAYTON, E. & RYAN, C.G. (1990) Weighting measures in fitting PIXE Spectra. Nuclear Instruments and Methods in Physics Research B., vol. 49, pp. 163-165.

COOTE, G.E. (1992) Ion beam analysis of fluorine: Its principles and applications. Nuclear Instruments and Methods in Physics Research B., vol. 65, pp. 191-204.

CORNELL, R & BHADESHIA, K.D.H. (2001) Metals and alloys: Metallographic specimen MO, Decarburization of steel. [Internet] Available from :<http://www.msm.cam.ac.uk/phase-trans/> [Accessed May 30th, 2001].

COTTON, F.A., WILKINSON, G., MURILLO, C.A. & BOCHMANN, M. (1999) Advanced Inorganic Chemistry, 6th edition, John Wiley & Sons, New York.

CURRIE, L.A. (1968) Limits for Qualitative Detection and Quantitative Determination. Analytical Chemistry., vol. 40, pp.586-593.

DAVIES, J. & KENT, D.B. (2002) Surface Complexation Modeling: A Review and Discussion.

[Internet] Available from :<http://www.cmd.edu/pr/ weekly/ > [Accessed July 10th, 2002].

DEBERTIN, K. & HELMER, R.G. (1988) Gamma- and X-ray Spectrometry with Semiconductor Detectors. North Holland Publishers, New York.

DECONNINCK, G. (1978) Introduction to Radioanalytical Physics. Elsivier Scientific Publishing Company, New York.

DOOLITTLE, L.R. (1985) Algorithms for the rapid simulation of Rutherford Backscattering. Nuclear Instruments and Methods in Physics Research B., vol. 9, pp. 344-351.

L'ECUYER, J.A., DAVIES, J.A. & MATSUNAMI, N. (1979) How accurate are absolute Rutherford backscattering yields. Nuclear Instruments and Methods in Physics Research B., vol. 160, pp. 337-346.

EHMANN, W.D. & VANCE, D. (1991) Radiochemistry and Nuclear Methods of Analysis. John Wiley and Sons Inc. New York, NY.

EISBERG R. & RESNICK, R. (1985) Quantum Physics of Atoms, Molecules, Solids, Nuclei and Particles. John Wiley & Sons, New York.

EURACHEM (2000) Eurachem/Citac Guide-Quantifying Uncertainty in Analytical Measurement.

FAZINIC, S., BOGDANOVIC, I., JAKSIC, M., VALKOVIC, V., & CEREDA, E. (1995) Stoichiometric determination of thin metal oxide films. Nuclear Instruments and Methods in Physics Research B., vol. 75, pp. 371-374.

FRIEDLANDER, G., KENNEDY, J.W., MACIAS, E. S. & MILLER, J.M. (1981) Nuclear and Radiochemistry (3rd Ed). John Wiley & Sons, New York.

GANESAN, S. & POIRIER, D.R. (1990) Conservation of mass and momentum for the flow of interdendritic liquid during solidification. Metallurgical Transactions B., vol. 21B, pp. 173-181.

GIANCOLI, C. G. (1997) Physics: Principles with Applications (5th Ed). Prentice-Hall Incorporated.

GIHWALA, D. (1982) Analytical Application of Proton-Induced Prompt Photon Spectrometry. Ph.D. Thesis, University of Cape Town.

GIHWALA, D. & PEISACH, M. (1982) Prompt-induced gamma-ray Spectrometry: A survey of its analytical significance and some applications. Journal of Radioanalytical Chemistry., vol. 70, pp. 287-309.

GIHWALA, D. & PEISACH, M. (1986) Determination of oxygen by deuteron-induced pipps. Journal of Radioanalytical and Nuclear Chemistry Letters., vol. 106, pp. 9-20.

GILES, I.S. (1978) Elemental Analysis by Alpha-Induced Prompt Gamma-ray Spectrometry. PhD. Thesis, University of Cape Town.

GILMORE, G. & HEMMINGWAY, J. (1995) Practical Gamma-ray Spectrometry. John Wiley and Sons, New York.

GULLIKSON, E.M. (2002) Mass absorption coefficients. <[Internet] Available from:<http:// http://xdb.lbl.gov/Section1/Sec_1-6.pdf/> [Accessed June 20th, 2002].

GURBICH, A.F. (1997) Evaluation of non-Rutherford proton elastic scattering cross section for oxygen. Nuclear Instruments and Methods Research in Physics Research B., vol. 129, pp. 311-316.

GURBICH, A.F. (1998) Evaluation of non-Rutherford proton elastic scattering cross section for carbon. Nuclear Instruments and Methods Research in Physics Research B., vol. 136-138, pp. 60-65.

GYARMATI, B., LOVAS, R.G., VERTSE, T. & HODGSON, P.E. (1981) Low-energy behaviour of the real depth of the proton optical potential. Journal of Nuclear Physics., vol 7(9), pp. L209-L213.

HENKE, B.L., GULLIKSON, E.M. & DAVIS, J.C. (1993) X-ray Interactions: Photonabsorption, scattering, transmission and Reflection at E = 50-30000 keV, z = 1-92. Atomic Data and Nuclear Data Tables., vol. 54, pp 181-368.

HOGAN, J. (2002) pSOSystem for Integrated Systems. [Internet] Available from: <http://www.realtime-info.be/magazine/97Q3/1997q3_p014.pdf> [Accessed Feb. 30th, 2002]

HONMA, H., HASEGAWA, A. & HOTTA, S. (1995) Electroless plating by disulfiteaurate complex. Plating and Finishing., vol. 50, pp 89-92.

ISHII, K. & MORITA, S. (1988) Theoretical estimation of PIXE detection limits. Nuclear Instruments and Methods in Physics Research B., vol. 34, pp. 209-216.

ISHII, A. & NAKAMURA, K. (1993) RBS-PIXE analysis on thin films of high-T_c oxide superconductors. Nuclear Instruments and Methods in Physics Research B., vol. 75(1-4), pp. 388-391.

IUPAC (1978) (International Union of Pure and Applied Chemistry) Minimum detection limits of peak areas. Spectrochimica Acta., vol. 33B, p 241.

JAKSIC, M., BOGDANOVIC, S. & FAZINIC, S. (1995) Limits of detection for PIXE analysis using proton microbeam. Nuclear Instruments and Methods in Physics Research B., vol. 104, pp. 152 -156.

JOHANSSON, S.A.E. & CAMPBELL, J.L. (1988) PIXE-A Novel Technique for Elemental Analysis. John Wiley & Sons, New York.

JOHANSSON, S.A.E., CAMPBELL, J.L. & MALMQVIST, K.G. (1995) Particle-Induced X-Ray Emission (PIXE). John Wiley & Sons, New York.

KIM, Y.S., CHOI, H.W., KIM, D.K., WOO, H.J. & KIM, N.B. (2000) Analysis of light elements by PIGE. Analytical Science and Technology., vol. 13(1), pp. 12-21.

KINNEY, J. (2002) Statistics for Science and Engineering. Addison Wesley Higher Education, New York.

KNOX, J.M. (1992) Non-Rutherford scattering of protons by light elements. Nuclear Instruments and Methods in Physics Research B., vol. 66, pp. 31-37.

KNOX, J.M., McLEOD, R.J., MAYO, D.R. & QIAN, X. (1990) Fits of non-Rutherford cross section and their inclusion in the RUMP simulator. Nuclear Instruments and Methods in Physics Research B., vol. 45, pp. 26-29.

LACKAY, L.G., GIHWALA, D. & PEISACH, M. (1990) Measurement of proton-induced prompt low energy photons by high resolution spectrometry: The analysis of noble metals. Journal of Radioanalytical and Nuclear Chemistry., vol. 151(1), pp. 213-220.

LACKAY, L.G., GIHWALA, D. & PEISACH, M. (1991) Nuclear analysis: basic studies. Measurement of proton-induced prompt low energy photons by high resolution spectrometry: the analysis of noble metals. National Accelerator Centre, Faure (South Africa). NAC Annual Report March 1991., p. 51.

LAPPALAINEN, R. ANTTILA, A. & RASIANEN, J. (1983) Absolute α-induced gamma-ray yields for the elemental analysis of light elements. Nuclear Instruments and Methods in Physics Research B., vol. 212, pp. 441-444.

LI, Q., FAN, W., SUN, C. & LIANG, W. (1997) Coating of nanotubes with nickel by Electroless plating method. Journal of Applied Physics., vol. 37, pp. 501-503.

LINKOV, V.M. & BELYAKOV, V. (1997) Support separation–electroconductive support. Progress Report summary to ESKOM.

MacFARLANE, R.E. & MOLLER, P. (1997) Qtool. [Internet] Available from :<http://t2.lanl.gov/cgi-bin/qtool > [Accessed July 30th, 2001].

MALMQVIST, K.G. (1995) Analytical techniques in nuclear microprobes. Nuclear Instruments and Methods in Physics Research B., vol. 104, pp. 138-151.

MARS, J.A., GIHWALA, D. & PRZYBYLOWICZ, W.J. (2000) Zirconium alumina tubes coated with rare-earth metals. Presentation at the 45th South African Physics Conference., Rand Afrikaanse University, Johannesburg, South Africa.

MARS, J.A., GIHWALA, D. & PRZYBYLOWICZ, W.J. (2001) Depth profiling of high temperature superconductors. Presentation at the Polish International Symposium on Condense Matter Studies by Nuclear Methods., XXXVI Zakopane School of Physics, Poland.

MARS, J.A., GIHWALA, D. & PRZYBYLOWICZ, W.J. (2003) Fits of Non-Rutherford cross sections of light elements. (In preparation).

MARS, J.A., GIHWALA, D. & PRZYBYLOWICZ, W.J. (2003) μ-IBA analysis of Al_2O_3 impregnated with ZrO_2. (In preparation).

MARS, J.A., GIHWALA, D. & PRZYBYLOWICZ, W.J. (2003) Depth profiling of YBCO prepared by pulsed-laser deposition. (In preparation).

MARS, J.A., GIHWALA, D. & PRZYBYLOWICZ, W.J. (2003) μ-IBA analysis of Steel: Quantification across the carbon nucleus. (In preparation).

MAXWELL, J.A., CAMPBELL, J.,L. & TEESDALE, W.,J. (1988) The Guelph PIXE Software Package. Nuclear Instrument and Methods in Physics Research B., vol. 43, pp. 218-230.

MAZZONI, S., CHIARI, M., GIUNTINI, L., MANDO, P.A. & TACCETTI, N. (1998) Proton elastic scattering cross section carbon from 350 keV to 3 MeV. Nuclear Instruments and Methods in Physics Research B., vol. 136-138, pp. 86-90.

MAZZONI, S., CHIARI, M., GIUNTINI, L., MANDO, P.A. & TACCETTI, N. (1998) Erratum to: Proton elastic scattering cross section carbon from 350 keV to 3 MeV. [Nuclear Instruments and Methods in Physics Research B., vol. 136-138, pp. 86-90.], Nuclear Instruments and Methods in Physics Research B., vol. 159, pp. 191.

MO, A. (1994) An internal variable description of solidification suitable for macrosegregation modeling. Metallurgical and Materials Transactions B., vol.25B, pp. 597-605.

MOOLLAN, R. (2002) Effluent analysis for the period July 2001 to June 2002. Scientific Services Department, Athlone Wastewater Treatment Works, Cape Town.

MOLLER, P., NIX, J.R., MYERS, W.D. & SWIATECKI, W.J. (1995) Nuclear ground-state masses and deformations. Atomic Data and Nuclear Data Tables., vol. 89, pp. 185-381.

MOORE, H., MAH, T. & BROWN, P.W. (1997) Carbon coating of Nextel 550 and 720 by pitch-toluene pyrolysis. Journal of the American Ceramic Society., vol. 80, pp. 1285-1288.

MORGAN, G. (2001) Nanotechnology. [Internet] Available from :<http://www.cmd.edu/pr/weekly/> [Accessed July 30th, 2001].

MORGAN, S. (2001) Nanotechnology. [Internet] Available from :<http://www.aeiveos.com/nanotech/info news/> [Accessed July 30th, 2001].

MOSBAH, M., METRICH, N. & MASSIOT, P. (1991) PIGME fluorine determination using a nuclear microprobe with application to glass inclusions. Nuclear Instruments and Methods in Physics Research B., vol. 58, pp. 227-231.

MOZER, F.S. (1956) Elastic scattering of protons by beryllium. Physics Review., vol. 104, pp. 1386-1389.

MULDER, M. (1996) Basic Principles of Support Technology. 2nd edition. Kluwer Academic Publishers, London.

MURILLO, G., POLICRONIADES, R., TENORIO, D., MENDEZ, B., ANDRADE, E., PINEDA, J.C., ZAVAL, E.P. & TORRES, J.L. (1998) Analysis of Mexican obsidians by IBA techniques. Nuclear Instruments and Methods in Physics Research B., vol. 136-138, pp. 888-892.

NAVE, C.R. (2001) X-ray Transitions. [Internet] Available from :<http://hyperphysics.phy-astr.gsu.edu/hbase/hframe.html> [Accessed July 30th, 2001].

NI, J. & BECKERMANN, C. (1990) A Two-phase Model for Mass, Momentum, Heat, and Species Transport During Solidification in: Transport Phenomena in Materials Processing, Editors. M. CHARMCHI et al., ASME, New York, HTD, vol. 132, pp. 45-56.

NIST (2001) American government National Institute of Standards and Technology. [Internet] Available from :< http://www.nist.gov/ > [Accessed July 20th, 2001].

OBUKHOV, G., GOTTWALD, T. & NIKIAS, T. (2002) POVRay. [Internet] Available from :< http://www.povray.org/ > [Accessed July 25th, 2002].

OLIVIER, C., GIHWALA, D., PEISACH, M., PINEDA, C.A. & PIENAAR, H.S. (1983) Determination of lithium in the gem mineral sugilite. Journal of Radioanalytical Chemistry., vol. 76, pp. 241-248.

OLNESS, J.W., VORONA, J. & LEWIS, H.W. (1958) Elastic and inelastic scattering of protons by N^{14}. Physical Review., vol. 112, pp. 475-480.

OXFORD Microbeams (1985) Quadruple Microbeam System, Sample Chamber OM-70e

PAUL, H. & SACHER, J. (1989) Fitted Empirical Reference Cross-Sections for K-shell Ionization by Protons. Atomic Data and Nuclear Data Tables., vol. 42, pp. 105-156.

PEISACH, M., LACKAY, J.G. & GIHWALA, D. (1989) Measurement of proton-induced prompt low energy photons by high resolution spectrometry. Analyst., vol. 114(3), pp. 279-286.

PEISACH, M., MATETA, N. A. & PILLAY, A. E. (1993) Simultaneous PIXE analysis of some adjacent elements. International Journal of PIXE., vol. 3(1), pp. 81-88.

POPESCU, I., BADICA, E., POPA, G., BESLIU, C. & OLARIU, A. (1994) PIXE-PIGE analysis of steel samples. Romanian Physical Society., PO Box MG-6, R-76900 Bucharest.

PROZESKY, V.M., PRZYBYŁOWICZ, W.J., VAN ACHTENBERG, E., CHURMS, C.L., PINEDA, C.A., SPRINGHORN, K.A., PILCHER, J.V., KRITZINGER, J., SCHMITT, H & SWART, T. (1995) The NAC nuclear microprobe facility. Nuclear Instruments and Methods in Physics Research B., vol. 104, pp. 36-42.

RAUHALA, E. (1992) Backscattering Spectrometry in: Elemental Analysis by Particle Accelerators. Editors: Alfassi, Z.B. & Peisach, M. CRC Press, London.

RAUHALA, E. (1994) Ion Backscattering and Elastic Recoil Detection in: Chemical Analysis by Nuclear Methods. Editor: Alfassi, Z.B., John Wiley and Sons.

REN, M.-Q., ONG, W.-Y., MAKJANIC, J. & WATT, F. (1999) Changes in calcium and iron levels in the brains of rats during kainite induced epilepsy. Nuclear Instruments and Methods in Physics Research B., vol. 158, pp. 418-423.

RENAN, M. (2001) Proton-Induced X-ray Emission. [Internet] Available from :< http://www.vulcan.mse.cwru.edu/ > [Accessed March, 20th, 2001].

RENAN, M.J. (1980) Optimization of trace analysis by PIXE (Particle-Induced X-ray Emission): angular dependence of the background continuum. X-Ray-Spectrometry., vol. 9(2), pp. 90-94.

ROUX, F., BAUD, G., BESSE, J.P., CAUDRON, E., JACQUET, M. & BLONDIAUX, G. (1997) Contribution of nuclear analytical techniques in optimization of Li-Ge-O films. Solid State Ionics., vol. 104(3-4), pp. 177-181.

RYAN, C.G., CLAYTON, E., GRIFFIN, D.R., SIE, S.H., SUTER, G.F. & COUSENS, W.L., (1988) SNIP, a statistics-sensitive background treatment for the quantitative analysis of PIXE spectra in geoscience applications. Nuclear Instruments and Methods in Physics Research B., vol. 34, pp. 396.

RYAN, C.G., COUSENS, D.R., SIE, S.H., GRIFFIN, W.L., SUTER, G.F. & CLAYTON, E. (1990) Quantitative Pixe microanalysis of geological material using the CSIRO microprobe. Nuclear Instruments and Methods in Physics Research B., vol. 47, pp. 55-71.

RYAN, C.G., JAMIESON, D.N., CHURMS, C.L. & PILCHER, J.V. (1995) A new method for on-line true-elemental imaging using PIXE and the proton microprobe. Nuclear Instruments and Methods in Physics Research B., vol.104, pp. 157-165.

SATOH, T., ISHII, K. & MATSUYAMA, S (1998) An attempt to suppress the Compton scattering background appearing in the PIXE spectrum. International Journal of PIXE., vol. 8(4), pp.283-288.

SAVAGE, J.M., WONG, A.S & ROBERTSON, J.D. (1992) Thick-target PIXE/PIGE analysis of complex matrices. Journal of Trace and Microprobe Techniques., vol. 10(2&3), pp 151-168.

SHYY, W. & UDAYKUMAR, H.S. (2002) Multi-scale modeling for solidification processing in: Computational Analysis of Convection Heat Transfer., pp. 141-198, WIT Press, Southampton, UK.

SIE, S.H., RYAN, C.G. & SUTER, G.F. (1991) Micro-PIXE (Particle-Induced X-ray Emission) applications in mineral research. Scanning Microscopy., vol. 5(4), pp. 977-987.

SIE, S.H., SUTER, G.F., CHEKMIR, A. & GREEN, T.H. (1995) Microbeam recoil detection for the study of hydration of minerals. Nuclear Instruments and Methods in Physics Research B., vol. 104, pp. 261-265.

SIGMABASE (2001) Cross sections. [Internet] Available from :< http://www.physics.isu.edu/sigmabase/> [Accessed August 20th, 2001].

STATS SA (2001) Manufacturing reports. [Internet] Available from :<http://www.statssa.gov.za/archoves/Reports/> [Accessed May 30th, 2001].

STENDEN, FH., KALTWASSER, S., REYNECKE, D. ANNANDALE, D. &ADAMS, A. (1997) Process theory S2. Saldanha Steel, Saldanha, South Africa.

STEWART, J. (2000) Calculus: Concepts and Contexts. Brooks Cole Publishing Company. USA.

SUNDMAN, B., AGREN, J. & JANSSOM, B. (2000) Computer Predictions of Phase Diagrams. Ashgate Publishing Company.

SUTTON, C.J. & CLAY, P. (2001) Astimex Standards. [Internet] Available from: < http:// www.proscitech.com.au/ > [Accessed July 30th, 2001].

TAPPER, U., VUORINEN, H. & MUSSALO-RUAHAMAA, H. (1990) Elemental analysis of log bones of infants from Ficana excavations. Nuclear Instruments and Methods in Physics Research B., vol. 49, pp. 245-249.

TAPPER, U.A.S., PRZYBYLOWICZ, W.J. & ANNEGARN, H.J. (1994) Particle-Induced X-ray Emission in: Chemical Analysis by Nuclear Methods, Editor Z.B. Alfassi, Wiley and Sons, New York.

TERWAGNE, G., BODART, F., PLANPAIN, B., MOHRBACHER, H. & CELIS, J.-P. (1995) Light elements analysis using ^{3}He microbeam. Nuclear Instruments and Methods in Physics Research B., vol. 105, pp. 266-270.

THEVOSZ, Ph., DESBIOLLES, J.L. & RAPPAZ, M. (2000) Modeling of microstructure formation in casting. Metallurgical Transactions A., vol. 20A, pp. 311-321.

TSENG, A.A., ZOU, J., WANG, H.P. & HOOLE, S.R.H. (1992) Numerical modeling of macro and micro behaviors of materials in processing: A review. Journal of Computational Physics., vol. 102, pp. 1-17.

VALKOVIC, O., JAKSIC, M., VALKOVIC, V., MOSCHINI, G. & MENAPACE, E. (1995) Quality control of PIXE and PIGE nuclear analytical techniques in geological and environmental applications. Nuclear Instruments and Methods in Physics Research B., vol. 99, pp. 372-375.

VAN DE BERG, G.D. (1998) Electroless plating of selected inorganic substances. M. Sc Thesis, University of Potchefstroom, South Africa.

VAN KAN, J.A., RECTOR, J.H., DAM, B. & VIS, R.D. (1994) RBS and PIXE analysis on μm scale thin film high-T_c superconductors. Nuclear Instruments and Methods in Physics Research B., vol. 89, pp. 204-207.

VOLFINGER, M. & ROBERT, J.-L. (1994) Particle-induced gamma-ray emission spectrometry applied to the determination of light elements in individual grains of granite minerals. Journal of Radioanalytical and Nuclear Chemistry, Articles., vol. 185, pp. 273-291.

WANG, C.Y. & BECKERMANN, C. (1993) A multiphase solute diffusion model for dendritic alloy solidification. Metallurgical Transactions A., vol. 24a, pp. 2787-2802.

WANG, C.Y. & BECKERMANN, C. (1993) Single -vs dual-scale volume averaging for heterogenous multiphase systems. International Journal of Multiphase Flow., vol. 19, pp. 397-407.

WILLEMSEN, M.F.C. & KUIPER, A.E.T. (1991) Particle-Induced X-ray emission of Light Elements. Nuclear Instruments and Methods in Physics Research B., vol. 61, pp. 213-220.

XSYS (1985) Xsys - A general purpose data acqusition system. Indianan University Report.

YANG, C-H. & WEN, T-C. (1998) Electrodeposited platinum particles in a sulfonatepolyaniline film for the electosorption of methanol and sorbitol. Electrochemica Acta., vol. 44, pp. 207-218.